MARII CURIE-SKŁODOWSKA UNIVERSITY
IN LUBLIN
Doctoral School of Quantitative and Natural Sciences

Scientific field: Physics
Discipline: Nuclear Physics

Pavel Vladimirovich Kostryukov
nr album: 299688

Dynamic Description of Low and Middle Energy Nuclear Fission

Doctoral dissertation prepared under the scientific supervision of
Dr hab. Artur Dobrowolski

LUBLIN, 30 September 2023

Жди меня, и я вернусь,
Всем смертям назло.
Кто не ждал меня, тот пусть
Скажет: – Повезло.
Не понять, не ждавшим им,
Как среди огня
Ожиданием своим
Ты спасла меня.
Как я выжил, будем знать
Только мы с тобой, –
Просто ты умела ждать,
Как никто другой.

К. М. Симонов, 1941

Dedicated to my wife – Margarita

Preface from the author

The present dissertation is a kind of half-finished compendium of ideas and representations of the description of the properties of the atomic nucleus and its fission process. It presents well-known approaches and methods used in nuclear fission theory, taken from textbooks and review articles, as well as compilations from the author's articles. Of course, the work also includes unpublished material of the author that has not been included in publications or has been developed in the last year.

Despite the enormous amount of work that has been done, the thesis may contain typos, errors, and difficult to understand parts of the text due to translation difficulties. Thinking in the native language was a very heavy obstacle in writing this text. It is also possible that the reader may not be able to understand the logic of the narrative, caused by the overabundance or, on the contrary, the lack of some important details that were omitted in the processes of narration. The reason for this is the inability to cover all the discussed areas of the subject even in a two hundred page research. Nevertheless, the author would be grateful for any questions and suggestions for the improvement of the present work.

Acknowledgements

This work would never have been accomplished (certainly not by me) without the help of a very large circle of people directly or indirectly involved in it. The number of these people is indeed large, and if I were to mention each of them with at least a brief outline of their help, I would have to write a text comparable to the length of a chapter of the thesis. Therefore, I will unfortunately have to limit myself to expressing my gratitude.

First of all, the author would like to express his gratitude to the members of the staff of the Department of Theoretical Physics of UMCS:

- **Dr hab Artur Dobrowolski**
- **Dr Anna Zdeb**
- **Prof Emer Bożena Nerlo-Pomorska**
- **mgr Jose Marin Blanco**
- **Dr hab Michal Warda**

under the supervision of **Prof Krzysztof Pomorski** for the opportunity to participate in the international SHENG-1 project as a PhD student. During the time spent there, none of the group members refused any help or advice. The project helped me to find a key to open the door to the world of big science.

Special thanks, of course, to **my mentor and supervisor – Artur Dobrowolski** for his help in the realization of the research. His concrete patience, unfailing desire to understand what the student is doing, as well as the gift to see the root of the problem have repeatedly helped to get the missing details or find the stupidest mistakes in the problems solved by the author. The supervisor's optimism often replaced my own, which was lost in the walls of my alma mater during the first attempt to obtain a scientific degree. I would also like to thank A. Dobrowolski and K. Pomorski for giving me a very wide autonomy in research and the chance to implement my own solutions, which did not always agree with their vision or methods. And if the honored reader or reviewer can catch the essence of the details of my research, then behind it is the supervisor's editing, his valuable questions and comments made it possible to improve the text of the work qualitatively.

The author is grateful to the other members of the Department of Theoretical Physics of UMCS for their kind attitude to his person and for accepting him into the large collective. In particular, I would like to express my gratitude to **Prof Karol I. Wysokiński**, **Prof Tadeusz Domański**, **Dr hab Nicholas Sedlmayr** for learning and expanding the basics of theoretical physics from their lectures, as well as for improving the applied skills during theirs seminars. I would also like to thank **Dr Szczepan Głodzik**, **PhD Bartłomiej Baran** and **PhD Bartłomiej Kiczek**, already graduated PhD students of this department, for their help in settling down and brightening up my stay in Lublin. And also KFT alumna **Dr Jie Jang**, for her helpful advice on organizing the writing of the

dissertation, which made the preparation easier. However, the author of the primary text was **Dr Irene Dedes**, to whom the author is also grateful.

Special thanks to the secretaries of the KFT – **Anna Wielgus**, of the UMCS Doctoral School – **Magdalena M. Wątróbka** and **Anna Jędrzejewska**, as well as to the deeply respect Director of the School – **Prof Aleksandra Szcześ**, whose saved me many times from my own bureaucratic crutinism. Each time they gave me advice or helped me with paperwork, I realized once again that understanding the nature of the universe cannot be separated from understanding the functioning of paperwork.

In spite of the unfinished research I had in my previous postgraduate studies, I cannot but thank the members of the Voronezh Theoretical Group, namely its permanent head and my supervisor **Prof Stanislav Kadmensky**, from whom I learned to look at the problem not only from different sides, but also under different "optics". To "Big Brother" **Prof Dmitry Lyubashevsky** and other mentors from the Faculty of Physics and Departmentof of Nuclear Physics, whose thoughts influenced the author's understanding of physics, as well as to the current head of the Department of Nuclear Physics VSU, **Dr hab Larisa Titova**, who gave a "ticket" to the Lublin group.

In addition, we would like to mention members of other research groups for very useful discussions and help in providing experimental data. These are **Dr hab Katarzyna Mazurek** from the Institute of Nuclear Physics PAN, **Dr hab Christelle Schmidt** from the Hubert Curie Institute for Interdisciplinary Studies CNRS in Strasbourg, **Dr hab Christo Christov** from the University of Bonn, **Prof Zhigang Xiao** from Tsinghua University and **Dr Lile Liu** from the Institute of Atomic Energy in Beijing, **Dr hab Michał Kowal** from the Polish National Nuclear Research Center, **Dr Rui Han** from Department of Physics University of Jyväskylä, and **Prof Fedir A. Ivanyuk** from the Institute for Nuclear Research NASU. .

Special thanks to **my parents** and **brother**, whose support allowed me to pursue my scientific activities in peace, without being distracted by the many problems and situations that arose during my studies.

Last but not least, the person to whom it would be a crime not to thank is **my wife** – **Margarita**. She has been my support and stronghold even before I started participating in the SHENG-1 project and studying at the Doctoral School of UMCS. Her endless supply of patience, belief in my success, understanding, love, and once more time patience was with me during the long four years of my studies. Even thousands of kilometers were no obstacle for her! The impossibility of her being with me in Poland and her faithful waiting was a great motivation for me to successfully complete this work. Their full support has become a debt that I will probably not be able to repay for the rest of my life. **I hope that this work will be a small contribution to the payment of this huge debt**.

Absrtact

This dissertation is devoted to the study of the dynamics of induced and spontaneous fission in heavy and superheavy nuclei. Despite tremendous progress in theoretical nuclear physics, the fission process still contains many unsolved problems, the ignorance of which leads to incomplete and/or inaccurate interpretation of the available experimentally measured properties.

In the brief review of available theoretical methods and approaches presented here, an effective model based on the solution of a three-dimensional stochastic system of Langevin equations coupled to the Master equation is developed, which provides a description of the evolution of the surface of a compound nucleus in a three-dimensional deformation space containing the elongation, mass asymmetry, and constriction parameters. The main purpose of the calculations was to obtain and compare with available experimental data the distributions of masses, charges and total kinetic energy of fission fragments. The overall agreement between the empirical and theoretical data allowed us to assess the applicability of the hypotheses put forward in this work.

The geometry of the nuclear surface was defined using a recently proposed Fourie shape parameterization, while the potential energy surfaces were calculated using the well-known macroscopic-microscopic approach.

The extensive discussions in the pages of this thesis focused mainly on the dependence of the obtained distributions on the excitation energy and the broadly understood boundary conditions. The model was then generalized to take into account the charge equilibration between the fission fragments and the particle evaporation mechanisms from the compound nucleus and the two fission fragments formed after fission. The master equation for neutron width is represented by a Weisskopf-type expression.

The fission characteristics obtained by the developed approach are in satisfactory agreement with available empirical data for nuclei with $Z \in [92, 104]$, indicating, in general, a correct treatment of the fission phenomenon.

Keywords: Nuclear fission, induced fission, spontaneous fission, fission characteristics, Langevin equation approach, nuclear temperature, Fourier parameterization, potential energy surface half-lives, potential energy surfaces, particle emission.

Contents

List of Figures

List of Tables

Chapter 1

Introduction

1.1 Motivation of my research

In December 2023, it will be 85 years since two german physicists, Otto Hahn and Fritz Strassmann, during neutron irradiation of uranium, were surprised to discover that instead of an even heavier element, the irradiated samples contained an impurity of barium, which was not present in the original samples and whose sequence number was about half that of uranium.

To understand the context of the researchers' surprise, it is necessary to go back a few years in the timeline to 1933, when the discovery of the neutron by Chadwick's group took place. It completed Rutherford's search for the missing piece of the atomic nucleus. It also provided a new source of radiation for understanding the structure of the nucleus. Using it, a group led by Enrico Fermi noticed that when a neutron-deficient (A, Z) nucleus absorbs a neutron, the system transforms into an $(A + 1, Z + 1)$ system that emits an electron, meaning the nucleus undergoes β^--decay. This brought physicists to the idea that in the case of irradiation of a very heavy nucleus (uranium at that time) from the chain of transformation can be obtained the next element in the Periodic Table of Mendeleev. What and began to do, in advanced laboratories throughout Europe.

At the same time, attempts were made to describe theoretically the characteristics of atomic nuclei, more precisely, their masses and why they are lower than the sum of the masses of protons and neutrons. The answer has the same roots as the well-known qualitative school problem: "How does the mass of a brick of 5 kg change when it is broken into two halves of 2.5 kg? The two halves are slightly heavier than 5 kg because of the broken bonds between them. Obviously, more energy must be expended for the nucleus than between the molecules or atoms of the brick. Assuming that the atomic nucleus has the properties of a liquid droplet, calculations have been made which show that heavy nuclei have lower bond energies than light nuclei. This is why heavier elements are not observed on Earth, which is about 4.5 billion years old–they have long since decayed into more stable elements. However, uranium could absorb a neutron and the system would simply undergo one of the already known decays.

Back to the discovery of Hahn and Strassmann. The strange result and repeated experiments with a detailed study of the chemical composition of the preparation led Hahn to the idea that, in addition to the known decays, there is a process by which the nucleus splits into lighter elements. With these data in hand, their colleagues Lisa Meitner and Otto Frisch proposed [1] that the nucleus "splits" as a cell into approximately two identical fission fragments, which was indeed shown in the experiment. They made a very simple estimate of the energy released by such a process. About 200 MeV! Colossal energy.

Soon, Bohr and Wheeler [2], and independently of them, Frenkel [3] were established the basis of the nuclear fission theory. It was based on the previously mentioned drop model of the nucleus. Nuclear and electrostatic forces act on the nucleons in the atomic nucleus, the latter tending to break the system. Deformation of the nucleus disturbs the equilibrium, and forces similar to the surface tension of a drop of liquid appear, tending to return the nucleus to the shape of the ground state. The deformation of the nucleus during fission is accompanied by an increase in its surface area and, like a drop of liquid, the surface tension forces increase and prevent further deformation. The lower the fission barrier, the shorter the period of spontaneous fission.

Thus began a new era, and with it the race to acquire nuclear weapons that changed our world forever. Astounding weapons, capable of instantly killing tens of thousands and painfully killing hundreds of thousands of people–all this is the result of the uncontrolled nuclear fission reaction of a few kilograms of uranium or plutonium, developed by American nuclear physicists [1]. Nevertheless, scientists looked for ways to contain this phenomenon for peaceful purposes. And they found it in the form of nuclear reactors, which do not store ^{239}Pu (aka weaponized), but rather burn out ^{235}U smoothly (although until recently combined-type reactors were used, the latter being discontinued in 2015). The boom in nuclear power that began in the 1960s gave humanity hope of a cleaner, larger energy source. It's about time we had unlimited power in our hands. Enough for big cities and small remote settlements alike. And progress is indeed being made. The leaders in nuclear power generation are the U.S., France, China, Russia, and South Korea. Satellites in space use heat from the decay of heavy isotopes as a power source, the most obvious being Voyager-1(or 2). Floating nuclear power plants that can power distant coastal cities and settlements, etc.

However, the man-made disasters at Three Mile Island in 1979, Chernobyl in 1986, and the relatively "fresh" Fukushima-1 in 2011 have dispelled any optimism that existed at the dawn of nuclear power, and in its place public opinion is filled with fear. This shows that, unfortunately, progress in the field of nuclear power has been achieved at the expense of many human lives and natural resources. The very long calculation and careful safety in building more powerful reactors is slowing down the whole nuclear industry.

Currently, the main source of energy in the nuclear industry is the fission reaction ^{235}U by thermal neutrons, that is, when a neutron has a kinetic energy $E_{kin_n} \approx 0.025$ eV. However, this reaction has some nuances.

Problem #1: ^{235}U is very small[2]. In nature it is about 0.7%, so there are only a few centers in the world capable of enriching uranium to the required $4-4.5\%$ on an industrial scale. The dependence on the quality of the uranium ore and the small number of facilities seriously limits the capabilities of the entire industry.

Problem #2: waste. Yes, nuclear power plants are environmentally friendly, the whole process is worked out to the smallest detail and improved every year. The heat generated by cooling the third circuit is released into the atmosphere. However, this does not include the problem of radioactive waste disposal. The fission products ^{235}U are both toxic and very active. The Chernobyl accident is an example of how dangerous they are. The extent of the contamination caused much more problems than after the bombs exploded in the sky over Japan in August 45. And the liquidation of the consequences of the explosion of the reactor of the fourth power unit required colossal efforts even within the framework of the state with a population of 280 million people!

Physicists, of course, are trying to find a way out of this situation. The first promising

[1] strictly speaking, a very large group of scientists from both the Old and the New World

[2] about 200 years at the current level of energy consumption

option is to use the fission of another uranium isotope – ^{238}U, not by thermal neutrons, but by fast neutrons, where $E_{kinn} \approx 1$ MeV. Moreover, the fission products of this reaction can also be used in repeated cycles to produce new fuel. Currently, the new successful pilot project of the fast neutron reactor is underway at the Beloyarsk NPP, for which russian specialists have been preparing for almost 15 years. Another similar option is the use of thorium, which is largely unused by mankind, but its reserves are very large.

Another option is the use of various admixtures of already available nuclear waste, the so-called MOX fuel, which has long been realized in Russia, but the problem of waste treatment does not disappear. On the contrary, very complex questions arise, such as how to separate the waste in the best possible way, which isotopes can be used and which cannot, in what quantities, etc. This also requires serious calculations.

Finally, let us return to the experiments that took place $80-90$ years ago. Their main purpose is to search for new elements in the Periodic Table of Mendeleev. During this time, 26 new elements were discovered, filling the actinide series and continuing into the so-called superheavy elements with $Z \geq 104$, ending with an element with ordinal number 118 in the form of a single isotope oganesson ^{294}Og. Ironically, physicists then hit a ceiling. It is now assumed that in the neighborhood of an element with $Z \geq 120$, the shell effects of proton (and neutron) shells will produce relatively stable nuclei, which has been called the "stability island". Obviously, the search for new elements located in this region of the atomic nucleus diagram will bring nuclear physics to a new qualitative level and attract a new wave of researchers.

The reasons for the problems mentioned above are the same – insufficient knowledge of the process of nuclear fission, which the physics community around the world is trying to overcome. A clear understanding of the processes occurring inside the nucleus will allow to accurately predict the products of fusion of heavy target nuclei, for the synthesis of new isotopes, and the behavior of nuclear fuel combustion. This will allow mankind to develop more rationally and productively not only on the home planet, but also in new homes. This is a serious motivation for this study.

The purpose of the present work is to take a small step (on the shoulders of giants) in the development of a simple tool, which with further modification to improve our understanding of the processes of fission of atomic nuclei, or at least try to make this step.

1.2 The current state of nuclear fission theory and its challenges

Very briefly, the current understanding is well described by figs. 1.1 and 1.2, which schematically show the evolution of the nuclear fission process, the formation of pre-fragments, the separation into two primary fragments, which subsequently appear in detectors as fission fragments, which then diverge at an accelerated rate.

They also show that fission is a time-dependent process that proceeds in several stages with characteristic time scales. A nucleus from an initial state undergoes a change followed by fission, usually into two excited fragments. They then undergo a sequence of rapid and/or delayed decay excitations leading to the ground or isomeric excited states.

As can be seen from Fig. 1.1, the elongation of the fissile nucleus plays an essential role, starting from the equilibrium form and evolving through different forms with diffusion behavior. Initially, the strain corresponds to the equilibrium shape of the parent nucleus, but during fission it changes due to the diffusive nature of the process. Eventually, the system is beyond the outer saddle point and evolves toward fission, forming an elongated

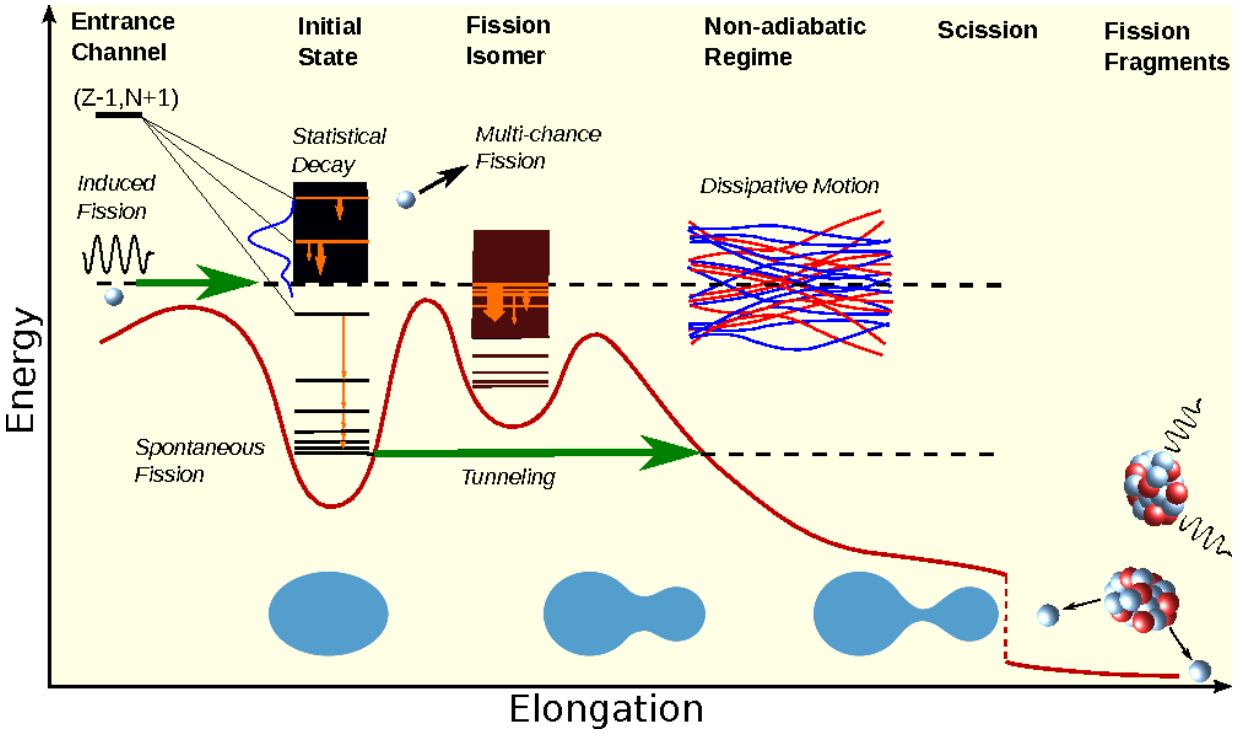

Figure 1.1: Schematic representation of the most important features of the fission phenomenon, taken from [4]. The red curve shows (in one-dimensional projection) the potential energy as a function of elongation.

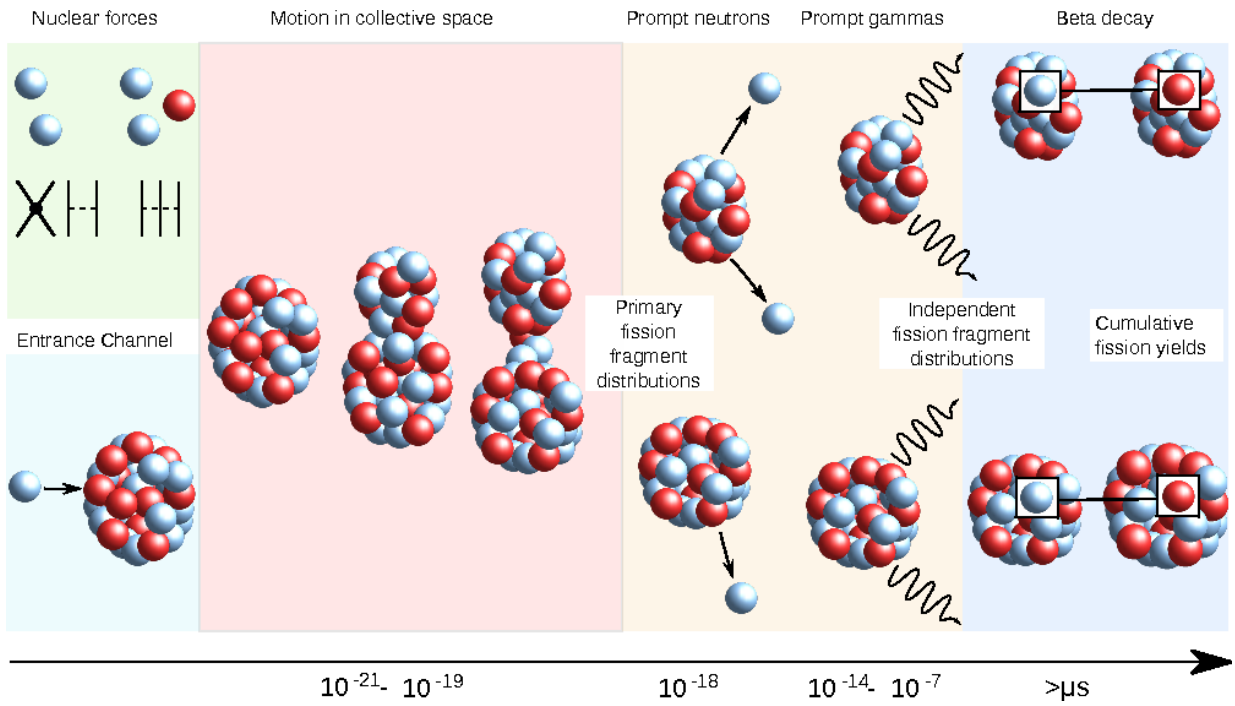

Figure 1.2: Schematic representation of the different stages of the fission process, taken from Ref. [4]

system of two fission pre-fragments.

In the experiments of Hahn and Strassmann, the barium isotopes were produced by induced fission, which results from a reaction or decay process in which energy is supplied from outside. It can be induced in a variety of ways, of which there are now many. In addition to neutron capture, it can be induced by electron capture and beta decay, photofission, reactions involving charged light particles or heavy ions. In all these processes, the fissile nucleus is in an excited state, which can be above or below the fission barrier.

However, relatively soon after the discovery of forced fission, it was discovered that the nucleus, can undergo spontaneous fission (SF). It occurs mainly from the ground state, but is also possible from isomeric states. This type of fission is one of the main decay modes of superheavy nuclei and is therefore of great interest for their experimental search. From the basic ideas described by Bohr and Wheeler, the relatively long lifetime is due to the existence of a potential barrier that must be overcome. Spontaneous fission is therefore, strictly speaking, a quantum process. In this context, the dependence of this phenomenon on the parity of the nucleus has been observed: in odd nuclei, it is usually hindered by several orders of magnitude compared to its even-even neighbors. It is probable that it is even more complicated for odd-odd nuclei, but it is not exact.

In theoretical descriptions of fission, it is very convenient to use Bohr's notion of compound nucleus formation at a given thermal excitation energy. And this is really useful for low energy fission. Today, however, there are discussions that this representation may be unreasonable for fast probes, where the nuclear system may not have time to cool down before fission begins. There is the possibility of emission of one or more nucleons before equilibrium is reached. Moreover, as the excitation energy of the compound nucleus increases, the competition between neutron evaporation and fission increases, so that one or more neutrons may be evaporated before fission occurs (so-called multichance fission). And so the use of temperature to determine the energy of the whole system is also questioned.

1.2.1 Important observable parameters

Of course, there is now a considerable set of quantities of interest that can be measured directly or modeled theoretically. Using the classification of the paper [] [Bertsch et al. (2015)], we will identify the most important of these:

- **Spontaneous fission half-lives $\mathbf{T_{SF}}$** from 10^{-6} to 10^{16} s.
- **Total and differential fission cross sections**. For example, the neutron-induced fission cross section $\sigma(n, f)$ and its energy and angle dependence, or the threshold fission energy observed in the photofission cross section, which is closely related to the fission barrier height.
- **The distributions $\mathbf{F(A)}$, $\mathbf{F(Z)}$, $\mathbf{F(Z, A)}$** (yields $\mathbf{Y(A)}$, $\mathbf{Y(Z)}$, $\mathbf{Y(Z, A)}$). They characterize the probabilities of forming fission fragments of a given mass and/or charge.
- **Fission spectrum.** This includes the average number of neutrons per fragment and their energies, the average number of photons per fragment and their energies, multiplicity distributions, angular correlations, etc.
- **Total Kinetic Energy (TKE)**. Kinetic energy of fission fragments after acceleration, its distribution and dependence on fragment mass.

– **Beta decay spectrum of fission products**. Particularly important for the fundamental theory of beta decay and includes the neutrino spectrum.

Correlations between the above quantities (e.g., between the mass of the fragment and the TKE) and with other quantities (e.g., the spin of the fission nucleus) are also important. These quantities can be obtained from experiments. However, even with the great progress in nuclear physics, one must realize that these "experimental quantities" are often the result of indirect changes. In them, the quantity of interest is extracted from measurements by means of some model or model-dependent assumptions.

It should also be realized that most of the quantities operated on in nuclear physics are unobservable, i.e. they cannot be observed directly. The most prominent examples are the fission barrier and the concept of the compound nucleus. For example, the height of the fission barrier can be theoretically defined as the energy difference between the ground state and the highest saddle point on the calculated potential energy surface (PES) that has the lowest energy for all possible paths leading from the ground state to fission. And the concept of a compound nucleus is based on a model that assumes complete thermalization of the system and ignores pre-equilibrium processes. Other useful but unobservable quantities include the fission point at which the nucleus splits into primary fragments, the shell energy on the way to fission, the mating energy at the barrier, the pre-fission fragments formed in the pre-fission region, etc.

1.2.2 The main approaches of fission theory

As was noted earlier, the theory of nuclear fission does not have a general formalism that could successfully describe all of the above features. Here we will spend only a small list of available methods and approaches with a short explanation.

But before giving a brief summary of the available models and approaches, it is necessary to touch upon a very frequently used term in the theory of nuclear fission, namely the notion of adiabaticity. Now, in nuclear physics, the term "adiabatic" has several meanings. For example, it can mean that the collective motion passes through a sequence of local ground states, each of which corresponds to a system bounded by a given set of collective coordinates and quantum eigenvalues. Alternatively, the notion of adiabatic motion means that the time-dependent wave function acquires collective kinetic energy through infinitesimal admixtures of local excited states, while non-adiabatic corrections correspond to significant admixtures. An obvious example [4] would be the representation of dissipative motion used in this study, which refers to a constant irreversible flow of energy from a local ground state. In the context of the time-depend Hartree-Fock method (TDHF) or DFT, adiabaticity denotes a very specific approximation of the time-dependent one-body density matrix, i.e. it is only valid for sufficiently slow motion. Another commonly used definition of adiabaticity involves the separation of variables into slow and fast coordinates. It is in the order of magnitude of the norm to use this notion from splitting theory to divide degrees of freedom into "collective" and "non-collective".

Adiabaticity is linked to time intervals, which vary with fission stage dependence. For example, fission through a compound nucleus is delayed by the lifetime of the compound nucleus, which is much longer than the time scales of the dynamics. At excitation energies below the fission barrier, the fission lifetime depends strongly on the tunneling probability and can vary by many orders of magnitude. Then there is the collective motion time from the outer turning point to fission, as shown in Fig. 1.2. The slower this motion is, the more accurate the diffusion and statistical modeling of the dynamics will be. The time to fission (descent from the fission barter) plays a special role, affecting in particular the excitation

energies of the fragments or the TKE.

For experimental studies, the determination of fission timescales is an extremely difficult problem because they affect the early stages of fission dynamics. They are generally not available for direct study, but must be inferred from the analysis of products at later stages of fission. To date, there are experiments measuring fission times published in Refs. [5–8]. However, they need to be combined with model description of e.g. the emitted neutrons and their dependence on angular momentum or excitation energy. As a result, it is likely that different experimental methods will yield different characterizations of the fission time distribution.

Mean-Field Theory The mean-field approximation is the basis of microscopic nuclear theory for all but the lightest nuclei. In the context of nuclear fission, a major advantage of mean-field theory is that it is formulated directly in the body-fixed reference frame of the nucleus, in which the notion of the deformed shape of the nucleus and its dynamical evolution is naturally present.

The self-consistent many-body wave functions are directly or indirectly composed of Slater determinants of orbitals, where orbitals are computed as eigenstates of the mean-field potential of a body. When the mean-field potential is determined by the expectation of the Hamiltonian in the Slater determinant, the solution is performed in the Hartree-Fock (HF) approximation. When the coupling field is included, the Hartree-Fock-Bogoliubov (HFB) approximation is used.

Another widely used approach is the macroscopic-microscopic method, which avoids the subtle problems of constructing an HFB that reproduces the systematic properties of heavy nuclei. Here, the basic properties of a nucleus are determined from its size and shape, expressed in some surface parameterization. The orbitals are constructed using a potential derived from the surface shape of the nucleus, and their energy is calculated using a liquid drop model together with shell corrections determined by the orbital energies. This is the method used in the present study (see Chapter 2).

In this approach, the potential energy surface (PES) is the lowest possible energy of an evolving system that corresponds to given values of the collective variables. The PES is usually multidimensional. Although the PES alone is not sufficient for the prediction of dynamical evolution, it is nevertheless very useful because its topography allows us to understand and anticipate the main features of the dynamics. Local minima, saddle points, and fission surface – key features that often allow us to predict isomeric properties, threshold energies, and fission fragment yields. For a given point in collective space, either by minimizing the total energy within the constrained HF (CHF) or HFB (CHFB) framework, or by calculating the macroscopic-microscopic energy for a given shape, the potential energy of the corresponding nuclear configuration and its internal structure can be obtained. The former method produces an optimized shape within the given constraints. The latter method may not consider aspects of the shape beyond the given shape parameterization.

Some approaches require energy in the presence of internal excitations, whereas the standard PES describes a configuration with no excited orbitals or quasiparticle excitations. In the macroscopin-microscopic method, a temperature-dependent DFT formalism can be used, while the self-consistent method requires the calculation of shell and pairwise corrections for finite excitations. In the CHF and CHFB framework, the PES is usually represented as a function of several multipole moments. However, the multipole moments have little control over the shape and do not provide sufficient discrimination between internal configurations at large strains.

Time-dependent DFT The time-dependent version of the DFT is an established approach in nuclear dynamics, and has been widely used to model heavy ion collisions [9, 10]. In principle, it can be easily generalized to the HFB approximation, but it is only now reaching the computational power to perform calculations without introducing artificial constraints and approximations [11–15]. These approaches have the important property that they observe energy and expectation conservation for conserved one-body observables, such as the number of particles. Their strength is that they usually provide a good description of the average behavior of the system under study. Its weakness is that since the TDHF equations arise as a classical field theory for interacting single-particle fields [16], the TDDFT approach cannot describe either the motion of the system in the classically forbidden part of the collective space or quantum fluctuations. As a consequence, the real-time TD approach cannot be applied to spontaneous fission.

Dissipative dynamics Although the self-consistent dynamics of the DFT is very powerful, it largely ignores the internal degrees of freedom, which can lead to large fluctuations in the observed parameters and energy dissipation [17, 18]. There are several ways to account for the additional degrees of freedom in the equation of motion. The simple leading diffusion equation assumes first-order time derivatives. This approach has been very successful in describing mass and charge yields in [19].

More generally, time-dependent models can be considered. These models combine even-time inertial dynamics with odd-time dissipative dynamics. The multidimensional Langevin equation [20–23] is a common classical formulation. In this approach, the dissipative energy is transferred to a thermal reservoir characterized by the temperature.

Quantum tunneling The tunneling motion in SF is usually considered by means of a quasi-classical one-dimensional formula for the action integral, which is based on two basic quantities that can be derived in the nuclear DFT: the PES and the collective inertia (or mass) tensor. The fission trajectory is computed in a reduced multidimensional space. Two to five collective coordinates are used to describe the shape and conjugation of the nuclei. The assumption of slow, nearly adiabatic motion is required for the mass tensor. The pairing gap makes this assumption most plausible for even-numbered nuclei, but even in such systems one can expect non-adiabatic effects due to the level crossing [24–26]. In order to make progress in NF research, the following questions are relevant

- **Generalized fission trajectories** Usually, the trajectories of HFs in the collective space are defined by considering several coordinates that bound the shape. It is better to assume that the collective motion occurs in a large space parameterized by a Tuless matrix characterizing the state of the HFB. An approach to define the collective trajectory in this way has been proposed in [27, 28]. There, the equations of motion have a canonical form (involving coordinates and moments) and the boundary operators are dynamically defined.

- **The multidimensional WKB formula** The current methodology for barrier penetration is based on minimizing the collective action along one-dimensional trajectories, although our experience with fission evolution above the barrier shows that it is important to use multiple degrees of freedom. It may be possible to generalize the one-dimensional quasi-classical WKB-like formulation to a more general solution of the tunneling problem in several dimensions [29].

- **Nonadiabatic effects** The admixture of non-adiabatic states can be crucial for understanding the fission barrier in odd nuclei. Excitations to higher configurations

can be caused by single-particle level crossing and Coriolis coupling.

The above list of representations represents only a fraction of the available spectrum in nuclear physics. The failure to describe more than three types of fission charectiristics presented in 1.2.1 is certainly striking. Moreover, some of them are of a phenomenological nature, which obviously has to be dealt with. In fact, as one of the main authors of the work [4] pointed out, it is necessary to move in the direction of generalization. However, as again correctly pointed out, even in spite of the present possibilities, the choice of methods and approximations still cause many problems. Including computational ones. Obviously, the creation of a unified fission model is a medium- or even long-term task.

Nevertheless, the use of combined methods, such as the coupling of dynamical dissipation method and the mean-field approach, can, in the author's opinion, shed light on obtaining new models allowing to describe as many fission characteristics of atomic nuclei as possible.

1.3 Research highlights of the thesis

This work represents PhD research devoted to the properties of the atomic nucleus and its fission process. The approaches and methods widely used in the theory of nuclear fission are reviewed here, although their development is attempted. In the author's opinion, for the understanding of the details of the study, the following paragraphs must be included in the later chapters:

1. Definition of the details of the macroscopic-microscopic approach, which methods and formalism lay the foundation for the study:
    - A brief overview of the concepts and properties of nuclear forces.
    - Concept of binding energy and its phenomenology from macroscopic parameters.
    - Representations of the liquid drop model and its further development to the present day.
    - Choice of the macroscopic model to be used.
    - The Hartree-Fock and Hartree-Fock-Bogoliubov approximations for calculating the energy states of nucleons.
    - The Mean-field approach and Yukawa-folding procedure. Calculation of the Coulomb potential in the HFB method
    - Application of harmonic oscillator potentials in calculations of the structure of deformed nuclei.
    - Strutinsky's method as a basis for the macroscopic-microscopic approach.
2. Parameterizations of atomic nuclei surface and related macro-characteristics, knowledge of which is necessary to account for the dynamics of the fission process:
    - Anthology of commonly used parameterizations.
    - Highlighting the most suitable type of parameterization for the problem considered in this paper.
    - The hydrodynamic method for determining the inertia of the nucleus. Werner-Wheeler approximation.

- Techniques for determining the friction tensor of the nucleus:
  - "Wall" formula;
  - "Window" formula;
  - "Wall-Window" formula.

3. Stochastic methods describing fission dynamics:

   - Langevin equation formalism.
   - Fokker-Planck equation formalism.
   - Relationship and comparison of the above formalisms.

4. The generalized description of evaporation of light particles from nuclei.

The first point corresponds to the Chapter 2 of this dissertation. The second point corresponds to the Chapter 3. The last two paragraphs were decided to combine into one Chapter 4. It is connected with the fact that these formalisms are either mutual (of course we are talking about the Langevin and Fokker-Planck equations) or complementary to the physical picture of the process.

Chapter 5 stands apart. Unlike the previous ones, it includes the author's complete study of the dynamics of nuclear fission. More precisely even-even heavy and superheavy nuclei, i.e., in the range of order number $Z \in [90, 116]$ and mass number $A \in [222, 294]$. Chapter includes model building based on numerical solution of the multidimensional system of Langevin equations and searching for optimal model parameters. Different hypotheses and assumptions are investigated. The model's liquidity is tested first by fission of the compound nucleus ^{236}U, which is extended further to other nuclei. Here are some of the points that will be addressed within this chapter:

- Behaviors and effects of temperature on fission system parameters
- Influence of initial conditions on the fission process
- Criteria for trajectory termination in fission modeling
- Characteristics of nuclear fission at the fission point
- Neutron evaporation process and its influence on characteristics
- The process of light particle emission from a compound fissile system

The last chapter summarizes the results obtained in this thesis. In addition, a brief critical review of the problems that should be addressed both when using the model developed in this work and when using the stochastic formalism to describe nuclear fission in general is carried out. Possible ways to improve the existing model and its future prospects will be identified.

Chapter 2

Description of the atomic nucleus properties with using of the macroscopic-microscopic method

As mentioned in the Introduction, there are several approaches to describe the fission of atomic nuclei, which are still under active development to strengthen their predictive power and cover a larger number of possible nuclei. The most advanced at present are microscopic approaches based on the formalism of quantum mechanics, such as the method of density functions for protons and neutrons, or the Hartree-Fock-Bogolyubov method, which includes pair effects. These ideological heirs of the shell model are quite good at describing the internal structure of the nucleus, including the deformed ones. However, when we talk about dynamic calculations, these models face the problem of the bulky nature of these calculations, even on modern computers. Therefore, the range of studies of nuclear fission by microscopic approach could be much higher and is limited by considering spontaneous or low-energy fission, where excitations of nucleons are small. Almost all of the excitation energy is used to overcome the barrier. Therefore, the generalized method that appeared in the mid-1960s, combining elements of both macroscopic and microscopic approaches, remains relevant and will be discussed further in this section.

2.1 Retrospective of macroscopic models

First of all, there was the question of the interaction of these particles. After it was discovered in the early 1930s that the atomic nucleus is composed of positively charged protons and zero charged neutrons, the question of revising the description of the structure of the nucleus was seriously raised. Experiments have shown that these forces have the following properties:

- Attractive.
- Short–range (at $r_n \approx 1$ fm repulsion, disappears at $2r_n$).
- High intensity (high magnitude $E \propto 10^6$ eV).
- Charge independent (except for the Coulomb force, the interaction is considered the same for p–p, n–n, n–p).
- Dependent on the relative distance of two nucleons ($V_{12} = V(|\vec{r}_{12}|)$).

- Saturated (as the number of nucleons A increases, the binding energy rises sharply and quickly reaches its limit).

2.1.1 Liquid drop model

This last point historically predates the first attempt to describe the atomic nucleus. In 1935, Weizsäcker and Bethe independently used two assumptions peculiar to the liquid droplet:

1. Uniform density of nuclear matter;
2. Average binding energy is the same for all nucleons forming the nucleus;

proposed [30, 31] to calculate the binding energy by the simple semi-empirical expression

$$\mathcal{B} = b_{\text{vol}}\, A - b_{\text{surf}}\, A^{2/3} - E_{Coul} \tag{2.1}$$

The first term corresponds to the constant nuclear energy per nucleon. The next term accounts for the nuclear surface tension effect, which reduces the total energy and is proportional to the surface area of the drop. The last term in the equation is the Coulomb repulsion between the protons. This results from the leptodermous expansion of the total energy, a power series in the term $A^{1/3}$.

Green and Bethe proposed a further modification of the basic version in 1953 with the introduction of the symmetry-energy term, the appearance of which is due to the Fermi gas model. In this model [32], taking into account the Pauli principle and the laws of conservation of energy and momentum, it turned out that the motion of nucleons has an independent character. Therefore, the additional term in the equation (2.1) should be proportional to $\frac{N-Z}{N+Z}$, which is usually called *nuclear reduced isospin* I. This introduced an additional dependence of the energy on the difference between the number of protons and neutrons in the nucleus. This more advanced Liquid Drop (LD) formula for the binding energy has the form

$$\mathcal{B} \equiv E_{\text{LD}} = b_{\text{vol}} A - b_{\text{surf}} A^{2/3} - b_{\text{Coul}} \frac{Z^2 e^2}{A^{1/3}} - \frac{1}{2} b_{\text{sym}} \frac{(N-Z)^2}{A}, \tag{2.2}$$

where the parameters have been fitted to experimentally measured masses and have the following values:

$$\begin{aligned} b_{\text{vol}} &= 15.56\,\text{MeV}, \\ b_{\text{surf}} &= 17.23\,\text{MeV}, \\ b_{\text{Coul}} &= \frac{3}{5}\frac{e^2}{r_0} = 0.697\,\text{MeV}, \\ b_{\text{sym}} &= 46.57\,\text{MeV}, \\ r_0 &= 1.24\,\text{fm}. \end{aligned}$$

2.1.2 Deformation dependence of binding energy

Soon it became clear that the atomic nucleus not only deformed during fission, but also had a non-spherical shape in the ground state. This was observed in studies of the scattering of gamma rays on nuclei. Consequently, the binding energy of the nucleus, which depends on surface effects, also depends on the degree of deformation of the nuclear shape.

This means that the surface and Coulomb terms in the LD formula (2.2) must be multiplied by the following factors

$$B_{\mathrm{surf}}(\mathrm{def}) = \frac{S(\mathrm{def})}{\mathrm{S}(0)}, \tag{2.3}$$

$$B_{\mathrm{Coul}}(\mathrm{def}) = \frac{E_{\mathrm{Coul}}(\mathrm{def})}{E_{\mathrm{Coul}}(0)}. \tag{2.4}$$

where $S(0)$ and $E_{\mathrm{Coul}}(0)$ denote the values calculated for the spherical case for all other unchanged parameters.
The LD formula (2.2) then has the form

$$\mathcal{B}(Z,N,\mathrm{def}) = b_{\mathrm{vol}}A - b_{\mathrm{surf}}A^{2/3}B_{\mathrm{surf}}(\mathrm{def}) - \frac{3}{5}\frac{Z^2e^2}{r_0A^{1/3}}B_{\mathrm{Coul}}(\mathrm{def}) - \frac{1}{2}b_{\mathrm{sym}}\frac{(N-Z)^2}{A}. \tag{2.5}$$

Of course, the definition of the deformation of the nucleus touches on the question of how to describe its surface. The introduction of additional deformation parameters into the particle coordinates is always associated with an artificial increase of the degrees of freedom of the nucleons in the nucleus, which is associated with the danger of obtaining unreliable information, such as false excited states in the nucleus. However, the macroscopic approach, which proved to be the most suitable for the description of atomic nuclei shapes, made such models very popular for a long time, until today. The most popular and convenient types of parameterization are discussed in Chapter 3, and the most fundamental of all types is presented below.

Spherical harmonic expansion

The first and most common way to represent the atomic surface is, of course, to decompose it into an infinite series of spherical functions

$$R(\vartheta,\varphi) = R_0\left(\{a_{\lambda\mu}\}\right)\left[1 + \sum_{\lambda=0}^{\infty}\sum_{\mu=-\lambda}^{\lambda} a_{\lambda\mu}Y_{\lambda\mu}(\vartheta,\varphi)\right] \tag{2.6}$$

where R_0 is obtained from the volume conservation condition of the deformed nucleus, the coefficients $a_{\lambda\mu}$ describe all possible shape variants. Even values of the λ index, for example, describe bodies with mirror symmetry. On the other hand, the index with $\mu = 0$ describes forms with axial symmetry. Their combination gives the following forms, a_{20} – quadrupole deformed nucleus, a_{30} – octupole deformed, pear-shaped forms, a_{40} – hexadecapole, and so on. The series (2.6) is limited to the listed variants and ends or, in connection with simplifying the calculations, some set of combinations of parameters $a_{\lambda\mu}$ is used. Consider the simplest example of a nuclear surface near an axially symmetric spheroid described by a quadrupole deformation with $\lambda = 2$ and $\mu = 0$. The surface equation is of the form

$$R(\vartheta) = R_0(\beta)\left[1 + \beta Y_{20}(\vartheta)\right], \tag{2.7}$$

where $\beta \equiv a_{20}$ is a quadrupole deformation parameter. For non-axial cases, but with mirror symmetry with respect to each major axis, one has $\lambda = 2$, and $\mu = 0, \pm 2$, and the surface of the nucleus is described by

$$R(\vartheta,\varphi) = R_0\left(\{a_{2\mu}\}\right)\left[1 + \sum_{\mu=-2,0,2} a_{2\mu}Y_{2\mu}(\vartheta,\varphi)\right]. \tag{2.8}$$

Then one can introduce [33] the Bohr parametrization β, γ, where

$$a_{20} = \beta \cos\gamma, \quad a_{22} = a_{2-2} = \frac{1}{\sqrt{2}}\beta \sin\gamma. \tag{2.9}$$

As you can see, the equation (2.9) has no term with $\mu = 1$ because the axes of the coordinate system coincide with the major axes of the ellipsoid.

If we use the parameter α, the value of the global deformation of the nucleus, introduced by Myers and Świątecki in 1966 [34], which is a measure of the relative deviation of the deformed surface from the sphere.

$$\alpha^2 = \iint \frac{[R(\vartheta,\varphi) - R_0]^2 \, d\cos\vartheta d\varphi}{R_0^2} = \sum_{\lambda\mu} (a_{\lambda\mu})^2 \tag{2.10}$$

and consider the case of quadrupole deformed nuclei, where

$$\alpha^2 = a_{20}^2 + a_{22}^2 + a_{2-2}^2 \equiv \beta^2, \tag{2.11}$$

The shape-dependent functions B_s and B_c in the parameterization eqs. (2.7) and (2.10) can be treated as

$$B_{\text{surf}}(\alpha,\gamma) = 1 + \frac{2}{5}\alpha^2 - \frac{4}{105}\alpha^3 \cos\gamma + 0\left(\alpha^4\right) \tag{2.12}$$

$$B_{\text{Coul}}(\alpha,\gamma) = 1 - \frac{1}{5}\alpha^2 - \frac{4}{105}\alpha^3 \cos\gamma + 0\left(\alpha^4\right) \tag{2.13}$$

Fissility of atomic nuclei

Then, knowing the analytical form of the surface change, we can estimate the potential barrier of the system, since in the LD representation the potential barrier appears when the surface energy increases faster than the Coulomb interaction decreases, i.e. to satisfy the following inequality

$$b_{\text{surf}} A^{2/3} \cdot \frac{2}{5}\alpha^2 \geq b_{\text{coul}} \frac{Z^2}{A^{1/3}} \cdot \frac{\alpha^2}{5} \tag{2.14}$$

or

$$\frac{B_{\text{Coul}} Z^2}{2 B_{\text{surf}} A} \leq 1 \tag{2.15}$$

The left value in (2.15) is usually defined as x, the fissility parameter of the nucleus.

$$x \equiv \frac{B_{\text{Coul}} Z^2}{2 B_{\text{surf}} A} = \frac{Z^2}{49A}, \tag{2.16}$$

which, in the liquid drop model, describes the properties of the nuclei as a result of fission. For example, for nuclei with a high potential fission barrier, the parameter $x \leq 0.7$, as for the heaviest stable isotope of lead ^{208}Pb, the fission parameter is 0.66, but for the spontaneously fissioning ^{240}Pu, the fission parameter is already 0.75. For the isotope of the superheavy element ^{292}Lv, the parameter $x \approx 0.94$ reaches a value close to 1.

It should be noted, however, that the fisslity parameter only affects the macroscopic part of the barrier. In addition, there is a microscopic part. This is the sum of shell and pairing effects, which act in a specific way when the nuclear surface changes, i.e. when symmetries are broken. This will be discussed in the next sections of this chapter.

2.1.3 Myers-Świątecki liquid drop formula

In parallel to the deformation studies, it was noticed that LD cannot correctly describe the experimental values of the binding energies of nuclei where the number of protons or neutrons takes on the values $\mathcal{N} = 2, 8, 20, 28, 50, 82, 126, 184$ (the last two currently only for neutrons), the so-called magic nuclei, which have a very strong connection. This result suggested [35] to Jensen and Goeppert-Mayer that nucleons form shells inside the nucleus, like electrons in an atom. This led to the emergence of explicit quantum mechanical models describing the structure of the atomic nucleus from a point of view that can generally be classified as a microscopic approach.

However, due to the problem of computing power in the middle of the last century, the calculation of the wave functions of all nucleons was a very non-trivial task, and in most cases approximate methods were used. It is therefore not surprising that a macroscopic-microscopic approach to the calculation of the binding energy was proposed, in which it was suggested to expand E into a sum:

$$\mathcal{B} = E_{\mathrm{LD}} + \delta E_{\mathrm{shell}}, \tag{2.17}$$

where the last term $\delta E_{\mathrm{shell}}$ is a shell correction.

The correction comes from the quantum effects of the shell in the nucleus, which is defined as the difference between the sum of the single-particle energies e_ν of the occupied levels and the energy of the nucleus without the shell structure $\tilde{E}$, i.e. with smoothed single-particle levels $\bar{e}_\nu$

$$\delta E_{\mathrm{shell}} = \sum_{\nu=1}^{A} e_\nu - \tilde{E}. \tag{2.18}$$

Instead of solving Schpödinger's equation within some arbitrary mean single-particle potential at certain levels $|\nu\rangle$ with energies e_ν, Myers and Świątecki used the general results of the Fermi gas model. They obtained the correction (2.18) by creating a discrete spectrum from the continuous energy spectrum $E(n)$, grouping the single-particle states of protons and neutrons into shells corresponding to their magic numbers.

The logic was as follows. The Fermi energy for N particles of one type is

$$e_{\mathrm{F}} = \frac{\hbar^2}{2M}\left(\frac{3\pi^2 N}{\Omega}\right)^{2/3}, \tag{2.19}$$

where M is the reduced mass, Ω is the volume of space. Thus, the energy of the level occupied by the nth particle can be estimated as

$$e(n) = \frac{\hbar^2}{2M}\left(\frac{3\pi^2 n}{\Omega}\right)^{2/3} = e_{\mathrm{F}}\left(\frac{n}{N}\right)^{2/3} \tag{2.20}$$

Then, assuming that the average energy $\bar{e}(n)$ changes according to the formula (2.20) and dividing the continuous energy spectrum by the difference between the filling levels of the shells $\mathcal{N}_i$, i.e. e.g. $\mathcal{N}_i - \mathcal{N}_{i-1} = 2, 6, 12, 8, 22, 32, 44, \ldots$ for $i = 1, 2, 3, \ldots$, the total energy of the nucleon in the i-th partition has the form

$$\begin{aligned} E_i &= \int_{\mathcal{N}_{i-1}}^{\mathcal{N}_i} e(n)dn = \frac{e_{\mathrm{F}}}{N^{2/3}}\int_{\mathcal{N}_{i-1}}^{\mathcal{N}_i} n^{2/3}dn = \\ &= \frac{3}{5}\frac{e_{\mathrm{F}}}{N^{2/3}}\left[\mathcal{N}_i^{5/3} - (\mathcal{N}_{i-1})^{5/3}\right]. \end{aligned} \tag{2.21}$$

In this case, the average energy per nucleon in the i-th region is

$$e_i = \frac{E_i}{\mathcal{N}_i - \mathcal{N}_{i-1}} = \frac{3}{5}\frac{e_{\mathrm{F}}}{N^{2/3}}\left(\frac{\mathcal{N}_i^{5/3} - \mathcal{N}_{i-1}^{5/3}}{\mathcal{N}_i - \mathcal{N}_{i-1}}\right). \tag{2.22}$$

The obtained energies e_i are substituted into Eq. (2.18) and when replacing the operation of summation by integration, the shell correction takes the form

$$\delta E_{\mathrm{shell}} = \int_0^N (e_i - \bar{e})\, dn = \int_0^N \frac{e_{\mathrm{F}}}{N^{2/3}}\left[\frac{3}{5}\left(\frac{\mathcal{N}_i^{5/3} - \mathcal{N}_{i-1}^{5/3}}{\mathcal{N}_i - \mathcal{N}_{i-1}}\right) - n^{2/3}\right] dn. \tag{2.23}$$

It is convenient to replace the first term in the integrand in Eq. (2.23) with function $f(n)$

$$f_i(n) \equiv \frac{3}{5}\left(\frac{\mathcal{N}_i^{5/3} - \mathcal{N}_{i-1}^{5/3}}{\mathcal{N}_i - \mathcal{N}_{i-1}}\right), \tag{2.24}$$

which has the character of a step function and is shown in Fig. 2.1 with successive values determined in the "centers of gravity" of the shells. Thus, the shell correction could be expressed as a function

$$F(N) \equiv \int_0^N \left[f(n) - n^{2/3}\right] = f_i(N)\,(N - \mathcal{N}_{i-1}) - \frac{3}{5}\left(N^{5/2} - \mathcal{N}_{i-1}^{5/2}\right), \tag{2.25}$$

here $\mathcal{N}_{i-1} < N < \mathcal{N}_i$ due to integral has a non-zero value only on the last interval.

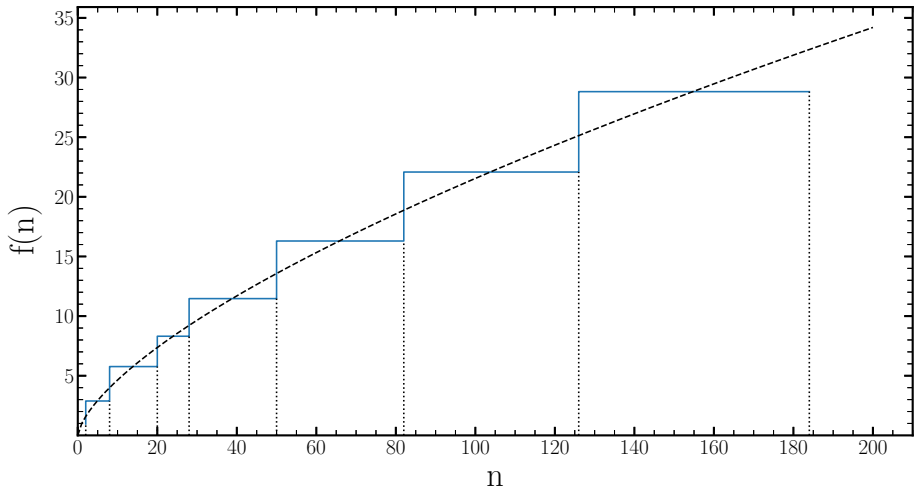

Figure 2.1: The single particle energies $f(n)$ in the discrete and degenerated spectrum by Myers-Świątecki (blue solid line) as a function of particle numbers compared to the Fermi gas energies $n^{2/3}$ (dashed line).

Then the so-called "flattening" of the function (2.25), i.e. its averaging around a certain curve $n^{2/3}$, is performed. This requires dropping f_i by about $cN/2^{2/3}$, since $n^{2/3}$ and $f(n)$ must be very close to each other for the shell correction to fluctuate around zero. In this case, the total shell correction for the nucleus is the sum of the corrections obtained from neutrons and protons

$$\delta E_{\mathrm{shell}} = \frac{e_{\mathrm{F}}^{\mathrm{n}}}{N^{2/3}}\left(F(N) - \frac{cN}{2^{2/3}}\right) + \frac{e_{\mathrm{F}}^{\mathrm{p}}}{Z^{2/3}}\left(F(Z) - \frac{cZ}{2^{2/3}}\right). \tag{2.26}$$

Assuming that $e_{\mathrm{F}}^{\mathrm{p}} \approx e_{\mathrm{F}}^{\mathrm{n}} = e_{\mathrm{F}}$ valid for nuclei close to β-stability Myers and Świątecki shell correction Eq. (2.26) can be written as

$$\begin{aligned} \delta E_{\mathrm{shell}} &= \frac{e_{\mathrm{F}}}{(A/2)^{2/3}} \left\{ F(N) + F(Z) - \frac{cA}{2^{2/3}} \right\} = \\ &= e_{\mathrm{F}} \left\{ \frac{F(N) + F(Z)}{(A/2)^{2/3}} - cA^{1/3} \right\} \equiv \mathcal{S}(N, Z). \end{aligned} \tag{2.27}$$

Before summarizing all elements of Eq. (2.17), it should be noted that the barrier height depends significantly on the deformation of the nucleus, which destroys the shell structure due to the symmetry breaking. This leads to a reduction of the shell correction energy, so the dependence of the shell correction $\mathcal{S}$ on the deformation parameter α (2.10) can be expressed in exponential form:

$$\mathcal{S}(Z, N, \alpha) = \mathcal{S}(Z, N) \exp\left(-\frac{\alpha^2}{\alpha_0^2}\right)`, \tag{2.28}$$

where α_0 is a phenomenological parameter adjusted over experimentally determined barrier heights. Nuclei with nucleon numbers far from the magic number have a positive shell correction, which creates a minimum at non-zero deformation α. On the other hand, nuclei with magic or near-magic nucleon numbers have a higher fission barrier and are more stable because they have a negative value, which, together with the drop energy, deepens the spherical minimum. It should also be noted that highly deformed nuclei can retain a strong shell structure in the case of isomeric forms.

Finally, the Myers-Świątecki formula for the binding energy (2.17), taking into account the deformation of the nucleus, has the following form

$$\begin{aligned} \mathcal{B}(Z, N, \alpha, \gamma) = & C_1 A - C_2 A^{2/3} B_{\mathrm{surf}}(\alpha, \gamma) - C_3 \frac{Z^2}{A^{1/3}} B_{\mathrm{Coul}}(\alpha, \gamma) \\ & + C_4 \frac{Z^2}{A} - \mathcal{S}(Z, N) e^{-(\alpha/\alpha_0)^2} - \delta E_{\mathrm{pair}}(Z, N). \end{aligned} \tag{2.29}$$

As seen in Eq. (2.29), in addition to the known first three terms and shell corrections, there are two more. The $C_4 Z^2/A$ term is a correction of the Coulomb energy of the nucleus due to the smooth surface charge density. Another δE_{pair} describes the pairing energy correction, which can be written as

$$\delta E_{\mathrm{pair}}(Z, N) = \begin{cases} \dfrac{11}{\sqrt{A}} \text{MeV for } Z, N \text{ odd}, \\ 0 \,\text{MeV for } A \text{ odd}, \\ -\dfrac{11}{\sqrt{A}} \text{MeV for } Z, N \text{ even}. \end{cases} \tag{2.30}$$

Unlike the modified Bethe-Weizsäcker formula (2.2), the symmetry energy is implicit and hidden in the coefficients of the volume C_1 and surface C_2 terms

$$\begin{aligned} C_1 &= a_1 \left(1 - \kappa I^2\right), \\ C_2 &= a_2 \left(1 - \kappa I^2\right). \end{aligned} \tag{2.31}$$

where $I = \frac{N-Z}{A}$.
Therefore, there are seven freely adjustable parameters in the formula (2.29). Based on

their classic work [34] Myers and Świątecki, using the then available experimental data of 1200 nuclear masses, 40 fission barriers, and 240 quadrupole moments, obtained this set of parameters

$$\begin{aligned} a_1 &= 15.4941 \text{ MeV}, & a_2 &= 17.9439 \text{ MeV}, & C_3 &= 0.7053 \text{ MeV}, \\ r_0 &= 1.2249 \text{ fm}, & C_4 &= 1.21129 \text{ MeV}, & \kappa &= 1.7826, \\ e_{\mathrm{F}} &= 5.8 \text{ MeV}, & c &= 0.26, & \alpha_0 &= 0.27. \end{aligned}$$

The error in the predictions of this formula was as high as 2 MeV, which at the time allowed the masses of the elements to be described and predicted very accurately. However, without the addition of shell and pairing corrections, the error reached up to 12 MeV in some cases, indicating the importance of these components. This rather simple phenomenological model became the basis of the so-called microscopic-macroscopic approach, which we will discuss later.

2.1.4 Droplet model

The Droplet Model (DM) provides a more sophisticated and accurate description of the average binding energy than the pure liquid droplet approach mentioned in the previous subsections. This model, like LD, attempts to incorporate surface curvature, which significantly improves the behavior of the macroscopic energy in deformed states, directly influencing it in the form of fission barriers. It also takes into account the nature of the decreasing nuclear density of the inner region of the nucleus upon deformation, since some of the nucleons that were in this region tend to occupy the increasing surface region. Therefore, the surface term proportional to $I^2A^{2/3}$ in the Myers-Świątecki formula (2.29) can be interpreted as a factor of increasing binding energy, which arises when an excess of neutrons forms the nuclear surface during deformation. Of course, we should not forget that this increase is compensated by the surface tension.

In this case, we can conclude that, in contrast to LD, the droplet model rejects the assumption of a uniform density of nucleons as well as protons and neutrons. Therefore, it has been proposed [36] to introduce the following additional parameters:

- t – thickness of the neutron skin,
- δ – relative excess of neutron density,
- ε – relative deviation of density from its nuclear matter value ρ_0,
- Σ – the effective nuclear surface area between the proton and neutron. distributions.

The neutron skin phenomenon has an obvious origin in the symmetry properties of nuclear matter, which tries to maintain an equal number of protons and neutrons. Thus, in real nuclei, where usually $N > Z$, there is a force that pushes excess neutrons to the surface. The Coulomb interaction of the protons reduces this tendency by trying to expand the region where they are located. However, this force competes with the surface tension, which also tends to hold the parity of the two types of nucleons, i.e. to eliminate the neutron skin. In this case, the neutron skin is understood as the distance t between the locations of the proton and neutron diffusion surface profiles, i.e. the shift required to place one profile on top of the other. It allows some neutrons to be added to the surface layer. Then the force responsible for the formation of the surface neutron skin can be expressed as follows

$$t = \frac{3}{2}\frac{r_0 JI}{Q}, \tag{2.32}$$

where r_0 is the constant radius of nuclear matter, J is the nuclear symmetry energy coefficient, and Q is the effective surface stiffness coefficient.
Then, taking into account the electrostatic energy for protons $\frac{3e^2}{5r_0}\frac{Z^2}{A^{1/3}}$, decreasing the given force JI leads to

$$t = \frac{3}{2}r_0\frac{JI - \frac{1}{12}c_1 ZA^{-1/3}}{Q}. \tag{2.33}$$

Further considerations lead to the modification of the denominator of this expression^:

$$t = \frac{3}{2}r_0\frac{JI - \frac{1}{12}c_1 ZA^{-1/3}}{Q + \frac{9}{4}JA^{-1/3}}, \tag{2.34}$$

where $c_1 = 3e^2/5r_0 \approx 0.7322$ MeV. Such a neutron skin correctly predicts that for an uncharged nucleus Q tends to zero and all excess neutrons are pushed into the surface ($t \to t_{max} = 2/3R_0I$). For a nucleus of arbitrary shape, t has the form

$$t = \tilde{t} + \bar{t},$$

where

$$\bar{t} = \frac{3}{2}r_0\frac{JI - \frac{1}{12}c_1 ZA^{-1/3}(B_{vol}/B_{surf})}{Q + \frac{9}{4}JA^{-1/3}B_{surf}}, \quad \tilde{t} = \frac{3}{8}r_0\frac{e}{Q}(\tilde{v}_s - \bar{\tilde{v}}),$$

where $\tilde{v}$ is the deviation from the electrostatic potential v produced by a uniformly distributed charge Ze, $\tilde{v}_s$ is the value of $\tilde{v}$ at the surface, and $\bar{\tilde{v}}$ is the surface average of $\tilde{v}_s$.

The macroscopic binding energy in the Droplet Model is then expressed in the following form [36]:

$$\begin{aligned}\mathcal{B}(A,Z,\mathrm{def}) = &\Big(-a_1 + J\,\bar{\delta}^2 - \frac{1}{2}\,K\,\bar{\varepsilon}^2 + \frac{1}{2}\,M\,\bar{\delta}^4\Big)\,A \\ &+ \Big(a_2 + \frac{9}{4}\,\frac{J^2}{Q}\,\bar{\delta}^2\Big)\,A^{2/3}B_{\mathrm{surf}}(\mathrm{def}) + a_3\,A^{1/3}\,B_{\mathrm{curv}}(\mathrm{def}) \\ &+ c_1\,Z^2\,A^{-1/3}\,B_{\mathrm{Coul}}(\mathrm{def}) - c_2\,Z^2\,A^{1/3}\,B_{\mathrm{r}}(\mathrm{def}) \\ &- c_5\,Z^2\,B_{\mathrm{w}}(\mathrm{def}) - c_3\frac{Z^2}{A} - c_4\frac{Z}{\sqrt[3]{2}} + E_{\mathrm{Wig}},\end{aligned} \tag{2.35}$$

where the factors B_{surf}, B_{curv}, B_{Coul}, B_{r}, B_{v}, and B_{w} are functionals depending on the shape of the nucleus. They describe the relative change of: nucleus surface area, curvature, Coulomb energy and its inhomogeneous spatial distribution with respect to the deviation of the Coulomb potential $W(r)$ from its mean value

$$\bar{W} = \frac{1}{\frac{4}{3}\pi R^3}\int_{\mathrm{V}} W(r)d\tau,$$

both inside and on the surface of the nucleus. These coefficients can be calculated by

integrating over volume V, or the S nucleus surface:

$$\begin{aligned}
B_{\text{surf}} &= \frac{1}{4\pi R^2}\int_{\text{S}} d\sigma \\
B_{\text{Coul}} &= \frac{1}{\frac{32}{15}\pi^2 R^5}\int_{\text{V}} W(r)d\tau \\
B_{\text{curv}} &= \frac{1}{8\pi R}\int_{\text{S}}\left(\frac{1}{R_1}+\frac{1}{R_2}\right)d\sigma \\
B_{\text{r}} &= \frac{1}{\frac{64}{1575}\pi^2 R^7}\int_{\text{V}}[W(r)-\overline{\text{W}}]^2 d\tau \\
B_{\text{v}} &= -\frac{1}{\frac{16}{15}\pi^2 R^4}\int_{\text{S}}[W(r)-\overline{\text{W}}]d\sigma \\
B_{\text{w}} &= -\frac{1}{\frac{64}{225}\pi^3 R^6}\int_{\text{S}}[W(r)-\overline{\text{W}}]^2 d\sigma.
\end{aligned} \tag{2.36}$$

All integrals (2.36) obtained for the deformed nucleus are divided by integrals calculated analytically for the spherical nucleus. The last in Eq. (2.35) component E_{Wig} is the Wigner term, which has the form [34]

$$E_{\text{Wig}}(A,Z) = -10\cdot\exp(-42|I|/10). \tag{2.37}$$

The variables $\bar{\delta}$ and $\bar{\varepsilon}$ are the averages δ, ε over the effective area Σ and are equal to:

$$\bar{\delta} = \frac{I+\frac{3}{16}\frac{c_1}{Q}ZA^{2/3}f(def)}{1+\frac{9}{4}\frac{J}{Q}A^{-1/3}B_{surf}}, \tag{2.38}$$

$$\bar{\varepsilon} = \frac{1}{K}\Big[-2a_2A^{-1/3}f(def)+L\bar{\delta}^2+C_1Z^2A^{-4/3}g(def)\Big], \tag{2.39}$$

All coefficients c_i can be expressed as follows:

$$\begin{aligned}
c_1 &= \frac{3}{5}\frac{e^2}{r_0}, \\
c_2 &= \frac{c_1^2}{336}\left(\frac{1}{J}+\frac{18}{K}\right), \\
c_3 &= \frac{5}{2}c_1\left(\frac{b}{r_0}\right), \\
c_4 &= \frac{5}{4}c_1\left(\frac{3}{2\pi}\right)^{2/3}, \\
c_5 &= \frac{1}{64}c_1\left(\frac{c_1^2}{Q}\right).
\end{aligned} \tag{2.40}$$

and coefficients entering the eqs. (2.32) and (2.40), which were fitted to the experimentally known masses and fission barriers at that time, have the following values [36]:

$$\begin{aligned}
a_2 &= 20.69\,\text{MeV}, & K &= 240\,\text{MeV}, \\
L &= 100\,\text{MeV}, & r_0 &= 1.18\,\text{fm} \\
J &= 36.8\,\text{MeV}, & Q &= 17\,\text{MeV}, \\
e^2 &= 1.44\,\text{MeV}\cdot\text{fm}, & b &= 1\,\text{fm}
\end{aligned}$$

2.1.5 Lublin-Strasbourg Drop formula

In the almost 90 years that have passed since the appearance of the main idea of Weizsäcker and Bethe, the expression for the average binding energy in the nucleus has been supplemented with new terms, including the microscopic properties of nucleons. At the same time, the basic concept of the charged liquid drop is still valid. Therefore, the terms in the phenomenological formula related to the surface properties have been studied and identified. For example, as Hill and Wheeler [32] concluded, based on the aforementioned Fermi gas model, that the liquid drop energy function should include a curvature-dependent term proportional to $A^{1/3}$. This term was later well studied [37], and its value was corrected according to the experimental data known at that time.

Since the classical model of the liquid drop does not explicitly use the surface curvature energy term, it is likely that its use only corrects the observed values. Surprisingly, the drop model formula is significantly improved by such an imperceptible modification. The starting point of the analysis here is the introduction [34] of extra curvature terms in a well-known expression MS-LD (2.29). This model overestimates the fission barrier heights in light nuclei up to about 12 MeV, although it is quite successful in reproducing the nuclear masses. Also, the MS-LD barriers are higher than Sierk [38] estimated within the macroscopic Yukawa folding framework, an improved version of DM. The final result of this analysis was the Lublin-Strasburg Drop (LSD) formula [39] – one of the most recent and advanced models for binding energy, combining elements of MS-LD and DM approaches, defined as

$$\begin{aligned}\mathcal{B}(Z,N,\mathrm{def}) = {} & b_{\mathrm{vol}}\,(1-\kappa_{\mathrm{vol}}I^2)\,A - b_{\mathrm{surf}}\,(1-\kappa_{\mathrm{surf}}I^2)\,A^{2/3}\,B_{\mathrm{surf}}(\mathrm{def}) \\ & - b_{\mathrm{curv}}\,(1-\kappa_{\mathrm{curv}}I^2)\,A^{1/3}\,B_{\mathrm{curv}}(\mathrm{def}) - \frac{3}{5}\frac{e^2Z^2}{r_0^{\mathrm{ch}}\,A^{1/3}}\,B_{\mathrm{Coul}}(\mathrm{def}) + C_4\,\frac{Z^2}{A} - E_{\mathrm{Wig}}.\end{aligned} \tag{2.41}$$

where the deformation dependent coefficients B_{surf}, B_{curv} and B_{Coul} are calculated in the same way as in (2.36).
The parameters of the LSD formula fitted to the 3760 experimental masses of nuclei are as follows:

$a_{\mathrm{vol}} = -15.4920$ MeV	$\kappa_{\mathrm{vol}} = 1.8601$
$a_{\mathrm{surf}} = 16.9707$ MeV	$\kappa_{\mathrm{surf}} = 2.2938$
$a_{\mathrm{curv}} = 3.8602$ MeV	$\kappa_{\mathrm{curv}} = -2.3764$
$r_0^{\mathrm{ch}} = 1.21725$ fm	$C_4 = 0.9181$ MeV

After the inclusion of the microscopic (shell and pairing) energy corrections, this formula reproduces all the available nuclear masses with an r.m.s. deviation equal to $\langle \delta M \rangle = 0.69$ MeV in comparison to 0.698 MeV with MS-LD, which is not significant. Nerveless it also gives fission barrier heights close [39–41] to the experimental values known at present. For example, for nuclei with $Z > 70$, $\langle \delta V_B \rangle = 0.88$ MeV versus 5.58 MeV for MS-LD. It must be emphasized that none of the LSD parameters were fitted to the barrier heights. The simplicity and the relatively small number of adjustable LSD parameters give hope for a reliable prediction of properties even for yet undiscovered nuclei. These advantages make the LSD formula a good tool for the development of nuclear fission studies, especially in the macroscopic-microscopic method that will be used later.

This section may be summed up as follows. Here has been an attempt at a restrospective view of the atomic nucleus from the point of view of semi-classical (macroscopic) physics. According to this view, the atomic nucleus is a one body with the properties of charged liquid drop, which is reflected in Bethe-Weisecker's phenomenological formula (2.2). Pioneering researchers were able to foresee its basic components by operating

on fundamental principles. However, it took a long time for such an approach to describe the more detailed structure of the atomic nucleus, introducing a more sophisticated view of the nucleon shells and deformations. The next iteration, in the form of the Myers-Świątecki Liquid Drop Model (2.29), was able to bring these representations together, allowing a large number of nuclear masses to be described, but also giving rise to a "race" to improve the macroscopic approach. Modern representatives of this are for DM, such as the work on the Finite Range Droplet Model developed by Möller's group [42], or improved LD, such as the previously mentioned Lublin-Strasbourg Model (2.41) and the works of Moretto [43].

We will return to other macroscopic parameters of the nucleus that depend on the deformation of the fissile nucleus in later chapters of this work. For now, we will focus on the determination of the energies of the nuclei, whose single-particle energies are necessary for the determination of the generalized potential of the system.

2.2 Microscopic approach

Although the macroscopic approach allows us to describe general properties of the nucleus such as mass, charge, radius, etc., detailed knowledge of its internal structure is required. This has already been shown indirectly in advanced droplet models, where there are shell corrections calculated from single-particle states of the nucleons, albeit to a rough approximation (see 2.1.3). Nevertheless, this quantity is a microscopic (quantum) property of the particle determined within the single-particle approach. Therefore, it is necessary to consider the methods and formalisms used in this approach, which will form the basis of a generalized model describing the properties of the nucleus in the most complete way.

The nucleus consists of a finite number of protons and neutrons that actively interact with each other through the strong interaction that holds this quantum system together. That is, from the point of view of theoretical physics, it is a finite multinuclear fermi-system described by the formalism of quantum mechanics based on solutions of the Schrödinger equations. These solutions allow us to obtain information about the energy of particles, spins, their distribution in the nucleus and other quantum properties. Therefore, to determine the energy we will use the well-known Hartree-Fock method.

2.2.1 Hartree-Fock method

Let's define the Hamiltonian of many-body system consisting from A nucleons

$$H = -\frac{\hbar^2}{2M_{\text{nucl}}} \sum_{n=1}^{A} \Delta_n + \sum_{n,n';n<n'}^{A} V\left(\mathbf{r}_n - \mathbf{r}_{n'}; \sigma_n\sigma_{n'}, \tau_n\tau_{n'}\right), \tag{2.42}$$

where the two-particle interaction $(\mathbf{r}_1 - \mathbf{r}_2; \sigma_1\sigma_2, \tau_1\tau_2)$ consists of long-range Coulomb interaction between protons and short-range, spin and isospin-dependent, effective nuclear interaction $V_{\text{eff}} = V\left(\mathbf{r}_1 - \mathbf{r}_2\right) \hat{A}\left(\hat{P}_\sigma, \hat{P}_{tau}\right)$ whereas the operator

$$\hat{A} = W + B\hat{P}_\sigma - H\hat{P}_\tau - M\hat{P}_\sigma\hat{P}_\tau \tag{2.43}$$

represents the standard dependence of the central part of the effective two-body potential on the spin and isospin exchange-operators $\hat{P}_\sigma = \frac{1}{2}\left(1 + \sigma_1\sigma_2\right)$ and $\hat{P}_\tau = \frac{1}{2}\left(1 + \boldsymbol{\tau}_1\boldsymbol{\tau}_2\right)$ with empirical parameters W, B, H, and M, which are the strength parameters of the Wigner, Bartlett, Heisenberg, and Majorana interactions, respectively.

Suppose then that there exist functions $\chi_i(\mathbf{r}, \sigma, \tau)$, forming complete set of orthonormal one-particle states and being eigenstates of the one-particle Hamiltonian of the shell model.

For such set the operators of nucleon creation and annihilation $\hat{a}_i^+$ and $\hat{a}_i$ are defined, and in the notation of which the Hamiltonian (2.42) in Fock-space representation can be written as

$$\hat{H} = \sum_{l,l'} t_{ll'} \hat{a}_l^+ \hat{a}_{l'} + \frac{1}{2} \sum_{l_1 l_2 l_1' l_2'} V_{l_1 l_2 l_1' l_2'} \hat{a}_{l_1}^+ \hat{a}_{l_2}^+ \hat{a}_{l_2'} \hat{a}_{l_1'} \tag{2.44}$$

where matrix elements $t_{ll'}$ and $V_{l_1 l_2 l_1' l_2'}$ have forms

$$t_{ll'} = -\frac{\hbar^2}{2M_{\text{nucl}}} \int \chi_l^*(\mathbf{r}) \Delta \chi_{l'}(\mathbf{r}) d^3 r,$$

$$V_{l_1 l_2 l_1' l_2'} = \int d^3 r \int d^3 r' \chi_{l_1}^* (\mathbf{r}_1 \sigma_1 \tau_1) \chi_{l_2}^* (\mathbf{r}_2 \sigma_2 \tau_2) \\ V(\mathbf{r}_1 - \mathbf{r}_2) \hat{A} \left(\hat{P}_\sigma, \hat{P}_\tau \right) \chi_{l_1'} (\mathbf{r}_1 \sigma_1 \tau_1) \chi_{l_2'} (\mathbf{r}_2 \sigma_2 \tau_2).$$

The Hartree-Fock method lies [44] in searching for an approximate solution of the N-body problem in the set of Slater determinants $\det [\chi_i (\mathbf{r}_j \sigma_j \tau_j)]$, $i, j{=}1, \ldots, A$, consisting of A wave functions χ_i. In Fock space these A-particle states are represented as

$$|\text{HF}\rangle = \prod_{i=1}^{A} \hat{a}_i^+ |0\rangle.$$

The goal of this approximation is to determine the one-particle basis

$$\varphi_i(\mathbf{r}, \sigma, \tau) = \sum_{i'} U_{ii'} \chi_{i'}(\mathbf{r}, \sigma, \tau) \tag{2.45}$$

connected to the original function basis χ_i by the unitary transformation $U_{ii'}$ with the creation and annihilation operators

$$\hat{c}_i^+ = \sum_{i'} U_{ii'} \hat{a}_{i'}^+ \quad \text{and} \quad \hat{c}_i = \sum_{i'} U_{ii'} \hat{a}_{i'}$$

for which Slater's determinant

$$|\text{HF}\rangle^{(0)} = \prod_{k=1}^{A} \hat{c}_k^+ |0\rangle \tag{2.46}$$

minimizes the expectation value

$$E^{\text{HF}} = \langle \text{HF} | \hat{H} | \text{HF} \rangle$$

conserving the proton and neutron numbers. Thus the density matrix is given as follows

$$\rho_{kl} = \left\langle \text{HF} \left| \hat{a}_l^+ \hat{a}_k \right| \text{HF} \right\rangle \tag{2.47}$$

which has a property $\operatorname{tr} \rho = A$.

So, in terms of the density matrix and the anti-symmetrized matrix element of the two-particle interaction

$$\bar{V}_{l_1' l_2' l_1 l_2} = V_{l_1' l_2' l_1 l_2} - V_{l_1' l_2' l_2 l_1}$$

the expectation value E^{HF} is

$$E^{\text{HF}} = \sum_{l_1 l_2} t_{l_1 l_2} \rho_{l_2 l_1} + \frac{1}{2} \sum_{l_1 l_1' l_2 l_2'} \rho_{l_1 l_1'} \bar{V}_{l_1' l_2' l_1 l_2} \rho_{l_2' l_2}. \tag{2.48}$$

Usually the effective two-particle nuclear interactions are density dependent: $V\left(\mathbf{r}_1-\mathbf{r}_2;\rho(\mathbf{R})\right)$ with $\mathbf{R}=\left(\mathbf{r}_1+\mathbf{r}_2\right)/2$. Assuming that

$$\rho(\mathbf{R})=\sum_{ij}\rho_{ij}\chi_i^*(\mathbf{R})\chi_j(\mathbf{R})$$

the variation of potential with respect to the density matrix has following dependency

$$\frac{\partial\bar{V}}{\partial\rho_{ij}}=\frac{\partial\bar{V}}{\partial\rho}\frac{\partial\rho}{\partial\rho_{ij}}=\frac{\partial\bar{V}(\rho(\mathbf{R}))}{\partial\rho}\chi_i^*(\mathbf{R})\chi_j(\mathbf{R}) \tag{2.49}$$

Then to obtain minimum of E^{HF} with respect to variations of the density matrix with the trace conservation constraint, it is necessary to take the derivative

$$\frac{\partial\left(E^{\mathrm{HF}}-\epsilon\,\mathrm{tr}\,\rho\right)}{\partial\rho_{kl}}=t_{kl}+\Gamma_{kl}-\epsilon\delta_{kl}=0 \tag{2.50}$$

where ϵ is a Lagrange multiplier and mean field Γ_{kl}, defined as

$$\Gamma_{kl}=\frac{\partial\,\mathrm{tr}[\rho\bar{V}\rho]}{\partial\rho_{kl}}=\sum_{l_2l_2'}\bar{V}_{kl_2'll_2}\rho_{l_2'l_2}+\frac{1}{2}\sum_{l_1l_2l_1'l_2'}\rho_{l_1l_1'}\left[\frac{\partial\bar{V}}{\partial\rho(\mathbf{r})}\chi_k^*\chi_l\right]_{l_1'l_2'l_1l_2}\rho_{l_2'l_2}. \tag{2.51}$$

In Eq. (2.51) the last term arises when the effective two-particle potential has an explicit density dependence. Then using the unitary transformation (2.45) which diagonalizes the eigenvalue Eq. (2.50), in spatial representation takes the form

$$\begin{aligned}&-\frac{\hbar^2}{2M_{\mathrm{nucl}}}\Delta\varphi_k(\mathbf{r},\sigma,\tau)+\sum_{j=1}^{A}\sum_{\sigma'\tau'}\int d\mathbf{r}'\varphi_j^*\left(\mathbf{r}',\sigma',\tau'\right)V\left(\mathbf{r}-\mathbf{r}'\right)\hat{A}\left(\hat{P}_\sigma,\hat{P}_\tau\right)\\&\times\left[\varphi_j\left(\mathbf{r}',\sigma',\tau'\right)\varphi_k(\mathbf{r},\sigma,\tau)-\varphi_j(\mathbf{r},\sigma,\tau)\varphi_k\left(\mathbf{r}',\sigma',\tau'\right)\right]=\epsilon_k\varphi_k(\mathbf{r},\sigma,\tau),\end{aligned} \tag{2.52}$$

where the sum is to be extended over the A eigenstates with the smallest eigenvalues ϵ_k.

Since in the basis $\varphi_i(\mathbf{r},\sigma,\tau)$, the density matrix is diagonal $\rho_{ij}=n_i\delta_{ij}$, i.e. for occupied states the eigenvalue is 1 and for unoccupied states it is 0. It can be described by the condition

$$n_i=\begin{cases}1 & \text{if}\quad i\le i_{\mathrm{Fermi}}\\0 & \text{if}\quad i>i_{\mathrm{Fermi}}\end{cases}$$

Therefore energy (2.48) can be rewritten following

$$E^{\mathrm{HF}}=\sum_{i=1}^{A}t_{ii}+\frac{1}{2}\sum_{i,j=1}^{A}\bar{V}_{ij,ij} \tag{2.53}$$

Due to eigenvalues ϵ_i of Hartree-Fock (2.52) are given by

$$\epsilon_i=t_{ii}+\Gamma_{ii}$$

so, the Eq. (2.53) transforms to simple expression

$$E^{\mathrm{HF}}=\sum_{i=1}^{A}\left(\epsilon_i-\frac{1}{2}\Gamma_{ii}\right) \tag{2.54}$$

It can be seen that the Hartree-Fock approximation is a powerful tool for describing the interaction of nucleons inside the atomic nucleus. However, this approach has its pitfalls. For example, as shown [45], there is a commutation of the form

$$[H,\rho]=0 \tag{2.55}$$

in the HF basis and variations of the type $\delta\rho_{k'k}$ are allowed, but these interactions can only be between particle states (i.e. states above the Fermi energy) k' and hole states (i.e. states below the Fermi energy) k or vice versa. Therefore, the behavior of the particle-particle interaction potential is irrelevant in the HF approximation.

Furthermore, it is easy to see that the Hartree-Fock equation (2.55) is a nonlinear eigenvalue equation. It is solved iteratively starting from the mean field $\Gamma^{(0)}$. The eigenfunctions $\varphi_i^{(1)}$ obtained by solving the equations HF with this mean field are used to compute the new mean field $\Gamma^{(1)}$ according to the equation (2.51) until self-consistent. However, there are nuances here as well.

First, although the HF equation is valid for any stationary point, it depends on the proximity of the shape of the initial potential of the shell model to a finite local minimum on the energy surface. This raises the question [46] of determining the minimum to which the iteration converges if there are multiple local minima.

Second, the iteration preserves the symmetry of the initial field. This means that if the desired solution does not have a spherical symmetry, but for example an axial symmetry, the initial field must have less symmetries. The same is valid for other kinds of symmetries and their breaking. So this is why it is not possible to get the saddle points of the surface. To do this, one has to add the corresponding bounding field qQ_{kl} to Γ_{kl}. Usually $\hat{Q}$ is the quadrupole momentum operator and q is the Lagrange parameter. The latter has the meaning of the generalized force required to keep the nucleus in equilibrium at a given value of the quadrupole strain $Q = \langle \mathrm{HF}|\hat{Q}|\mathrm{HF}\rangle$. Moreover, depending on the force parameter $q(Q)$, the zeros of this function correspond to the stationary points (including the saddle points), and the sign of the derivative at these points gives the difference between the minima and the saddle points.

2.2.2 Basics of the Hartree-Fock-Bogolyubov method

Let us now try to solve the above-mentioned disadvantage of the self-consistent Hartree-Fock approximation by adding [47] to the mean field the pairing correlations through which one can consider the particle-particle interactions. To do this, we will use the Bogolyubov transformation [48] formalism, which introduced the quasi-particle creation and annihilation operators $\hat{\alpha}_i^+$ and $\hat{\alpha}_i$

$$\begin{aligned} \hat{\alpha}_i &= \sum_{j=1}^{M} \left(u_{ij}^* \hat{a}_j + v_{ij}^* \hat{a}_j^+ \right), \\ \hat{\alpha}_i^+ &= \sum_{j=1}^{M} \left(u_{ij} \hat{a}_j^+ + v_{ij} \hat{a}_j \right), \end{aligned} \tag{2.56}$$

where M is the dimension of the single-particle space and u and v are transformation matrices. Introducing the $2M \times 2M$ matrix

$$\hat{B} = \begin{pmatrix} \hat{u} & \hat{v}^* \\ \hat{v} & \hat{u}^* \end{pmatrix} \tag{2.57}$$

which due to the ortho-normalization of quasi-particle states should be unitary

$$\hat{B}\hat{B}^+ = \hat{B}^+\hat{B} = \hat{I}, \tag{2.58}$$

where $\hat{B}^+$ is the hermitian conjugate of the $\hat{B}$ matrix.

Using this matrix $\hat{B}$ the transformation (2.56) and its inverse operation can be written as

$$\begin{pmatrix} \hat{\alpha} \\ \hat{\alpha}^+ \end{pmatrix} = \hat{B}^+ \begin{pmatrix} \hat{a} \\ \hat{a}^+ \end{pmatrix}; \quad \begin{pmatrix} \hat{a} \\ \hat{a}^+ \end{pmatrix} = \hat{B} \begin{pmatrix} \hat{\alpha} \\ \hat{\alpha}^+ \end{pmatrix}. \tag{2.59}$$

One assumes that the ground-state wave-function $|\mathrm{HFB}\rangle$ of a nucleus with pairing correlations is a state of independent quasi-particles

$$|\mathrm{HFB}\rangle = \prod_{i=1}^{M} \hat{\alpha}_i |0\rangle. \tag{2.60}$$

that demonstrates the state $|\mathrm{HFB}\rangle$ is the quasi-particle vacuum

$$\hat{\alpha}_i |\mathrm{HFB}\rangle = 0.$$

From the hermitian density matrix

$$rho_{ij} = \left\langle \mathrm{HFB} \left| \hat{a}_j^+ \hat{a}_i \right| \mathrm{HFB} \right\rangle = \left[v^* v^T \right]_{ij} \tag{2.61}$$

and the skew-symmetric pairing tensor

$$\kappa_{ij} = \langle \mathrm{HFB} \left| \hat{a}_j \hat{a}_i \right| \mathrm{HFB} \rangle = \left[v^* u^T \right]_{ij} = - \left[u v^+ \right]_{ij} \tag{2.62}$$

a generalised hermitian density matrix is formed

$$\hat{R} = \begin{pmatrix} \hat{\rho} & \hat{\kappa} \\ -\hat{\kappa}^* & 1 - \hat{\rho}^* \end{pmatrix}. \tag{2.63}$$

Thus the expectation value of the Hamiltonian could be given in terms ρ_{ij} and κ_{ij} as

$$\langle \mathrm{HFB} | \hat{H} | \mathrm{HFB} \rangle = \sum_{ij} t_{ij} \rho_{ji} + \frac{1}{2} \sum_{ijkl} \langle ij | \bar{V} | kl \rangle \rho_{lj} \rho_{ki} + \frac{1}{4} \sum_{ijkl} \langle ij | \bar{V} | kl \rangle \kappa_{lk} \kappa^*_{ji} \tag{2.64}$$

also the expectation value of the particle number by

$$\langle \mathrm{HFB} | \hat{N} | \mathrm{HFB} \rangle = \sum_i \rho_{ii} \tag{2.65}$$

Now minimise the total energy with the constraint where the expectation of particle number has the required value and leads to the stationarity condition HFB of the ground state

$$\delta \left\{ \langle \mathrm{HFB} | \hat{H} - \lambda \hat{N} | \mathrm{HFB} \rangle - \mathrm{tr} \left[\Lambda \left(\hat{R}^2 - \hat{R} \right) \right] \right\} = 0, \tag{2.66}$$

where $\mathrm{tr}\left[\Lambda\left(\hat{R}^2 - \hat{R}\right)\right]$ is subtracted to account for the Bogolyubov condition (2.58), expressed here in terms of the generalized density (2.63). The variation is to be performed with respect to $\delta\rho$, $\delta\rho^*$, $\delta\kappa$ and $\delta\kappa^*$, and Λ is a hermitian matrix whose elements are Lagrange multipliers.

After performing the variation and eliminating the matrix Λ using its hermiticity, the condition (2.66) can be expressed by the commutator:

$$[\hat{\mathcal{H}}, \hat{R}] = 0, \tag{2.67}$$

where operator $\hat{\mathcal{H}}$ is given by

$$\hat{\mathcal{H}} = \begin{pmatrix} \hat{h} & \hat{\Delta} \\ -\hat{\Delta}^* & -\hat{h}^* \end{pmatrix} \tag{2.68}$$

with

$$h_{ij} = \frac{\partial}{\partial \rho_{ji}} \langle \mathrm{HFB} | \hat{H} - \lambda \hat{N} | \mathrm{HFB} \rangle \tag{2.69}$$

and

$$\Delta_{ij} = 2\frac{\partial}{\partial \kappa^*_{ji}}\langle \mathrm{HFB}|\hat{H}|\mathrm{HFB}\rangle. \tag{2.70}$$

Equation (2.67) is the analog of Eq. (2.55) in HF theory. To solve Eq. (2.67) it is sufficient to choose as Bogolyubov transformation $\hat{B}$ the unitary matrix which diagonalizes $\hat{\mathcal{H}}$. This leads to the HFB equations in their standard form

$$\hat{\mathcal{H}}\hat{B} = \hat{B}\hat{\mathscr{E}} \quad \text{with} \quad \mathscr{E}_{ij} = \mathcal{E}_i\delta_{ij} \tag{2.71}$$

where $\mathcal{E}_i$ denotes the quasi-particle energy.

With the definition (2.70) the explicit form of the pairing matrix becomes

$$\Delta_{ij} = \frac{1}{2}\sum_{kl}\langle ij|\bar{V}|kl\rangle\kappa_{lk} \tag{2.72}$$

The matrix elements of h (2.69) can be obtained in a similar way. For density dependent interactions one gets from Eqs. (2.69) and (2.49)

$$h_{ij} = t_{ij} - \lambda\delta_{ij} + \Gamma_{ij}, \tag{2.73}$$

where is the quasi-particle mean-field.

$$\Gamma_{ij} = \sum_{kl}\langle ik|\bar{V}(\rho)|jl\rangle\rho_{lk} + \frac{1}{2}\sum_{klmn}\left\langle mn\left|\frac{\partial\bar{V}(\rho)}{\partial\rho}\varphi^*_i\varphi_j\right|kl\right\rangle\left[\rho_{ln}\rho_{km} + \frac{1}{2}\kappa_{lk}\kappa^*_{nm}\right] \tag{2.74}$$

Thus the total binding energy represents as

$$E = \mathrm{tr}\left\{\left(\hat{t} + \frac{1}{2}\hat{\Gamma}\right)\hat{\rho} + \frac{1}{2}\hat{\Delta}\hat{\kappa}^*\right\} + E_{\mathrm{R}} \tag{2.75}$$

where

$$E_{\mathrm{R}} = -\frac{1}{4}\sum_{ijklmn}\left\langle mn\left|\frac{\partial\bar{V}(\rho)}{\partial\rho}\varphi^*_i\varphi_j\right|kl\right\rangle\left[\rho_{ln}\rho_{km} + \frac{1}{2}\kappa_{lk}\kappa^*_{nm}\right]\rho_{ij} \tag{2.76}$$

is the rearrangement energy resulting from the dependence of the effective interaction potential on the density [49].

It is clear from the equation (2.75) that in the case of density-dependent interactions the mean field depends not only on the density matrix (2.61) but also on the coupling tensor (2.62). In fact, this is the main difference between the HF theory and the HFB theory. Indeed, it is not difficult to see that the latter is a generalization of the Hartree-Fock equation (2.54), if one sets the κ and Δ matrices to zero, since the self-consistent HF field depends only on the density matrix. And this means that, in contrast to the HF theory, in the HFB theory the result depends on the contribution of both the particle-hole channel and the particle-particle effective interaction potential channel.

2.2.3 Pairing effects within Bardeen-Cooper-Schrieffer method

More rigorous consideration of pairing effects allows one to describe the nuclear structure well, but the solution of the HFB equations is a rather bulky procedure, which is especially inconvenient for the computation of very large numbers of states. The question is how to find an alternative approximation that might be less tedious and also takes into account the pairing effects described in the previous subsection. The answer was found in the form of a simple HF-BCS approximation, where first the single-particle energies ϵ_i and

the $|i\rangle$ eigenstates are self-consistent in the Hartree-Fock framework without considering any pairing contribution from the mean field, and then the pairing correlations are included in the BCS step. Moreover, this approach is extremely efficient when the effective interaction potential determining the mean field poorly describes the particle-particle channel, which is quite common in practice.

In BCS theory, the pairing potential is assumed to act only between the $|i\rangle$ states and their time-reversed counterparts $|\bar{i}\rangle = \mathcal{T}|i\rangle$. For spherically symmetric systems $|i\rangle \equiv |nljm\rangle$ and time-reversed states it is defined [46] by the following relation

$$|\bar{i}\rangle = \mathcal{T}|nljm\rangle = (-1)^{j+m}|nlj-m\rangle. \tag{2.77}$$

Thus, these pairs of degenerate states are singlet in their relative spin and orbital angular momentum, and must be isotriplets to satisfy the Pauli principle. In non-symmetric but time-reversal symmetric systems, the single-particle states $|i\rangle$ can be decomposed into a spherical basis, and the rule of equation (2.77) can be extended to such states. In this work it is possible to limit the discussion to time-invariant systems with pairs of degenerate states ("Kramers' degeneracy"), since there is no discussion of the rotation of the fissile system, which is non-invariant under the mentioned symmetry type.

The BCS Hamiltonian is

$$\hat{H} = \sum_{i\lessgtr 0} \epsilon_i \hat{a}_i^+ \hat{a}_i + \frac{1}{2} \sum_{i,j>0} \bar{V}_{i\bar{i},j\bar{j}} \hat{a}_i^+ \hat{a}_{\bar{i}}^+ \hat{a}_{\bar{j}} \hat{a}_j. \tag{2.78}$$

where the summation limits $i \lessgtr 0$ indicate a summation over all states i and their conjugates $\bar{\imath}, i > 0$ means a summation over the pairs $(i, \bar{\imath})$ in this order only. According to the representations [45] of BCS theory (as compared to HFB), the transformation to quasi-particle operators is simplified, and the Eqs. (2.56) take the form

$$\hat{\alpha}_i = u_i \hat{a}_i - v_i \hat{a}_{\bar{i}}^+, \; \hat{\alpha}_i^+ = u_i \hat{a}_i^+ - v_i \hat{a}_{\bar{i}}, \tag{2.79}$$

with real u_i and v_i with the normalization condition, which instead (2.58) guarantees that they obey Fermi commutation rules

$$u_i^2 + v_i^2 = 1. \tag{2.80}$$

The ansatz for the BCS ground-state of an even proton-number and even neutron-number state is

$$|\mathrm{BCS}\rangle = \prod_{i>0} \left(u_i + v_i \hat{a}_i^+ \hat{a}_{\bar{i}}^+\right) |0\rangle, \tag{2.81}$$

where $i > 0$ indicates the product over all single particle states of $|i\rangle$, excluding the time-reversed counterparts. Clearly, the state $|\mathrm{BCS}\rangle$ is a quasi-particle vacuum

$$\hat{\alpha}_k |\mathrm{BCS}\rangle = 0.$$

Then the state of the BCS is not eigenstate of the particle number operator. In such a case, in the representation u_i and v_i the expectation value of the particle number operator $\hat{N} = \sum_i \hat{a}_i^+ \hat{a}_i$. is

$$N = \langle \mathrm{BCS}|\hat{N}|\mathrm{BCS}\rangle = 2 \sum_{i>0} v_i^2. \tag{2.82}$$

So the expectation value of the Hamiltonian is

$$E_{\mathrm{BCS}} = \langle \mathrm{BCS}|\hat{H}|\mathrm{BCS}\rangle = 2 \sum_{i>0} \epsilon_i v_i^2 + \sum_{i>0} \bar{V}_{i\bar{i}i\bar{i}} v_i^4 + \frac{1}{2} \sum_{i,j>0} \bar{V}_{i\bar{i}j\bar{j}} u_i v_i u_j v_j. \tag{2.83}$$

Minimization of the expectation value of the Routhian $\hat{H}' = \hat{H} - \lambda\hat{N}$ with respect to variations of the v_i, observing the constraint (2.80), yields the equation

$$\left(\frac{\partial}{\partial v_i} + \frac{\partial u_i}{\partial v_i}\frac{\partial}{\partial u_i}\right)\langle \mathrm{BCS}|\hat{H} - \lambda\hat{N}|\mathrm{BCS}\rangle = 0, \tag{2.84}$$

from which the BCS equations following

$$2\tilde{\epsilon}_i u_i v_i + \Delta_i\left(v_i^2 - u_i^2\right) = 0, \quad i > 0, \tag{2.85}$$

where

$$\tilde{\epsilon}_i = \epsilon_i - \lambda + \bar{V}_{i\bar{i}i\bar{i}}v_i^2 \tag{2.86}$$

and

$$\Delta_i = -\sum_{j>0}\bar{V}_{i\bar{i}j\bar{j}}u_j v_j. \tag{2.87}$$

From Eqs. (2.80) and (2.85) one obtains

$$\begin{aligned} v_i^2 &= \frac{1}{2}\left(1 - \frac{\tilde{\epsilon}_i}{\sqrt{\tilde{\epsilon}_i^2 + \Delta_i^2}}\right) \\ u_i^2 &= \frac{1}{2}\left(1 + \frac{\tilde{\epsilon}_i}{\sqrt{\tilde{\epsilon}_i^2 + \Delta_i^2}}\right). \end{aligned} \tag{2.88}$$

Inserting Eqs. (2.88) into Eq. (2.87) we get the gap equation

$$\Delta_i = -\frac{1}{2}\sum_{j>0}\bar{V}_{i\bar{i},j\bar{j}}\frac{\Delta_j}{\sqrt{\tilde{\epsilon}_j^2 + \Delta_j^2}} \tag{2.89}$$

which together with the constraint (2.82) and Eq. (2.86)) the gap equation allows to determine the Lagrange multiplier λ and the v_i in terms of the ϵ_i and the matrix elements $\bar{V}_{i\bar{i},j\bar{j}}$ by an iterative procedure.

For the pairing potential in Eq. (2.89) sometimes a zero-range interaction is used [50, 51]

$$V^q\left(\boldsymbol{r}_1, \sigma_1; \boldsymbol{r}_2, \sigma_2\right) = V_0^q\frac{1 - \boldsymbol{\sigma}_1\cdot\boldsymbol{\sigma}_2}{4}\delta\left(\boldsymbol{r}_1 - \boldsymbol{r}_2\right), \quad q = n, p \tag{2.90}$$

With this interaction one obtains:

$$V^q_{i\bar{i}j\bar{j}} = V_0^q\int d^3r\rho_i^q(\boldsymbol{r})\rho_j^q(\boldsymbol{r}), \tag{2.91}$$

where

$$\rho_i^q(\boldsymbol{r}) = \left|\varphi_i^q(\boldsymbol{r})\right|^2 \tag{2.92}$$

and V_0^q is the pairing strength.
The term proportional to v_i^2 in the equation (2.86) only leads to a shift of the energies ϵ_i, i.e. it renormalizes the single-particle potential. Therefore, to avoid double counting, they have to be excluded, since ϵ_i already corresponds to the full mean field.

The states of an odd nucleus with particle number $N+1$ are given in BCS theory by

$$\hat{\alpha}_k^+|\mathrm{BCS}\rangle = \hat{a}_k^+\prod_{i>0;i\neq k}\left(u_i + v_i\hat{a}_i^+\hat{a}_{\bar{i}}^+\right)|0\rangle \tag{2.93}$$

where $|\mathrm{BCS}\rangle$ is the BCS ground state of the even nucleus with N particles. The expectation value of the Routhian $\hat{H}' = \hat{H} - \lambda\hat{N}$ of an odd nucleus is

$$E^{(k)}_{\mathrm{BCS}} = \left\langle \mathrm{BCS} \left| \hat{\alpha}_k \hat{H}' \alpha^+_k \right| \mathrm{BCS} \right\rangle = \left\langle \mathrm{BCS} \left| \hat{H}' \right| \mathrm{BCS} \right\rangle + \mathcal{E}_k \tag{2.94}$$

with the quasi-particle energy

$$\mathcal{E}_k = \sqrt{\tilde{\epsilon}^2_k + \Delta^2_k}. \tag{2.95}$$

It is supposed that addition of an additional odd particle does not affect the correlation structure of paired particles N, which is true only partially, since it is feasible [45] only if many particles participate in formation of the correlated state. A more detailed consideration of the odd system is given below for the model with the state-independent pairing matrix element.

The ground state k_0 corresponds to $\epsilon_{k_0} \approx \lambda$. From eq. (2.86) follows, again neglecting the v^2_i terms, $\mathcal{E}_{k_0} = 0$. To get the odd-even mass difference, usually defined as the second finite difference

$$E_{\mathrm{oe}} = -(1/2)\left[E^{\mathrm{GS}}_{N+2} - E^{\mathrm{GS}}_{N+1} - \left(E^{\mathrm{GS}}_{N+1} - E^{\mathrm{GS}}_{N}\right)\right], \quad N \text{ even}, \tag{2.96}$$

one uses the following relations between ground-state energies

$$E^{\mathrm{GS}}_{N+2} \approx E^{\mathrm{GS}}_N + 2\lambda, \quad E^{\mathrm{GS}}_{N+1} \approx E^{\mathrm{GS}}_N + \lambda + \mathcal{E}_{k_0}, \tag{2.97}$$

and obtains

$$E_{\mathrm{eo}} = \mathcal{E}_{k_0} \approx \Delta_{k_0}. \tag{2.98}$$

Note, however, that the even-odd staggering of nuclear binding energies exists in the absence of pairing, i.e., in the HF approximation, since it is related to the breaking of time reversal symmetry in odd systems.

Figure 2.2 shows that on average $\Delta_p = 12 \cdot A^{-1/2}$MeV and $\Delta_n = 11 \cdot A^{-1/2}$ MeV roughly describe the data for protons and neutrons. In the equation (2.96) it is assumed that the ground state binding energies of the three nuclei on the right hand side depend smoothly on N, except for pairing effects. This is not always the case, for example when the ground state strain changes rapidly as a function of N. Of course, this difficulty arises even more often when fourth differences of the equation (2.96) are used instead of second differences.

Pairing energy corrections

The calculation of pairing corrections to the ground state binding energies, on the other hand, is basically a rather schematic BCS calculation, where the interaction potential in the Hamiltonian Eq. (2.78) is assumed to have state-independent matrix elements.

$$\frac{1}{2}\sum_{i,j>0} \bar{V}_{i\bar{i}j\bar{j}} \hat{a}^+_i \hat{a}^+_{\bar{i}} \hat{a}_{\bar{j}} \hat{a}_j = -G \sum_{i,j>0}^{(\omega)} \hat{a}^+_i \hat{a}^+_{\bar{i}} \hat{a}_{\bar{j}} \hat{a}_j, \tag{2.99}$$

where ω indicates that the sum is restricted to states i, j which lie in a band of width 2ω around the Fermi energy calculated in HF theory. Thus the gap parameter Δ from eq. (2.87) also becomes state-independent.

$$\Delta = G \sum_{i>0}^{(\omega)} u_i v_i \tag{2.100}$$

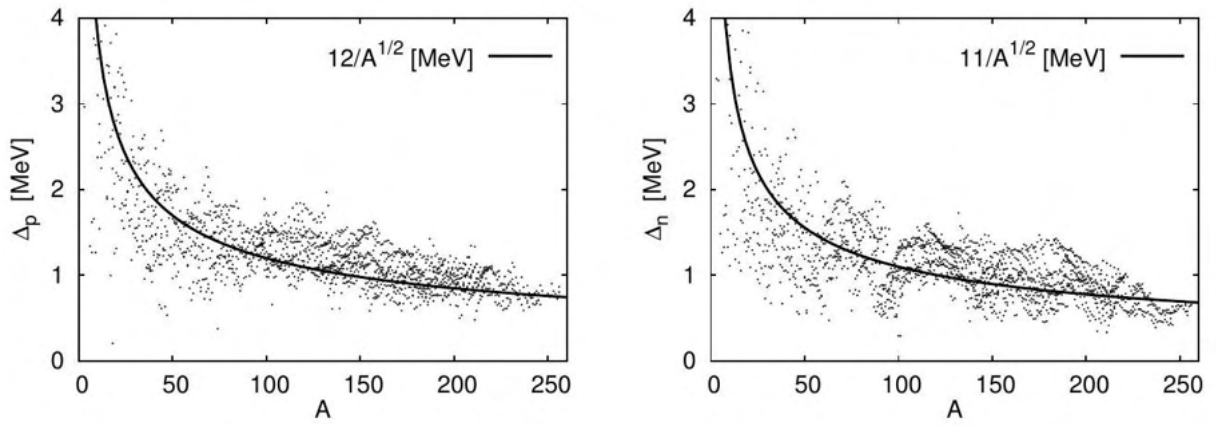

Figure 2.2: The dependence of the proton and neutron gaps on the mass number, data from the mass table of Ref. [52], taken from Ref. [46].

and therefore Eq. (2.86) is simplified to the following expression

$$\tilde{\epsilon}_i = \epsilon_i - \lambda - G v_i^2. \tag{2.101}$$

The expectation value of the Routhian $\hat{H}' = \hat{H} - \lambda \hat{N}$ is

$$\left\langle \mathrm{BCS} \left| \hat{H}' \right| \mathrm{BCS} \right\rangle = 2 \sum_{i>0}^{(\omega)} \tilde{\epsilon}_i v_i^2 + \sum_{i>0}^{(\omega)} G v_i^4 - \Delta^2 / G \tag{2.102}$$

with the new gap equation

$$\Delta = \frac{G}{2} \sum_{i>0}^{(\omega)} \frac{\Delta}{\sqrt{\tilde{\epsilon}_i^2 + \Delta^2}}. \tag{2.103}$$

Again, the term $G v_i^2$ in eq. (2.101) and $G v_i^4$ in eq. (2.102) can be dropped and v_i^2 from (2.88) can be inserted into Eqs. (2.82) and (2.101), together with Eq. (2.103) one obtains two nonlinear coupled equations for Δ and λ.

$$\begin{aligned} u_i = 0,\ v_i = 1 \quad &\text{for} \quad i \leq i_{\mathrm{Fermi}} \\ u_i = 1,\ v_i = 0 \quad &\text{for} \quad i > i_{\mathrm{Fermi}} \end{aligned} \tag{2.104}$$

for which $\Delta = 0$. It has been found that for magic nuclei there is no pairing solution for realistic parameters, while for mid-subshell nuclei there is a solution. However, it has been shown that this sharp transition is due to the finite particle number fluctuation in the BCS state. Various proposals have been made to solve this problem, such as the projection of the BCS wave function onto the eigenstates of the particle number operator [45]. To obtain non-trivial solutions describing pairing-correlated states, a large level density around the Fermi energy and a sufficiently large pairing strength G are required.

The Lipkin-Nogami approach [53–55] is most commonly used in conjunction with Strutinsky's shell correction. This approach introduces a constraint on the variance of the particle number in the Routhian $\hat{H}'$, with the Lagrange multiplier for the additional constraint denoted as λ_2. This changes Eq. (2.101) to

$$\tilde{\epsilon}_i^{\mathrm{LN}} = \epsilon_i - \lambda + (4\lambda_2 - G)\, v_i^2 \tag{2.105}$$

and the quasi-particle energy becomes

$$\mathcal{E}_i^{\mathrm{LN}} = \sqrt{\epsilon_i^2 + \Delta^2} + \lambda_2 \tag{2.106}$$

with

$$\lambda_2 = \frac{G}{4}\frac{\left(\sum_i^{(\omega)} u_i^3 v_i\right)\left(\sum_i^{(\omega)} u_i^2 v_i^3\right) - \sum_i^{(\omega)} u_i^4 v_i^4}{\left(\sum_i^{(\omega)} u_i^2 v_i^2\right)^2 - \sum_i^{(\omega)} u_i^4 v_i^4}. \tag{2.107}$$

The gap and particle number equations. (2.79) and (2.82) must be solved with the modified definition of $\tilde{\epsilon}_i$.

Attempts have been made to determine the pairing strength constant G for a given range ω from empirical mass differences within the BCS and Lipkin-Nogami schemes [56]. However, the assumption of a state-independent pairing matrix element G does not accurately describe the physical situation along the fission path. Around the fission, the single particle states separate into those localized in one of the two nascent fragments and those above the Fermi energy, which are still distributed throughout the entire nuclear volume. This leads to four different characteristic values of G. After scission, the states above the Fermi energy are also localized in one of the fragments, resulting in different pairing strengths in the two fragments and consequently different chemical potentials and pairing gaps. Therefore, there is a phase transition in the pairing degrees of freedom around scission [57]. After scission, the particle numbers of the two fragments are separate constants of motion, whereas for a compact nucleus only the total number of particles is a constant of motion. Thus, one should not interpolate G between the ground state of the fissioning nucleus and the separated fragments using the shape function B_{surf}, nor assume a constant G.

For an odd system, the equations

$$N' = 1 + \sum_{i\neq k_0}^{(\omega)} \left(1 - \frac{\tilde{\epsilon}_i}{\mathcal{E}_i}\right) \quad \text{and} \quad \frac{2}{G} = \sum_{i\neq k_0}^{(\omega)} \frac{1}{\mathcal{E}_i} \tag{2.108}$$

must be solved for Δ and λ instead of for (2.82) and (2.103). The notation $\mathcal{E}_i = \sqrt{\tilde{\epsilon}_i^2 + \Delta^2}$ is used again, and N' is the number of particles occupying states in the 2ω band. The gap parameter Δ is smaller than for the neighboring even systems due to the fact that the state k_0 is "blocked" and inaccessible for the establishment of pairing correlations. If the term v_i^4 in eq. (2.102) is omitted, then the ground state expectation value of the Routhian of an odd system is given by

$$\left\langle \mathrm{BCS}\left|\hat{H}'\right|\mathrm{BCS}\right\rangle = 2\sum_{i\neq k_0}^{(\omega)} \tilde{\epsilon}_i v_i^2 + (\epsilon_k - \lambda) - \Delta^2/G. \tag{2.109}$$

If the pairing gap Δ is much larger than the level spacing, then one can obtain simple, analytic expressions for the pairing energy and the pairing gap by introducing a continuous, smooth single-particle level density $g(e)$ (which should include the time-reflected states). The gap equation (2.103) then becomes

$$\frac{2}{G} = \int_{\lambda-\omega}^{\lambda+\omega} \frac{\frac{1}{2}g(e)de}{\sqrt{(e-\lambda)^2+\Delta^2}} \approx \frac{g(\lambda)}{2}\ln\frac{\sqrt{\omega^2+\Delta^2}+\omega}{\sqrt{\omega^2+\Delta^2}-\omega}. \tag{2.110}$$

Since the pairing-window half-width ω should be large compared to the pairing gap, $\omega \gg \Delta$, Eq. (2.110) can be simplified to

$$\frac{2}{G} \approx g(\lambda)\ln\left(\frac{2\omega}{\Delta}\right). \tag{2.111}$$

This approximation is sometimes called the "uniform model". The relation (2.111) allows to estimate the pairing strength G when the average pairing gap is known from experimental

data. One can also see that G depends on the width of the window 2ω, i.e. on the number of states included in the sum in Eq. (2.99): G decreases with increasing number of states, included in the pairing Hamiltonian.

The BCS energy-gain with respect to the energy of a system without pairing correlations is

$$\Delta E = \left\langle \mathrm{BCS} \left| \hat{H}' + \lambda \hat{N} \right| \mathrm{BCS} \right\rangle - 2 \sum_{i \leq i_{\mathrm{Fermi}}} \epsilon_i = 2 \sum_{i>0}^{(\omega)} \epsilon_i v_i^2 - \Delta^2/G - 2 \sum_{i \leq i_{\mathrm{Fermi}}} \epsilon_i$$

for an even particle number, where the Gv^4 term in Eq. (2.102) is neglected and $N = 2\sum_i v_i^2$ is used. The quantity ΔE can be calculated analytically in the uniform model. Using Eq. (2.101) we obtain

$$\widetilde{\Delta E} = \frac{1}{2} \int_{\lambda-\omega}^{\lambda+\omega} e \left(1 - \frac{e-\lambda}{\sqrt{(e-\lambda)^2 + \Delta^2}} \right) g(e) de - \frac{\Delta^2}{G} - \int_{\lambda-\omega}^{\lambda} e g(e) de. \tag{2.112}$$

After evaluation of the integrals and eliminating $1/G$ with Eq. (2.109), the pairing energy becomes

$$\widetilde{\Delta E} = \frac{1}{2} g(\lambda) \omega^2 \left(1 - \sqrt{1 + \left(\frac{\Delta}{\omega} \right)^2} \right). \tag{2.113}$$

With $\omega \gg \Delta$ the last equation can be approximated by

$$\widetilde{\Delta E} \approx -\frac{1}{4} g(\lambda) \Delta^2. \tag{2.114}$$

The Lipkin-Nogami approach was also reformulated in the uniform model by Möller and Nix [56], where the expression for λ_2, Eq. (2.107), becomes rather lengthy.

2.2.4 Yukawa-folding methods

In 1935 Hideki Yukawa proposed [58] the theory of strong interaction, where nucleons exchange with each other through special kind of particles-mesotrons (now its known as mesons introduced by Heisenberg), which play similar role to photons in electromagnetic interactions. The form of the interaction potential is

$$V_{Yuk}(r) = G \frac{e^{-\frac{m_{mes}c}{\hbar} r}}{r} \tag{2.115}$$

where G is the coupling constant of the given interaction. According to Yukawa's estimates, the meson mass (later known as the $\pi-$meson) was about 140 MeV/c^2, giving a characteristic strong interaction length corresponding to the Compton wavelength of the pion

$$\lambda\!\!\!^{-}_{\pi} = \frac{\hbar}{m_\pi c} \approx .1.4 \ fm,$$

Thus, the nuclear density $\rho(\vec{r}_1)$ can be described by the folding procedure proposed in [59], where uniform density distribution.

$$\rho_0(\vec{r}) = \begin{cases} \frac{3}{4\pi} A \cdot R_0^{-3} & \text{for} \quad r \leq R_0 \\ 0 & \text{for} \quad r > R_0 \end{cases} \tag{2.116}$$

which satisfies the nucleon number conservation condition

$$\int_V \rho_0(\vec{r}\,)\, d^3r = N(Z). \tag{2.117}$$

Folding with the function $g(|\vec{r}_1 - \vec{r}_2|)$ as follows

$$\rho(\vec{r}_1) = \rho_0 \int_V d^3r_2\, g(|\vec{r}_1 - \vec{r}_2|). \tag{2.118}$$

This function is selected in the form of a Yukawa function (2.115) with a width parameter $a = \lambda\!\!\!^{-}_{\pi}$.

$$g(|\vec{r}_1 - \vec{r}_2|) = \frac{1}{4\pi a^3} \frac{e^{-|\vec{r}_1 - \vec{r}_2|/a}}{|\vec{r}_1 - \vec{r}_2|/a}. \tag{2.119}$$

with normalization condition

$$\int_V g\,(\,|\vec{r}_1 - \vec{r}_2|\,)\, d^3r_2 = 1. \tag{2.120}$$

It should be noted that $g(|\vec{r}_1 - \vec{r}_2|)$ does not represent the interaction potential of two nucleons, but rather the fact that the short-range interaction between N nucleons generates a density distribution which has a diffuse surface, analogous to Eq. (2.118).

Coulomb potential

After determining the charge distribution in the nucleus according to Eq. (2.118), the Coulomb potential can be calculated [59] as

$$V_c(\vec{r}_1) = e \int_V d^3r_2 \frac{\rho(\vec{r}_2)}{|\vec{r}_1 - \vec{r}_2|}. \tag{2.121}$$

Use the following relation for the functions f and g

$$\int_V d^3r_2 f(\vec{r}_1 - \vec{r}_2) g(\vec{r}_1 - \vec{r}_2) = \int_{-\infty}^{\infty} d^3k f(\vec{k}) g(\vec{k}) e^{i\vec{k}\cdot(\vec{r}_1 - \vec{r}_3)}. \tag{2.122}$$

and replacing $f \cdot g$ by Fourier transforms of $g(\vec{r}_2 - \vec{r}_3)\frac{1}{|\vec{r}_1 - \vec{r}_2|}$, one can obtain such an expression:

$$V_c(\vec{r}_1) = \frac{4\pi e \rho_0}{(2\pi)^{\frac{3}{2}}} \int_V d^3r \int_{-\infty}^{\infty} d^3k \frac{1}{k^2} g(k) e^{i\vec{k}\cdot(\vec{r}_1 - \vec{r}_3)}, \tag{2.123}$$

where the Fourier transform of the Yukawa function (2.119) has the form

$$g(k) = \frac{1}{2\pi} \frac{1}{(1 + a^2k^2)}. \tag{2.124}$$

Due to the fact that the function g depends only on the norm of $\vec{k}$, inserting it into the explicit form of Eq. (2.124) and using the trigonometric relation, the final expression (2.121) is

$$V_c(\vec{r}_1) = \frac{e\rho_0}{\pi i} \int_V d^3r_3 \frac{1}{|\vec{r}_1 - \vec{r}_3|} \int_{-\infty}^{+\infty} dk \frac{1}{a^2 k (k^2 + \frac{1}{a^2})} e^{i\vec{k}\cdot(\vec{r}_1 - \vec{r}_3)}. \tag{2.125}$$

The last integral can be computed with the residue method in complex space, giving the form

$$V_c(\vec{r}_1) = V_c(\vec{r}_1; sharp) + \triangle V_c(\vec{r}_1), \tag{2.126}$$

where $V_c(\vec{r}_1; sharp)$ is the dominant term in the Coulomb potential due to the uniform charge distribution, while $\triangle V_c(\vec{r}_1)$ is the correction due to the diffuseness of the charge distribution. Explicitly, these expressions are

$$V_c(\vec{r}_1; sharp) = \rho_0 e \int_V d^3r_2 \frac{1}{|\vec{r}_1 - \vec{r}_2|} \tag{2.127}$$

and

$$\Delta V_c(\vec{r}_1) = -\rho_0 e \int_V d^3r_2 \frac{1}{|\vec{r}_1 - \vec{r}_2|} e^{-\frac{|\vec{r}_1 - \vec{r}_2|}{a}}. \tag{2.128}$$

The integrals in Eqs. (2.129) can be converted to surface integrals using the Gauss-Ostrogradsky theorem, which makes them more suitable for numerical integration using e.g. the Gauss-Legendre quadrature method. Finally, the potential can be expressed [60] as

$$V_c(\vec{r}_1; sharp) = -\frac{\rho_0 e}{2} \oint_{S_2} [d\vec{S}_2 \cdot (\vec{r}_1 - \vec{r}_2)] \frac{1}{|\vec{r}_1 - \vec{r}_2|}, \tag{2.129}$$

$$\Delta V_c(\vec{r}_1) = \frac{\rho_0 e}{a} \oint_{S_2} [d\vec{S}_2 \cdot (\vec{r}_1 - \vec{r}_2)] \Big(\frac{|\vec{r}_1 - \vec{r}_2|}{a}\Big)^3 \left[1 - \left(1 + \frac{|\vec{r}_1 - \vec{r}_2|}{a}\right) e^{-\frac{|\vec{r}_1 - \vec{r}_2|}{a}}\right]. \tag{2.130}$$

For a spherical nucleus with radius R_0, these integrals can be evaluated analytically.

Coulomb energy

By analogy, one can derive the expressions for the Coulomb energy of a deformed nucleus, which is defined [59] as

$$E_c = \frac{1}{2} \int_V \int_V d^3r_1 \, d^3r_2 \, \frac{1}{|\vec{r}_1 - \vec{r}_2|} \, \rho(\vec{r}_1) \, \rho(\vec{r}_2). \tag{2.131}$$

Inserting the folded density (2.118) into the above equation yields

$$E_c = \frac{{\rho_0}^2}{2} \int_V \int_V d^3r_1 \, d^3r_2 \, \frac{1}{|\vec{r}_1 - \vec{r}_2|} \int_V \int_V d^3r_3 \, d^3r_4 \, g(|\vec{r}_1 - \vec{r}_3|) \, g(|\vec{r}_2 - \vec{r}_4|). \tag{2.132}$$

Generalized relation (2.122) for three functions f, g, h.

$$\begin{aligned} \int_V \int_V d^3r_1 \quad & d^3r_2 \, f(|\vec{r}_1 - \vec{r}_2|) \, g(|\vec{r}_1 - \vec{r}_3|) \, h(|\vec{r}_2 - \vec{r}_4|) = \\ & = (2\pi)^{\frac{3}{2}} \int_\infty d^3k \, f(\vec{k}) \, g(-\vec{k}) \, h(\vec{k}) \, e^{i\vec{k}\cdot(\vec{r}_3 - \vec{r}_4)}. \end{aligned} \tag{2.133}$$

and substituting in the Eq. (2.132) we get

$$E_c = 4\pi \, \frac{{\rho_0}^2}{2} \int_V \int_V d^3r_1 \, d^3r_2 \int_\infty d^3k \, \frac{1}{k^2} \, g^2(k) \, e^{i\vec{k}\cdot(\vec{r}_1 - \vec{r}_2)}. \tag{2.134}$$

Completing the integral over k and using the Fourier transform of the function g given in Eq. (2.124), one obtains

$$E_c = \frac{{\rho_0}^2}{(2\pi)} \, \frac{1}{i} \int_V \int_V \frac{d^3r_1 d^3r_2}{|\vec{r}_1 - \vec{r}_2|} \int_{-\infty}^{+\infty} dk \, \frac{e^{i\vec{k}|\vec{r}_1 - \vec{r}_2|}}{k(1 + a^2k^2)^2}. \tag{2.135}$$

The residuum theorem then leads to the same expression as in Eq. (2.126):

$$E_c = E_c(sharp) + \triangle E_c, \tag{2.136}$$

where $E_c(sharp)$ is the part of the Coulomb energy produced by the uniform density distribution, and ΔE_c is the negative correction from the surface charge.

$$\begin{aligned} E_c(sharp) &= \frac{{\rho_0}^2}{12} \int_V \int_V d^3r_1\, d^3r_2\, \frac{1}{|\vec{r}_1 - \vec{r}_2|}, \\ \Delta E_c &= \frac{-{\rho_0}^2}{2} \int_V \int_V d^3r_1\, d^3r_2\, \frac{1}{|\vec{r}_1 - \vec{r}_2|}\; e^{-|\vec{r}_1 - \vec{r}_2|/a} \left(1 + \frac{1}{2}\, \frac{|\vec{r}_1 - \vec{r}_2|}{a}\right). \end{aligned} \tag{2.137}$$

Transforming the double volume integral into two surface integrals yields an expression that is easier to calculate numerically:

$$\begin{aligned} E_c(sharp) &= -\frac{\rho_0^2}{12} \oint_S \oint_S \frac{[d\vec{S}_1 \cdot (\vec{r}_1 - \vec{r}_2)]\; [d\vec{S}_2 \cdot (\vec{r}_1 - \vec{r}_2)]}{|\vec{r}_1 - \vec{r}_2|}, \\ \Delta E_c &= \frac{\rho_0^2}{2a} \oint_S \oint_S \frac{[d\vec{S}_1 \cdot (\vec{r}_1 - \vec{r}_2)]\; [d\vec{S}_2 \cdot (\vec{r}_1 - \vec{r}_2)]}{|\vec{r}_1 - \vec{r}_2|/a^4} \\ &\quad \times \left[2\frac{|\vec{r}_1 - \vec{r}_2|}{a} - 5 + \left(5 + 3\frac{|\vec{r}_1 - \vec{r}_2|}{a} + \frac{1}{2}\frac{|\vec{r}_1 - \vec{r}_2|^2}{a^2}\right) e^{\frac{-|\vec{r}_1 - \vec{r}_2|}{a}}\right]. \end{aligned} \tag{2.138}$$

Yukawa-folded effective potentials

The form of the mean-field single-particle potential can be generated by convolution of the nuclear density with a Yukawa-like function, which can be understood as a spin-independent two-body interaction between two infinitesimal volume elements of a nuclear drop.

$$V(r_{12}) = -\frac{V_0}{4\pi\lambda^3} \frac{e^{-|\vec{r}_1 - \vec{r}_2|/\lambda}}{|\vec{r}_1 - \vec{r}_2|/\lambda}, \quad r_{12} = |\vec{r}_1 - \vec{r}_2|. \tag{2.139}$$

To obtain the central part of the single-particle potential, one folds [60] the Yukawa interaction (2.139) with the density distribution (2.118) as described in [59]

$$V_{sp}\,(\vec{r}_1) = \int_V d^3r_2\, V(r_{12})\, \frac{\rho\,(\vec{r}_2)}{\rho_0}. \tag{2.140}$$

The above integral can be rewritten using the Fourier transform of the Yukawa function $g(k)$ (2.124) as

$$V_{sp}\,(\vec{r}_1) = -\frac{V_0}{(2\pi)^{3/2}} \int_V d^3r_3 \int_{-\infty}^{\infty} d^3k\, \frac{g(k)}{1 + \lambda^2 k^2}\, e^{i\,\vec{k}\cdot(\vec{r}_1 - \vec{r}_3)}. \tag{2.141}$$

By performing the second integral over the angles θ and φ in the momentum space, the expression for the potential is obtained:

$$V_{sp}\,(\vec{r}_1) = -\left(\frac{2}{\pi}\right)^{1/2} V_0 \int_V \frac{d^3r_3}{|\vec{r}_1 - \vec{r}_3|} \int_0^{\infty} dk\, k\, \frac{g(k)}{1 + \lambda^2 k^2}\, \sin(k\,|\vec{r}_1 - \vec{r}_3|). \tag{2.142}$$

By substituting the explicit Fourier transform (2.124) for the function $g(k)$, an expression can be obtained that is suitable for integration by the residue method in the complex plane.

$$V_{sp}\left(\vec{r}_1\right) = -\frac{V_0}{4\pi^2 i}\int\limits_V \frac{d^3r_3}{|\vec{r}_1-\vec{r}_3|}\int\limits_{-\infty}^{\infty} dk\, k\, \frac{e^{ik|\vec{r}_1-\vec{r}_3|}}{\left(1+\lambda^2k^2\right)\left(1+a^2k^2\right)}. \tag{2.143}$$

In general, it is assumed that the range λ of the Yukawa interaction is different from the range a of the folding function of the same type used to generate the density distribution in eq. (2.118). After performing an analytical integration in the complex plane, it is found [60] that the single-particle potential is the sum of two terms, namely

$$V_{sp}\left(\vec{r}_1\right) = V\left(\vec{r}_1; sharp\right) + \Delta V\left(\vec{r}_1\right), \tag{2.144}$$

where the *sharp-density* potential independent on the density diffuseness a

$$V\left(\vec{r}_1; sharp\right) = -\frac{V_0}{4\pi\lambda^3}\int\limits_V \frac{e^{-|\vec{r}_1-\vec{r}_2|/\lambda}}{|\vec{r}_1-\vec{r}_2|/\lambda}\, d^3r_2, \tag{2.145}$$

the correction to the function is dependent on both the diffuseness parameters λ and a, which reads as follows

$$\Delta V\left(\vec{r}_1\right) = -\frac{a^2}{a^2-\lambda^2}\, V\left(\vec{r}_1; sharp\right) - \frac{V_0}{4\pi(a^2-\lambda^2)}\int\limits_V \frac{e^{-|\vec{r}_1-\vec{r}_2|/a}}{|\vec{r}_1-\vec{r}_2|}\, d^3r_2. \tag{2.146}$$

Transforming the above spatial integrals into surface integrals in the same manner, we obtain

$$\begin{aligned} V\left(\vec{r}_1; sharp\right) = \frac{V_0}{4\pi\lambda^3}\oint\limits_S \left(d\vec{S}_2\cdot\vec{r}_{12}\right)\left(\frac{|\vec{r}_1-\vec{r}_2|}{\lambda}\right)^{-3} \\ \left[1-\left(1+\frac{|\vec{r}_1-\vec{r}_2|}{\lambda}\right)e^{\frac{|\vec{r}_1-\vec{r}_2|}{\lambda}}\right] \end{aligned} \tag{2.147}$$

and

$$\begin{aligned} \Delta V\left(\vec{r}_1\right) = \; & -\frac{a^2}{a^2-\lambda^2}\, V\left(\vec{r}_1; sharp\right) + \frac{V_0}{4\pi(a^2-\lambda^2)}\oint\limits_S \left(d\vec{S}_2\cdot\vec{r}_{12}\right)\times \\ & \left(\frac{|\vec{r}_1-\vec{r}_2|}{a}\right)^{-3}\left[1-\left(1+\frac{|\vec{r}_1-\vec{r}_2|}{a}\right)e^{\frac{|\vec{r}_1-\vec{r}_2|}{a}}\right]. \end{aligned} \tag{2.148}$$

Evaluating expression (2.147) for a spherical nucleus with radius R_0 can be done analytically [59] with the result

$$V_{sph}(r_1; sharp) = \begin{cases} -V_0\left[1-\left(1+\frac{R_0}{\lambda}\right)e^{-R_0/\lambda}\frac{\sinh(r_1/\lambda)}{(r_1/\lambda)}\right] & \text{for} \quad r_1 \le R_0 \\ -V_0\left[\frac{R_0}{\lambda}\cosh(\frac{R_0}{\lambda}) - \sinh(\frac{R_0}{\lambda})\right]\frac{e^{-r_1/\lambda}}{(r_1/\lambda)} & \text{for} \quad r_1 \ge R_0, \end{cases} \tag{2.149}$$

while (2.148)

$$\begin{aligned} \Delta V_{sph}(r_1) = & -\frac{a^2}{(a^2-\lambda^2)}\, V_{sph}(r_1; sharp) \\ & + \begin{cases} \frac{a^2V_0}{(\lambda^2-a^2)}\left[1-\left(1+\frac{R_0}{a}\right)e^{-R_0/a}\frac{\sinh(r_1/a)}{(r_1/a)}\right] & \text{for} \quad r_1 \le R_0 \\ \frac{a^2V_0}{(\lambda^2-a^2)}\left[\frac{R_0}{a}\cosh(\frac{R_0}{a}) - \sinh(\frac{R_0}{a})\right]\frac{e^{-r_1/a}}{(r_1/a)} & \text{for} \quad r_1 \ge R_0. \end{cases} \end{aligned} \tag{2.150}$$

Splitting the Coulomb and nuclear potentials, as well as the associated folding energies, into *sharp* and *diffuse* components is mathematically precise but, as shown by Ref. [59], not really necessary since the effect of density diffuseness can be effectively mimicked by a *renormalization* of the λ parameter in the *sharp–density* contribution. Furthermore, according to Ref. [59], the *diffuse–density* correction appears to vary very slowly with nuclear deformation. Therefore, corrections in the form given in (2.128), (2.137) and (2.148) were no longer used in later works, such as Ref. [61].

The spin-orbit component of the total single-particle mean-field interaction can be constructed using the central part of the single-particle potential V_{sp} in the standard way of

$$V_{s.o.} = i\,\lambda^q \left(\frac{\hbar}{2Mc}\right)^2 \vec{\nabla} V_{sp} \cdot \left[\vec{\sigma} \times \vec{\nabla}\right], \quad q = \{n, p\}, \tag{2.151}$$

where $\vec{\sigma}$ denotes the vector of 2×2 Pauli matrices $(\sigma_x, \sigma_y, \sigma_z)$.

The parametrization of the depths of central parts of the single-particle potentials for protons and neutrons used is given [61]

$$V_0^p = V_s + V_a\,\bar{\delta}, \qquad V_0^n = V_s - V_a\,\bar{\delta}, \tag{2.152}$$

where

$$\begin{aligned} \bar{\delta} &= \left(I + \frac{3}{8}\frac{c_1}{Q}\frac{Z^2}{A^{5/3}}\right) \Big/ \left(1 + \frac{9}{4}\frac{J}{Q}\frac{1}{A^{1/3}}\right), \\ \lambda^p &= 6.0\left(\frac{A}{240}\right) + 28.0, \quad \lambda^n = 4.5\left(\frac{A}{240}\right) + 31.5 \end{aligned} \tag{2.153}$$

Table 2.1: Constants used in the Yukawa–folding procedure taken from Ref. [60].

constant	value	unit
λ	0.8	fm
a	0.7	fm
V_s	52.5	MeV
V_a	48.7	MeV
J	35.0	MeV
Q	25.0	MeV
c_1	$\frac{3}{5}\frac{e^2}{r_0}$	MeV
M	938.9	MeV/c^2
r_0	1.16	fm

2.2.5 The harmonic-oscillator potential

In the case of an axially symmetric system, the harmonic oscillator potential can be expressed as

$$V_{h.o.}(\rho, z) = \frac{1}{2} m\omega_\perp^2 \rho^2 + \frac{1}{2} m\omega_z z^2. \tag{2.154}$$

To introduce dimensionless coordinates, the oscillator constants $\beta_\perp$ and β_z can be defined:

$$\begin{aligned} \beta_z &= \frac{1}{b_z} = \sqrt{\frac{m\omega_z}{\hbar}}, \qquad \zeta = z\beta_z \\ \beta_\perp &= \frac{1}{b_\perp} = \sqrt{\frac{m\omega_\perp}{\hbar}}, \qquad \eta = \rho^2\beta_\perp^2. \end{aligned} \tag{2.155}$$

The eigenstates of this axially symmetric h.o. potential can then be expressed using Laguerre polynomials in the $\perp$ direction and Hermite polynomials in the z direction:

$$\phi_{n_\rho,n_z,\Lambda,\Sigma}(\vec{R},\vec{\sigma}) = \psi^\Lambda_{n_\rho}(\rho)\,\psi_{n_z}(z)\,\frac{e^{i\Lambda\phi}}{\sqrt{2\pi}}\,\chi_\Sigma(\sigma), \tag{2.156}$$

where

$$\begin{aligned} \psi_{n_z}(z\,) &= \mathcal{N}_{n_z}\,(\beta_z)^{1/2} e^{\zeta^2/2} H_{n_z}(\zeta), \qquad & \mathcal{N}_{n_z} &= \sqrt{\frac{1}{\sqrt{\pi}\,2^{n_z} n_z!}} \\ \psi^\Lambda_{n_\rho}(\rho) &= \mathcal{N}^\Lambda_{n_\rho}\beta_\perp\sqrt{2}\,\eta^{\Lambda/2} L^\Lambda_{n_\rho}(\eta), \qquad & \mathcal{N}^\Lambda_{n_\rho} &= \sqrt{\frac{n_\rho!}{(n_\rho+\Lambda)\,!}} \end{aligned} \tag{2.157}$$

The single-particle energies of this Hamiltonian are given by

$$E_\alpha = (2n_\rho + |\Lambda| + 1)\,\bar{\omega}_\perp + (n_z + 1/2)\,\bar{\omega}_z, \qquad \alpha = \{n_\rho, n_z, \Lambda, \Sigma\}. \tag{2.158}$$

In addition, the eigenstates of any axially symmetric single-particle potential can be written in terms of these h.o. eigenstates as

$$\Phi_i(\vec{R},\sigma,q) = \chi_{q_i(q)} \sum_\alpha C^i_\alpha \phi_\alpha(\vec{R},\sigma), \tag{2.159}$$

where C^i_α are complex coefficients.

In the Schrödinger equation

$$H\Phi_i(\vec{R},\sigma,q) \equiv [T_{kin} + V_{sp} + V_{s.o.} + V_{Coul}\,\delta_{p\,q}] = e_i\Phi_i(\vec{R},\sigma,q), \quad q = \{p,n\} \tag{2.160}$$

for which the set of eigensolutions $\Phi_i(\vec{R},\sigma,q)$ is expressed by the series expansion (2.159), where the coefficients C^i_α play the role of eigenvectors of the Hamiltonian matrix $H_{\alpha\beta}$ with the corresponding eigenvalue e_i, the sum $\sum_\beta H_{\alpha\beta}\,C^i_\beta$ leads to $e_i\,C^i_\alpha$. The matrix elements $H_{\alpha\beta}$ of the axial effective Hamiltonian are

$$H_{\alpha\beta} = \left\langle\, \alpha \,\middle|\, -\vec{\nabla}\cdot\frac{\hbar^2}{2m^*_q}\,\vec{\nabla} + V^{(q)}_{sp} + V^{(q)}_{s.o.} \,\middle|\, \beta \,\right\rangle \tag{2.161}$$

can be expressed explicitly as

$$\begin{aligned} \left\langle\, \alpha \,\middle|\, -\vec{\nabla}\cdot\frac{\hbar^2}{2m^*_q}\,\vec{\nabla} \,\middle|\, \beta \,\right\rangle &= \sum_\sigma \int d^3R \frac{\hbar^2}{2m^*_q(\rho,z)} \vec{\nabla}\phi^*_\alpha(\vec{R},\sigma)\cdot\vec{\nabla}\phi_\beta(\vec{R},\sigma) \\ \left\langle\, \alpha \,\middle|\, V^{(q)}_{sp} \,\middle|\, \beta \,\right\rangle &= \delta_{\Lambda,\Lambda'}\delta_{\Sigma,\Sigma'} N_{n_z} N_{n'_z} N^\Lambda_{n_\rho} N^{\Lambda'}_{n'_\rho} \int_0^\infty d\eta\eta^\Lambda e^{-\eta} \\ &\quad \times \int_{-\infty}^{\infty} e^{-\zeta^2} d\zeta H_{n_z}(\zeta)\, H_{n'_z}(\zeta) L^\Lambda_{n_\rho}(\eta)\, L^{\Lambda'}_{n'_\rho}(\eta)\, V^{(q)}_{sp}(\rho,z)(\eta,\zeta)\,, \end{aligned} \tag{2.162}$$

where the left gradient operator is chosen to act on the left (as the hermitian conjugate).

Non-axial Hamiltonian symmetries

Let us define the following operation:

$$\hat{y} = \hat{K}\hat{\pi}_y^{-1}, \tag{2.163}$$

where $\hat{\pi}_y^{-1}$ here denotes [33] is the inverse of the reflection operation with respect to the $xOz-$ plane, while $\hat{K}$ is the time reversal operation, which can be defined as

$$\hat{K} = \hat{K}_0\, e^{-i\pi\hat{s}_y} \tag{2.164}$$

where $\hat{K}_0$ is the complex conjugation operator. Immediately notice that the time-reversal operation includes the rotation operation by an angle π around the y-axis in the spin space. Let h be a single-particle Hamiltonian operator.If

$$\hat{h}|\mu\rangle = \epsilon_\mu|\mu\rangle \tag{2.165}$$

and

$$\hat{y}\hat{h}\hat{y}^{-1} = \hat{h}, \tag{2.166}$$

then it is obviously true that

$$\hat{y}|\mu\rangle = |\mu\rangle. \tag{2.167}$$

It explicitly means that if the eigenstates of the single-particle Hamiltonian are invariant with respect to this symmetry and

$$|\mu\rangle = \sum_\alpha C_\alpha^\mu|\alpha\rangle, \tag{2.168}$$

then the coefficients of the expansion C_α^μ are real in the orthogonal basis. For the density distribution and the total mean-field potential V, respectively, this implies

$$\rho(x,y,z) = \rho(x,-y,z) \tag{2.169}$$

$$V(x,y,z) = V(x,-y,z) \tag{2.170}$$

Let us consider the case of a non-axial potential in more detail. First, one can introduce the set of three operators associated with the rotation by the angle π with respect to the i-axis (where $\{i = x,y,z\}$), acting together with the parity operator $\hat{P}$ (with parity eigenvalues equal to $\pi = \pm 1$) as

$$\hat{\pi}_i \equiv \hat{P}\hat{R}_i(\pi). \tag{2.171}$$

The action of these operators on an arbitrary spatial function $\psi(x,y,z)$ gives

$$\begin{aligned}
\hat{\pi}_x\psi(x,y,z) &= \hat{P}\hat{R}_x(\pi)\psi(x,y,z) = \hat{P}\psi(x,-y,-z) = \psi(-x,y,z),\\
\hat{\pi}_y\psi(x,y,z) &= \hat{P}\hat{R}_y(\pi)\psi(x,y,z) = \hat{P}\psi(-x,y,-z) = \psi(x,-y,z),\\
\hat{\pi}_z\psi(x,y,z) &= \hat{P}\hat{R}_z(\pi)\psi(x,y,z) = \hat{P}\psi(-x,-y,z) = \psi(x,y,-z).
\end{aligned} \tag{2.172}$$

Remember that the rotation around the $i-$axis by the angle π, called the *i–signature* operation, is performed by the operator

$$\hat{R}_i(\pi) = e^{-i\pi\hat{j}_i/\hbar}, \qquad \hat{j}_i = \hat{l}_i + \hat{s}_i, \tag{2.173}$$

where $\hat{l}_i$ and $\hat{s}_i$ are the i-components of the orbital angular momentum and spin operators, respectively. The action of $\hat{R}_z$ on an arbitrary eigenfunction $\varphi(\vec{r};s)$ of the mean-field Hamiltonian $\hat{h}$.

$$\hat{R}_z(\pi)\,\varphi(\vec{r};s) = r\,\varphi(\vec{r};s) \tag{2.174}$$

yields the eigenvalues $r = \pm 1$. We recall that for the spin functions χ_{s,m_s} represented by $|+\rangle$ and $|-\rangle$ we have that

$$\begin{aligned}
\hat{s}_x|+\rangle &= \frac{1}{2}\hbar\,|-\rangle, & \hat{s}_x|-\rangle &= \frac{1}{2}\hbar\,|+\rangle,\\
\hat{s}_y|+\rangle &= \frac{1}{2}\hbar(+i)\,|-\rangle, & \hat{s}_y|-\rangle &= \frac{1}{2}\hbar(-i)\,|+\rangle,\\
\hat{s}_z|+\rangle &= \frac{1}{2}\hbar\,|+\rangle, & \hat{s}_z|-\rangle &= -\frac{1}{2}\hbar\,|-\rangle,
\end{aligned} \tag{2.175}$$

where

$$|+\rangle = \begin{pmatrix} 1 \\ 0 \end{pmatrix}, \quad |-\rangle = \begin{pmatrix} 0 \\ 1 \end{pmatrix}.$$

It is also instructive to demonstrate the action of the rotation operators $\{e^{-i\pi\hat{s}_i}\}$ on the spin functions $|+\rangle$ and $|-\rangle$, namely

$$e^{-i\pi\hat{s}_x/\hbar}\,|+\rangle = \left(\hat{I} - i\frac{\pi}{2}\hat{\sigma}_x - \frac{1}{2}\left(\frac{\pi}{2}\right)^2\sigma_x^2 + \frac{1}{6}i\left(\frac{\pi}{2}\right)^3\hat{\sigma}_x^3 + \frac{1}{24}\left(\frac{\pi}{2}\right)^4\hat{\sigma}_x^4 + \ldots\right)\Big|+\Big\rangle \tag{2.176}$$

Noting that $(\hat{\sigma}_i)^{2n} = \hat{I}$, $(i = 1, 2, 3, \ldots)$ and reordering the terms in the above as

$$\begin{aligned}
&\left[\left(1 - \frac{1}{2}\left(\frac{\pi}{2}\right)^2 + \frac{1}{24}\left(\frac{\pi}{2}\right)^4 + \ldots\right) - i\hat{\sigma}_x\left(\frac{\pi}{2} - \frac{1}{6}\left(\frac{\pi}{2}\right)^3 - \frac{1}{120}\left(\frac{\pi}{2}\right)^5\right)\right]\Big|+\Big\rangle =\\
&\left(\cos\left(\frac{\pi}{2}\right) - i\hat{\sigma}_x\sin\left(\frac{\pi}{2}\right)\right)\Big|+\Big\rangle = -i\hat{\sigma}_x|+\rangle = -i|-\rangle
\end{aligned} \tag{2.177}$$

we obtain explicitly that

$$\begin{aligned}
e^{-i\pi\hat{s}_x/\hbar}\,|+\rangle &= (-i)|-\rangle, & e^{-i\pi\hat{s}_x/\hbar}\,|-\rangle &= (-i)|+\rangle,\\
e^{-i\pi\hat{s}_y/\hbar}\,|+\rangle &= (+1)|-\rangle, & e^{-i\pi\hat{s}_y/\hbar}\,|-\rangle &= (-1)|+\rangle,\\
e^{-i\pi\hat{s}_z/\hbar}\,|+\rangle &= (-i)|+\rangle, & e^{-i\pi\hat{s}_z/\hbar}\,|-\rangle &= (+i)|-\rangle.
\end{aligned} \tag{2.178}$$

Collecting the properties described by section 2.2.5 and admitting [60] that in general a single-particle wave function $\varphi(\vec{r}; s)$ is the product of the spatial and spin components: $\varphi(\vec{r}; s) = \psi(\vec{r})\,\chi_{s,m_s}$, the parity operator $\hat{P}$ can be rewritten in terms of the operators $\hat{\pi}_i$ as

$$\hat{P} = -\hat{\pi}_x\hat{\pi}_y\hat{\pi}_z, \tag{2.179}$$

whereas, the z-signature operator $\hat{S}_z$ is given by

$$\hat{S}_z \equiv \hat{R}_z(\pi) = i\hat{\pi}_x\hat{\pi}_y. \tag{2.180}$$

The latter acting on an arbitrary wave function $\varphi(\vec{r}; s)$

$$S_z\,\varphi(\vec{r}; s) = q\,\varphi(\vec{r}; s) \tag{2.181}$$

gives four eigenvalues $q = \{\pm 1, \pm i\}$.

Examining the commutation properties of above introduced operators leads to the following properties

$$\left[\hat{P}, \hat{S}_z\right] = 0,$$

$$\begin{aligned} &\left[\hat{\pi}_i, \hat{\pi}_j\right] \neq 0, \qquad \{i = x, y, z\}, \\ &\hat{\pi}_i^2 = -I. \end{aligned} \tag{2.182}$$

Let us study the consequences of the combined symmetries $\hat{y}\hat{P}$ and $\hat{y}\hat{S}_z$. If $\hat{y} = \hat{K}\hat{\pi}_y^{-1}$ follows the parity operator $\hat{P}$ or the z signature operator $\hat{S}_z$, then one has the following properties for the density and for the total single-particle potential:

- For the $\hat{y}\hat{P}$ operation

$$\rho(x, y, z) = \rho(-x, y, -z), \; V(x, y, z) \; = V(-x, y, -z). \tag{2.183}$$

- And for the operation $\hat{y}\hat{S}_z$ (parity is broken)

$$\rho(x, y, z) = \rho(-x, y, z), \; V(x, y, z) \; = V(-x, y, z). \tag{2.184}$$

For the symmetry (2.183) we conclude from the commutation rules (2.182) that both quantum numbers π and q can be used to identify the eigenstates of the Hamiltonian $\hat{h}$. Thus the Hamiltonian matrix consists of four quasi-diagonal blocks corresponding to the four possible combinations of quantum numbers $\{\pi, q\}$: $\{1, 1\}$, $\{1, -1\}$, $\{-1, 1\}$, $\{-1, -1\}$. However, when the parity symmetry is broken, as in the expression (2.184), the z signature and $\hat{y}$ symmetries are still preserved. This means that the single-particle states can only be signed by the quantum number q (then the Hamiltonian matrix reduces to two blocks corresponding to $q = \pm 1$). On the other hand, if the z signature symmetry is broken while the parity and $\hat{y}$ are conserved, then the only good quantum number is the parity π (the Hamiltonian matrix reduces to two blocks corresponding to $\pi = \pm 1$). If this is the case, both the parity and the z signature symmetries are broken, and the only symmetry to be conserved in all the above cases is $\hat{y}$, which is in principle the time-reversal symmetry; then there is no good quantum number.

Matrix elements of a triaxial arbitrary potential in the h.o. basis

To describe the average single-particle field in the absence of spherical or axial symmetry, the Cartesian coordinate system is preferred, since all three coordinates are treated equally and no symmetry conditions are imposed on the basis wave functions. However, even if the system turns out to be spherically or axially symmetric, the angular momentum algebra cannot be applied directly to the resulting wave functions, so in the following let us explicitly derive expressions for the matrix elements of all components of the total single-particle Hamiltonian.

A triaxial harmonic oscillator potential can be written as

$$V_{h.o.}(x, y, z) = \frac{1}{2}m\omega_x^2 x^2 + \frac{1}{2}m\omega_y^2 y^2 + \frac{1}{2}m\omega_z^2 z^2, \tag{2.185}$$

where an energy eigenvalue is

$$E(n_x, n_y, n_z) = \hbar\omega_x\left(n_x + \frac{1}{2}\right) + \hbar\omega_y\left(n_y + \frac{1}{2}\right) + \hbar\omega_z\left(n_z + \frac{1}{2}\right) \tag{2.186}$$

with corresponding normalized eigenstate

$$\begin{aligned} |n_x, n_y, n_z, \Sigma\rangle \equiv &\Psi_{n_x}(x)\Psi_{n_y}(y)\Psi_{n_z}(z)\,\chi\,(\Sigma) = \\ &\sqrt{a_x a_y a_z} H_{n_x} H_{n_y} H_{n_z} \chi\,(\Sigma)\, e^{-\frac{1}{2}\left[(a_x x)^2 + (a_y y)^2) + (a_z z)^2\right]}. \end{aligned} \tag{2.187}$$

Where H_{n_i} is the normalized Hermite polynomial of order n^{th}, and

$$a_i \equiv \sqrt{\frac{M\omega_i}{\hbar}} \tag{2.188}$$

are characteristic lengths. These parameters are scaling factors for transforming Cartesian coordinates $\{x, y, z\}$ to $\{\xi, \eta, \zeta\}$, $(i = \{1, 2, 3\})$, in the following way:

$$\xi \equiv a_1 x, \quad \eta \equiv a_2 y, \quad \zeta \equiv a_3 z. \tag{2.189}$$

It is possible to choose these three oscillator constants ω_i arbitrarily, but one must consider that the volume does not change with the papering of the nuclear deformations. The following equation is often used

$$\hbar\omega_0 = \hbar(\omega_x\,\omega_y\,\omega_z)^{1/3} \approx \frac{41}{A^{1/3}}\,MeV \tag{2.190}$$

which deals with the energy distance between the main shells in the harmonic oscillator spectrum. However, matrix elements that are fixed in a given basis are not expected to be noticeably affected, regardless of the values of the oscillator parameters.

Now we establish some recursive relations of Hermite polynomials:

$$H_{n+1}(x) = 2xH_n(x) - 2nH_{n-1}(x), \tag{2.191}$$

$$\frac{d}{dx}H_n(x) = 2nH_{n-1}, \tag{2.192}$$

where $H_0(x) = 1$, $H_1(x) = 2x$.
Multiplying both sides of (2.191) by $H_{n'}(x)$ and eliminating the undesirable factor x, yields

$$H_n H_{n'} = \sqrt{\frac{n'+1}{n}}H_{n-1}H_{n'+1} + \sqrt{\frac{n'}{n}}H_{n-1}H_{n'-1} - \sqrt{\frac{n-1}{n}}H_{n-2}H_{n'}\,. \tag{2.193}$$

The matrix elements of the one-body kinetic energy operator in the basis of the triaxial h.o. potential can be found analytically by means of Eqs. (2.191) and (2.192):

$$\begin{aligned}\left\langle n'_x, n'_y, n'_z, \Sigma' \middle| T_{kin} \middle| n_x, n_y, n_z, \Sigma \right\rangle = \delta_{\Sigma'\Sigma}\Big\{\delta_{n_x n'_x}\,\delta_{n_y n'_y}\hbar\omega_z\Big[\frac{1}{2}(n_z+\frac{1}{2})\delta_{n_z n'_z} \\ - \frac{1}{4}\sqrt{n_z(n_z-1)}\,\delta_{n_z-2,n'_z} - \frac{1}{4}\sqrt{n'_z(n'_z-1)}\,\delta_{n_z,n'_z-2}\Big] + cycl.\Big\}.\end{aligned} \tag{2.194}$$

The elements of the local mean-field effective potential which is only invariant with respect to time-reversal can be calculated in a similar way:

$$\left\langle n'_x, n'_y, n'_z, \Sigma' \middle| V_{sp} | n_x, n_y, n_z, \Sigma \right\rangle = \delta_{\Sigma'\Sigma}\left\langle n'_x, n'_y, n'_z \middle| V_{sp} | n_x, n_y, n_z \right\rangle, \tag{2.195}$$

where

$$\begin{aligned}\left\langle n'_x, n'_y, n'_z \middle| V_{sp} | n_x, n_y, n_z \right\rangle = \int_{-\infty}^{\infty} d\xi e^{-\xi^2} H_{n'_x}(\xi)H_{n_x}(\xi) \int_{-\infty}^{\infty} d\eta e^{-\eta^2} H_{n'_y}(\eta)H_{n_y}(\eta) \\ \times \int_{-\infty}^{\infty} d\zeta e^{-\zeta^2} H_{n'_z}(\zeta)H_{n_z}(\xi)\,V(\xi,\eta,\zeta).\end{aligned} \tag{2.196}$$

It can be shown that most of the above matrix elements can be obtained recursively from the relation (2.193) for products of normalized Hermite polynomials. Thus, the matrix elements of V_{sp} can be rewritten as

$$\begin{aligned}\langle n'_x, n'_y, n'_z|V_{sp}|n_x, n_y, n_z\rangle =& \sqrt{\frac{n'_z+1}{n_z}}\,\langle n'_x, n'_y, n'_z+1|V_{sp}|n_x, n_y, n_z-1\rangle \\ &+\sqrt{\frac{n'_z}{n_z}}\,\langle n'_x, n'_y, n'_z-1|V_{sp}|n_x, n_y, n_z-1\rangle \\ &-\sqrt{\frac{n_z-1}{n_z}}\,\langle n'_x, n'_y, n'_z|V_{sp}|n_x, n_y, n_z-2\rangle.\end{aligned} \tag{2.197}$$

From Eq. (2.195) it is possible to derive equivalent recurrence relations in both x and y directions due to the symmetry conditions. Partial parity, determined by the Cartesian coordinates $(-1)^{n_i}$, allows us to identify matrix elements equal to zero, as shown for axially symmetric potentials in section 2.2.5. This gives a conserved quantity which is used to characterize the full wave function (see eq. (2.159)) in a block diagonal Hamiltonian matrix. The blocks can be further subdivided by considering the parity π. For a more detailed introduction to methods of calculating matrix elements, the author refers to Ref. [62] as an example.

Finally, let is describe the potential that connects the spin and orbital motions in the quantum system, the so-called spin-orbit potential. This potential, as shown in (2.151) for the two nucleon charge states (q=$\{p, n\}$), is derived from the respective central potential V^q_{sp}, $(q = \{p, n\})$ by

$$V^{s.o.}_q(\vec{r}) = i\,\lambda_q \left(\frac{\hbar}{2Mc}\right)^2 \vec{\nabla} V^{(q)}_{sp} \cdot \left[\vec{\sigma} \times \vec{\nabla}\right], \tag{2.198}$$

where the parameters λ_q indicating the intensity of the spin-orbit coupling are given by the expressions (2.153) and $\vec{\sigma}$ is the vector $(\sigma_x, \sigma_y, \sigma_z)$ of (2×2) Pauli matrices.

After some algebraic manipulations, the potential can be expressed in a form consisting of products of space and spin operators as follows

$$\begin{aligned}V_{s.o.} = -\frac{i\kappa}{\hbar}\Bigg[&\hat{\sigma}_x\left(\partial_y\frac{\partial V_{sp}}{\partial z} - \partial_z\frac{\partial V_{sp}}{\partial y}\right) + \hat{\sigma}_y\left(\partial_z\frac{\partial V_{sp}}{\partial x}\partial_x\frac{\partial V_{sp}}{\partial z}\right) \\ &+ \hat{\sigma}_z\left(\partial_x\frac{\partial V_{sp}}{\partial y} - \partial_y\frac{\partial V_{sp}}{\partial z}\right)\Bigg].\end{aligned} \tag{2.199}$$

Since the spin-orbit interaction involves distinctions between protons and neutrons, we will omit the index "q" in all subsequent expressions, including V_{sp}. As a result, the matrix elements of $V_{s.o.}$ have this shape:

$$\begin{aligned}\left\langle n'_x, n'_y, n'_z\middle|V_{s.o.}|n_x, n_y, n_z\right\rangle = -\frac{i\kappa}{\hbar}\Bigg\{&\left\langle n'_x, n'_y, n'_z\middle|\hat{\sigma}_x\left(\partial_y\frac{\partial V_{sp}}{\partial z} - \partial_z\frac{\partial V_{sp}}{\partial y}\right)\middle|n_x, n_y, n_z\right\rangle \\ &+\left\langle n'_x, n'_y, n'_z\middle|\hat{\sigma}_y\left(\partial_z\frac{\partial V_{sp}}{\partial x} - \partial_x\frac{\partial V_{sp}}{\partial z}\right)\middle|n_x, n_y, n_z\right\rangle \\ &+\left\langle n'_x, n'_y, n'_z\middle|\hat{\sigma}_z\left(\partial_x\frac{\partial V_{sp}}{\partial y} - \partial_y\frac{\partial V_{sp}}{\partial z}\right)\middle|n_x, n_y, n_z\right\rangle\Bigg\}\end{aligned} \tag{2.200}$$

For easier use in further calculations, it is convenient to express the spin operators $\{\hat{\sigma}_x, \hat{\sigma}_y, \hat{\sigma}_z\}$

in terms of the operators $\{\hat{\sigma}_+, \hat{\sigma}_-, \hat{\sigma}_0\}$, which are given as

$$\begin{aligned} \hat{\sigma}_+ &= (\hat{\sigma}_x + i\hat{\sigma}_y), \\ \hat{\sigma}_- &= (\hat{\sigma}_x - i\hat{\sigma}_y), \\ \hat{\sigma}_0 &= \hat{\sigma}_z, \end{aligned} \tag{2.201}$$

which act on the spin part of the general wave function in the following way:

$$\begin{aligned} \hat{\sigma}_+|\downarrow\rangle = |\uparrow\rangle, \quad \hat{\sigma}_+|\uparrow\rangle = 0, \\ \hat{\sigma}_-|\uparrow\rangle = |\downarrow\rangle, \quad \hat{\sigma}_-|\downarrow\rangle = 0. \end{aligned} \tag{2.202}$$

The complexity of finding the partial derivatives of a given local potential, such as Eq. (2.147), usually precludes its analytic expression. However, by integrating over the parts in Eq. (2.200), and remembering that $\Psi_{n_i} \to 0$ at infinity, the derivative of the potential can be transferred to the basis wave functions. This is convenient to do analytically. Using eq. (2.191) and the form of the derivative of the basis wave function, e.g. given in x-direction as

$$\begin{aligned} \frac{d\Psi_{n_x}(a_x x)}{dx} &= \mathcal{N}_{n_x}\sqrt{a_x}\left(aH'_{n_x-1}(a_x x) - a_x^2 x H_{n_x}(a_x x)\right)e^{-\frac{1}{2}a_x^2 x^2} \\ &= a_x\left[\sqrt{\frac{n_x}{2}}\Psi_{n_x-1}\Big(x\Big) - \sqrt{\frac{n_x+1}{2}}\Psi_{n_x+1}\Big(x\Big)\right] \end{aligned} \tag{2.203}$$

we obtain that

$$\Big\langle n'_x, n'_y, n'_z, \Sigma'\Big|V_{s.o.}|n_x, n_y, n_z, \Sigma\Big\rangle = \frac{1}{2}\kappa\Big[\langle\Sigma'|\sigma_+|\Sigma\rangle B_- + \langle\Sigma'|\sigma_-|\Sigma\rangle B_+ + 2\langle\Sigma'|\sigma_z|\Sigma\rangle B_z\Big],$$

where

$$B_\pm \equiv B_x \mp B_y, \tag{2.204}$$

$$\begin{aligned} B_x =& \frac{1}{2}\Big(1 - (-1)^{n'_y+n_y}\Big)\, a_y a_z \times \\ &\Big[- \sqrt{n'_z(n_y+1)}\Big\langle n'_x, n'_y, n'_z - 1, \Big|V_{sp}|n_x, n_y+1, n_z\Big\rangle \\ &- \sqrt{n_y(n'_z+1)}\Big\langle n'_x, n'_y, n'_z + 1, \Big|V_{sp}|n_x, n_y-1, n_z\Big\rangle \\ &+ \sqrt{n'_y(n_z+1)}\Big\langle n'_x, n'_y - 1, n'_z, \Big|V_{sp}|n_x, n_y, n_z+1\Big\rangle \\ &+ \sqrt{n_z(n'_y+1)}\Big\langle n'_x, n'_y + 1, n'_z, \Big|V_{sp}|n_x, n_y, n_z-1\Big\rangle\Big], \end{aligned} \tag{2.205}$$

$$\begin{aligned} B_y =& \frac{1}{2}\Big(1 + (-1)^{n'_y+n_y}\Big)\, a_x a_z \times \\ &\Big[- \sqrt{n'_x(n_z+1)}\Big\langle n'_x - 1, n'_y, n'_z, \Big|V_{sp}|n_x, n_y, n_z+1\Big\rangle \\ &- \sqrt{n_z(n'_x+1)}\Big\langle n'_x + 1, n'_y, n'_z, \Big|V_{sp}|n_x, n_y, n_z-1\Big\rangle \\ &+ \sqrt{n'_z(n_x+1)}\Big\langle n'_x, n'_y, n'_z - 1, \Big|V_{sp}|n_x+1, n_y, n_z\Big\rangle \\ &+ \sqrt{n_x(n'_z+1)}\Big\langle n'_x, n'_y, n'_z + 1, \Big|V_{sp}|n_x-1, n_y, n_z\Big\rangle\Big], \end{aligned} \tag{2.206}$$

$$
\begin{aligned}
B_z =& \frac{1}{2}\Big(1-(-1)^{n'_y+n_y}\Big)\, a_x a_y \times \\
&\Big[-\sqrt{n'_y(n_x+1)}\Big\langle n'_x, n'_y-1, n'_z, \Big|V_{sp}\Big|n_x+1, n_y, n_z\Big\rangle \\
&-\sqrt{n_x(n'_y+1)}\Big\langle n'_x, n'_y+1, n'_z, \Big|V_{sp}\Big|n_x-1, n_y, n_z\Big\rangle \\
&+\sqrt{n'_x(n_y+1)}\Big\langle n'_x-1, n'_y, n'_z, \Big|V_{sp}\Big|n_x, n_y+1, n_z\Big\rangle \\
&+\sqrt{n_y(n'_x+1)}\Big\langle n'_x+1, n'_y, n'_z, \Big|V_{sp}\Big|n_x, n_y-1, n_z\Big\rangle\Big].
\end{aligned}
$$

The spin-orbit interaction, which is proportional to B_- and B_+, binds only antiparallel spin states, in contrast to the central potential, which contributes only between states with the same spin projection. This peculiarity leads to the splitting of each single-particle level (except for s-states) into two levels with the same orbital angular momentum but opposite spin orientations. To recursively construct the mean potential matrix, it is sufficient to numerically compute all the diagonal elements and a small percentage of the off-diagonal elements. The remaining off-diagonal elements are determined in successive rows up to the main diagonal of the matrix. After calculating the elements of the mean potential matrix, the same must be done for the spin-orbit potential using the equation (2.204). Several matrix elements must be calculated numerically. They can also be calculated recursively [60] by first calculating some additional matrix elements of the central potential with $n_x+n_y+n_z = N_{max}+1$ (where N_{max} is the cut-off condition related to the number of main h.o. shells used in the wave function expansion). The ground states (2.187) (omitting the quantum number of the spin σ) are ordered as follows:

$$
\begin{array}{cccc}
|0,0,0\rangle, & |0,0,1\rangle, & |0,0,\rangle, & \dots \\
|0,1,0\rangle, & |0,1,1\rangle, & |0,1,\rangle, & \dots \\
|1,0,0\rangle, & |1,0,1\rangle, & |1,0,\rangle, & \dots \\
|1,1,0\rangle, & |1,1,1\rangle, & |1,1,\rangle, & \dots \\
. & . & . & \dots \\
. & . & . & \dots \\
. & . & . & \dots
\end{array}
$$

Diagonaliztion of the symmetric potentials in the original h.o. basis

Consider a single-particle Hamiltonian $\hat{H}$ with axial symmetry, e.g. in the case of a prolate deformed mean-field, the central potential is independent of the angle φ in cylindrical coordinates. Consequently, the single-particle Hamiltonian commutes with the third component of the total angular momentum operator $\hat{J}_z = \hat{l}_z + \hat{s}_z$ and with the parity operator $\hat{P}$, leading to the equations:

$$
[\hat{H}, \hat{J}_z] = 0, \qquad [\hat{H}, \hat{P}] = 0. \tag{2.207}
$$

It can be seen that the action of the parity operator $\hat{P}$ on an arbitrary spatial function $\psi(x,y,z)$ is given by

$$
\hat{P}\,\psi(x,y,z) = \psi(-x,-y,-z) \tag{2.208}
$$

with its eigenvalues equal to $\pi = \pm 1$. Thus the eigenstates of such a Hamiltonian are characterized by a set of quantum numbers $\{\Omega = \Lambda + \Sigma, \pi\}$, where Ω and π are the total angular momentum and parity quantum numbers, respectively. In addition, when octupole deformations are taken into account, the reflection symmetry with respect to the xOy-plane is broken, and thus parity is no longer a good quantum number as $[\hat{H}, \hat{P}] \neq 0$.

It can be shown by Eq. (2.198) that both the central and the spin-orbit potentials share the same spatial symmetries, which can be described parametrically and are able to describe nuclear shapes if the cross section perpendicular to the $z-$-axis is at most an ellipse. Alternatively, one can consider many other geometric shapes for which

$$V(x, y, z) = V(-x, -y, z). \tag{2.209}$$

is satisfied, with no constraints on the shape in the $z-$ direction.
Returning to the original h.o. basis, it can be concluded that the only good quantum number for these potentials is given by

$$q = (-1)^{n_x+n_y} \, \Sigma/|\Sigma| \,, \tag{2.210}$$

where Σ is the spin projection, equal to $\{1/2, -1/2\}$. This implies that the Hamiltonian matrix is split into two identical blocks with $q = 1$ and $q = -1$ respectively. For further simplification, only one of these blocks needs diagonalization; following Kramer's theorem [33], each state can then be occupied by two particles, and this transformation already contains the time inversion operation.

In this case, the Hamiltonian matrix can be represented schematically as follows

$\lvert b_{odd}\uparrow\rangle$	$\lvert b_{even}\downarrow\rangle$	$\lvert b_{odd}\downarrow\rangle$	$\lvert b_{even}\uparrow\rangle$	
$V_{cent} + V_{s.o.;3}$	$V_{s.o.1} + V_{s.o.;2}$	0	0	$\lvert b_{odd}\uparrow\rangle$
$V_{s.o.1} - V_{s.o.;2}$	$V_{cent} - V_{s.o.;3}$	0	0	$\lvert b_{even}\downarrow\rangle$
0	0	$V_{cent} + V_{s.o.;3}$	$V_{s.o.,1} + V_{s.o.;2}$	$\lvert b_{odd}\downarrow\rangle$
0	0	$V_{s.o.;1} - V_{s.o.;2}$	$V_{cent} - V_{s.o.;3}$	$\lvert b_{even}\uparrow\rangle$

with the notation of $|b_{odd}\uparrow\rangle$ denoting the set of basis states $(+i)^{n_y} |n_x, n_y, n_z\rangle |s_z\rangle$, for which $n_x + n_y$ is an odd number with spin projection 1/2, symbolized by the up arrow, and the other three types of basis states having analogous meanings. The quantities V_{centr} and $V_{s.o.;n}$ $(n = \{1, 2, 3\})$ are as follows: $V_{centr} = V_{kin} + V_{sp} + V_{Coul}\,\delta_{pq}$ $(q = \{p, n\})$ and $V_{s.o.;n}$ corresponding to the spin-orbit term entering Eq. (2.204) proportional to B_x, B_y, and B_z, respectively. Consequently, the upper-left and lower-right blocks of the full matrix must be identical, i.e., they must have the same eigensolutions.

So, this section was devoted to a comprehensive overview of the microscopic approach to understanding the internal structure of the atomic nucleus. To determine the energy of the nucleus, the well-known Hartree-Fock method was used, which involves solving the many-body problem of the nucleons using a set of orthonormal one-particle states. The Hamiltonian of the system includes a two-particle interaction consisting of a long-range Coulomb interaction between the protons and a short-range nuclear interaction. In addition, the BCS method, which incorporates pairing correlations between nucleons, was mentioned, detailing the inclusion of the pairing potential in the Hamiltonian and the solution of the BCS equations to determine pairing gaps and binding energies. The Coulomb potential and energy corrections in the nucleus have also been considered. In section 2.2.4

it was described the folding procedure and how the density dependent Coulomb potential can be calculated. It was explained how the Coulomb energy can be corrected for the diffuseness of the charge distribution. Finally, the role of the harmonic oscillator potential in describing the single-particle states in the nucleus was mentioned. In particular, the eigenstates of the axially symmetric harmonic oscillator potential and how they can be used as a basis for describing the nuclear structure.

2.3 Macroscopic-microscopic method

Having discussed the details of the macroscopic and microscopic approaches separately, it is time to generalize these two approaches. The advantage of unification lies in the number of described properties and characteristics of the atomic nucleus, including those possessing deformations. Earlier (see 2.1.3) an example was given where an attempt was made to estimate the binding energy by including pair correlations of nucleons within the nucleus, but there was no dependence on the deformation parameters. To remedy this weakness, the idea of extracting the shell effect of the averaged nuclear properties, which with the BCS method could approximate the effect of the short-range pairwise interaction, came up.

As mentioned earlier, the deformation of nuclei is described by the introduction of collective coordinates. Their minimization by energy gives information about the ground state of the nuclear system. Therefore, to find this point (and other extrema), a coordinate grid with energy values at its nodes is used. This is described in more detail in Chapter 5. Here it can be said that the macroscopic energy can always be calculated within the framework of the LD and DM models presented above, taking into account deformations. But these deformations are always caused by quantum-mechanical effects.

2.3.1 Single-partcle energy summation

Real nuclei often exhibit nonspherical ground state shapes due to shell effects. Therefore, the single-particle energies of the deformed mean-field potentials must be used to calculate the microscopic contribution to their potential energy.

In the first attempt [46], Mottelson and Nilsson have proposed the evaluate the sum of energies of occupied single-particle states

$$E_{\mathrm{MN}}(N,Z,\mathrm{def}) = \sum_{\mathrm{occ}} \mathrm{e}_{\nu}^{\mathrm{p}} + \sum_{\mathrm{occ}} \mathrm{e}_{\nu}^{\mathrm{n}} + E_{\mathrm{Coul}}\,. \tag{2.211}$$

Here e_ν are the single-particle energies of protons (p) and neutrons (n), obtained by diagonalizing the Hamiltonian with the deformed mean-field potential $V(\mathbf{r};\mathrm{def})$

$$\hat{h} = \widehat{T} + V(\mathbf{r};\mathrm{def}). \tag{2.212}$$

The Coulomb energy of protons can be obtained by the integral after all single-particle coordinates of protons

$$E_{\mathrm{Coul}} = \sum_{i>j} \iint \ldots \int \Psi^{*}\left(\mathbf{r}_1,\ldots,\mathbf{r}_z\right) \frac{\mathrm{e}^2}{|\mathbf{r}_i-\mathbf{r}_j|} \Psi\left(\mathbf{r}_1,\ldots,\mathbf{r}_z\right) d\tau_1 \ldots d\tau_z \tag{2.213}$$

where Ψ is a Slater determinant consisting of single-particle functions. Substituting the squares of these functions for the single-particle proton densities ρ_i^{p} gives the formula

$$E_{\mathrm{Coul}} = \sum_{i>j} \iint \rho_i^{\mathrm{p}}\left(\mathbf{r}_i\right) \rho_j^{\mathrm{p}}\left(\mathbf{r}_j\right) \frac{\mathrm{e}^2}{|\mathbf{r}_i-\mathbf{r}_j|} d\tau_i d\tau_j \tag{2.214}$$

Bethe and Bacher have estimated [63] this integral as

$$E_{\text{Coul}} = \frac{3}{5}\frac{Z^2e^2}{R_0}B_c(\text{def}) - \frac{\pi^2}{2}\frac{5}{3}\frac{a}{R_0^2} - \frac{0.7636}{Z^{2/3}}, \tag{2.215}$$

where a is the value of the diffuseness of the nucleus surface and $R_0 = r_0A^{1/3}$ is the radius of the spherical charge distribution.
The single-particle energy summation method gave the minimum energy for non-zero deformations, but it did not reproduce either the experimental masses of the nuclei or their fission barrier heights. Its main error was the double counting of nucleon-nucleon interactions in the total energy, which cannot be separated. In the energy sum (2.211) it is impossible to separate a part of the energy coming from the mean-field potential. Therefore one has to find another method to include the shell effects.

Taking into account the short-range pairing correlations, the method proposed by Bés and Szymański improves the Mottelson-Nilsson method:

$$\begin{aligned} E_{\text{BS}} = &\left(\sum_{\nu=1}^{\nu_F} 2e_\nu V_\nu^2 - \frac{\Delta^2}{G} - G\sum_{\nu>0} V_\nu^4\right)_{\text{p}} \\ &+ \left(\sum_{\nu=1}^{\nu_F} 2e_\nu V_\nu^2 - \frac{\Delta^2}{G} - G\sum_{\nu>0} V_\nu^4\right)_{\text{n}} + E_{\text{Coul}}\,. \end{aligned} \tag{2.216}$$

For odd nuclei, a quasi-particle energy must be added. With these microscopic methods the nuclear energy can be determined with an accuracy to a constant. But only its variance with deformation can be evaluated from the microscopic structure, and its absolute value must be estimated from the masses of known nuclei.

2.3.2 Idea of the macroscopic-microscopic method

Strutinsky proposed a method of renormalizing the energy to a liquid drop or other macroscopic energy by means of a microscopic energy correction in order to reproduce absolute values of the potential energy and to avoid double summation of nuclear two-body coupling. The microscopic energy consists of the part responsible for shell effects and the term associated with pairing correlations. Thus, the total energy of the nucleus is

$$E_{\text{Strut}} = E_{\text{LD}} + \delta E_{\text{shell}} + \delta E_{\text{pair}}\,. \tag{2.217}$$

On Fig. 2.3 schematically shows the contribution of the individual terms to the Strutinsky energy (2.217).

The pairing correction consists of a difference of the microscopic energy calculated with (2.216) and without short-range interactions (2.211), from which the term describing the average energy of the pairing correlations $\langle E_{\text{pair}}\rangle \approx -2.3\text{MeV}$ is subtracted, since it is already included in the phenomenological parameters of the liquid-drop model.

$$\delta E_{\text{pair}} = E_{\text{BCS}} - 2\sum_{\nu>0}^{\nu_F} e_\nu - \langle E_{\text{pair}}\rangle\,. \tag{2.218}$$

The shell correction is given by the difference between the sum of the single-particle energies and an average energy ($\tilde{E}$) in which the shell structure is washed out

$$\delta E_{\text{shell}} = 2\sum_{\nu=1}^{\nu_F} e_\nu - \tilde{E}. \tag{2.219}$$

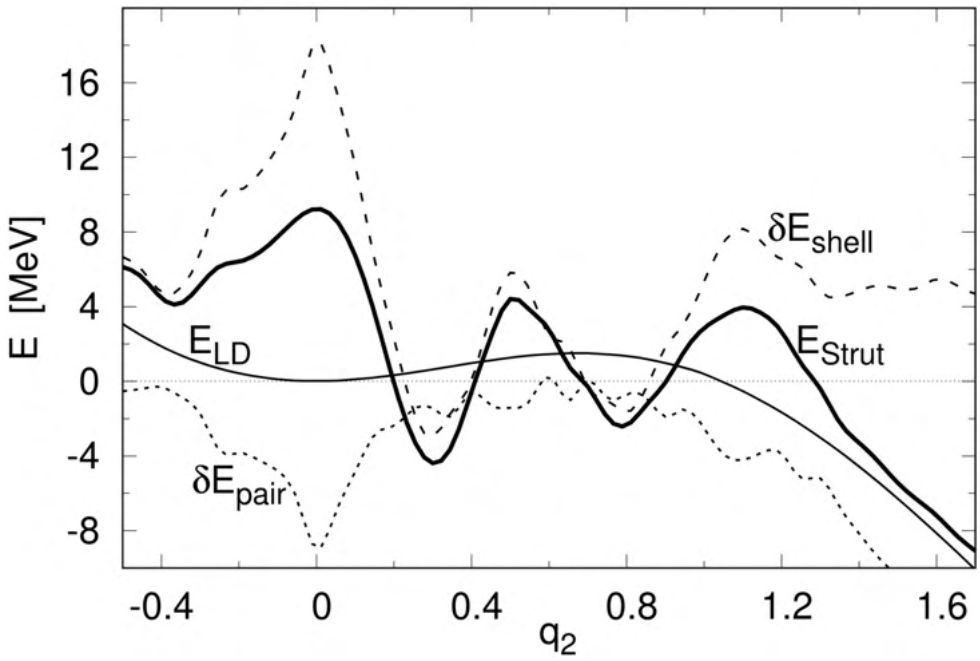

Figure 2.3: Various terms of the potential energy of the nucleus as a function of the elongation of the nucleus: E_{LD} – macroscopic drop energy (thin solid line), $\delta E_{\mathrm{shell}}$ – shell correction (dashed line), δE_{pair} – pair correction (dotted line), E_{Strut} – total Strutinsky energy (thick solid line). Taken from Ref. [64].

The idea of separating pure shell effects from nuclear energy, postulated by Myers and Świątecki in the Fermi gas model, was independently developed by Strutinsky in a more rigorous mathematical model. More details can be found in the classic work [65]. By inserting the corrections δE_{pair} (2.218) and $\delta E_{\mathrm{shell}}$ (2.219) into the equation (2.217) we obtain the equation for the potential energy of the nuclei in the form

$$E_{\mathrm{Strut}} = E_{\mathrm{LD}} + E_{\mathrm{BCS}} - \langle E_{\mathrm{pair}} \rangle - \tilde{E}. \tag{2.220}$$

Strutinsky's method provides a good reproduction of atomic nucleus shapes and energies in ground states, as well as width and height of fissionbarriers. It should be noted [64] that this method involves two apparently contradictory models of the nucleus: one based on the assumption of strong interactions, the macroscopic nuclear drop, and the other based on the assumption of independent particles moving in an average mean-field potential. These two approaches are not contradictory if the Pauli exclusion principle is taken into account.

2.3.3 Strutinsky shell corrections

An efficient way of extracting from the nucleus energy the so-called smooth part, free from shell structure was proposed by Strutinsky. In the following, we recall his argumentation with later improvements made by other authors.

Let us consider a system of A nucleon which coordinates are $\mathbf{x}_i, i = 1, \ldots, A$, where $\mathbf{x}_i = \{\mathbf{r}_i, \mathbf{s}_i, \mathbf{t}_i\}$. The density of i-th nucleon is given by the product $\rho_i(\mathbf{x}_i) = \varphi^{\star}(\mathbf{x}_i) \cdot \varphi(\mathbf{x}_i)$, where $\varphi(\mathbf{x}_i)$ is its single-particle wave function. The energy of the system consists of a kinetic part, being the sum of the single-particle kinetic energies $T_i(\mathbf{x}_i)$ and potential term originating from the two-body interaction $V(\mathbf{x}_i, \mathbf{x}_j)$

$$E = \sum_{i=1}^{A} \int T_i(\mathbf{x}_i)\, \rho_i(\mathbf{x}_i)\, d\mathbf{x}_i + \sum_{\substack{i,j \\ i>j}}^{A} \iint \rho_i(\mathbf{x}_i)\, V(\mathbf{x}_i, \mathbf{x}_j)\, \rho_j(\mathbf{x}_j)\, d\mathbf{x}_i d\mathbf{x}_j \tag{2.221}$$

Assuming the single-particle mean-field potential in the form

$$U\left(\mathbf{x}_i\right) \equiv \sum_{j \neq i} \int V\left(\mathbf{x}_i, \mathbf{x}_j\right) \rho_j\left(\mathbf{x}_j\right) d\mathbf{x}_j \tag{2.222}$$

and taking half of this to not double the nucleon-nucleon interactions, energy of nucleus is expressed by the sum of the integrals below:

$$E = \sum_{i=1}^{A} \int \left[T_i\left(\mathbf{x}_i\right) + \frac{1}{2} U_i\left(\mathbf{x}_i\right)\right] \rho_i\left(\mathbf{x}_i\right) d\mathbf{x}_i \tag{2.223}$$

Separating the density ρ into a smooth function $\bar{\rho}$ and a fluctuating part $\delta\rho$ containing shell effects

$$\rho_i\left(\mathbf{x}_i\right) = \bar{\rho}_i\left(\mathbf{x}_i\right) + \delta\rho_i\left(\mathbf{x}_i\right) \tag{2.224}$$

and applying the smooth density $\bar{\rho}$ to Eq. (2.221) to evaluate a non-fluctuating part

$$\tilde{E} = \sum_{i=1}^{A} \int T_i\left(\mathbf{x}_i\right) \bar{\rho}_i\left(\mathbf{x}_i\right) d\mathbf{x}_i + \sum_{i,j,i>j}^{A} \int \bar{\rho}_i\left(\mathbf{x}_i\right) V\left(\mathbf{x}_i, \mathbf{x}_j\right) \bar{\rho}_j\left(\mathbf{x}_j\right) d\mathbf{x}_i d\mathbf{x}_j. \tag{2.225}$$

The formula for the total energy of the nucleus can now be written in the form

$$\begin{aligned} E = \tilde{E} + \left\{ \sum_{i=1}^{A} \int T_i\left(\mathbf{x}_i\right) + \sum_{j \neq i}^{A} \int V\left(\mathbf{x}_i, \mathbf{x}_j\right) \bar{\rho}_j\left(\mathbf{x}_j\right) d\mathbf{x}_j \right\} \delta\rho_i\left(\mathbf{x}_i\right) d\mathbf{x}_i \\ + \text{ terms of higher powers of } \delta\rho. \end{aligned} \tag{2.226}$$

By introducing a smooth potential field

$$\tilde{U}\left(\mathbf{x}_i\right) = \sum_{j \neq i}^{A} \int V\left(\mathbf{x}_i, \mathbf{x}_j\right) \bar{\rho}_j\left(\mathbf{x}_j\right) d\mathbf{x}_j, \tag{2.227}$$

one can convert the formula (2.221) for the total energy of the nucleus to form containing shell correction (2.219)

$$E = \tilde{E} + \sum_{i=1}^{A} \int \left[T_i\left(\mathbf{x}_i\right) + \tilde{U}\left(\mathbf{x}_i\right)\right] \left[\rho_i\left(\mathbf{x}_i\right) - \bar{\rho}_i\left(\mathbf{x}_i\right)\right] d\mathbf{x}_i \equiv E_{\mathrm{LD}} + \delta E_{\mathrm{shell}} \tag{2.228}$$

Usually, having deformed the mean potential $\tilde{U}\left(\mathrm{def}_{\mathrm{U}}\right)$, it is assumed that the surface of the nucleus coincides with the equipotential surface and that the potential deformation $\mathrm{def}_{\mathrm{U}}$ as well as the density deformation def_{ρ} are the same. But this is not always the case, so to enhance the quality of the model, it is possible to use def_{U} for the calculation of the microscopic correction

$$\mathrm{def}_{\mathrm{U}} \rightarrow U\left(\mathrm{def}_{\mathrm{U}}\right) \rightarrow e_{\nu} \rightarrow \delta E_{\mathrm{shell}}\ \left(\mathrm{def}_{\mathrm{U}}\right), \tag{2.229}$$

and def_{ρ} to calculate macroscopic energy

$$\mathrm{def}_{\rho} \rightarrow R\left(\mathrm{def}_{\rho}\right) \rightarrow E_{\mathrm{LD}}\left(\mathrm{def}_{\rho}\right). \tag{2.230}$$

in most calculations it is simply assumed that $\mathrm{def}_{\mathrm{U}} = \mathrm{def}_{\rho}$. Such an approximation is well justified if, for example, one uses the Yukawa-folded potential generated from a given deformed density distribution. In other cases, it is possible to determine the deformation of the density from a given deformation mean-field potential. Namely, the density deformation

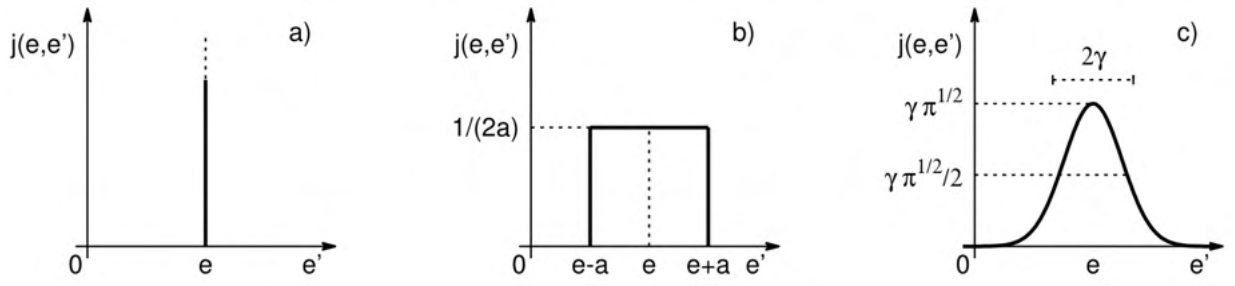

Figure 2.4: Weight functions $j\,(e,e')$: Dirac δ with strictly localized levels (a), smoothing over a given interva (b), local smoothing function (c). Taken from Ref. [64]

of def_ρ can be evaluated assuming the equality of the multipole moments of the density distributions calculated in the microscopic and macroscopic way:

$$\mathrm{def}_\mathrm{U} \to U\,(\mathrm{def}_\mathrm{U}) \to \rho\,(\mathrm{def}_\mathrm{U}) \to Q_{\lambda\mu}^{\mathrm{micr}}\,(\mathrm{def}_\mathrm{U}) = Q_{\lambda\mu}^{\mathrm{macr}}\,(\mathrm{def}_\rho) \to \mathrm{def}_\rho \tag{2.231}$$

The application of such a simplified consistency condition can improve the estimates obtained with the Nilsson or Wood-Saxon potentials.

This raises the question of how to calculate the smoothed sum of single particle energies. Strutinsky proposed to represent the smoothed energy in the form of the following integral over the single-particle energies:

$$\tilde{E} = 2\int_{-\infty}^{\tilde{\lambda}} \bar{\rho}(e) e \cdot de. \tag{2.232}$$

The upper limit of the integral, i.e. the Fermi level $\tilde{\lambda}$ in the smoothed shell, is determined from the conservation of the number of particles

$$Z(N) = 2\int_{-\infty}^{\tilde{\lambda}} \bar{\rho}(e) de \longrightarrow \tilde{\lambda}. \tag{2.233}$$

The function $\bar{\rho}$ will be obtained by averaging the true density of single-particle levels ρ using the weight function $j\,(e,e')$

$$\bar{\rho}(e) = \int_{-\infty}^{+\infty} \rho\,(e')\, j\,(e,e')\, de', \tag{2.234}$$

where j must satisfy the condition

$$\int_{-\infty}^{+\infty} j\,(e,e')\, de' = 1. \tag{2.235}$$

The next question is the choice of the weight function, which has to be implemented in order to be able to wash out the structure at the single-particle level. Let us take a look at a few examples of such functions, shown in Fig 2.4: Dirac δ function to preserve discrete levels (a), smoothing over a given interval (b), and a local smoothing function (c).

In practical computations, the third case is used. To better understand the meaning of the $j\,(e,e')$ functions shown in Fig 2.4, lets discuss each case separately:
a) For discrete levels, the j weight function would be the Dirac δ-function

$$j\,(e,e') = \delta\,(e'-e)\,, \qquad \text{where} \int_{-\infty}^{+\infty} \delta\,(e'-e)\, de' = 1 \tag{2.236}$$

and then

$$\bar{\rho}(e) = \int_{-\infty}^{+\infty} \rho\left(e'\right) \delta\left(e - e'\right) de' = \rho(e). \tag{2.237}$$

The folding with δ-function remains the density unchanged.
b) When the function j is defined as the difference of the Heaviside step functions, the following applies:

$$j\left(e, e'\right) = \frac{1}{2a} \left\{\theta\left[e' - (e - a)\right] - \theta\left[e' - (e + a)\right]\right\}, \tag{2.238}$$

then one obtains the following smooth density:

$$\bar{\rho}(e) = \frac{1}{2a} \int_{-\infty}^{+\infty} \left\{\theta\left[e' - (e - a)\right] - \theta\left[e' - (e + a)\right]\right\} \rho\left(e'\right) de' = \frac{1}{2a} \int_{e-a}^{e+a} \rho\left(e'\right) de' \tag{2.239}$$

c) It is also possible to use a modified Gaussian function to smooth the spectrum of the single-particle levels.

$$j\left(e, e'\right) = \frac{1}{\gamma\sqrt{\pi}} \mathrm{e}^{-\left(\frac{e-e'}{\gamma}\right)^2} f\left(\frac{e - e'}{\gamma}\right), \tag{2.240}$$

where γ is a smoothing parameter approximately equal to the energy distance between the major shells ($\sim \hbar\omega_0$). The f function is a fit polynomial that ensures that the average slope of the $\bar{\rho}(e)$ curve is the same as that of the $\rho(e)$ curve.

When a weight function is Gaussian, how do you determine the f correction polynomial? Let us introduce a variable

$$u = \frac{e - e'}{\gamma} \tag{2.241}$$

belonging to the range $u \in (-\infty, +\infty)$. The weight function (2.240) can be written as

$$j\left(e, e'\right) = \frac{\mathrm{e}^{-u^2}}{\gamma\sqrt{\pi}} f(u) \tag{2.242}$$

and the smoothed density function $\bar{\rho}$ depends on the new variable u :

$$\begin{aligned} \bar{\rho}\left(e'\right) &= \bar{\rho}(e - \gamma u) \equiv \bar{\rho}'(u), \\ \bar{\rho}(e) &= \bar{\rho}(e + \gamma 0) \equiv \bar{\rho}'(0). \end{aligned} \tag{2.243}$$

Prove that if $\bar{\rho}$ is a polynomial of degree p, then the function f is in the form of a polynomial of the same degree p, satisfying the condition

$$\bar{\rho}(e) = \int_{-\infty}^{+\infty} \bar{\rho}\left(e'\right) j\left(e, e'\right) de', \tag{2.244}$$

to ensure that further averaging does not add anything new to the already smoothed density distribution $\bar{\rho}$.

Let us decompose $\bar{\rho}'(u)$ into a series of Hermite polynomials $H_i(u)$

$$\bar{\rho}'(u) = \sum_{i=1}^{p} a_i H_i(u). \tag{2.245}$$

From the condition (2.244) one receives:

$$\bar{\rho}'(0) = \frac{1}{\sqrt{\pi}} \int_{-\infty}^{+\infty} \bar{\rho}'(u) \mathrm{e}^{-u^2} f(u) du \tag{2.246}$$

or after insertion Eq. (2.245)

$$\sum_{i=1}^{\mathrm{p}} a_i \left\{ \frac{1}{\sqrt{\pi}} \int_{-\infty}^{+\infty} \mathrm{e}^{-u^2} H_i(u) f(u) du - H_i(0) \right\} = 0. \tag{2.247}$$

Assuming that $a_i \neq 0$, the last equation will be satisfied when

$$\frac{1}{\sqrt{\pi}} \int_{-\infty}^{+\infty} \mathrm{e}^{-u^2} H_i(u) f(u) du = H_i(0). \tag{2.248}$$

If one also represent the function $f(u)$ in the form of a polynomial of degree r

$$f(u) = \sum_{k=1}^{r} C_k H_k(u), \tag{2.249}$$

then

$$H_i(0) = \sum_{k=1}^{r} C_k \frac{1}{\sqrt{\pi}} \int_{-\infty}^{+\infty} \mathrm{e}^{-u^2} H_i(u) H_k(u) du. \tag{2.250}$$

Using the orthogonality properties of the Hermite polynomials one obtains the last integral equal to : $2^i i! \delta_{ik}$. So,

$$H_i(0) = C_i 2^i i!, \qquad \text{hence} \qquad C_i = \frac{H_i(0)}{2^i i!}. \tag{2.251}$$

Using the values of the Hermite polynomials at $u = 0$

$$H_i(0) = \begin{cases} 1 & \text{for } i = 0 \\ 2^n (-1)^n (2n-1)!! & \text{for } i = 2n \\ 0 & \text{for } i = 2n+1 \end{cases} \tag{2.252}$$

one obtains

$$C_i = \begin{cases} 1 & \text{for } i = 0, \\ (-1)^n \frac{(2n-1)!!}{2^n (2n)!} & \text{for } i = 2n > 0 \\ 0 & \text{for } i = 2n+1 \end{cases} \tag{2.253}$$

Table 2.2 gives the first few expansion coefficients of C_i in the Hermite polynomial series. When evaluating the Strutinsky shell correction energy, one often uses the 6th order correction polynomial, which is1

$$f(u) = \frac{35}{16} - \frac{35}{8} u^2 + \frac{7}{4} u^4 - \frac{1}{6} u^6. \tag{2.254}$$

Table 2.2: Expansion coefficients C_i of the correction polynomial (2.249) and the Hermite polynomials $H_i(u)$

i	C_i	$H_i(u)$
0	1	1
2	$-\frac{1}{4}$	$4u^2 - 2$
4	$+\frac{1}{32}$	$16u^4 - 48u^2 + 12$
6	$-\frac{1}{384}$	$64u^6 - 480u^4 + 720u^2 - 120$

Let us summarize the steps for calculating the potential energy of the nucleus using the Strutinsky shell correction method for an even number of particles:

1. Solve the eigenproblem of a single-particle Hamiltonian $\widehat{h}$ with a mean-field potential that is generally deformation dependent.

$$\widehat{h}|\nu\rangle = e_\nu|\nu\rangle \tag{2.255}$$

and obtains the single-particle energy system e_ν as well as eigenfunctions $|\nu\rangle$ labeled with a set of quantum numbers ν.

2. Then compute the smooth part of the single-particle level distribution

$$\bar{\rho}(e) = \frac{1}{\gamma\sqrt{\pi}} \int_{-\infty}^{+\infty} \rho\left(e'\right) \mathrm{e}^{-\left(\frac{e-e'}{\gamma}\right)^2} f\left(\frac{e-e'}{\gamma}\right) de', \tag{2.256}$$

where γ is a smoothing constant equal to the average distances between the major shells $\left(\sim \hbar\, \mathring{\omega}_0\right)$.

3. For a given atomic nucleus with Z protons and N neutrons, we determine the Fermi level $\tilde{\lambda}$ from the following condition

$$\int_{-\infty}^{\tilde{\lambda}} \bar{\rho}(e) de = Z(N). \tag{2.257}$$

4. Next, calculate the energy of the spectrum of the smoothed levels

$$\tilde{E} = 2 \int_{-\infty}^{\tilde{\lambda}} e\bar{\rho}(e) de. \tag{2.258}$$

for protons and neutrons.

5. Solve the system of BCS equations and evaluate the energy of the protons and neutrons in this approximation.

$$E_{\mathrm{BCS}} = \sum_{\nu>0} 2e_\nu V_\nu^2 - \frac{\Delta^2}{G} - G \sum_{\nu>0} V_\nu^4. \tag{2.259}$$

6. Calculate the deformation dependent part of the macroscopic energy, which, e.g., in the liquid-drop model:

$$E_{\mathrm{LD}} = a_2 \left(1 - \kappa I^2\right) A^{2/3} \left[B_{\mathrm{s}}(\mathrm{def}) - 1\right] + \frac{3}{5} \frac{Z^2 \mathrm{e}^2}{r_0} A^{1/3} \left[B_{\mathrm{c}}(\mathrm{def}) - 1\right]. \tag{2.260}$$

7. Also calculate the total energy of the nucleus as a function of the deformation at appropriate grid points.

$$E_{\mathrm{Strut}}\,(\mathrm{def}) = E_{\mathrm{LD}} + E_{\mathrm{BCS}} - \langle E_{\mathrm{pair}}\,\rangle - \tilde{E}. \tag{2.261}$$

8. Then minimize the energy relative to the deformation parameters

$$E_{\mathrm{Strut}}\,(\mathrm{def}) = \text{ minimum } \longrightarrow \mathrm{def}_{\mathrm{min}} \tag{2.262}$$

thus determining all local minima. The lowest one corresponds to the equilibrium (ground state) point of the nucleus def f_{eq}.

9. The shape of the nucleus $R\,(def_{\mathrm{eq}}\,)$ and its ground state energy can be determined with the deformation parameters of the equilibrium point:

$$E_0 = E_{\mathrm{Strut}}\ (\mathrm{def}_{\mathrm{eq}})\,. \tag{2.263}$$

The calculations described in points 1 to 5 are performed separately for protons and neutrons, and then the resulting energies $\tilde{E}$ and E_{BCS} are summed. The Strutinsky method is used for various single-particle mean potentials. The liquid-drop model is often replaced by some other macroscopic model.

The Strutinsky method is a combination of single-particle effects: microscopic, macroscopic and collective. It is widely used for evaluation of potential energy surfaces of nuclei in multidimensional space of deformation parameters. Figure 2.3 shows an example of the contribution of individual terms to the total Strutinsky energy.

Let's sum up the whole chapter. Here the theoretical approaches to the description of the properties of atomic nuclei have been discussed, both from the point of view of classical (semiclassical) – macroscopic, and from the point of view of quantum mechanics – microscopic.

Both approaches have their advantages and disadvantages. This is particularly evident in the case of the binding energy of nuclei. For example, the macroscopic approach includes a liquid-drop representation of the nucleus, of which the Bethe-Weizsäcker semiphemonological formula (2.1) is an example. It takes into account the basic concepts of nucleon-nucleon interactions corresponding to various factors such as volume, surface tension, and Coulomb repulsion. In addition to the mentioned formula, better models based on this representation have been given.

Nevertheless, the deformation of nuclei, which is observed for the overwhelming number of nuclei from the present nuclear chart, is caused precisely by the internal structure and collective interaction of the nucleons individually and cannot be described without applying the quantum mechanical approach. This also affects the binding energy of the nucleus. Therefore, the HFB method has been considered in Section 2.2. It involves solving the many-body problem by finding approximate solutions in a set of Slater determinants, taking into account particle-hole and particle-particle interactions. To account for pair correlations, a BCS approximation has been described that simplifies the HFB method by solving the Hartree-Fock equations separately and including pair correlations, which is well suited when the effective interaction potential poorly describes the particle-particle channel. Their complete accounting leads to a high accuracy in the description of the internal structure of the nucleus. However, these approaches face computational difficulties associated with a large volume of calculations, which limits their range of applications.

To overcome these limitations, in the chapter emphasizes the relevance of the macroscopic-microscopic method in Section 2.3, which combines elements of both approaches. This method, which appeared in the mid-1960s, allows studies of nuclear fission on a larger scale and is still considered a very valuable tool in this field.

Chapter 3

Surface parametrization and hydrodynamic properties of atomic nuclei

3.1 Nuclear shape parametrization

Having discussed general methods of describing the properties of nuclei in a macroscopic-microscopic approach, it is necessary to consider in detail the choice of parametrization of the nuclear shape. As shown earlier, parameterization helps to understand the structure of nuclei, which affects their properties. Briefly, nuclear shape parameterization involves describing nuclei as a set of points in space, as well as their motion through time. There are a large number of nuclear shape parametrisations, each with its own advantages and disadvantages. This paper introduces three of the most common types: the Cassini ovaloids, the Trentalange-Koonin-Sierke, and the Funny-Hills methods. In addition to these, the Fourier parametrization developed by the research group of which the co-author is a member is considered in detail in the argumentation. This parametrization is quite fresh and innovative, so a considerable part will be devoted to its characteristics and properties.

The main goal of the shape definition in cylindrical coordinates is its simplicity and the relatively small number of physically relevant deformation degrees of freedom that need to be included. To accurately describe the nuclear fission process, i.e. to reproduce the extensive fission barriers that occur, for example, in some actinide nuclei, one must include a substantial number of octupole, hexadecapole, and higher-multipolarity deformation parameters, up to β_{14}. This is theoretically possible, but in practice it is not very convenient in terms of computational time, even for high performance clusters. Specifically, for each deformation degree of freedom, a grid of at least 20 points must be constructed. For a four-dimensional deformation space, the total number of points is $N_g = 20^4 = 1.6 \times 10^5$ grid points, and for a five-dimensional space, $N_g = 3.2 \times 10^6$ points. At each of these points, the set of single-particle states for a given nucleus must be determined. Then we can proceed to the evaluation of the total macroscopic-microscopic energy.

One of the fundamental problems in nuclear structure is the adequate description of nuclear shapes. Indeed, in the study of heavy ion reactions, fusion, fission, nuclear rotations and collective oscillations, the nuclear deformation energy landscape plays a predominant role. It is then obvious that the parameterization of the nuclear shape must be both simple (involving only a few relevant collective parameters) and flexible, i.e. it must allow a reliable description of the large variety of the above phenomena. A very successful description of the nuclear surface, known as the ”Funny Hills” nuclear surface parametrization, was proposed

in Ref [66]. This formula has been the reference for more than 50 years. In this Chapter, a slightly modified version (see [67] and subsection 3.1.4) is presented which describes the nuclear shape in cylindrical coordinates.

3.1.1 Calculations based on shape parameterizations

By far the most common shape of energy surfaces has been calculated using the macroscopic-microscopic approach. To do this, one must first define a class of shapes that is believed to contain the true fission path. As a natural choice, the multipole expansion is used to represent smooth and compact shapes, especially those close to the ground state shape. However, for highly constricted shapes, points on the surface that are not near the origin (often called star points) cannot be represented correctly. Even for the most compact saddle point of the lighter actinides in the liquid-drop model, more than 14 multipoles are required to achieve convergence [36]. Thus, to be economically efficient, new shape parameterizations have been proposed.

A one-parameter family of shapes was first introduced by Hill and Wheeler [32], which they presented as a sequence of saddle-point shapes (Fig. 3.1) in the liquid-drop model, as a function of the fissility x (mentioned in 2.1.2) and its "deformation" parameter $y = 1 - x$, now known as the y family of shapes.

In addition, many other shape classes have been introduced and their suitability is often tested by their ability to accurately describe fission saddle points with a few deformation parameters. However, it is important to note that mass and friction can greatly influence the results of a cleavage path and may not always cross the fission barrier. As a result, there is no exact mapping from one shape class to another, as can be seen by plotting the first two "important" shape parameters against the same two parameters in another shape class, although this may seem possible for a small fraction of the shape variables. For more information on this topic, see the book by Hasse and Myers [68] as also book by Krappe and Pomorski [46].

3.1.2 Nilsson's parametrization

One of the popular parameterizations was that first used in [69], where the oscillator potential is represented as

$$V_{osc}(\rho, z) = \frac{1}{2} M \left(\omega_{\perp}^2 \rho^2 + \omega_z^2 z^2 \right) \tag{3.1}$$

Thus the equipotential surfaces labeled by the constant $\mathring{\omega}_0$ are given by

$$\rho_s^2 \omega_{\perp}^2 + z^2 \omega_z^2 = R_0^2 \, \mathring{\omega}_0^2 \tag{3.2}$$

where the half-axes of the spheroid have the form

$$\begin{aligned} a &= R_0 \frac{\omega_0}{\omega_{\perp}} \\ c &= R_0 \frac{\omega_0}{\omega_z}. \end{aligned} \tag{3.3}$$

By replacing the deformation parameters $\omega_z, \omega_{\perp}$ by ε, $\omega_0(\varepsilon)$, defined as

$$\begin{aligned} \omega_z &= \omega(\varepsilon) \left(1 - \frac{2}{3} \varepsilon \right) \\ \omega_{\perp} &= \omega(\varepsilon) \left(1 + \frac{1}{3} \varepsilon \right) \end{aligned} \tag{3.4}$$

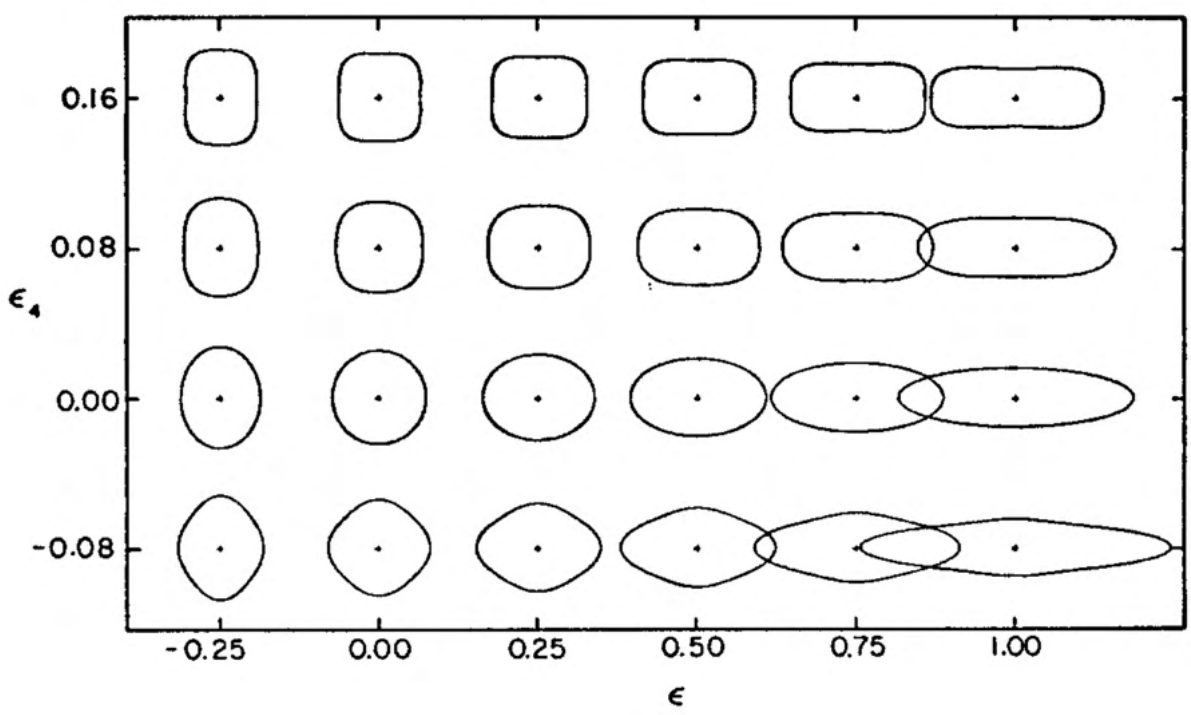

Figure 3.1: Shapes in the Nilsson $\{\varepsilon_2, \varepsilon_4\}$-parameterization, taken from Ref. Ref> [70].

and using the conservation of volume $\omega_\perp^2 \omega_z = \omega_0^3$ it is not difficult to show that

$$\frac{\omega(\varepsilon)}{\omega_0} = \left[1 - \frac{\varepsilon^2}{3} - \frac{2\varepsilon^3}{27}\right]^{-1/3},$$

Then the transformation into the so-called stretched cylindrical coordinates $\{\rho_t, z_t\}$.

$$\begin{aligned} \rho_t &= \rho\sqrt{M\omega_\perp/\hbar} \\ z_t &= z\sqrt{M\omega_z/\hbar} \end{aligned} \tag{3.5}$$

and the corresponding stretched polar coordinates (r_t, θ_t).

$$r_t^2 = \rho_t^2 + z_t^2, \qquad \cos\theta_t = z_t/r_t, \tag{3.6}$$

The potential (3.1) takes a simple one-dimensional form

$$V_{osc}(\rho_t, z_t) = \frac{\hbar}{2}\left(\rho_t^2\omega_\perp + z_t^2\omega_t\right) = \frac{\hbar}{2}\omega_0(\varepsilon) r_t^2 \left(1 - \frac{2}{3}\varepsilon P_2(\cos\theta_t)\right) \tag{3.7}$$

where $P_2(\cos\theta_t)$ is the second order Legendre polynomial.

Later this parameterization was extended to the multidimensional case, where in addition to the spheroidal form parameter $\varepsilon(\varepsilon_2)$ an expansion by additional parameters $\varepsilon_3, \ldots, \varepsilon_N$ was introduced (for details see [68, 70]). Figure 3.1 shows an example of the representation of $\{\varepsilon_2, \varepsilon_4\}$-coordinates.

3.1.3 Cassinian ovaloids shapes and its extension

The Cassini ovaloid method is the simplest way to describe a nucleus. It describes the nucleus as an ellipse or oval with two foci at the center of the nucleus. The parameters used

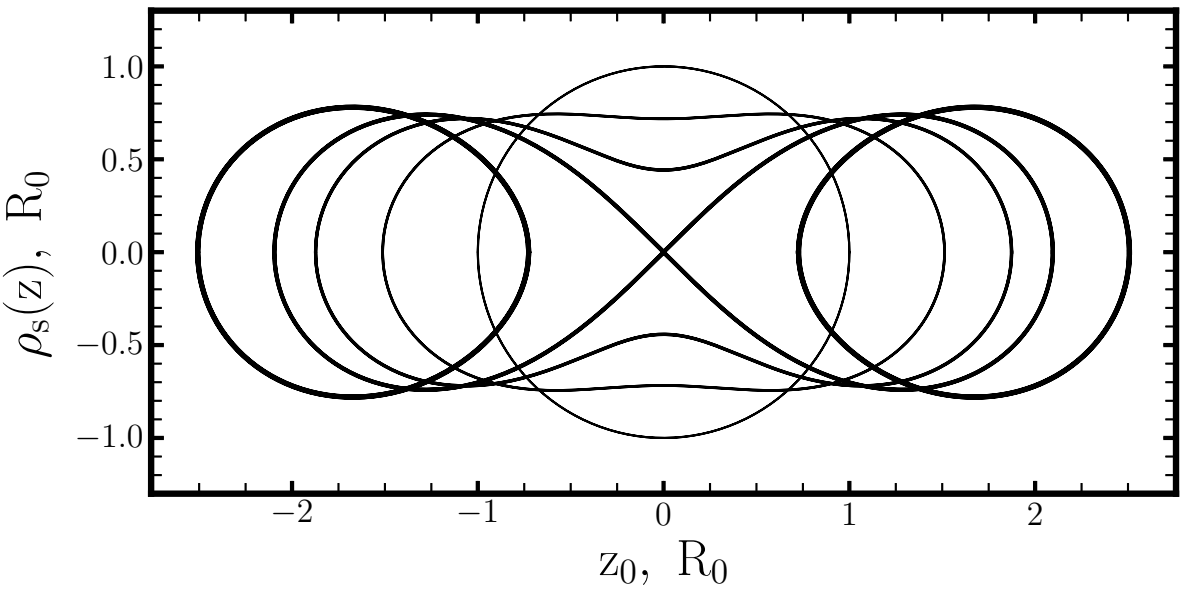

Figure 3.2: Symmetric nuclear shapes in the representation of Cassini ovaloids parametrization for u^4 in set [0, 0.4, 0.8, 1, 1.4]

to describe this ellipse are the semi-major axis, the semi-minor axis, and the eccentricity, which is often used to describe prolate spheroidal nuclei, which have a longer semi-major axis than the semi-minor axis. The advantage of this method is that it is easy to calculate and understand. However, it does not provide an accurate description of nuclei that are not prolate spheroidal.

A one-parameter parametrization covering the spherical, constricted, split, and separated forms is the family of Cassinian ovaloids [Stavinsky 68]

$$\rho_s^2 = \sqrt{a^4 + 4c^2z^2} - \left(c^2 + z^2\right). \tag{3.8}$$

With usage of representation $u = c/a$ the value a is eliminated by volume conservation

$$4\left(\frac{R_0}{a}\right)^3 = \begin{cases} \sqrt{1+u^2}\,(1-2u^2) + \frac{3}{2u}\,\mathrm{arsinh}\left(2u\sqrt{1+u^2}\right) & ,u \le 1 \\ \frac{3}{2u}\,\mathrm{arsinh}\left[u\cdot((2u^2-1)\sqrt{1+u^2} - (2u^2+1)\sqrt{u^2-1})\right] & ,u \ge 1 \end{cases}$$

Examples of the shapes in the Cassini parametrization are shown in Fig. 3.2.

To represent the mass asymmetry of the Cassini ovaloids, an additional parameter ε is introduced [71] into the (3.8) equation:

$$\rho_s^2 = \sqrt{a^4 + 4c^2z^2} - \left(c^2 - \varepsilon^2 + z^2\right) \tag{3.9}$$

On the other hand, another extension of the shape class was proposed in [72], where Cassini's oval coordinates are considered as a system of orthogonal, curvilinear coordinates (R, x), in terms of which the cylinder coordinates (ρ, z) are given by

$$\begin{aligned} \rho_s(R,x) &= \frac{1}{\sqrt{2}}\left\{p_s(R,x) - R^2\left(2x^2-1\right) - c^2\right\}^{1/2} \\ z(R,x) &= \frac{\mathrm{sign}(x)}{\sqrt{2}}\left\{p_s(R,x) + R^2\left(2x^2-1\right) + c^2\right\}^{1/2} \end{aligned} \tag{3.10}$$

where $p_s^2(R,x) = R^4 + 2c^2R^2(2x^2-1) + c^4$. In case $R = a = const$, x is eliminated and this profile ρ can be derived (3.8).

The extension of the deformation class of the shape profile is achieved by representing R as a decomposition

$$R = R(x) = R_0 \left(1 + \sum_l \alpha_l P_l(x)\right) \tag{3.11}$$

on Legendre polynomials $P_l(x)$ with additional deformation parameters α_l and should be substituted in (3.10). Moreover, the α_l was introduced in the paper [72] instead of a deformation parameter α (similar to ε in (3.9)), implicitly defined as

$$\begin{aligned} u^2 = \frac{\alpha - 1}{4} \left\{ \left(1 + \sum_l \alpha_l\right)^2 + \left(1 + \sum_l (-1)^l \alpha_l\right)^2 \right\} \\ + \frac{\alpha + 1}{2} \left\{ 1 + \sum_l (-1)^l \frac{(2l-1)!!}{2^l l!} \alpha_{2l} \right\}^2 . \end{aligned} \tag{3.12}$$

From this relationship, we can see that α would be equal to u^2 if $\alpha_l = 0$, and also that the set α inherits the vanishing neck property at 1.

This method gives a fairly good description of the fission valley in the liquid-drop model compared to the constrained, self-consistent calculation.

3.1.4 Generalized spheroids

A quartic type of nuclear surface profile description

$$\rho_s^2 = az^4 + bz^2 + c, \tag{3.13}$$

was first used by Lawrence [73] to describe spherical, spheroidal, compressed, dissected, and split shapes. The parameters a, b, c are determined by the requirement of volume conservation.

However, such a simple formula cannot describe asymmetric surfaces. Therefore, proposed [74] a more convenient method generalizing to asymmetric shapes, which has the form

$$rho_s^2 = R_0^3 \lambda \left[z_0^2 - (z + z_{sh})^2\right] \left[z_2 \left|z_2\right| + (z + z_{sh} - z_1)^2\right]. \tag{3.14}$$

Here z_0 is the half length, z_2 is a constriction parameter, z_1 is the asymmetry parameter, i.e. with $z_1 = 0$ the shapes are symmetric. To ensure volume preservation, the parameter λ is determined as a function of the other parameters

$$\lambda^{-1} = \begin{cases} z_0^3 \left(\frac{1}{5} z_0^2 + z_1^2 + z_2^2\right) & , z_2 \geq 0 \\ z_0^3 \left(\frac{1}{5} z_0^2 + z_1^2 - z_2^2\right) + z_2^3 \left(\frac{1}{5} z_2^2 + z_1^2 - z_0^2\right) & , z_2 \leq 0 \end{cases} \tag{3.15}$$

The quantity z_{sh} is the shift of the coordinate $z-$, which makes sure that the center of mass of the nucleus remains at $z = 0$. Thus, using the conservation of the center of mass

$$z_{cm} = \frac{2\pi \int \rho_s^2(z) z \, dz}{2\pi \int \rho_s^2(z) \, dz} = 0, \tag{3.16}$$

the following value can be derived by means of the relation

$$-z_{sh} = \begin{cases} \frac{2}{5} \lambda z_1 z_0^5 & , z_2 \geq 0 \\ \lambda z_1 \left[\frac{2}{5} z_0^2 + z_2^3 \left(z_0^2 - z_1^2 - \frac{3}{5} z_2^2\right)\right] & , z_0 \leq 0 \end{cases} \tag{3.17}$$

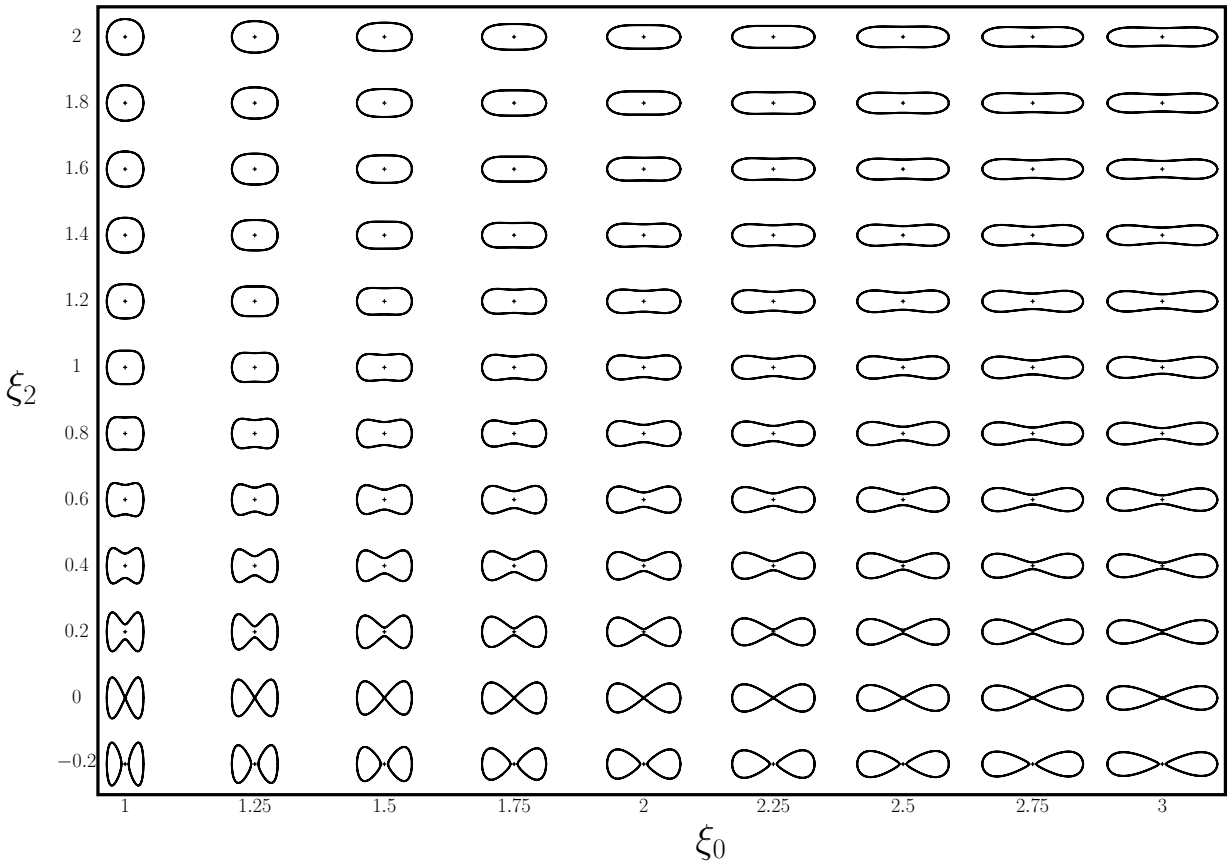

Figure 3.3: Symmetric nuclear shapes in the representation proposed by Hasse (3.19)

Also in Ref. [75] dimensionless parameters remind of ε parameterization (3.4) Nilsson:

$$\zeta_i = z_i/R_0, i = 0, 1, 2, s \tag{3.18}$$

Thus, for connected symmetric forms ($\zeta_1 = 0, \zeta_2 \geq 0$), the geometric quantities can be rewritten in dimensionless coordinates in compact form:

$$\lambda^{-1} = \zeta_0^3 \left(\frac{1}{5}\zeta_0^2 + \zeta_2^2\right) \tag{3.19}$$

$$\rho_n = \zeta_2 \left[\zeta_0 \left(\frac{1}{5}\zeta_0^2 + \zeta_2^2\right)\right]^{-1/2} = \zeta_0\zeta_2\sqrt{\lambda} \tag{3.20}$$

Figure 3.3 shows the surface variations for symmetric fission constructed using the parameterization (3.19). Note that the fission configuration is not given by two tangent spheres.

Funny-Hills

A new step in modifying the quadratic shape class (3.13), called Funny–Hills (FH), was introduced by Brack et al. [66] to improve the description of deformed ground-state shapes.

$$\rho_s^2(u) = R_0^2 c^2 \left(1 - u^2\right)\left(A + \alpha u + Bu^2\right), \tag{3.21}$$

with the dimensionless coordinate u defined as

$$u = \frac{z - z_{sh}}{z_0} \tag{3.22}$$

where $z_0 = cR_0$, so the parameter c measures the elongation of the nucleus in units of the radius R_0 of the corresponding spherical nucleus of the same volume. From (3.21) it can be seen that A is responsible for the elongation of the shape, the parameter B for the formation of the neck, and α for the left-right asymmetry of the mass.

Thus, this parameter could be obtained from the volume conservation condition:

$$c = \left(A + \frac{1}{5}B\right)^{-1/3}. \tag{3.23}$$

The coordinate z_{sh} is determined from the same to (3.16) condition, which yields

$$z_{sh} = -\frac{1}{5}\alpha c^3 \, z_0. \tag{3.24}$$

To simplify the FH parameterization, the core shapes are usually defined in terms of the stretch c and neck h parameters, which can be expressed using the hexadecapole deformation parameter B by the relation

$$B = 2h + \frac{1}{2}(c-1)\,. \tag{3.25}$$

The parameter A can be easily evaluated from the volume conservation condition and is equal to

$$A = \frac{1}{c^3} - \frac{1}{10}(c-1) - \frac{2}{5}h\,. \tag{3.26}$$

In order to avoid non-physical forms (three-body) for certain z values where $\rho_s^2 < 0$ for certain combinations of $\{c, h, \alpha\}$ parameters, in particular for small nuclear elongations, and in addition to be able to better describe diamond-like forms preferred in particular by nuclear ground states in the actinide range, an alternative analytical form was proposed [66] for negative values of the parameter B, namely

$$\rho_s^2(u) = \begin{cases} R_0^2 c^2 \ (1-u^2)\,(A + \alpha u + Bu^2)\,, & B \geq 0 \\ R_0^2 c^2 \ (1-u^2)\ (A+\alpha u)\ e^{Bc^3u^2}, & B < 0 \end{cases} \tag{3.27}$$

Trentalange–Koonin–Sierk parametrization

Further extension of the shape class following the idea of Ref. [76], which generalizes the FH parameterization (3.27) by expanding the axially symmetric shape of the fission nucleus into a series of Legendre polynomials P_n:

$$\rho_s^2(z) = R_0^2 \sum_{n=0,2,4,\ldots}^{\infty} \alpha_n P_n\left(\frac{z - z_{sh}}{z_0}\right), \tag{3.28}$$

where P_n are n-order Legendre polynomials. The values R_0, z_0 and z_{sh} are defined in the same way as in the Funny Hills parameterization. Note that the quantity z_{sh} is zero only if all odd deformation parameters are α_n. The boundary condition $\rho_s(z_{min}) = \rho_s(z_{max}) = 0$ implies the following relations:

$$\begin{aligned} \sum_{n=0}^{\infty} a_n P_n(-1) = \ & \sum_{n=0}^{\infty} (-1)^n \alpha_n = 0 \\ \sum_{n=0}^{\infty} a_n P_n(1) = \ & \sum_{n=0}^{\infty} \alpha_n = 0 \end{aligned} \tag{3.29}$$

So the parameters α_0 and α_1 can be easily evaluated from the above equations:

$$\alpha_0 = -\sum_{n=2,4,}^{\infty} \alpha_n \,, \quad \alpha_1 = -\sum_{n=3,5,}^{\infty} \alpha_n \,. \tag{3.30}$$

Note that the spherical nucleus shape corresponds to $\alpha_2 = \alpha_0 = -\frac{2}{3}$, oblate forms to $\alpha_2 < -\frac{2}{3}$, and prolate forms to $-\frac{2}{3} > \alpha_2 < 0$. When α_2 tends to zero, the nucleus becomes infinitely long.

The volume conservation condition gives the following relation

$$z_0 = \frac{2}{3}\frac{R_0}{\alpha_0} \,, \tag{3.31}$$

where $z_0 = (z_{max} - z_{min})/2$ is the half length of the deformed core. Thus, the strain parameter c used in the Funny Hills parameterization can be described as

$$c = z_0/R_0 = \frac{2}{0} \,. \tag{3.32}$$

In the presence of odd multipolar deformations it is necessary to introduce an additional condition that fixes the position of the center of mass of the deformed nucleus at the origin of the coordinate system. The above relation allows to evaluate the value of the coordinate z_{sh} as

$$z_{sh} = -\frac{1}{3}\frac{\alpha_1}{\alpha_0} z_0 = \frac{2}{9}\frac{\alpha_1}{\alpha_0^2} R_0 \,. \tag{3.33}$$

It should also be noted that (3.28) cannot describe shapes with non-axial symmetry. To overcome this disadvantage, Sierk extended [38] TKS parametrization with the approach

$$\rho(z,\phi) = \rho^{(0)}(z)\eta(\phi)/\lambda \tag{3.34}$$

with $\eta(\phi) = 1 + \alpha_1 P_2(\cos\phi) + \alpha_2 P_4(\cos\phi)$ and $\lambda = 1 + \alpha_1/4 + 9\alpha_2/64$ with respect to two additional deformation parameters α_1 and α_2.

Modified Funny–Hills parametrizations

There is a problem of obtaining negative roots $\rho_s^2(z)$ between the boundary points z_{min} and z_{max} despite the widespread use of very efficient FH and TKS parameterizations given by eqs. (3.21) and (3.28). A modification of the FH parameterization proposed in [77], where the surface of the axially symmetric nucleus is given by the following equation, is a successful attempt to eliminate this problem:

$$\rho_s^2(z) = \frac{R_0^2}{c\, f(a,B)} (1-u^2)\,(1 + \alpha u - B\, e^{-a^2u^2}) \tag{3.35}$$

The values of z_0 and u are defined as in the previous parameterizations, and the function

$$f(a,B) = 1 - \frac{3\,B}{4\,a^2}\left[e^{-a^2} + \sqrt{\pi}(a - \frac{1}{2a})\,\mathrm{Erf}(a)\right] \tag{3.36}$$

keeps the volume of the deformed nucleus.

The physical meaning of the deformation parameters contained in the equation (3.35) is similar to the one discussed in the subsection (3.1.4). The neck width parameter a, which is obtained by minimizing the energy of the liquid droplet along the fission paths,

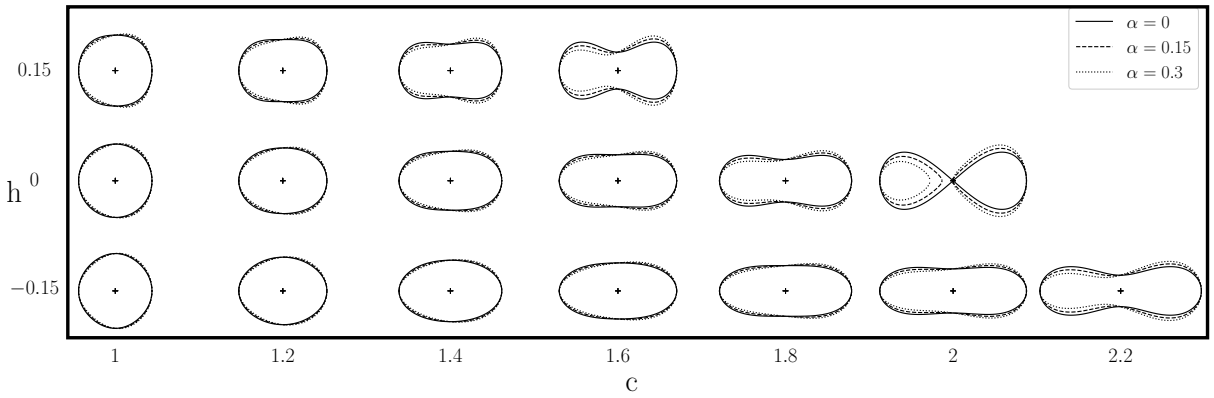

Figure 3.4: Nuclear shapes in the modified Funny-Hills $\{c, h, \alpha\}$ rendering

usually has a value of $a = 1$. A detailed study of the effect of the parameters can be found in [67].

In a similar way [66], it is more convenient to introduce a linear combination of c and B.

$$h = \frac{1}{2}[B - (c - 1)] \tag{3.37}$$

as the neck parameter. Note that the parameters B and h do not directly correspond to the parameters (3.25), but have a similar physical meaning.

The shift coordinate z_{sh} is obtained from an equation similar (3.16), and equals

$$z_{sh} = -\frac{4}{15}\frac{\alpha\, z_0}{f(a,b)}\ , \tag{3.38}$$

where the Eq. (3.36) gives the normalization factor $f(a, B)$.

An important achievement of the modification (3.35) is the better description of *rhomboid* shapes, in contrast to the original FH parametrization. Another advantage of the parametrization is that it does not allow non-physical three-body configurations, i.e. forms where $\rho_s^2(z) < 0$, which might appear in eqs. (3.21) and (3.27).

The scission point defined by $z_{sc} = 0$ is reached here at $B = 1$ for a symmetric ($\alpha = 0$) shape. For asymmetric ($\alpha \neq 0$) shapes

$$B \approx 1 - \frac{\alpha^2}{4\,a^2} \quad \text{at} \quad u_{sc} \approx -\frac{\alpha}{2\,B_{sc}} \tag{3.39}$$

To describe non-axial shapes, the profile function, Eq. (3.35), is dominated by:

$$\varrho_s^2(z,\varphi) = \rho_s^2(z) f(\eta,\varphi) = \frac{1-\eta^2}{1+\eta^2+2\eta\cos(2\varphi)}, \tag{3.40}$$

where φ is defined as usual in cylindrical coordinates (see Fig. 3.5). This leaves four independent, dimensionless deformation parameters: c, h, α, and η. The non-axial symmetry parameter η is the relative difference of the cross-sectional semi-axes perpendicular to the assumed ellipsoidal symmetry axis.

$$\eta = \frac{b-a}{b+a}, \tag{3.41}$$

where volume conservation for the non-axially deformed nucleus is ensured by the condition $ab = \rho_s^2$. This definition, together with the expressions for the half-axis of the nucleus

$$a(z) = \rho_s(z)\sqrt{\frac{1-\eta}{1+\eta}} \text{and} b(z) = \rho_s(z)\sqrt{\frac{1+\eta}{1-\eta}} \tag{3.42}$$

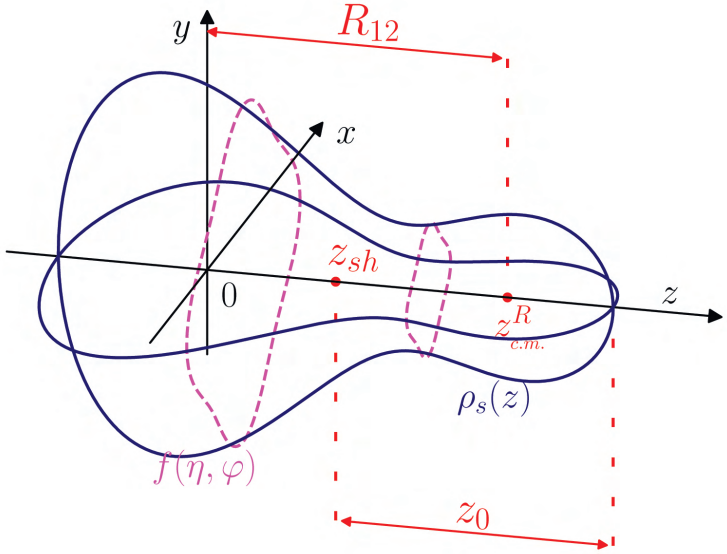

Figure 3.5: Example of elongated non-axial shape in representation (3.42) modified Funny-Hills

shows that η is independent of z. This formula can be generalized to η dependent on z and non-ellipsoidal cross sections, which may lead to more energetically favorable configurations as fragment separation approaches.

3.1.5 Fourier series expansion

As shown in the previous subsections, several approaches to the parameterization of the nuclear surface shape have been developed over the last 55 years. In general, the quadratic approaches, such as Funny-Hills or Cassini, and the polynomial decomposition, such as TKS, have proven to be well established in the micro-macro approach. However, they all have advantages and disadvantages that limit their applicability in one way or another.

Recently [40], another approach has been proposed that allows to cover many shapes and overcomes the limitations of the previous methods. In addition, it has fast convergence, is easy to use, and has approximately the same set of parameters needed to describe surface profiles.

In cylindrical coordinates, the profile function $\rho_s(z)$ of the core shape is expanded in a Fourier series:

$$\rho_s^2(z) = R_0^2 \sum_{n=1}^{\infty} \left[a_{2n} \cos\left(\frac{(2n-1)\pi}{2} \frac{z - z_{sh}}{z_0} \right) + a_{2n+1} \sin\left(\frac{2n\pi}{2} \frac{z - z_{sh}}{z_0} \right) \right], \tag{3.43}$$

Analogous to the Funny Hills parameterizations in 3.1.4, the length of the nucleus is given by $2z_0 = 2cR_0$ and can be obtained from the conservation of volume:

$$\frac{\pi}{3c} = \sum_{n=1}^{\infty} (-1)^{n-1} \frac{a_{2n}}{2n-1}. \tag{3.44}$$

where the coefficients a_2, a_3, a_4 describe quadrupole, octupole, and hexadecapole deformations, respectively. Thus, the Fourier parametrization has fully inherited the physical meaning of the stretch parameter c, which at 1 gives shapes close to spherical and at less (greater) than 1 oblate (stretched) configurations.

Table 3.1: Values of Fourier expansion coefficients for a spherical shape.

$2n$	2	4	6	8	10
a_{2n}^0	1.03205	−0.03822	0.00826	−0.00301	0.00142

Imposing the condition (3.16), after evaluation, one obtains the following expression:

$$z_{sh} = -\frac{z_0}{2}\frac{\sum_n (-1)^{n-1}\frac{a_{2n+1}}{n}}{\sum_n (-1)^{n-1}\frac{a_{2n}}{2n-1}} = \frac{3c^2}{2\pi}R_0\sum_n (-1)^n\frac{a_{2n+1}}{n} \tag{3.45}$$

An additional feature of this type of parameterization is the easy determination of the distance between centers of mass of the pre-fragments, which can be calculated analytically. For example, for symmetrical shapes it has the simple form:

$$R_{12} = 2R_0 c\left[1 - \frac{6}{\pi^2}c\sum_{n=1}\frac{a_{2n}}{(2n-1)^2}\right] \tag{3.46}$$

The main advantage of Fourier parametrization, however, is the ability to adjust the desired accuracy of the parametrization by adding or subtracting terms a_n to the series (3.43). To do this, let us proceed with the following analysis of the convergence properties of the parametrization. Suppose there is a given surface ρ_x. Then the shape coefficients a_n can be determined by a Fourier analysis [40], taking advantage of the orthogonality relations of the trigonometric functions, leading to

$$a_{2n} = \int_{-1}^{1}\rho_s^2(u)\cos\left(\frac{2n-1}{2}\pi u\right)du, \tag{3.47}$$

$$a_{2n+1} = \int_{-1}^{1}\rho_s^2(u)\sin(n\pi u)du, \tag{3.48}$$

where u is the dimensionless variable defined in (3.22).
The trivial case can be obtained for a spherical curve, i.e. when a_{2n+1}^0 values of a_{2n}^0 are given in Table 3.1 and will be needed later. It can be seen that the series converges quickly, since the coefficient of a_6^0 is much smaller than a_2^0, and the higher terms fade smoothly. But lets return to the case of an arbitrary curve, which can be observed in Fig. 3.6. The surface profile ρ_x is given in the Funny–Hills parameterization with parameters $c = 2$ and $\alpha = 0.43$, that is a long asymmetric system configuration. In addition, the curve ρ_s^2 and contributions of different orders, whose amplitude is calculated according to Eqs. (3.47), are shown. One can easily see that the behavior of the contributions is close to the spherical case except for a_4. It is also possible to notice the meaning of the presented components. The lowest-order factor a_2 determines elongation, and the next, a_4, the formation of the neck. The addition of the term a_3 generates left-right asymmetry, over which the inclusion of the next odd parameter a_5 generates only minor distortions. As has been shown, the shape changes introduced by higher orders (even or odd) are mostly small or negligible. However, mentioned amplitudes not the optimal for using as deformation coordinates.

Now one can check the accuracy of the parameterization with a limited number of coefficients by considering the configurations of the saddle points of the liquid-drop model. Figure 3.7 shows the deformation energy calculated within the LSD model for ^{232}Th as a function of the elongation variable R_{12} in units of R_0. It can be seen that when a_6 is included in addition to a_2 and a_4, the height of the macroscopic fission barrier B_f^{LSD} decreases by about ≈ 100 keV. Naturally, the addition of higher order terms reduces B_f^{LSD}

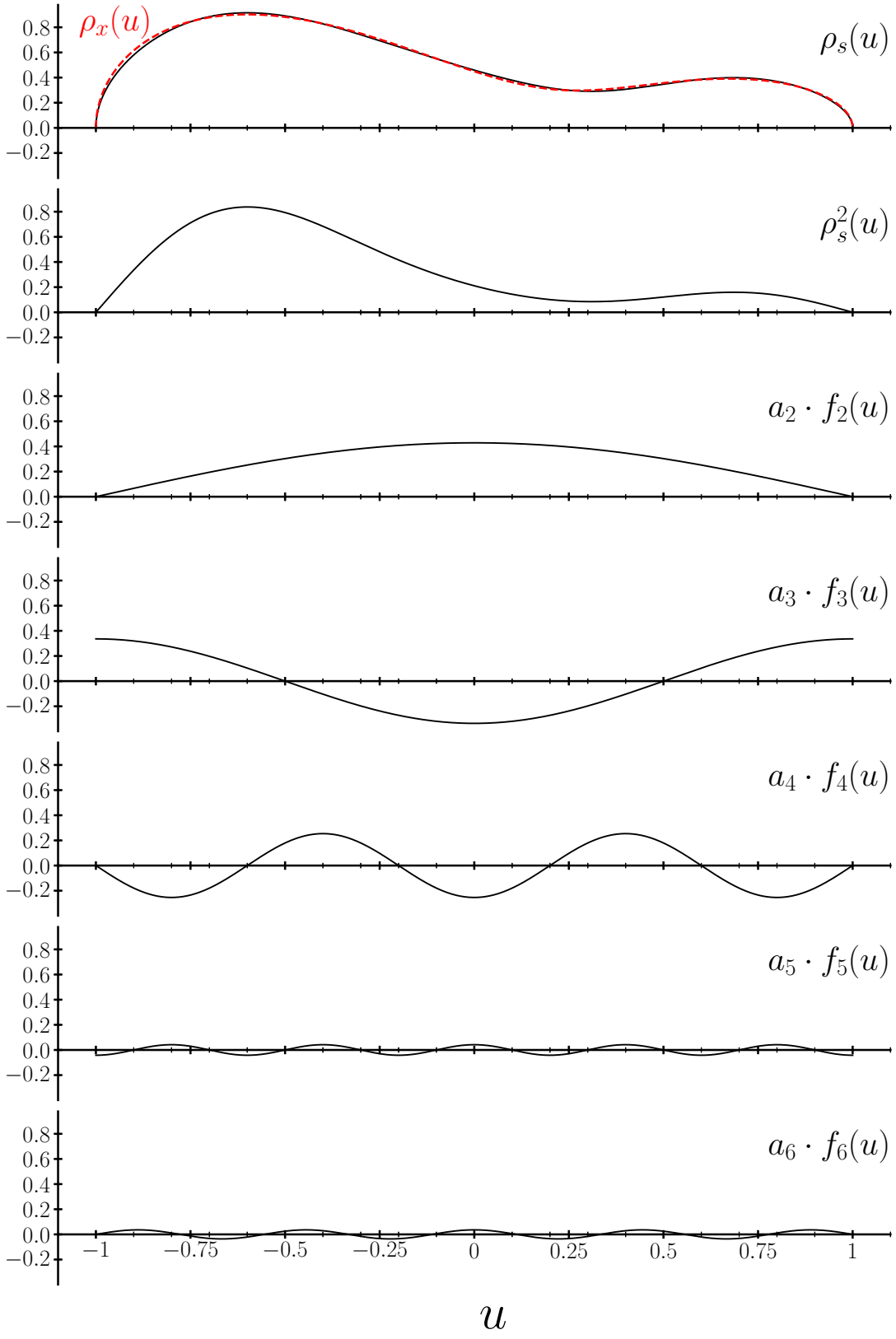

Figure 3.6: The contributions to the shape function $\rho_s^2(u)$ (3.43), of different orders of a_n Fourier series for the non-axial left-right asymmetric form. As profile $\rho_x^2(u)$ were taken elongated non-axial shape described by MFH (3.42)

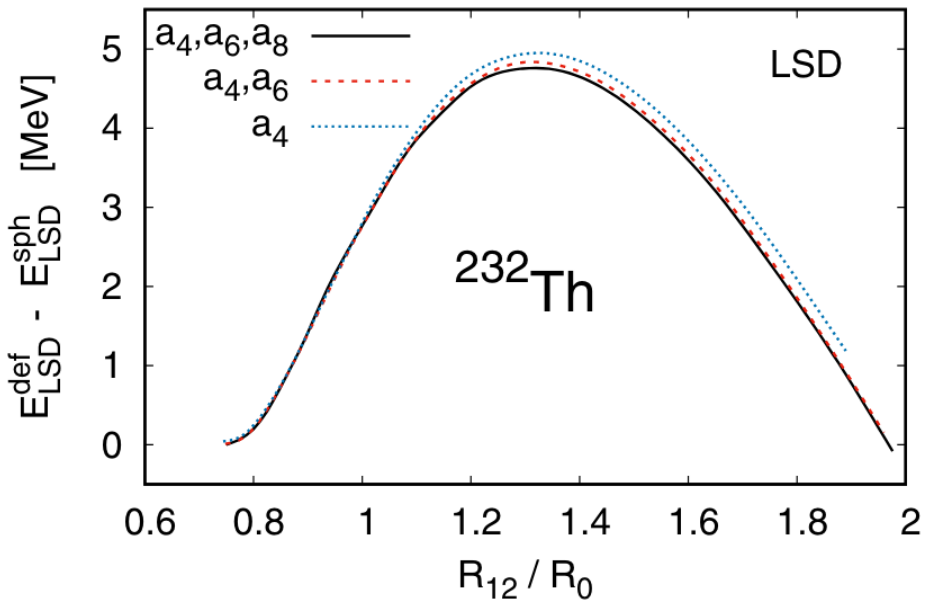

Figure 3.7: LSD deformation energy relative to the spherical ground state as a function of R_{12} for ^{232}Th with the Fourier series limited up to a_4 (blue dotted), a_6 (red dashed), and a_8 (black full line) taken from Ref. [40].

by a few tens more keV, but this will have very little effect when using the Langevin approach, where the temperature has a value $\gtrsim 200$ keV.

However, in the decomposition (3.43), the coefficients a_n are not physical deformation parameters yet, which can be denoted as "collective" coordinates q_n. In the original paper [40] the authors have shown that there is a specific linear combinations transformation of the original a_n amplitudes to the physical deformation parameters q_n, which has the following form:

$$\begin{aligned} q_2 &= a_2^0/a_2 - a_2/a_2^0, \\ q_3 &= a_3, \\ q_4 &= a_4 + \sqrt{(q_2/9)^2 + (a_4^0)^2}, \\ q_5 &= a_5 - (q_2 - 2)\cdot a_3/10, \\ q_6 &= a_6 - \sqrt{(q_2/100)^2 + (a_6^0)^2}, \end{aligned} \tag{3.49}$$

This representation helps to better understand the meaning of this parameterization. Thus, the coordinate q_2 is directly related to the elongation of the system, the coordinate q_3 is also strictly associated with the left-right asymmetry, q_4 for the formation of the system neck and the first "perturbation" by elongation, when the odd q_5 by the asymmetry a_3, q_6 and q_7 already in the second order, etc. Of course, one should keep in mind that there is an additional coordinate η which determines the neosymmetry profile function $\varrho(\eta)$ of the compound nucleus. But fortunately, the function $f(\eta, \varphi)$ (3.40), presented earlier for the modernized Funny-Hills, also perfectly fits into the Fourier parameterization. This convenience also expresses itself in a very efficient representation of the potential energy in the deformation space, for describing the fission process. As shown in [40] the coordinates q_5, q_6 and higher order are set to zero. This allows one to analytically parameterize higher-order coefficients through lower-order coefficients and gives a significant simplification of the analysis of multidimensional surfaces, without losing precision in the definition of PES. On the other hand, a similiar rhetoric also applies for the degree of freedom of non-axiality, which is known [41, 78] to have an effect on the PES for fission barriers, varying its height

by a value of the order of 0.5–1 MeV. However, due to the detailed study of the fission process after it overcomes the barrier and goes to fission, such a property in the actinide region allows, in the first approximation, to neglect its influence.

Therefore, using the Fourier parameterization within reasonably high accuracy makes it possible to quickly describe all possible forms of the fissile nucleus and its related characteristics by only three variables related to elongation, left-right asymmetry, and neck thickness, which will be used in the following section and chapter.

Here is a diagram for a better understanding of the meaning of the parameterization. Thus, the coordinate q_2 is directly related to the elongation of the system, the coordinate q_3 is also strictly related to the left-right asymmetry, q_4 for the formation of the system neck and the first "perturbation" by elongation, while the odd q_5 by the asymmetry a_3, q_6 and q_7 already in the second order, and so on. Of course, one should keep in mind that there is an additional coordinate η which determines the neosymmetry profile function $\varrho(\eta)$ of the compound nucleus. Fortunately, the function $f(\eta, \varphi)$ (3.40) presented earlier for the modernized Funny Hills also fits perfectly into the Fourier parameterization. This convenience is also reflected in a very efficient representation of the potential energy in the deformation space for describing the fission process. The coordinates q_5, q_6 and higher are set to zero as shown in [40]. This allows the analytic parameterization of higher order coefficients by lower order coefficients and gives a significant simplification of the analysis of multidimensional surfaces without loss of precision in the definition of PES. On the other hand, a similar rhetoric also applies to the degree of freedom of non-axiality, which is known to have an effect on the PES for fission barriers, varying its height by a value of the order of 0.5 – 1 MeV. However, due to the detailed study of the fission process after it has crossed the barrier and proceeded to fission, such a property in the actinide region allows its influence to be neglected to a first approximation.

Therefore, using the Fourier parametrization with reasonably high accuracy, it is possible to quickly describe all possible forms of the fissile nucleus and its related properties by only three variables related to elongation, left-right asymmetry and neck thickness. These variables will be used in the following section and chapter.

3.2 Hydrodynamical description of nuclear properties

As shown in 2.1, the representation of the nucleus as a liquid droplet has an advantage. It is not only about the binding energy, but also about other properties like the inertia tensor or the friction tensor. For example, in the non-adiabatic fission process, the inertial parameters of the nucleus play a crucial role. After a review of the bibliography [46, 67, 79–81], a hydrodynamic model is considered in this subsection, which is based on the work of the Nix or Świątecki theoretical groups and their interpretation by Pomorski group within the modified Funny-Hills or Fourier shape parametrization. The friction tensor, which plays an important role in fission dynamics because it reflects the nature dissipation of energy in fissioning nuclei, is considered here.

3.2.1 Tensor of inertia. Werner–Wheeler approximation.

In the hydrodynamic conception, the non-adiabatic fission process is a consideration of the inertial parameters via the representation of the nucleus as an irrotational, incompressible liquid drop. The kinetic energy can be expressed in terms of the classical velocity

field $\mathbf{v}(\mathbf{r})$ and constant mass density ρ_0.

$$E_{\text{kin}} = \frac{1}{2}\rho_0 \int \mathbf{v}^2(\mathbf{r}) d^3r \tag{3.50}$$

which are written in terms of the collective velocities $\dot{q}_i$ of the generalized coordinates considered in [46]. In this case, the field of an ideal fluid can be obtained from the velocity potential ϕ, which satisfies the Laplace equation with Dirichlet boundary conditions on the surface of the nucleus

$$\begin{cases} \Delta\phi = 0 \\ \partial_n \phi = \dot{n}(\mathbf{r};\mathbf{q}) = \dot{q}^i \partial_{q_i} n(\mathbf{q}), \end{cases} \tag{3.51}$$

where $n(\mathbf{r};\mathbf{q})$ is the displacement field of the boundary in the direction normal to the surface. Obviously, the velocity field has a linear dependence on $\dot{q}^i$, and therefore the kinetic energy could be represented in the classical way

$$E_{\text{kin}} = \frac{1}{2}\mathcal{M}_{ij}\dot{q}^i\dot{q}^j.$$

The lower limit of inertia for the considered hydrodynamic model can then be obtained using Kelvin's theorem [82], where for an ideal fluid the flow field gives the minimum possible kinetic energy related to the given boundary velocities $\dot{\mathbf{q}}$.

Unfortunately, explicit analytical solutions of the boundary problem are known only for quite limited classes of shapes. They are well presented in [82–85]. Therefore, the Werner–Wheeler approximation [79] is often used to calculate the velocity field. For axially symmetric shapes, the velocity has a radial component v_ρ and an axial component v_z. The key idea of the approximation is that v_z is independent of the radial coordinate ρ and thus can be represented by the vector field $a_i(z;\mathbf{q})$.

$$v_z = a_i(z;\mathbf{q})\dot{q}^i \tag{3.52}$$

and that v_ρ is proportional to ρ and can be represented by the second vector field $B_i(z;\mathbf{q})$

$$v_\rho = (\rho/\rho_{\text{s}})\, B_i(z;\mathbf{q})\dot{q}^i \tag{3.53}$$

where $\rho_{\text{surf}}(z;\mathbf{q})$ is the value of ρ on the nuclear surface at position z. Since the velocity field must be sourceless

$$\partial_\rho(\rho v_\rho) + \rho\partial_z v_z = 0,$$

one can obtain

$$B_i = -\frac{1}{2}\rho_{\text{s}}\frac{\partial a_i}{\partial z} \tag{3.54}$$

Substituting this result into Eq. (3.50) we get the following form of the mass tensor

$$\mathcal{M}_{ij} = \pi\rho_0 \int_{z_{\min}}^{z_{\max}} \left(a_i a_j + \frac{1}{8}\rho_{\text{s}}^2 a_i' a_j'\right)\rho_{\text{s}}^2(z;\mathbf{q})dz, \tag{3.55}$$

where $a_i' = \partial_z a_i$. If the center of mass coordinate $z_{\text{c.m.}}$ changes with time in the chosen shape parameterization, the perturbation velocity will be

$$\dot{z}_{\text{c.m.}} = \pi\frac{\rho_0}{M_{\text{total}}}\dot{q}^i\partial_{q_i}\int_{z_{\min}}^{z_{\max}} z\rho_{\text{s}}^2(z;\mathbf{q})dz \tag{3.56}$$

has to be subtracted from v_z in the equation (3.52) before substituting a_i in the equation (3.55).

The Werner–Wheeler approximation implies that a slice of fluid confined between two planes perpendicular to the axis retains its volume and flat surfaces as it moves. In particular, let us define the volumes of

$$V^{+}(z;\mathbf{q}) = \pi \int_{z}^{z_{\max}} \rho_{\mathrm{s}}^{2}\left(z';\mathbf{q}\right) dz' \tag{3.57}$$

and

$$V^{-}(z;\mathbf{q}) = \pi \int_{z_{\min}}^{z} \rho_{\mathrm{s}}^{2}\left(z';\mathbf{q}\right) dz' \tag{3.58}$$

whose full (convective) time derivatives disappear

$$\frac{d}{dt}V^{\pm}(z;\mathbf{q}) = \partial_{z}V^{\pm}\dot{z} + \partial_{q_i}V^{\pm}\dot{q}^{i} = 0. \tag{3.59}$$

Substitute equation (3.56)

$$\dot{z} = \frac{1}{\rho_{\mathrm{surf}}^{2}(z;\mathbf{q})}\dot{q}^{i}\partial_{q_i}\int_{z}^{z_{\max}} \rho_{\mathrm{surf}}^{2}\left(z';\mathbf{q}\right) dz' \tag{3.60}$$

and with Eq. (3.52) an explicit expression for the vector $a_i(z;\mathbf{q})$ could be given in terms of the form function $\rho_{\mathrm{surf}}(z;\mathbf{q})$.

$$a_i(z;\mathbf{q}) = \frac{1}{\rho_{\mathrm{s}}^{2}(z;\mathbf{q})}\partial_{q_i}\int_{z}^{z_{\max}} \rho_{\mathrm{s}}^{2}\left(z';\mathbf{q}\right) dz'. \tag{3.61}$$

A similar result can be obtained with $V^{-}(z;\mathbf{q})$.

The Werner–Wheeler field is incompressible, but in general not irrotational. Therefore, the kinetic energy E_{kin} is not less than the kinetic energy of an ideal fluid. The Werner–Wheeler velocity is irrotational only for spheroidal deformations of arbitrary eccentricity and for quadrupole oscillations of small amplitude [79]. However, it should be emphasized that in some important limiting cases the Werner–Wheeler mass tensor has very desirable properties... It is translationally invariant, it becomes infinite for the degree of freedom asymmetry when the neck radius disappears [86], because the flow between the emerging fragments must disappear in the hydrodynamic model when the neck disappears. This causes the inertia associated with the neck radius ρ_{neck} to approach zero as the neck disappears, resulting in a mass reduction in the distance coordinate $r_{\mathrm{c.m.}}$ between the centers of mass of the post-fission fragments. For non-axial cases, the Werner–Wheeler approximation has been generalized for modified Funny Hills and Fourier parameterizations. Keeping the ansatz (3.52) and introducing components x and y for the velocity field instead of the equation (3.53) in [79], obtained

$$\begin{aligned} v_x &= x\left[\alpha_i(z;\mathbf{q}) + \beta_i(z;\mathbf{q})\right]\dot{q}^{i} \\ v_y &= y\left[\alpha_i(z;\mathbf{q}) - \beta_i(z;\mathbf{q})\right]\dot{q}^{i}. \end{aligned} \tag{3.62}$$

The elimination of the velocity field divergence leads to the equation

$$\alpha_i(z;\mathbf{q}) = -(1/2)\partial_z a_i(z;\mathbf{q})$$

instead of the equation (3.54).

The value β_i follows from the condition that the x and y components of the velocity field at the surface must coincide with the surface velocity expressed by $\dot{\mathbf{q}}$. The condition (3.58)

again defines $A_i(z;\mathbf{q})$ as a function of the surface shape. In Fourier parameterization coordinates definition, the mass tensor has the form

$$a_i(z;\mathbf{q}) = -\frac{1}{\tilde{\rho}^2_{\text{surf}}(z;\mathbf{q})}\int_z^{z_{\max}} \frac{\partial \tilde{\rho}^2_{\text{surf}}(z';\mathbf{q})}{\partial q_i} dz', \tag{3.63}$$

where $\tilde{\rho}^2_{\text{surf}}$ obtained from Eq. (3.43). In terms of quantity

$$A^{\rho}_i(z;\mathbf{q}) = \frac{1}{2}\tilde{\rho}^2_{\text{surf}}\left(\frac{\partial \tilde{\rho}^2_{\text{surf}}}{\partial q_i} + \frac{\partial \tilde{\rho}^2_{\text{surf}}}{\partial z}a_i\right) \tag{3.64}$$

the mass tensor becomes

$$\mathcal{M}_{ij} = \pi\rho_0 \begin{cases} \frac{1}{2}\frac{1+\eta^2}{1-\eta^2}\int_{z_{\min}}^{z_{\max}} \left[\tilde{\rho}^4_s A^{\rho}_{a_\nu} A^{\rho}_{a_\mu} + 2\tilde{\rho}^2_s A^{z}_{a_\nu} A^{z}_{a_\mu}\right] dz, & q_i, q_j \in \{q_2, q_3, q_4\}, \\ \frac{\eta}{1-\eta^2}\int_{z_{\min}}^{z_{\max}} \tilde{\rho}^4_s A^{\rho}_{a_\nu} dz, & q_i = \eta, q_j \in \{q_2, q_3, q_4\}, \\ \frac{1}{2}\,\frac{1}{1-\eta^2}\int_{z_{\min}}^{z_{\max}} \tilde{\rho}^4_s dz, & \eta, \eta. \end{cases} \tag{3.65}$$

3.2.2 The friction tensor

In order to explain how the collective degrees of freedom can be related to the "inner" system, different mechanisms have been proposed, leading to different types of friction tensors. The classical understanding considers the excited state nucleus as a viscous liquid droplet. This is based on a microscopic view of the interactions of the molecules. Their mean free path is too small to matter much on the scale of the flow field. At the excitation energies of the nucleus, however, the mean free path is larger than the radius of the fissile nucleus. This was first noted by Hill and Wheeler [32]. Based on this, they proposed that the fissioning motion is controlled by surface interactions with nearly free nucleons. This behavior is similar to that of the Knudsen gas. Groß [87] applied this concept to a cylinder closed by a moving piston to calculate the energy exchange between the gas and the piston as a function of its velocity. Later, the group Świątecki [80] extended this model of the piston to a more realistic geometry, where the nuclear surface served as a conductor that changed it's shape along the fission path, transferring energy to the gas.

In addition, various models of particle and hole excitation have been proposed that take into account the energy exchange between the time-dependent mean field and the quasi-particle gas [46, 88], with different assumed mechanisms by which the energy extracted from the collective motion is eventually thermalized. All of these friction models are of the quirky type, i.e. they lack self-consistency at the microscopic level.

Finally, a number of authors suggest that the width of giant resonances is caused by the same damping process as in fission [89–91]. It should be noted, however, that these collective modes derive their character from the residual two-particle interaction rather than from the single-particle potential surface as in fission [46]. This raises the question of whether the two types of collective modes share the same damping mechanism.

In the framework of the present research, the classical representation of the friction tensor, which will be discussed below, is considered.

Hydrodynamical viscosity

Let us assume that the behavior of the above nuclear fluid flow is very similar to the laminar flow of a viscous incompressible fluid. Then the energy converted from the flow

field into heat with velocity can be determined by the well-known hydrodynamic Rayleigh dissipation function F from classical mechanics.

$$-\dot{E} = 2F = \eta_0 \int \Phi(\mathbf{r}) d^3r \tag{3.66}$$

with viscosity constant η_0 and

$$\Phi(\mathbf{r}) = \sum_{ij} \partial_{x_i} v_j(\mathbf{r}) \left[\partial_{x_i} v_j(\mathbf{r}) + \partial_{x_j} v_i(\mathbf{r})\right] \tag{3.67}$$

where v_i are the components of the velocity field and x_i are the coordinates in terms of the Cartesian coordinate representation. This expression can be written generically [79] as

$$\Phi = \nabla^2 \mathbf{v}^2 + (\mathrm{rot}\,\mathbf{v})^2 - 2\,\mathrm{div}(\mathbf{v} \times \mathrm{rot}\,\mathbf{v}). \tag{3.68}$$

Inserting the Werner-Wheeler expression eqs. (3.52) to (3.54) for the velocity field into Eq. (3.67) using the cylindrical coordinates as well as the first and second order derivatives $a_i(z;\mathbf{q})$ (3.61) over z, we get [79]

$$-\dot{E} = \eta_{ij}\dot{q}^i\dot{q}^j = \eta_0 \pi \int_{z_{\min}}^{z_{\max}} \left[3a_i' a_j' + \frac{1}{8}\rho^2(z;\mathbf{q}) a_i'' a_j''\right] \rho^2(z;\mathbf{q}) dz \dot{q}^i \dot{q}^j. \tag{3.69}$$

The volume integral $\Phi(\mathbf{r})$ can be transformed into the following surface integral, since the velocity field flow satisfies the (3.51)

$$\dot{E} = -\eta_0 \int \left(\mathrm{grad}\, v^2\right) \cdot d\boldsymbol{\sigma}\ . \tag{3.70}$$

Note that for the correct determination of the velocity field in the case of a viscous liquid, even in classical mechanics, one must approximate the Navier-Stokes equation for a free surface, as shown in Hasse [68]. Unfortunately, even in the extremely simplified representation, which is actually the classical one, the values of the mean free path length in the fission process have rather high values. Thus, the value of η_0 in the expression (3.70) does not have a constant nature. However, as correctly pointed out in [46], η_0 is often used as a fitting parameter by combining it with the mass tensor of a generalized quantity called the dissipation parameter $\beta = \eta_{ij}\left[\mathcal{M}^{-1}\right]_{ij}$. According to Krappe and Pomorski's textbook, this leads to the significant difference in the parameter β obtained in the different dynamical models shown in Fig. 3.8. It is really difficult to disagree with their conclusion, and therefore it is necessary to go deeper into the question of the description of the η coefficient. The work of Blocki et al. [80], in which the dynamic viscosity of the nuclear fluid was studied, is a classic work on the description of the properties of the nuclear friction tensor in the hydrodynamic approach. In this work, two mechanisms of the formation of the friction tensor are considered by means of the "wall" and "window" formula, where the first formula is related to the single-body dissipation representation and the second to two connected bodies, as in the pre-fission configuration of a fissile system. Of course, there is a union of these two approaches, in the form of the "wall-window" formula. This formula defines the transition from one variant of the mechanism to the other. The first approach plays a dominant role in the studied problem, i.e. in the fission process. As it is shown in [], the "window" mechanism plays a role only at certain moments of formation and rupture of the nucleus neck. These moments can be neglected. It is a different matter if we consider the reverse process, the so-called "fusion-separation" reactions, in which the formation of the neck and the transfer of energy (and of course the nucleons) play a decisive role, but this is a completely different story.

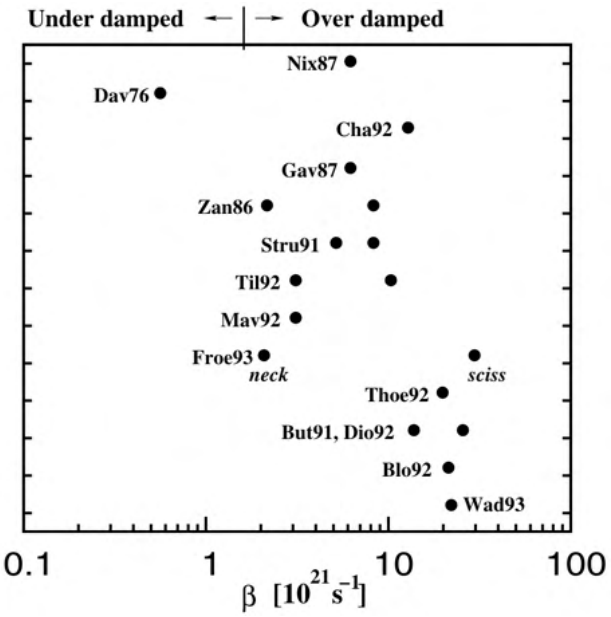

Figure 3.8: Determined reduced dissipation coefficients β from experimental data in various approaches (see Ref. [46]).]

The wall formula

As mentioned above, in the context of a detailed study of the concept of the nuclear Doppler effect introduced by Hill and Wheeler [32], the one-body dissipation mechanism was proposed by the "wall" formula for relatively compact surfaces in [80]. Assume that the Knudson gas has an isotropic velocity distribution characterized by a distribution function $\rho_0\, f(v)$, where ρ_0 is the density and f is the standardized velocity distribution, i.e.

$$\int f(v) d^3v = 1$$

Then the number of particles in the velocity interval $v_z, v_z + dv_z$ can be determined as

$$g\,(v_z)\, dv_z = \rho_0 dv_z \int f(v)\, dv_\phi\, v_\rho\, dv_\rho \tag{3.71}$$

If we substitute $v = \sqrt{v_z^2 + v_\rho^2}$ instead of v_ρ as the new integration variable, we get

$$g\,(v_z) = 2\pi\rho_0 \int_{v_z}^{\infty} v\, f(v)\, dv$$

and thus

$$\frac{dg(v_z)}{dv_z} = -2\pi\rho_0 v_z f(v_z) \tag{3.72}$$

In this case, all particles hitting the surface element $dx\, dy$ of a plane wall in the x, y-plane during the time interval dt will be in a tilted column with the surface $dx\, dy$ and height $v_z\, dt$, as shown in Fig. 3.9. The number of particles in the selected region is $dN_0 = v_z\, dt\, dx\, dy\, g(v_z)$. Since the wall is moving with velocity $\dot{n}$ relative to the main mass of the gas in the z direction, this number is equal to

$$dN = dx\, dy\, dt\, (v_z - \dot{n})\, g(v_z) \tag{3.73}$$

During the collision each particle transfers the momentum $2M_{\text{nucl}}\,(v_z - \dot{n})$, if the wall is ideally elastic and the total momentum transfer during dt on the surface element $dxdy$ of

the wall is $2M_{\text{nucl}}\,dx\,dy\,dt\int dv_z\,(v_z-\dot{n})^2\,g(v_z)$. The momentum transfer per time and per surface element is the pressure p

$$p = 2M_{\text{nucl}}\int_{\dot{n}}^{\infty}(v_z-\dot{n})^2\,g\,(v_z)\,dv_z \tag{3.74}$$

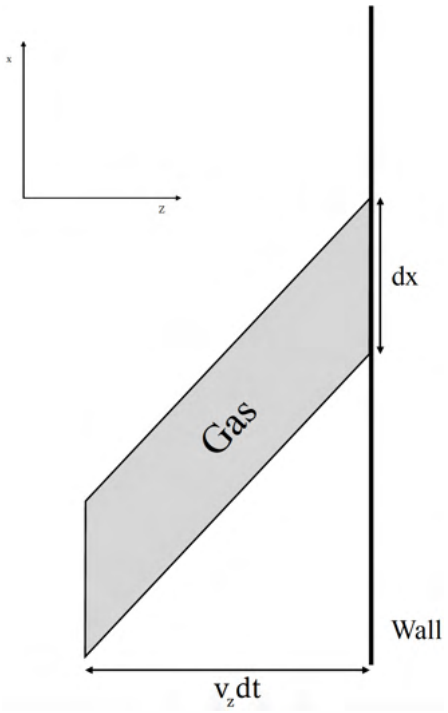

Figure 3.9: Schematic geometry of wall friction.

Assuming that $g(v_z)$ decreases rapidly at large v_z such that $\lim_{v_z\to\infty} v_z^3 g(v_z) = 0$ and substituting ratio (3.72), we partially integrate the expression. Then the pressure becomes

$$p = \frac{4\pi}{3}\rho_m\int_{\dot{n}}^{\infty}(v_z-\dot{n})^3\,v_z f\,(v_z)\,dv_z,$$

where $\rho_m = \rho_0 M_{\text{nucl}}$ is the mass density. This expression is rewritten as a series in increasing powers of $\dot{n}$, as follows

$$p = \frac{1}{3}\rho_m\overline{v^2} - \rho_m\bar{v}\dot{n} + \rho_m\dot{n}^2 - \frac{1}{3}\rho_m\overline{(1/v)}\dot{n}^3 + p_{\text{corr}} \tag{3.75}$$

where the averages are result of

$$\overline{v^n} = 4\pi\int_0^{\infty} v^{n+2}f(v)dv \tag{3.76}$$

and

$$p_{\text{corr}} = -\frac{4\pi}{3}\rho_m\int_0^{\dot{n}}(v-\dot{n})^3 v f(v)dv \tag{3.77}$$

is of the order of $(\dot{n}/v)^5$ compared to the leading term on the r.h.s. of Eq. (3.75) and is neglected below.

The energy transferred from the surface element $dx\,dy$ to the gas is $\delta E = -p\,\delta n\,dx\,dy$ when the wall displaces δn in the normal direction. Dividing by δt and integration over the whole surface of the nucleus gives the energy transfer from the surface of the nucleus to the gas per unit time.

$$\dot{E} = -\oint p\,\dot{n}d\sigma \tag{3.78}$$

Inserting Eq. (3.75) into this equation gives

$$\dot{E} = -\frac{1}{3}\rho_m\overline{v^2}\frac{\oint\delta n d\sigma}{\delta t} + \rho_m\bar{v}\oint\dot{n}^2 d\sigma + \mathcal{O}\left(\dot{n}^3/v^3\right). \tag{3.79}$$

For volume-conserving deformations δn, the integral in the first term in r.h.s. vanishes. Thus, the formula for the wall has the simple form

$$\dot{E} = \rho_m\bar{v}\oint\dot{n}^2 d\sigma = \rho_m\bar{v}\oint\frac{dn}{dq^i}\frac{dn}{dq^j}d\sigma\dot{q}^i\dot{q}^j. \tag{3.80}$$

Note here [46] that the wall is assumed to be rigid, i.e. it can compensate the local momentum transfer from one side of the surface with the same momentum transfer on the opposite side without changing the shape of the core.

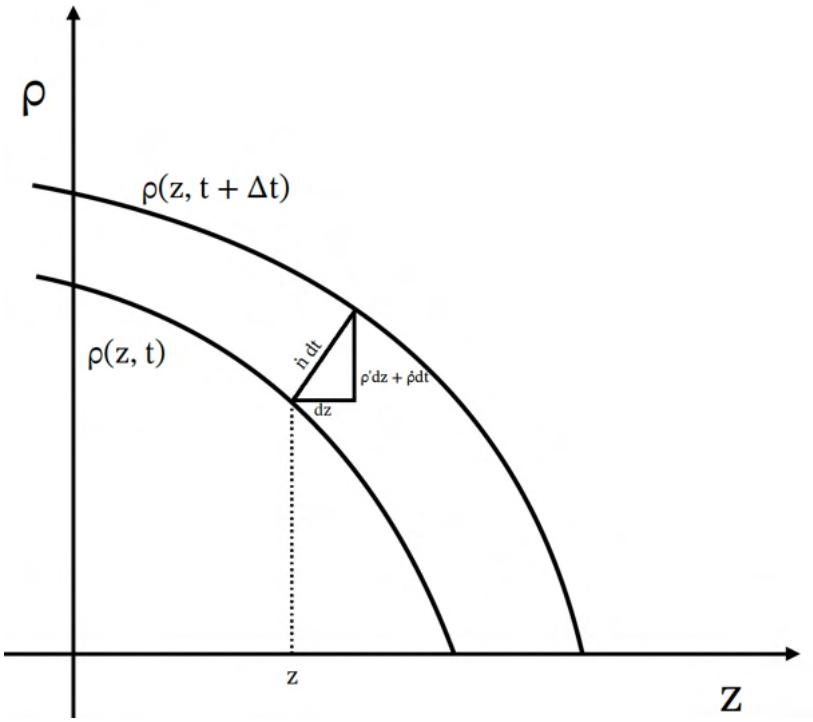

Figure 3.10: Geometry of $\dot{n}$ used to derive Eq. (3.81).

For an axially symmetric shape, given by a shape function $\rho(z;\mathbf{q})$ in cylindrical coordinates, the velocity $\dot{n}$ is given by

$$\dot{n} = \mathbf{v}_s \cdot \hat{n} = \dot{\rho}\left[1 + \left(\frac{\partial \rho}{\partial z}\right)^2\right]^{-1/2} \tag{3.81}$$

where $\mathbf{v}_s$ is the velocity of the surface and $\hat{n}$ is the unit vector in the direction of the surface normal, which points outwards. To do this, we need to look at Fig. 3.10, from which we get the relation

$$\dot{n}dt = dz\sqrt{\left(\dot{\rho}\frac{dt}{dz} + \rho'\right)^2 + 1} \tag{3.82}$$

Here $\dot{\rho}$ is the time derivative of ρ and $\rho' = \partial\rho/\partial z$. The slope of the surface normal with respect to the z axis is $-1/\rho'$. This results in the equation

$$\rho' dz + \dot{\rho}dt = -\frac{1}{\rho'}dz \tag{3.83}$$

from which follows

$$\dot{\rho}\frac{dt}{dz} = -\frac{1}{\rho'}\left(1 + \rho^2\right). \tag{3.84}$$

Insertion into Eq. (3.82) gives Eq. (3.81). It is convenient to rewrite the latter equation in the form

$$\dot{n} = \dot{q}^i \rho \frac{\partial \rho}{\partial q^i}\left[\rho^2 + \left(\rho\frac{\partial \rho}{\partial z}\right)^2\right]^{-1/2} \tag{3.85}$$

Using this result, the friction tensor η_{ij} becomes [92]

$$\eta_{ij}^{\text{wall}} = \rho_m \bar{v} \oint \frac{dn}{dq^i}\frac{dn}{dq^j}d\sigma = \frac{\pi}{2}\rho_m \bar{v}\int_{z_{\min}}^{z_{\max}} dz \frac{\partial \rho^2}{\partial q^i}\frac{\partial \rho^2}{\partial q^j}\left[\rho^2 + \frac{1}{4}\left(\frac{\partial \rho^2}{\partial z}\right)^2\right]^{-1/2} \tag{3.86}$$

The average $\bar{v}$ can be calculated in the grand canonical ensemble with the temperature $T = 1/\beta$ and the chemical potential $\mu \approx \epsilon_f = (1/2)M^*_{\text{nucl}}v_f^2$ if $\mu\beta \gg 1$, where ϵ_f and v_f are the Fermi energy and Fermi velocity, respectively,

$$\bar{v} = \frac{4\pi \int v^3[1+\exp(\epsilon-\mu)\beta]^{-1}dv}{4\pi \int v^2[1+\exp(\epsilon-\mu)\beta]^{-1}dv} \tag{3.87}$$

Using the Sommerfeld expansion

$$\int_0^\infty \frac{f(\epsilon)}{e^{(\epsilon-\mu)\beta}+1}d\epsilon = \int_0^\mu f(\epsilon)d\epsilon + \frac{\pi^2}{6\beta^2}f'(\mu) + O\left((\mu\beta)^{-4}\right)$$

and writing $\epsilon = (1/2)M^*_{\text{nucl}}v^2$, the numerator and denominator can be expanded in powers of $1/(\mu\beta)$. Up to the second order in the expansion parameter you get

$$\bar{v} = \frac{3}{4}v_f\left[1+\frac{1}{12}\left(\frac{\pi}{\epsilon_f\beta}\right)^2\right] \tag{3.88}$$

The temperature-dependent term is small and neglected in applications of the wall formula, usually taking only $\bar{v} = \frac{3}{4}v_f$. Thus, in the context of the Thomas-Fermi approximation, the factor in front of the integral in the "wall" formula (3.80) can be rewritten as

$$\rho_m\bar{v} = \frac{\bar{k}_f^4}{2\pi^2} \tag{3.89}$$

in terms of the Fermi wave number $k_f = v_f/\hbar$, whic In Ref. [93] the numerical value $1.026\times10^{-22}\text{MeV}\cdot\text{s}\cdot\text{fm}^{-4}$ was proposed for the constant (3.89).

From this derivation of the "wall" formula it is clear that $\dot{n}$ is the surface velocity with respect to the bulk of the gas in thermal equilibrium. In the case of a moving or rotating nucleus, $\dot{n}$ should be measured in a co-moving, co-rotating coordinate system. For pre-fission configurations, it is natural to relate the average velocity of the particles in each of the two emerging fragments to the velocity of the fragment center of mass $\dot{D}_\nu, \nu = L, R$. Thus the friction tensor becomes [94]

$$\eta_{ij}^{\text{wall Ad}} = \frac{\pi}{2}\rho_m\bar{v}\left(\int_{z_{\min}}^{z_N} I_L(z)dz + \int_{z_N}^{z_{\max}} I_R(z)dz\right) \tag{3.90}$$

where

$$I_\nu = \left(\frac{\partial\rho^2}{\partial q^i} + \frac{\partial\rho^2}{\partial z}\frac{\partial D_\nu}{\partial q^i}\right)\left(\frac{\partial\rho^2}{\partial q^j} + \frac{\partial\rho^2}{\partial z}\frac{\partial D_\nu}{\partial q^j}\right)\left(\rho^2 + \left[\frac{\partial\rho^2}{2\partial z}\right]^2\right)^{-1/2} \tag{3.91}$$

with the smallest neck radius at z_N and D_L and D_R are the center of mass distances of the nuclear volume to the left and right of z_N, respectively.

An infinite rectangular potential box would be required for the assumption of particle reflection at a sharp surface. Since the actual single particle potentials are smooth and finite, it is expected that the momentum transfer will be smeared out over a surface layer whose thickness is of the order of the thickness of the surface. Randrup and Swiatecki [93] therefore introduced a surface-peaked function $Y_{\text{fric}}(\mathbf{r})$ in close analogy to the surface-peaked function $g(\mathbf{r}) = \mathcal{E}(\mathbf{r}) - c_1\rho(\mathbf{r})$ [46]. The one-dimensional integral over Y_{fric} in the direction of the surface normal and the higher surface moments are assumed to be independent of the nuclear shape. The leptodermous expansion then leads to expand as follows

$$\begin{aligned}\dot{E} = \int Y_{\text{fric}}(\mathbf{r})d^3r &= \int Y_{\text{fric}}(z)dz\cdot\int d\sigma + \int Y_{\text{fric}}(z)zdz\cdot\int\kappa d\sigma \\ &+ \text{Terms with higher moments of } Y_{\text{fric}},\end{aligned} \tag{3.92}$$

where z is in the direction of the surface normal and κ is twice the mean curvature.

The window formula

The further development of the idea of the wall formula introduced by Swiatecki [95], in Ref. [80], led to the window formula. Let us assume that the nuclear system is close to rupture. That is, there are two different pre-fragments A and B, which have already acquired the relative velocity of the center of mass $\dot{\mathbf{D}}$. Then there can still be a hole of size $\Delta\sigma$ in the one-particle potential in the neck region. Particles can pass through this hole from A to B, transferring their momentum and angular momentum from one pre-fragment to the other. It is then assumed that if the transferred momentum is thermally equilibrated in the new environment of the transferred particle, such a mechanism will result in a slowing down of the dynamic motion of the coordinate $\mathbf{D}$.

In order to discuss this effect in more detail, we will use a coordinate system in which the bulk of the gas in the container A is at rest. The window is in the plane x, y, and the direction z perpendicular to the window is from A to B. In this case, the change in the momentum of the gas in the container A per unit of time has three contributions:

- Leaving particles from A. Similar to the wall formula, there exists

$$dN = \Delta\sigma dt \left(v_z - \dot{n}\right) g\left(v_z\right)$$

particles reaching the hole of size $\Delta\sigma$ in time dt, taking away from A the momentum $M_{\text{nucl}}\mathbf{v}$. Averaging in the x, y-plane leaves only v_z. Hence, the drag force in the $-z$ direction is

$$F_{AB} = -\int_{\dot{n}}^{\infty} \frac{dN}{dt} M_{\text{nucl}} v_z dv_z = -M_{\text{nucl}}\Delta\sigma \int_{\dot{n}}^{\infty} \left(v_z - \dot{n}\right) v_z g\left(v_z\right) dv_z \tag{3.93}$$

Partial integration and using the equation (3.72) gives

$$F_{AB} = -2\pi\rho_m\Delta\sigma \int_{\dot{n}}^{\infty} \left(\frac{1}{3}v_z^3 - \frac{\dot{n}}{2}v_z^2\right) v_z f\left(v_z\right) dv_z$$

By neglecting terms of order $(\dot{n}/v)^3$, the lower limit of the integral can be moved to 0. Substituting the moments $\overline{v^n}$ defined in equation (3.76), we find

$$F_{AB} = -\frac{1}{2}\rho_m\Delta\sigma\left(\frac{1}{3}\overline{v^2} - \frac{\dot{n}}{2}\bar{v}\right) \tag{3.94}$$

- Particles arriving from B. For this, introduce the velocity $\mathbf{v}'$ with respect to the moving frame B. Then the number of particles reaching the "window" in time dt inside B is

$$dN = dt\Delta\sigma\left(v_z' + \dot{n} - \dot{D}_z\right) g\left(v_z'\right),$$

where $\dot{D}_z$ is the z-component of the relative velocity $\dot{\mathbf{D}}$ of B with respect to A. In this case, the nucleon transmits momentum

$$M_{\text{nucl}}\left(-v_z'\hat{z} + \dot{\mathbf{D}}\right) = M_{\text{nucl}}\left[\left(\dot{D}_z - v_z'\right)\hat{z} + \dot{D}_\rho\hat{\rho}\right],$$

where $\hat{z}$ is a unit vector in the direction of z, and $\hat{\rho}$ is a unit vector in the direction of the component $\dot{\mathbf{D}}$ perpendicular to $\hat{z}$. Hence, the force on the volume A associated with the transmission of momentum from B equals

$$\mathbf{F}_{BA} = M_{\text{nucl}}\Delta\sigma \int \left(v_z' + \dot{n} - \dot{D}_z\right)\left(-v_z'\hat{z} + \dot{D}_z\hat{z} + \dot{D}_{rho}\hat{\rho}\right) g\left(v_z'\right) dv_z' \tag{3.95}$$

By performing similar transformations from equation (3.93) to (3.94) and neglecting the quadratic terms, one can obtain an approximate form of the second contribution

$$\mathbf{F}_{BA} = \frac{1}{2}\rho_m\Delta\sigma\left[-\frac{1}{3}\overline{v^2}\hat{z} + \frac{1}{2}\bar{v}\left[\left(2\dot{D}_z - \dot{n}\right)\hat{z} + \dot{D}_\rho\hat{\rho}\right]\right] \tag{3.96}$$

- Finally, the force resulting from the collision with the surface $\Sigma_A - \Delta\sigma$ of the volume A

$$\mathbf{F}_{\text{surf}} = -\int_{\Sigma_A - \Delta\sigma} p_{\text{stat}} d\boldsymbol{\sigma} \tag{3.97}$$

with static pressure $p_{\text{stat}} = (1/3)\rho_m \overline{v^2}$ (see e.g. Eq. (3.75)).

Summing eqs. (3.94), (3.96) and (3.97), the total force $\mathbf{F}_A$ is

$$\mathbf{F}_A = \frac{\rho_m}{2}\left[-\frac{2\overline{v^2}}{3}\left(\int_{\Sigma_A-\Delta\sigma} d\boldsymbol{\sigma} + \Delta\sigma\hat{z}\right) + \Delta\sigma\bar{v}\left(\dot{D}_z\hat{z} + \frac{\dot{D}_\rho}{2}\hat{\rho}\right)\right]. \tag{3.98}$$

Analyzing the last formula, it can be seen that the first term vanishes because it integrates the momentum transfer between the gas and the container A over its entire surface. The remaining term is responsible for the rate of change of the energy of the gas in A associated with the container B and has the form

$$\dot{E} = \frac{1}{2}\Delta\sigma\rho_m\bar{v}\left(\frac{\partial D_z}{\partial q^i}\frac{\partial D_z}{\partial q^j} + \frac{1}{2}\frac{\partial D_\rho}{\partial q^i}\frac{\partial D_\rho}{\partial q^j}\right)\dot{q}^i\dot{q}^j \tag{3.99}$$

Note, however, that the z-component $\mathbf{F}_A$ contributes to the radial friction force while the ρ-component contributes to the tangential friction force when using this formula to model heavy ion fusion and deep inelastic reactions.

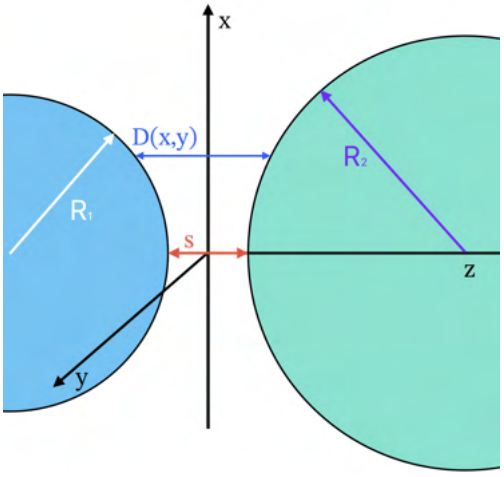

Figure 3.11: Proximity interaction between two spheres with center radii R_1 and R_2 and the shortest distance s between their surfaces (see details in [46]).

It should be noted, however, that the above model uses a rectangular form of the potential. The nucleon flux through the "window" is represented as a classical flux in matter. To account for the more real ("diffusive") form of the potential, in [96] using Thomas-Fermi theory with two-body Seiler-Blanchard interactions [97] for the case of two spheres (see Fig 3.11) for the factor $\Delta\sigma\rho_m\bar{v} = \Delta\sigma n_0$ in the equation (3.99), ratio

$$n_0\Delta\sigma \to \int n d\sigma \approx 2\pi\bar{R}\int_s^\infty n\left(s'\right)ds' \tag{3.100}$$

where $\bar{R} = R_1R_2/\left(R_1+R_2\right)$ is the reduced radius, and $s = D - R_1 - R_2$ is the closest distance between the two faces. By introducing the dimensionless variable $\zeta = s/b$, where b is the diffusivity of the surface, and the dimensionless function $\psi(\zeta) = n(b\zeta)/n_0$ with the property

$$\Psi(\zeta) = \int_\zeta^\infty \psi\left(\zeta'\right)d\zeta'$$

wherefore

$$n_0\Delta\sigma \to 2\pi\bar{R}n_0b\Psi(s/b) \tag{3.101}$$

must be substituted into the Eq. (3.99).

There is a net induced mass flow in the neck, given the change in asymmetry over time. The mechanism is also related to the transfer of energy from the walls to the gas.

This energy acts as a drag force in the asymmetry degree of freedom. Therefore, the energy transfer rate is defined [98] as

$$\dot{E} = \frac{16}{9}\rho_m \bar{v} \frac{1}{\Delta\sigma}\dot{V}_1^2 = \frac{16}{9}\rho_m \bar{v} \frac{1}{\Delta\sigma}\frac{\partial V_1}{\partial q^i}\frac{\partial V_1}{\partial q^j}\dot{q}^i\dot{q}^j, \tag{3.102}$$

where V_1 is the volume on one side of the window. Then, adding the contributions from the equations (3.99) and (3.102) to the friction tensor, we get

$$\eta_{ij}^{(\text{window})} = \frac{1}{2}\rho_m \bar{v}\left[\Delta\sigma\left(\frac{\partial D_z}{\partial q^i}\frac{\partial D_z}{\partial q^j} + \frac{1}{2}\frac{\partial D_\rho}{\partial q^i}\frac{\partial D_\rho}{\partial q^j}\right) + \frac{32}{9}\frac{1}{\Delta\sigma}\frac{\partial V_1}{\partial q^i}\frac{\partial V_1}{\partial q^j}\right], \tag{3.103}$$

without the correction (3.101) in the first term.

The wall-window formula

As it has been pointed out before, there should be a generalized form of the two forms of the friction tensor that fully characterizes the dissipative processes that take place during the nuclear reactions. That is, if there is a drift velocity between the gas in A and in B, it should include both the energy transfer to the gas due to collisions with the wall and the momentum flux between A and B. The limit transition in the generalized friction tensor η_{ij}^{total} should of course be smooth. The first attempt at unification was proposed in [99]

$$\eta_{ij}^{\text{total}} = [1 - c(\mathbf{q})]\eta_{ij}^{\text{wind+w}} + c(\mathbf{q})\eta_{ij}^{\text{wall}} \tag{3.104}$$

where $\eta_{ij}^{\text{wind+w}} = \eta_{ij}^{\text{window}} + \eta_{ij}^{\text{wall Ad}}$ and $c(\mathbf{q})$ is chosen as

$$c = \sin^2\left(\frac{\pi}{2}x\right) \tag{3.105}$$

In the formula (3.105) at $x = \rho_{\text{neck}}^2/\min(\rho_1^2, \rho_2^2)$, where ρ_1 and ρ_2 are the transverse half axes of two outer ellipsoids in the three quadratic surface shape parameterization [100] and ρ_{neck} is the radius of the neck, which is zero when the fragments are separated. The function $c(\mathbf{q})$ was modified in [101]

$$c = \begin{cases} 0 & \text{for } 0 \le x \le 0.8 \\ \sin^2\left(\frac{x-0.8}{0.2}\frac{\pi}{2}\right) & \text{for } 0.8 \le x \le 1 \\ 1 & \text{for } x \ge 1 \end{cases} \tag{3.106}$$

It is also worth mentioning the work of [102], where another variant for $c(\mathbf{q})$ is proposed, containing additional parameters for fitting to individual nuclei.

Improvements in nucleon momentum transfer mechanisms and thermalization are associated with the further development of the model. For example, in [103] a measure μ (shape) was introduced. It represents the degreef three-dimensional axisymmetric billiard of a given shape. This was done by determining the Lyapunov coefficient λ for a trajectory and comparing it to the deviation $\delta(t)$ in phase space from the adjacent trajectory with an initial small deviation $\delta_0 = \delta(0)$. In chaotic dynamics, trajectories are expected to deviate exponentially with time, $\delta(t) \sim \exp(\lambda t)$ at large values of time. To determine λ, the Benettin method [104] of the type

$$\lambda = \lim_{\delta_0 \to 0}\lim_{k\to\infty}\frac{1}{k\tau}\sum_{i=1}^{k}\ln\frac{\delta(\tau)}{\delta_0} \tag{3.107}$$

which has a good convergence with increasing time $t = k\tau$. The trajectory is chaotic at $\lambda > 10^{-3}$. The motion of a particle in a static spherical billiard with multipole deformations of order l gives μ values ranging from 0 to 1, which increase with increasing amplitude and with increasing multipole order. For a spherical cavity, the motion is regular and $\mu = 0$. As the strain increases, the chaotic coefficients $\mu(c)$, as shown in [105] for the Funny Hills class of surfaces, increase monotonically up to system rupture. The resulting dissipation parameter $\beta = \mu(c)\eta^{\text{wall Ad}}(c)/m(c)$ – with the Werner-Wheeler mass parameter $m(c)$ is shown in Fig. 3.12.

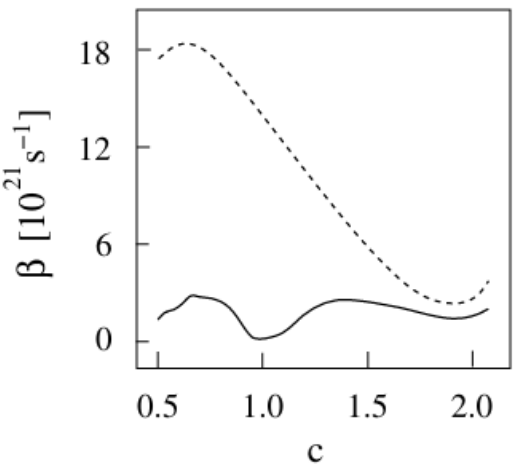

Figure 3.12: Dissipation parameter $\beta(c)$ with chaoticity reduction (solid line) and original wall formula (dashed line) (taken from Ref. Ref. [46]])

Going forward, it could be mentioned that in Langevin equations (see detailed in sections 4.1 and 5.2.2) seem to require much less wall friction than the classical formulas (3.80) and (3.90). The simplest way to solve this problem is to introduce [106] a shape independent "reducing" coefficient k_s. Values for k_s in the range $0.2 < k_s < 0.5$ have been obtained by fitting various data. However, this violates the wall-and-window formalism, which, as shown, has no fitting parameter. Another possibility is to use the temperature dependent parameter [107]. However, the introduction of such a parameter is no longer strictly classical.

Let us summarize this chapter. The development of different parameterization methods for the description of the shape of atomic nuclei, the choice of which has an important role in the understanding of the structure and properties of nuclei, such as the potential energy, has been reviewed here in some form. The first step was the consideration of one of the first simplifications of the Nillson parameterization surface on the basis of the representation of the oscillation potential. The next step was the use of Cassini's ovaloid method, which represents the surface of the nucleus as ellipses or ovals with two foci in the center. In spite of its simplicity, it has limitations in the description of elongated nuclei. To solve this problem, quadratic methods have been developed, which allow for a wider range of shapes (Funny-Hills, Trentalange-Cunin-Sierk), which allow us to obtain a wider range of shapes.

The last point was the Fourier parametrization, developed within the research group in which the researcher is involved and which is the subject of the paper, is a newer and more innovative approach. It uses a Fourier expansion (similar to the Trentalange-Cunin-Sierk parametrization where there is an expansion in Legendre polynomials) to represent the shape of the nucleus and has the advantage of accurately describing the different shapes of nuclei with a relatively small number of deformation parameters.

In addition, the chapter discussed the hydrodynamic representation of the properties of the nuclei, such as the inertia tensor and the friction tensor. The inertia tensor is related to the inertial properties of the nucleus, while the friction tensor describes the energy and momentum transfer between the nucleus and its environment. Different approaches such as the wall formula and the window formula are used to calculate the friction tensor based on the interaction between the nucleus and its environment.

Chapter 4

Statistical approaches to description of nuclear fission

4.1 Langevin approach

In this respect, another statistical approach, introduced at the end of the 1980s, came to the rescue. Abe, Grégoire and Delagrange were the first [108] who proposed to use the Langevin equations for describing the fission process. But note that the fission process was related to the description of the fission of highly excited heavy compound nuclei after the fusion reaction. The first models based on this approach were also one-dimensional and used elongation as the only form variable, which also described similar processes. Soon, however, more complex multidimensional models [94, 109–111] appeared, which take into account in detail the specificity of nuclear shape. And in the last decade, attempts were made, not without success [20–23, 78, 94, 112–116], to use this approach in low-energy fission, which is the focus of the present thesis. In this section, the main elements of the formalism based on the Langevin equations will be discussed.

Let us introduce a set of deformation parameters q_i $(i = 1, \dots N)$, of which contains all real fission paths. Moreover, so that the dynamical equations of motion, remain covariant under coordinate transformations within the chosen class of forms, we will use tensor notation, where $\mathbf{q} = q_i$ represents a contravariant vector.

Now let us construct a scalar Lagrangian for the classical dynamical problem with the introduced variables q_i. Substantial changes in the nucleus surface are related with the flow of matter and, therefore, the kinetic energy must have a quadratic form of the velocity vector $\dot{q}^i$:

$$E_{\text{kin}} = \frac{1}{2}\mathcal{M}_{ij}\dot{q}^i\dot{q}^j \tag{4.1}$$

Here $\mathcal{M}_{ij}(\mathbf{q})$ is a positively defined symmetric inertia tensor which depends in general on the coordinates q_i.

Conservative forces can be derived from the derivatives of the potential $V(\mathbf{q})$, for which it is often taken as the liquid drop energy. Then the Lagrangian for the classical system $\mathcal{L} = E_{\text{kin}} - V$ with obtaining the conjugated momenta

$$p_i = \frac{\partial \mathcal{L}}{\partial \dot{q}^i} = \mathcal{M}_{ij}\dot{q}^j \tag{4.2}$$

Note that the degrees of freedom of the form cannot be completely separated from the internal degrees of freedom. One of the simplest methods to relate to collective motion is to introduce a frictional force proportional to velocity.

$$K_i^{(\text{fric})} = \gamma_{ij}\dot{q}^j \tag{4.3}$$

in terms of a covariant, symmetric, positive-semi-definite friction tensor $\gamma_{ij}(\mathbf{q})$. The equation of motion becomes in this case

$$\frac{d}{dt}\frac{\partial \mathcal{L}}{\partial \dot{q}^i} - \frac{\partial \mathcal{L}}{\partial q_i} = \dot{p}_i - \frac{1}{2}\frac{\partial \mathcal{M}_{kl}}{\partial q_i}\dot{q}^k\dot{q}^l + \frac{\partial V}{\partial q_i} = -\gamma_{ij}\dot{q}^j \tag{4.4}$$

It is useful to know the following properties for the coordinate-dependent inertial tensor $\mathcal{M}_{ij}(\mathbf{q})$

$$\dot{p}_i = \mathcal{M}_{ij}\ddot{q}^j + \dot{q}^k\frac{\partial \mathcal{M}_{ij}}{\partial q^k}\dot{q}^j \quad \text{and} \quad \dot{q}^k\frac{\partial \mathcal{M}_{kl}}{\partial q_i}\dot{q}^l = -p_k\frac{\partial\left[\mathcal{M}^{-1}\right]_{kl}}{\partial q_i}p_l. \tag{4.5}$$

More detailed information about the inertia and friction tensors will be discussed in the next chapter. For now, let us specify that they are calculated within the framework of the hydrodynamic approach using the Werner-Wheeler approximation.

In the description of the fission of excited nuclei, it is usually characterized by the temperature $T(\mathbf{q})$. Then the value $U(\mathbf{q})$ is understood as the sum of the potential energy at zero temperature $V(\mathbf{q})$ and the excitation energy in the Fermi-gas approximation $E^* = a(\mathbf{q})T^2$. The shape-dependent coefficient $a(\mathbf{q})$ is the level density parameter, Eq. (3.28). In this case, the total energy is

$$E_{\text{total}} = E_{\text{kin}} + V + E^* = E_{\text{kin}} + U.$$

From the general thermodynamic relations it follows

$$dU = TdS - K_i dq_i \tag{4.6}$$

and

$$dF = -SdT - K_i dq_i \tag{4.7}$$

where K_i is the generalized force vector, S is the entropy, and $F(\mathbf{q};T)$ is the Gibbs free energy. From eqs. (4.6) and (4.7) it follows

$$-K_i = \left(\frac{\partial U}{\partial q_i}\right)_{S=\text{const}} = \left(\frac{\partial F}{\partial q_i}\right)_{T=\text{const}}. \tag{4.8}$$

Suppose that the temperature T can be determined at each point of the fission trajectory. This means an almost immediate thermalization of the excitation energy E^* on the time scale of motion along the trajectory. Unlike macroscopic systems with almost infinite degrees of freedom, in small systems the fluctuations associated with friction are not negligible. Hence, the intrinsic single-particle motion must be much faster than the collective motion, and their coupling generates a stochastic force, the Langevin force,

$$K_i^{(\text{Langevin})}(\mathbf{q};t) = \sum_j g_{ij}(\mathbf{q})\Gamma_j(t) \tag{4.9}$$

which is added to the right-hand side of the equation (4.4). This force is the product of the force factor $g_{ij}(\mathbf{q})$, which depends directly on the collective variables $\mathbf{q}$, and the time-dependent stochastic factor $\Gamma_j(t)$. The Γ_j is random function distribution, where numbers with zero mean $\langle\Gamma_j(t)\rangle = 0$ and a delta-correlated variance

$$\langle\Gamma_i(t)\Gamma_j(t')\rangle = 2\delta_{ij}\delta(t-t') \tag{4.10}$$

For coordinate transformations, the expression $\sum_j g_{ij}\Gamma_j$ is a covariant vector, but Γ_j is not. Therefore, it is required that the equation (4.10) is valid for any coordinate system.

The delta-function in Eq. (4.10) shows the ideal case where the dynamics internal to the system are random and change almost instantly. Coupling "white" noise to the slow motion of the collective variables leads to a Markov process with frequency-independent Fourier amplitudes. To account for the finite "memory time" τ, it is necessary to replace the delta-function by a Gaussian with width τ, which leads to a non-Markovian process.

The same origin of friction and Langevin forces implies a relation between the transport parameters η_{ij} and g_{ij}. From the fluctuation-dissipation theorem [17, 117] follows the relation

$$\sum_k g_{ik} g_{jk} = T\eta_{ij} \stackrel{\text{def}}{=} \mathcal{D}_{ij}. \tag{4.11}$$

where D_{ij} is the diffusion tensor.

Considering the assumed finite system temperature, no quantum corrections in Eq. (5.91) are taken into account. Adding the Langevin force to the deterministic equations of motion generates a bundle of trajectories, which latter create a probability distribution $w(\mathbf{q}, \mathbf{p}, t)$ at a given time t and point $\mathbf{q}, \mathbf{p}$ in its phase space.

Even though we have been using statistical mechanics of the canonical ensemble, it would be unrealistic to keep the temperature constant during the whole Langevin process. The energy transferred per unit time into the intrinsic system by the friction and Langevin forces should be equal to the rate of increase of the internal energy

$$\frac{dE^*}{dt} = \eta_{ij}\dot{q}_i\dot{q}_j - \dot{q}_i \sum_j g_{ij}\Gamma_j \tag{4.12}$$

with the local excitation energy

$$E^* = U(\mathbf{q}, T) - V(\mathbf{q}) = aT^2.$$

Equation (4.12) may be seen as the equation of motion for the temperature. In case shape-independent level-density parameter a, where (4.12) guarantees conservation of the total energy E_{total}. To see this let use $\partial_{q_i} F|_{T=\text{ const}} = \partial_{q_i} V$ and multiply the balance of all forces

$$\mathcal{M}_{ij}\ddot{q}_j + \frac{1}{2}\frac{\partial \mathcal{M}_{jk}}{\partial q_i}\,\dot{q}_j\dot{q}_k + \frac{\partial V}{\partial q_i} + \eta_{ij}\dot{q}_j - \sum_j g_{ij}\Gamma_j = 0 \tag{4.13}$$

by $\dot{q}_i$ and obtain

$$\frac{d}{dt}\left(\frac{1}{2}m_{jk}\dot{q}_j\dot{q}_k + V + E^*\right) = \dot{E}_{\text{total}} = 0 \tag{4.14}$$

If the $\mathbf{q}$-dependence of a is considered, then Eq. (4.12) needs to be replaced by

$$a(\mathbf{q})\frac{dT^2}{dt} = \eta_{ij}\dot{q}_i\dot{q}_j - \dot{q}_i \sum_j g_{ij}\Gamma_j, \tag{4.15}$$

which shows that the excitation energy is changed only by a change in temperature, not its shape-dependence.

The fluctuations Γ_j can be different. For example, it may happen that a large negative fluctuation would pump more energy out of the internal system than it actually contains. To avoid such unphysical events the tail of the Gaussian distribution $P_{norm}(\mathbf{\Gamma})$, from which the Γ_j are taken, has to be cut off. This trick is the price one has to pay for using the convenient canonical formalism instead of the microcanonical one, required in principle by the boundary condition of a fixed total energy, but such truncation of the Gaussian distribution is quite rare event.

Finally this set of equations

$$\begin{cases} \dot{q}_i = \left[\mathcal{M}^{-1}\right]_{ij} p_j, \\ \dot{p}_i = -\partial_{q_i} F|_{T=\text{const}} + \dfrac{\partial \left[\mathcal{M}^{-1}\right]_{jk}}{2\partial q_i} p_j p_k - \eta_{ij} \left[\mathcal{M}^{-1}\right]_{jk} p_k + \sum\limits_j g_{ij}\Gamma_j(t) \\ 2a(\mathbf{q})T\dot{T} = \eta_{ij}\dot{q}_i\dot{q}_j - \dot{q}_i \sum\limits_j g_{ij}\Gamma_j \end{cases} \tag{4.16}$$

shall be referred to as Langevin equations. One can prove the identity

$$\partial_{q_i} F|_{T=\text{const}} = -T\partial_{q_i} S|_{U=\text{const}} \tag{4.17}$$

with the temperature $T(\mathbf{q})$, the free energy $F = V - a(\mathbf{q})T^2$, and the entropy $S = 2a(\mathbf{q})T$ in terms of the level-density parameter $a(\mathbf{q})$. Some authors [118] therefore write $T\partial_{q_i} S$ instead of $-\partial_{q_i} F$ in Eq. (4.16).
To obtain these equations a set of assumptions was established, including

a) having two distinct time scales in considered system;

b) slow motion collective de2grees of freedom adhering from classical mechanics;

c) linear dependence of friction force on velocity;

d) presence of the second law of thermodynamics for the intrinsic system.

A specific knowledge of the intrinsic system was not needed for this step, but when deriving the mass and friction tensors as a function of collective variables, it will be required.

For the numerical solution of the Langevin equations, a time discretization will be used, where the first equation of the system (4.16) applies the Heun procedure of second order, and for the second equation the Euler procedure of first order.

$$\begin{aligned} q_i(t_{n+1}) - q_i(t_n) =& \frac{1}{2}\left[\mathcal{M}^{-1}(\mathbf{q}(t_n))\right]_{ij} \left[p_j(t_n) + p_j(t_{n+1})\right]\tau \\ p_i(t_{n+1}) - p_i(t_n) =& -\left[\gamma_{ij}(\mathbf{q}(t_n))\left[\mathcal{M}^{-1}(\mathbf{q}(t_n))\right]_{jk} p_k(t_n) + \frac{\partial F(\mathbf{q}(t_n))}{\partial q_i}\right. \\ & \left. -\frac{1}{2}\frac{\partial \left[\mathcal{M}^{-1}(\mathbf{q}(t_n))\right]_{jk}}{\partial q_i} p_j(t_n) p_k(t_n)\right]\tau + I_i \end{aligned} \tag{4.18}$$

where the integral

$$I_i = \int_{t_n}^{t_{n+1}} \sum_j g_{ij}(\mathbf{q}(t'))\,\Gamma_j(t')\,dt' \tag{4.19}$$

Unfortunately, right-hand expression in (4.19) cannot be represented by a sum in the limit $\tau \to 0$ since $\Gamma_j(t')$ is a distribution rather than an integrable function. Therefore let introduce the auxiliary quantity $W_j(t) = \int_0^t \Gamma_j(t')\,dt'$, and use it to rewrite integral (4.19) as

$$I_i = \int \sum_j g_{ij}(\mathbf{q}(t'))\,dW_j(t') \tag{4.20}$$

which can be approximated by

$$I_i \approx \sum_j g_{ij}(\mathbf{q}(t_n))\left[W_j(t_{n+1}) - W_j(t_n)\right] \tag{4.21}$$

This expression is known as the Ito version for the discretization of the stochastic equation (4.18). Alternative discretization of the form

$$I_i \approx \sum_j g_{ij}(\mathbf{q}(t_n + \lambda[t_{n+1} - t_n]))\left[W_j(t_{n+1}) - W_j(t_n)\right] \tag{4.22}$$

with various values for λ have been proposed. To account for this, the $W(t)$ are expressed in terms of normalized, Gaussian-distributed random numbers $w_j(n)$ with properties

$$\langle w_j \rangle = 0, \qquad \left\langle (w_j)^2 \right\rangle = 2. \tag{4.23}$$

This is carried out through the ansatz

$$W_j = a w_j \tag{4.24}$$

with scaling factor determined by equating the variances of aw_j and of $\int \Gamma_j(t')\, dt'$. This yields

$$I_i = \sum_j g_{ij}\left(\mathbf{q}(t_n)\right)\left[w_j(n+1) - w_j(n)\right]\sqrt{\tau}, \tag{4.25}$$

where τ is the time step.

Lastly, to ensure the third of the Langevin equations is satisfied, the temperature T is readjusted [46] after each time step such that

$$T^2(\mathbf{q}) = E^*/a = \left[E_{\text{total}} - E_{\text{kin}}(\mathbf{q}) - V(\mathbf{q})\right]/a(\mathbf{q}). \tag{4.26}$$

A few words about the level density parameter. In this paper we use the fitting made in the paper [119], where the temperature-dependent Hartree-Fock calculations were performed in the relativistic mean-field approximation. Subtracting the shell correction from the free energy gave a quadratic T^2 dependence:

$$\frac{a}{A} = 0.032\left(1 - 3,265I^2\right) + 0.22A^{-1/3}\left(1 + 5,644I^2\right) + 0.0021Z^2/A^{4/3} \tag{4.27}$$

For a detailed discussion of these and other fits, see Chapter 3 of the Krappe and Pomorski book [46].

4.2 The Fokker-Planck equation

Instead of numerically generating the probability $w(\mathbf{q}, \mathbf{p}, t)$ in the phase space of the collective variables from bunches of fission trajectories, one can try to derive a differential equation for $w(t)$ and obtain solutions for a given initial probability $w(t = t_0)$. Volume elements in phase space refer to the contravariant components of the coordinates $d\{q^i\}$ and the covariant components of the moments $d\{p_i\}$, in short $d\mathbf{q}$ and $d\mathbf{p}$. So the volume element $d\mathbf{q}d\mathbf{p}$ is scalar. The probability density $w(\mathbf{q}, \mathbf{p}, t)$ has to be a scalar as well. Covariance of all equations with respect to general transformations in phase space is required in some treatments of transport theory [120, 121]. This is also the case in Risken's textbook [117]. It is recommended for a detailed discussion of the Fokker-Planck equation and its solution techniques. In the present context, this global covariance would be somewhat artificial. In our case, a transformation in coordinate space induces the inverse transformation in momentum space, since coordinates and momenta are connected by Newtonian equations.

4.2.1 The Kramers-Moyal expansion

One introduces the conditional probability $P(\mathbf{q}, \mathbf{p}; t + \tau \mid \mathbf{q}'\mathbf{p}'; t)$ to find the system at time $t + \tau$ at the phase space point $(\mathbf{q}, \mathbf{p})$ if it was at point $(\mathbf{q}', \mathbf{p}')$ at time t. The equation of motion for $w(t)$, called the Chapman-Kolmogorov equation, in terms of this transition probability is

$$w(\mathbf{q}, \mathbf{p}, t + \tau) = \int P(\mathbf{q}, \mathbf{p}; t + \tau \mid \mathbf{q}', \mathbf{p}'; t)\, w(\mathbf{q}', \mathbf{p}', t)\, d\mathbf{q}' d\mathbf{p}' \tag{4.28}$$

For small τ one expects the transition probability P to peak at $\mathbf{q} = \mathbf{q}'$ and $\mathbf{p} = \mathbf{p}'$. This is because points in phase space far away from the point $(\mathbf{q}, \mathbf{p})$ should not influence the situation there in a very short time. One is therefore led to the evaluation of the integral in eq. (4.28) by a moment expansion. In the Kramers-Moyal expansion one introduces new integration variables $\mathbf{Q} = \mathbf{q} - \mathbf{q}'$ and $\mathbf{P} = \mathbf{p} - \mathbf{p}'$ and expands the integrand in a Taylor series with respect to the new variables $\mathbf{Q}$ and $\mathbf{P}$ up to terms of the second order.

$$\begin{aligned} w(\mathbf{q}, \mathbf{p}, t+\tau) = \int \Bigg([Pw] - \frac{\partial [Pw]}{\partial q^i} Q^i - \frac{\partial [Pw]}{\partial p_i} P_i + \frac{1}{2} \frac{\partial^2 [Pw]}{\partial q^i \partial q^j} Q^i Q^j \\ + \frac{\partial^2 [Pw]}{\partial q^i \partial p_j} Q^i P_j + \frac{1}{2} \frac{\partial^2 [Pw]}{\partial p_i \partial p_j} P_i P_j \Bigg) d\mathbf{Q} d\mathbf{P} \end{aligned} \tag{4.29}$$

using the abbreviation $[Pw] = P(\mathbf{q} + \mathbf{Q}, \mathbf{p} + \mathbf{P}, t+\tau \mid \mathbf{q}, \mathbf{p}; t) w(\mathbf{q}, \mathbf{p}, t)$. Since $\mathbf{Q}$ and $\mathbf{P}$ do not explicitly depend on $\mathbf{q}$ and $\mathbf{p}$, it is possible to write

$$\frac{\partial^2 [Pw]}{\partial q^i \partial q^j} Q^i Q^j = \frac{\partial}{\partial q^i} \left(\frac{\partial [Pw] Q^j}{\partial q^j} \right) Q^i \tag{4.30}$$

where the right side is a properly covariant expression, which also holds for the second partial derivative expression on the left side of the equation. Introducing moments

$$\begin{aligned} 1 &= \int P(\mathbf{q} + \mathbf{Q}, \mathbf{p} + \mathbf{P}; t+\tau \mid \mathbf{q}, \mathbf{p}; t) d\mathbf{Q} d\mathbf{P} \\ M_{Q_i} &= \int P(\mathbf{q} + \mathbf{Q}, \mathbf{p} + \mathbf{P}; t+\tau \mid \mathbf{q}, \mathbf{p}; t) Q^i d\mathbf{Q} d\mathbf{P} \\ M_{Q_i Q_j} &= \int P(\mathbf{q} + \mathbf{Q}, \mathbf{p} + \mathbf{P}; t+\tau \mid \mathbf{q}, \mathbf{p}; t) Q^i Q^j d\mathbf{Q} d\mathbf{P} \end{aligned} \tag{4.31}$$

as well as analogous moments $M_{P^i}, M_{P^i P^j}$, and $M_{Q_i P^j}$, Eq. (4.29) becomes

$$\begin{aligned} w(\mathbf{q}, \mathbf{p}, t+\tau) = w(\mathbf{q}, \mathbf{p}, t) - \frac{\partial \left(w M_{Q_i} \right)}{\partial q^i} - \frac{\partial \left(w M_{P^i} \right)}{\partial p_i} \\ + \frac{1}{2} \left(\frac{\partial^2 \left(w M_{Q_i Q_j} \right)}{\partial q^i \partial q^j} + \frac{\partial^2 \left(w M_{P^i P^j} \right)}{\partial p_i \partial p_j} + 2 \frac{\partial^2 \left(w M_{Q_i P^j} \right)}{\partial q^i \partial p_j} \right). \end{aligned} \tag{4.32}$$

We relate the Kramers-Moyal moments to the coefficients of the Langevin equations in order to give a concrete meaning to the previous formalism. Kramers transport theory is assumed to describe systems at fixed temperature in its standard form. Therefore, assume that the temperature is constant. Integrating the first two Langevin equations (4.16) over a short time interval τ we get

$$\begin{aligned} q^i(t+\tau) - q^i(t) &= \tau \left(\mathcal{M}^{-1} \right)^{ij} p_j(t) \\ p_i(t+\tau) - p_i(t) &= \tau K_i^{(\mathrm{det})} + \sum_j g_{ij} \int_t^{t+\tau} \Gamma_j(t')\, dt' \end{aligned} \tag{4.33}$$

where

$$K_i^{(\mathrm{det})} = -\left(\partial_{q^i} F + (1/2) \partial_{q^i} \left(\mathcal{M}^{-1} \right)^{jk} p_j p_k + \eta_{ij} \left(\mathcal{M}^{-1} \right)^{jk} p_k \right) \tag{4.34}$$

is the deterministic force and the Ito discretization of the stochastic integral was used. These equations yield the following averages over $\mathbf{q}(t+\tau)$ and $\mathbf{p}(t+\tau)$ for fixed $\mathbf{q}(t)$ and

$\mathbf{p}(t)$

$$
\begin{aligned}
M_{Q_i} &= \left\langle q^i(t+\tau) - q^i(t) \right\rangle = \tau \left(\mathcal{M}^{-1}\right)^{ij} p_j(t) \\
M_{P^i} &= \left\langle p_i(t+\tau) - p_i(t) \right\rangle = \tau K_i^{(\mathrm{det})} + \sum_j g_{ij} \int \left\langle \Gamma_j\left(t'\right) \right\rangle dt' = \tau K_i^{(\mathrm{det})} \\
M_{Q_iQ_j} &= \left\langle \left(q^i(t+\tau) - q^i(t)\right)\left(q^j(t+\tau) - q^j(t)\right) \right\rangle = \tau^2 \left(\mathcal{M}^{-1}\right)^{ik} \left(\mathcal{M}^{-1}\right)^{jl} p_k(t) p_l(t) \\
M_{Q_iP^j} &= \left\langle \left(q^i(t+\tau) - q^i(t)\right)\left(p_j(t+\tau) - p_j(t)\right) \right\rangle = \tau^2 \left(\mathcal{M}^{-1}\right)^{ik} p_k(t) K_j^{(\mathrm{det})} \\
M_{P^iP^j} &= \left\langle \left(p_i(t+\tau) - p_i(t)\right)\left(p_j(t+\tau) - p_j(t)\right) \right\rangle = \tau^2 K_i^{(\mathrm{det})} K_j^{(\mathrm{det})} + \\
&\quad + \sum_{kl}^{t+\tau} g_{ik} g_{jl} \int_t^{t+\tau} dt' \int_t^{''} dt'' \left\langle \Gamma_k\left(t'\right) \Gamma_l\left(t''\right) \right\rangle = \tau^2 K_i^{(\mathrm{det})} K_j^{(\mathrm{det})} + 2\tau \sum_k g_{ik} g_{jk}
\end{aligned}
\tag{4.35}
$$

where $\langle \Gamma_j(t) \rangle = 0$ and Eq. (5.90) were used. Inserting these results into Eq. (4.32), dividing the equation by τ, and letting τ go to zero, one obtains the Fokker-Planck equation

$$
\dot{w} = -\frac{\partial\left(\left(\mathcal{M}^{-1}\right)^{ij} p_j w\right)}{\partial q^i} - \frac{\partial\left(K_i^{(\mathrm{det})} w\right)}{\partial p_i} + \frac{\partial^2\left(D_{ij} w\right)}{\partial p_i \partial p_j} \tag{4.36}
$$

with the diffusion tensor $D_{ij} = \sum_k g_{ik} g_{jk}$.

Often the fission dynamics is assumed to be "overdamped", i.e. the inertial term $\dot{p}$ in the Langevin equations (4.16) is neglected compared to the friction term $\eta_{ij}\left(\mathcal{M}^{-1}\right)^{jk} p_k$. By introducing the contravariant inverse friction tensor $\left(\eta^{-1}\right)^{ij}$, one obtains the set of first-order differential equations in time instead of two sets.

$$
\dot{q}^j = \left(\eta^{-1}\right)^{ji} \left(-\partial_{q^i} F + \sum_k g_{ik} \Gamma_k\right) \tag{4.37}
$$

In this case, the Kramers-Moyal moments are given by

$$
\begin{aligned}
M_{Q_i} &= -\tau \left(\eta^{-1}\right)^{ij} \partial_{q^j} F \\
M_{Q_iQ_j} &= \tau \left(\eta^{-1}\right)^{il} \left[\tau \partial_{q^l} F \partial_{q^k} F + 2 \sum_r g_{lr} g_{kr}\right] \left(\eta^{-1}\right)^{jk}
\end{aligned}
\tag{4.38}
$$

and all other moments are of the order of τ^2. Eq. (4.32) thus yields

$$
\dot{w} = \frac{\partial\left[\left(\eta^{-1}\right)^{ij}\left(\partial_{q^j} F\right) w\right]}{\partial q^i} + \frac{\partial^2\left[\left(\eta^{-1}\right)^{ik} D_{kl} \left(\eta^{-1}\right)^{jl} w\right]}{\partial q^i \partial q^j} \tag{4.39}
$$

which is called the Smoluchowski equation.

In order to allow for a change in temperature along each Langevin trajectory in accordance with the last eqation in the system (4.16), one can introduce the temperature as an additional stochastic variable in probability w. Some additional terms are then added to the resulting Fokker-Planck equation by the Kramers-Moyal expansion.

In order to account for the emission of particles during the fission process, Strumberger, Dietrich, and Pomorski added the vector $\mathcal{N} = \left\{n_{\alpha\beta}^i\right\}$ to the arguments of $w(\mathbf{q}, \mathbf{p}; t)$ [122], where $n_{\alpha\beta}^i$ are the integer numbers ≥ 0 of the evaporated particles of type i that were emitted in the energy interval α and the angular momentum interval β. The quantities $w(\mathbf{q}, \mathbf{p}, \mathcal{N}; t) d\mathbf{q} d\mathbf{p}$ is therefore the probability that the system is at time t in the phase-space cell $d\mathbf{q}d\mathbf{p}$ around the point $(\mathbf{qp})$ in phase space and has emitted $n_{\alpha\beta}^i$ particles of

type i into the energy and angular momentum bins α and β, respectively. Changing the value of the function w for a given value, say 1, of one of the arguments $n^{i_0}_{\alpha_0\beta_0}$ during a short time interval τ can have two reasons: either the cell (i_0, α_0, β_0) was empty and a particle was emitted into this cell with the rate $r^{i_0}_{\alpha_0\beta_0}\left(\mathbf{q}, \mathbf{p}, \ldots, n^{i_0}_{\alpha_0\beta_0} = 0, \ldots\right)$ from an initial configuration with $n^{i_0}_{\alpha_0\beta_0} = 0$, whose probability is $w\left(\ldots, n^{i_0}_{\alpha_0\beta_0} = 0, \ldots; t\right)$; this increases the value of w, or a second particle is emitted into the same cell from a configuration with $n^{i_0}_{\alpha_0\beta_0} = 1$, in which case $w\left(\ldots, n^{i_0}_{\alpha_0\beta_0} = 1, \ldots; t\right)$ is reduced, since such events now belong to the argument $n^{i_0}_{\alpha_0\beta_0} = 2$. By this reasoning, the Master equation

$$\begin{aligned}\dot{w}\left(\ldots, n^i_{\alpha\beta}, \ldots; t\right) =& r^i_{\alpha\beta}\left(\ldots, n^i_{\alpha\beta} - 1, \ldots\right) w\left(\ldots, n^i_{\alpha\beta} - 1, \ldots; t\right) \\ &- r^i_{\alpha\beta}\left(\ldots, n^i_{\alpha\beta}, \ldots\right) w\left(\ldots, n^i_{\alpha\beta}, \ldots; t\right)\end{aligned} \tag{4.40}$$

is obtained if all other variables of w were fixed. Allowing all quantities to vary [122] derived the generalized Fokker-Planck equation

$$\begin{aligned}\dot{w} = &- \frac{\partial\left(\left(\mathcal{M}^{-1}\right)^{ij} p_j w\right)}{\partial q^i} - \frac{\partial\left(K^{(\mathrm{det})}_i w\right)}{\partial p_i} + \frac{\partial^2\left(D_{ij} w\right)}{\partial p_i \partial p_j} \\ &+ \sum_{i,\alpha,\beta}\Big[r^i_{\alpha\beta}\left(\ldots, n^i_{\alpha\beta} - 1, \ldots\right) w\left(\ldots, n^i_{\alpha\beta} - 1, \ldots; t\right) \\ &- r^i_{\alpha\beta}\left(\ldots, n^i_{\alpha\beta}, \ldots\right) w\left(\ldots, n^i_{\alpha\beta}, \ldots; t\right)\Big]\end{aligned} \tag{4.41}$$

In this expression $w\left(\ldots, n^i_{\alpha\beta} - 1, \ldots; t\right)$ is defined to disappear when $n^i_{\alpha\beta} - 1 = 0$. The mass ΔM_{nucl}, the charge ΔZ, the energy ΔE and the angular momentum ΔJ of the emitted particles can be calculated for a given vector $\mathcal{N}$. Besides their dependence on $\mathbf{q}$ and temperature T, the force K_i, the transport matrices $\mathcal{M}_{ij}$ and D_{ij}, and the emission rates $r^i_{\alpha\beta}$ depend on these quantities. Thus, although treated [46] as statistically independent in Eq. (4.41), evaporation and collective motion are dynamically coupled.

4.2.2 Approximate solution techniques for the Fokker-Planck equation

In early applications of the Fokker-Planck equation in nuclear fission theory, the global moment expansion technique was used, see e.g. Ref. [123] and the papers cited there. This approach introduces averaged coordinates and momenta

$$\overline{\mathbf{q}}(t) = \int \mathbf{q} w(\mathbf{q}, \mathbf{p}, t) d\mathbf{q} d\mathbf{p}, \quad \overline{\mathbf{p}}(t) = \int \mathbf{p} w(\mathbf{q}, \mathbf{p}, t) d\mathbf{q} d\mathbf{p} \tag{4.42}$$

and the mass and friction tensors $\mathcal{M}_{ij}(\mathbf{q})$ and $\eta_{ij}(\mathbf{q})$ in the Fokker-Planck equation (4.36) are replaced by their values at $\overline{\mathbf{q}}, \mathcal{M}_{ij}(\overline{\mathbf{q}})$ and $\eta_{ij}(\overline{\mathbf{q}})$, respectively. Another approximation of the free energy around $\overline{\mathbf{q}}$ is its quadratic expansion sion $\partial_{q^i} F(\mathbf{q}) \approx \partial_{q^i} F(\mathbf{q})\Big|_{\mathbf{q}=\overline{\mathbf{q}}} + C_{ij}(\overline{\mathbf{q}})\left(q^j - \bar{q}^j\right)$ with $C_{ij} = \partial_{q^i}\partial_{q^j} F(\mathbf{q})\Big|_{\mathbf{q}=\overline{\mathbf{q}}}$. For simplicity we will neglect the term $\partial_{q^i}\left(\mathcal{M}^{-1}\right)^{jk}$; see Ngô and Hofmann [124] for a relaxation of this latter assumption. The deterministic force (4.34) in the Fokker-Planck equation is then given by the following equation

$$K^{(\mathrm{det})}_i = -\left[\partial_{q^i} F(\overline{\mathbf{q}}) + C_{ij}(\overline{\mathbf{q}})\left(q^j - \bar{q}^j\right) + \eta_{ij}(\overline{\mathbf{q}})\left(\mathcal{M}^{-1}\right)^{jk} p_k\right] \tag{4.43}$$

With these approximations the Fokker-Planck equation becomes linear in $\mathbf{q}$ and $\mathbf{p}$

$$\begin{aligned}\dot{w} = &- \left(\mathcal{M}^{-1}\right)^{ij} p_j \frac{\partial w}{\partial q^i} + \left[\partial_{q^i} F + C_{ij}\left(q^j - \bar{q}^j\right)\right] \frac{\partial w}{\partial p_i} \\ &+ \eta_{ij}\left(\mathcal{M}^{-1}\right)^{jk} \frac{\partial p_k w}{\partial p_i} + T\eta_{ij} \frac{\partial^2 w}{\partial p_i \partial p_j}\end{aligned} \tag{4.44}$$

Multiplying this equation by $\mathbf{q}$ or $\mathbf{p}$ and integrating over all phase space variables, one obtains, after partial integration, Newton's equations of motion for $\overline{\mathbf{q}}$ and $\overline{\mathbf{p}}$.

$$\begin{aligned}\dot{\bar{q}}^i &= \left(\mathcal{M}^{-1}\right)^{ij} \bar{p}_j \\ \dot{p}_i &= -\partial_{q^i} F - \eta_{ij}\left(\mathcal{M}^{-1}\right)^{jk} \bar{p}_k\end{aligned} \tag{4.45}$$

where we assumed that w vanishes sufficiently fast for $|\mathbf{q}| \to \infty$ and $|\mathbf{p}| \to \infty$.

For the three variance matrices

$$\begin{aligned}S_{q^iq^j} &= \int \left(q^i - \bar{q}^i\right)\left(q^j - \bar{q}^j\right) w d\mathbf{q}d\mathbf{p}, \quad S_{p_ip_j} = \int \left(p_i - \bar{p}_i\right)\left(p_j - \bar{p}_j\right) w d\mathbf{q}d\mathbf{p}, \\ S_{q^ip_j} &= \int \left(q^i - \bar{q}^i\right)\left(p_j - \bar{p}_j\right) w d\mathbf{q}d\mathbf{p}\end{aligned} \tag{4.46}$$

allows the derivation of the set of ordinary coupled differential equations. By multiplying Eq. (4.44) with $\left(q^i - \bar{q}^i\right)\left(q^j - \bar{q}^j\right)$ and integrating over the whole phase space one gets $\dot{S}_{q^iq^j}$. In the same way the time derivatives of the other two variances are computed. The result is

$$\begin{aligned}\dot{S}_{q^iq^j} &= \left(\mathcal{M}^{-1}\right)^{il} S_{q^jp_l} + \left(\mathcal{M}^{-1}\right)^{jl} S_{q^ip_l} \\ \dot{S}_{q^ip_j} &= \left(\mathcal{M}^{-1}\right)^{il} S_{p_lp_j} - C_{jl} S_{q^lq^i} - \left(\mathcal{M}^{-1}\right)^{lk} \eta_{lj} S_{q^ip_k} \\ \dot{S}_{p_ip_j} &= -C_{il} S_{q^lp_j} - C_{jl} S_{q^lp_i} - \left(\mathcal{M}^{-1}\right)^{lk}\left[\eta_{il} S_{p_kp_j} + \eta_{jl} S_{p_ip_k}\right] + \eta_{ij} T.\end{aligned} \tag{4.47}$$

Observables O are typically functions of the phase space variables $O = f(\mathbf{q}, \mathbf{p})$. Their mean and variance are given by

$$\bar{O}(t) = \int f(\mathbf{q}, \mathbf{q}) w(\mathbf{p}, \mathbf{q}; t) d\mathbf{q}d\mathbf{p}$$

and

$$\Delta O = \int [f(\mathbf{q}, \mathbf{p}) - \bar{O}]^2 w(\mathbf{q}, \mathbf{p}; t) d\mathbf{q}d\mathbf{p}$$

with

$$\begin{aligned}w(\mathbf{q}, \mathbf{p}; t) = &\pi^{-n}\left(\det \begin{vmatrix} S_{q^iq^j} & S_{q^ip_j} \\ S_{q^jp_i} & S_{p_ip_j} \end{vmatrix}\right)^{1/2} \exp\left\{-S_{q^iq^j}\left(q^i - \bar{q}^i\right)\left(q^j - \bar{q}^j\right)\right. \\ &\left. -2S_{q^ip_j}\left(q^i - \bar{q}^i\right)\left(p_j - \bar{p}_j\right) - S_{p_ip_j}\left(p_i - \bar{p}_i\right)\left(p_j - \bar{p}_j\right)\right\}.\end{aligned} \tag{4.48}$$

The scheme was first applied to the asymmetry degree of freedom of strongly necked-in configurations in quasi-fission reactions [124–126] and was used in Ref. [127] or Ref. [128] to describe fission dynamics.

In the case of diffusion problems with only one collective variable, there are several additional approaches to solve the Fokker-Planck equation numerically. The simplest approach is to solve it on a grid in phase space and time. This has been done for example in [129, 130]. Scheuter and Hofmann have developed a solution technique which they call

the propagator method [131]. It is designed to give more accurate results than the global moment expansion method. A variety of solution methods are also described in Risken book [117], including expansions of the distribution function into eigenfunctions of Hermite operators related to the Fokker-Planck operator on the r.h.s. of Eq. (4.36). Most of these methods can, in principle, be applied to multidimensional systems, but, usually, for more than one-dimensional problems it seems to be easier to solve the equivalent Langevin equations.

4.2.3 Connection between Fokker-Planck and Langevin equatuions

As it was shown the Langevin equations were introduced strictly from phenomenological basis. But some authors [129] prefer to derive them from the Fokker-Planck equation (4.36). Assuming that there are stochastic, first-order equations of motion for the phase space variables $\mathbf{q}$ and $\mathbf{p}$ of the form

$$\begin{aligned} \dot{q}^i &= \left(h_1(\mathbf{q},\mathbf{p})\right)^i + \sum_j \left(g_1(\mathbf{q},\mathbf{p})\right)^i_j \left(\Gamma_1(t)\right)_j \\ \dot{p}_i &= \left(h_2(\mathbf{q},\mathbf{p})\right)_i + \sum_j \left(g_2(\mathbf{q},\mathbf{p})\right)_{ij} \left(\Gamma_2(t)\right)_j , \end{aligned} \tag{4.49}$$

Let is proove that the Fokker-Planck equation (4.36) implies that the functions $\mathbf{h}(\mathbf{q},\mathbf{p})$ and $\mathbf{g}(\mathbf{q},\mathbf{p})$ have just the form which leads to the Langevin equations (4.16). In Eqs. (4.49) it is assumed that the $\Gamma_i(t)$ are Gaussian-distributed random numbers with

$$\left\langle \left(\Gamma_\nu(t)\right)_i \right\rangle = 0 \quad \text{and} \quad \left\langle \left(\Gamma_\nu(t)\right)_i \left(\Gamma_\mu\left(t'\right)\right)_j \right\rangle = 2\delta_{\nu\mu}\delta_{ij}\delta\left(t-t'\right), \quad \nu,\mu = 1,2. \tag{4.50}$$

For a sufficiently small time step τ the equations of motion (4.49) yield

$$\begin{aligned} &q^i(t+\tau) - q^i(t) = \\ &\tau\left(h_1(\mathbf{q},\mathbf{p})\right)^i + \sum_j \left(g_1(\mathbf{q},\mathbf{p})\right)^i_j \int_t^{t+\tau} \left(\Gamma_1\left(t'\right)\right)_j dt' + \mathcal{O}\left(\tau^{3/2}\right) \end{aligned} \tag{4.51}$$

and

$$\begin{aligned} &p_i(t+\tau) - p_i(t) = \\ &\tau\left(h_2(\mathbf{q},\mathbf{p})\right)_i + \sum_j \left(g_2(\mathbf{q},\mathbf{p})\right)_{ij} \int_t^{t+\tau} \left(\Gamma_2\left(t'\right)\right)_j dt' + \mathcal{O}\left(\tau^{3/2}\right). \end{aligned} \tag{4.52}$$

From the Fokker-Planck equation follows for the Kramers-Moyal moments

$$\begin{aligned} &\lim_{\tau\to 0}\tfrac{1}{\tau}M_{Q_i} = \left(\mathcal{M}^{-1}\right)^{ij}\langle p_j\rangle, \quad \lim_{\tau\to 0}\tfrac{1}{\tau}M_{P^i} = \left(\mathcal{M}^{-1}\right)^{ij}K^{(\mathrm{det})}, \\ &\lim_{\tau\to 0}\tfrac{1}{\tau}M_{P^iP^j} = D_{ij}, \qquad \lim_{\tau\to 0}\tfrac{1}{\tau}M_{Q_iQ_j} = \lim_{\tau\to 0}\tfrac{1}{\tau}M_{Q_iP^j} = 0. \end{aligned}$$

Using these results and inserting the expressions (4.51) and (4.52) into Eqs. (4.35) yields

$$\begin{aligned} &\left(h_1(\mathbf{q},\mathbf{p})\right)^i = \left(\mathcal{M}^{-1}(\mathbf{q})\right)^{ij} p_j, \quad \left(h_2(\mathbf{q},\mathbf{p})\right)_i = K_i^{(\mathrm{det})}(\mathbf{q},\mathbf{p}), \\ &\left(g_1(\mathbf{q},\mathbf{p})\right)^i_j = 0, \qquad\qquad \sum_k \left(g_2\right)_{ik}\left(g_2\right)_{jk} = D_{ij}(\mathbf{q}), \end{aligned}$$

which completes the proof.

4.3 Basics of the particle emission

Conceptually, each Langevin trajectory should have a simultaneous evaporation cascade with light particle emission generalized to deformed emitters [132–134]. After each emission event, the dynamics of the fission must be corrected for the charge, the mass, the excitation energy, and, of course, the angular momentum that remains in the daughter system. It is assumed [46] that after such an event, the system will undergo instantaneous thermalization. This is due to the condition $B_{fiss} > T$, where the emitting rate remains low enough to allow thermal equilibrium to be restored between emitting events.

In fact, these models show direct correlation between process dynamics and particle evaporation. The energy and angular momentum dissipated by the particles prior to the passage of the trajectory through the fission barrier results in an increase in the barrier height and hence an increase in the fission lifetime. However, going further, this work aims to study the fissioning process already beyond the barrier, where the fissioning configuration will depend on the angular momentum and the temperature. Recall that the radiation rate also depends on the shape of the level density, light particle binding energies, and charged particle transfer coefficients.

The one-dimensional approximation that is associated with both the [135, 136] FPE solution and the LE solution is often used for such calculations. Relatively recently, the multidimensional [23, 111, 116] approach has been considered. At the same time, the method of determination remains unchanged from Abe's first works [108, 132], which is given below.

4.3.1 Weisskopf decay rate

The process of light particle emission from a compound nucleus is governed by the emission rate Γ_ν^α, at which a particle of type ν (neutrons, protons and α particles are considered here) is emitted at an energy in the range $\left[e_\alpha - \frac{1}{2}\Delta e_\alpha, e_\alpha + \frac{1}{2}\Delta e_\alpha\right]$ before the compound nucleus finally undergoes fission.

To describe the emission from a deformed, highly excited and rotating nucleus, several theoretical approaches have been proposed [122, 137]. The method we present below is close in spirit to the one used in [122], but in our description the widths Γ_ν^α for particle emission will additionally depend on the deformation and angular momentum of the compound nucleus.

According to the conventional evaporation theory of Weisskopf [138], the partial decay rate $\Gamma_\nu^{\alpha\beta}(E^*, L)$ for the emission of a light particle of type ν with energy e_α and orbital angular momentum ℓ_β from a compound nucleus with excitation energy E^* rotating with angular momentum L can be written as

$$\Gamma_\nu^{\alpha\beta}(E^*, L) = \frac{2S_\nu + 1}{2\pi\hbar\rho(E^*, L)} \sum_{L_R=|L-\ell_\beta|}^{L+\ell_\beta} \int_{e_\alpha-\Delta e_\alpha/2}^{e_\alpha+\Delta e_\alpha/2} w_\nu(e, \ell_\beta; \chi)\, \rho_R(E_R^*, L_R)\, de, \tag{4.53}$$

where

$$\rho(E^*, L) = (2L+1)\left(\frac{\hbar^2}{2\mathcal{J}}\right)^{3/2} \sqrt{a}\frac{e^{2\sqrt{aE^*}}}{12E^{*2}} \tag{4.54}$$

is the level density in the emitting nucleus. The level density ρ_R in the remaining (daughter) nucleus with excitation energy E_R and angular momentum L_R is obtained in the same way. Both of these quantities also depend on the mass and the number of charges as well as on the deformation of the nucleus. The quantities $\mathcal{J}$ and a are the moment of inertia and

the level density parameter of the compound nucleus, and S_ν is the intrinsic spin of the emitted particle. The quantity $w_\nu(e,\ell;\chi)$ is the transmission coefficient for the emission of a particle of type ν with energy e and angular momentum ℓ from the deformed compound nucleus. The parameter χ in the argument list of w_ν stands for all the quantities that are not explicitly mentioned here, such as the mass and the charge number, the deformation of the nucleus, the direction in space in which the particle ν is emitted. However, this approach would lead to hardly tractable numerical problems. In the Langevin formalism we are attempting here, we have to follow the dynamics of the fissioning nucleus plus evaporation for a very large number of trajectories (on the order of 10^6). Therefore, we use a simplified procedure which introduces a transmission coefficient $\bar{w}_\nu(e,\ell;\chi)$. This coefficient is obtained by double averaging over the different emission directions and over the whole surface of the deformed compound nucleus. A detailed description of the calculation of $\bar{w}_\nu(e,\ell;\chi)$ in the Hill-Wheeler approximation [32]. The width Γ_ν^α for the emission of a particle of type ν and energy e_α is given by this averaged transmission coefficient $\bar{w}$

$$\Gamma_\nu^\alpha\left(E^*,L\right)=\frac{2S_\nu+1}{2\pi\hbar\tilde{\rho}\left(E^*\right)}\int_{e_\alpha-\Delta e_\alpha/2}^{e_\alpha+\Delta e_\alpha/2}w_\nu^{\mathrm{eff}}(e;\chi)\tilde{\rho}_R\left(E_R^*\right)de \tag{4.55}$$

where

$$\tilde{\rho}\left(E^*\right)=\frac{\rho\left(E^*,L\right)}{2L+1} \tag{4.56}$$

is the angular momentum independent part of density (4.54) and similarly for $\tilde{\rho}_R$. By performing a summation over all allowed angular momenta of the emitted particle and those of the daughter nucleus, the effective transmission coefficient in (8) is obtained:

$$w_\nu^{\mathrm{eff}}(e;\chi)=\frac{1}{2L+1}\sum_{\ell_\beta=0}^{\ell_{\max}}\sum_{L_R=\left|L-\ell_\beta\right|}^{L+\ell_\beta}\left(2L_R+1\right)\bar{w}_\nu\left(e,\ell_\beta;\chi\right) \tag{4.57}$$

Here $\ell_{\max}$ is the maximum angular momentum available to the particle with energy e. As already mentioned, the emission width Γ_ν^α also depends on the mass and charge A and Z as well as on the deformation of the compound nucleus.

Once the emission widths Γ_ν^α are known, the emission algorithm can be set up [136]. This algorithm decides at each time step $[t,t+\tau]$ along each of the trajectories whether a particle is emitted from the compound nucleus. It is the value of the emission width Γ_ν^α that finally decides which light particle is emitted at which energy. Since Γ_ν^α represents the rate of emission for a particle of type ν and energy e_α, the total emission rate for a particle of a given type, independent of the energy at which it is emitted, is given by

$$\Gamma_\nu\left(E^*,L\right)=\frac{2S_\nu+1}{2\pi\hbar\tilde{\rho}\left(E^*\right)}\int_0^{e_{\max}}w_\nu^{\mathrm{eff}}(e;\chi)\tilde{\rho}_R\left(E_R^*\right)de=\sum_{\alpha=1}^{n}\Gamma_\nu^\alpha\left(E^*,L\right), \tag{4.58}$$

where we have replaced the upper integration limit by a sufficiently large constant $e_{\max}$ (which a priori will be different for the different particles). At this constant, the probabilities for particle emission will essentially vanish, n is the number of energy bins of width Δe_α in the interval $[0,e_{\max}]$. The emission rate Γ for the emission of any particle type is the sum of the Γ_ν:

$$\Gamma=\Gamma_n+\Gamma_p+\Gamma_\alpha \tag{4.59}$$

First we have to decide whether a particle will be emitted at all in the given time interval $[t,t+\tau]$. The probability of emitting a particle is given, for a sufficiently small time step τ, by

$$P(\tau)=1-e^{-\Gamma\tau}\approx\Gamma\tau \tag{4.60}$$

Then draw a random number η_1 in the interval $[0,1]$. If $\eta_1 < P(\tau)$, a light particle is emitted. If the time step τ is sufficiently small, the probability of emitting a particle will be small. In this way, we avoid considering the emission of more than one particle in each time interval, and we guarantee that at most one particle is emitted in each time interval.

In the case that a particle is emitted, the next thing to do is to decide what type of particle it is. To do this, draw a second random number η_2 in the interval $[0,1]$ and determine the localization of η_2 regarding the coverage of this interval by the three bins $\Gamma_n/\Gamma, \Gamma_p/\Gamma$, and Γ_α/Γ. Depending on which bin η_2 is in, a neutron, a proton, or a α particle will be emitted.

It is still necessary to determine the energy with which this particle is emitted, and we do this in the following way. Introducing the set

$$\Pi_\nu\left(e_\alpha\right) = \frac{1}{\Gamma_\nu}\left\{\frac{2S_\nu+1}{2\pi\tilde{\tilde{\rho}}\left(E^*\right)}\int_0^{e_\alpha} w_\nu^{\text{eff}}(e;\chi)\tilde{\rho}_R\left(E_R^*\right)de\right\} \tag{4.61}$$

which represents the probability that a particle of type ν is emitted with an energy less than e_α. The quantity covers interval $[0,1]$. By dividing the interval $[0,1]$ into a certain number of equal bins, one decides with which energy the light particle is emitted by drawing a third random number η_3 in the interval $[0,1]$. By inverting the function in equation (4.61), $\Pi_\nu^{-1}\left(\eta_3\right)$ will fall into an energy bin.

$$\Pi_\nu^{-1}\left(\eta_3\right) \in \left[e_\alpha - \frac{1}{2}\Delta e_\alpha, e_\alpha + \frac{1}{2}\Delta e_\alpha\right] \tag{4.62}$$

of the total interval $[0, e_{\max}]$ and thus determine the energy with which the particle is emitted. The coupling between the collective motion, as described by the Langevin equation, and the particle emission enters as follows The decision whether, for a given trajectory in deformation space, a particle (n,p,α) is emitted in a given time interval depends on the value of the particle emission widths of Eq. (4.58). The emission widths in turn depend on the deformation (see parameter χ in Eq. (4.58), the angular momentum L and the excitation energy E^* of the emitting nucleus. When an emission occurs, the corresponding change in excitation energy and angular momentum of the remaining nucleus is taken into account in the Langevin equation.

Thus, in this chapter we have considered some methods taken from the statistical approach to the description of nuclear fission. In particular, the multivariate Langevin equations, which take into account in detail the behavior of the nuclear surface, are proposed to explain the fission dynamics. It is assumed that, under certain assumptions, they can be used to describe low-energy fission, to which a considerable part of this thesis is devoted. Since the temperature of the nucleus plays a role in the fission process, in the section devoted to the Langevin equations, attention is paid to the relationship between temperature and other quantities included in this equation. In addition, an alternative approach to the description of fission Fokker-Planck, which describes the probability distribution of the motion of the nucleus, was considered. And the relation of the differential equations was shown. At the end it was briefly mentioned about emission of particles from the fissile nucleus together with agloritm of modeling of this process. A method of determining the emission rate and the energy of the emitted particles on the basis of the parameters of the fissile nucleus was shown.

Chapter 5

Fission dynamics of the heavy and super-heavy nuclei

This chapter is the central part of the present research, including the study of problems accompanying the numerical solution of the multidimensional system of Langevin equations together with the search for optimal model parameters. In general, all these problems can be classified according to the following criteria:

- Choice of the dimension of the collective space,
- Treatment of energy minimization,
- Stability of the solutions with respect to the time step,
- Methods for the calculation of transport coefficients,
- Boundary conditions on finite potential energy grids.

In addition, questions arise about the choice of optimal parameters, e.g. with respect to temperature effects, single-particle energy spectra, etc. The results of the model will be analyzed by comparing the obtained results with available data from experiments or from other well-established theoretical models. This analysis will make it possible to assess the extent to which the developed model can fully describe the phenomenon under study, the limits of its applicability, and to diagnose the most sensible weak points.

5.1 Main elements of the toy model

5.1.1 Role of the potential energy surfaces

Within the framework of the macroscopic-microscopic approach presented in Chapter 2, it is possible to define the generalized potential energy function corresponding to the collective motion of the nucleons inside the nucleus by the sum:

$$V(\mathbf{q}) = E_{macro}(\mathbf{q}) + E_{micro}(\mathbf{q}) + E_{rot}(\mathbf{q}). \tag{5.1}$$

where the macroscopic part, $E_{macro}(\mathbf{q})$, is the energy of the nuclear liquid drop, $E_{micro}(\mathbf{q})$ is the microscopic energy contribution describing the quantum effects felt by the nucleons in an atomic nucleus. The quantity $E_{rot}(\mathbf{q})$ is the rotational energy caused by the center potential, the term which is not considered here because the orbital angular momentum of the system is assumed to be $L = 0$. In this model, the energy of the liquid drop is defined

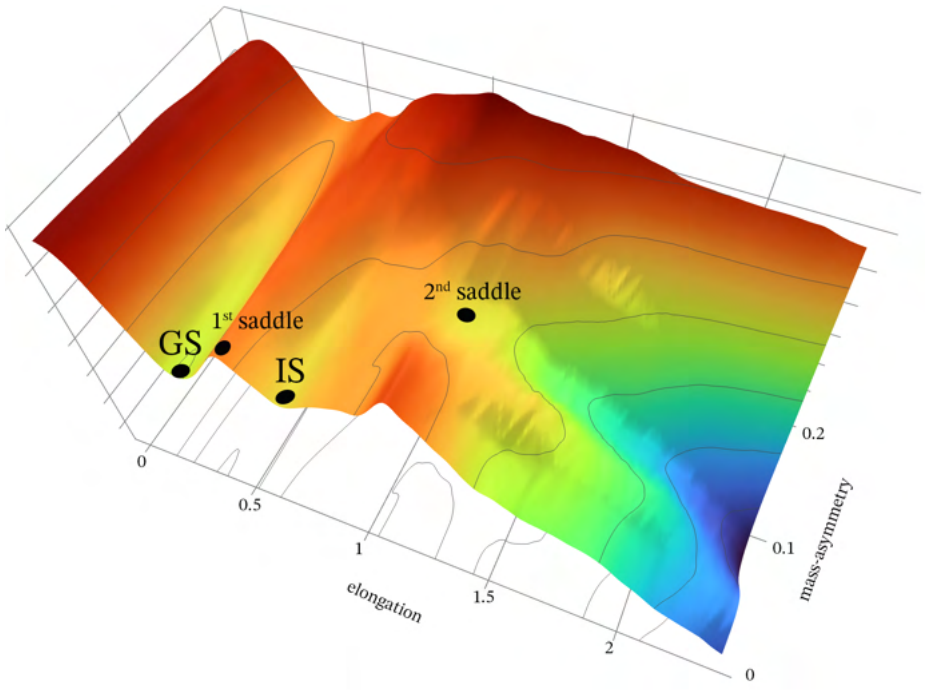

Figure 5.1: PES for Pu-238 with demonstration main turning points

within the LSD model (2.41) (see subsection 2.1.5). As was mentioned in section 2.3 the microscopic part is calculated using the two components, shell and pairing:

$$E_{\text{shell}} = \sum_k e_k - \tilde{E}, \tag{5.2}$$

$$E_{\text{pair}} = E_{\text{BCS}} - \sum_k e_k - \tilde{E}_{\text{pair}}, \tag{5.3}$$

where e_k are the energies of the single-particle states calculated in the Yukawa-folded potential of Ref. [60, 62] and $\tilde{E}$ denotes the average Strutinsky energy presented in section 2.3.3.

By setting the surface shape of the nucleus in one of the methods proposed in the previous chapter, it is now possible to determine the values of the potential energy function at an arbitrary deformation point. By varying one degree of freedom and defining the other variables according to the imposed rules, we obtain a curve describing the fission barrier, classic examples of which are the one-hump barrier proposed by Bohr and Wheeler or the two-hump Strutinsky-like barrier. By introducing another independent deformation parameter, one obtains a plane shown in a three-dimensional plot as in Fig. 5.1, which is called the potential energy surface (PES). As can be deduced, the addition of another degree of freedom to the PES function transforms it into a more complex multidimensional object, much more complicated for qualitative analyses. In this case, the following treatments are used:

- Consideration of a slice of the potential energy surface at a fixed value of one or more (in the case of more than 2 degrees of freedom) coordinates,
- Minimization of the potential energy function with respect to one or more coordinates,
- Combination of the two previous approaches.

In this work, all of the above options will be used.

For the study of the fission process it is very convenient to consider the contour plots (maps) of the PES in the coordinate plane $\{elongation,\ mass-asymmetry\}$, i.e. in the

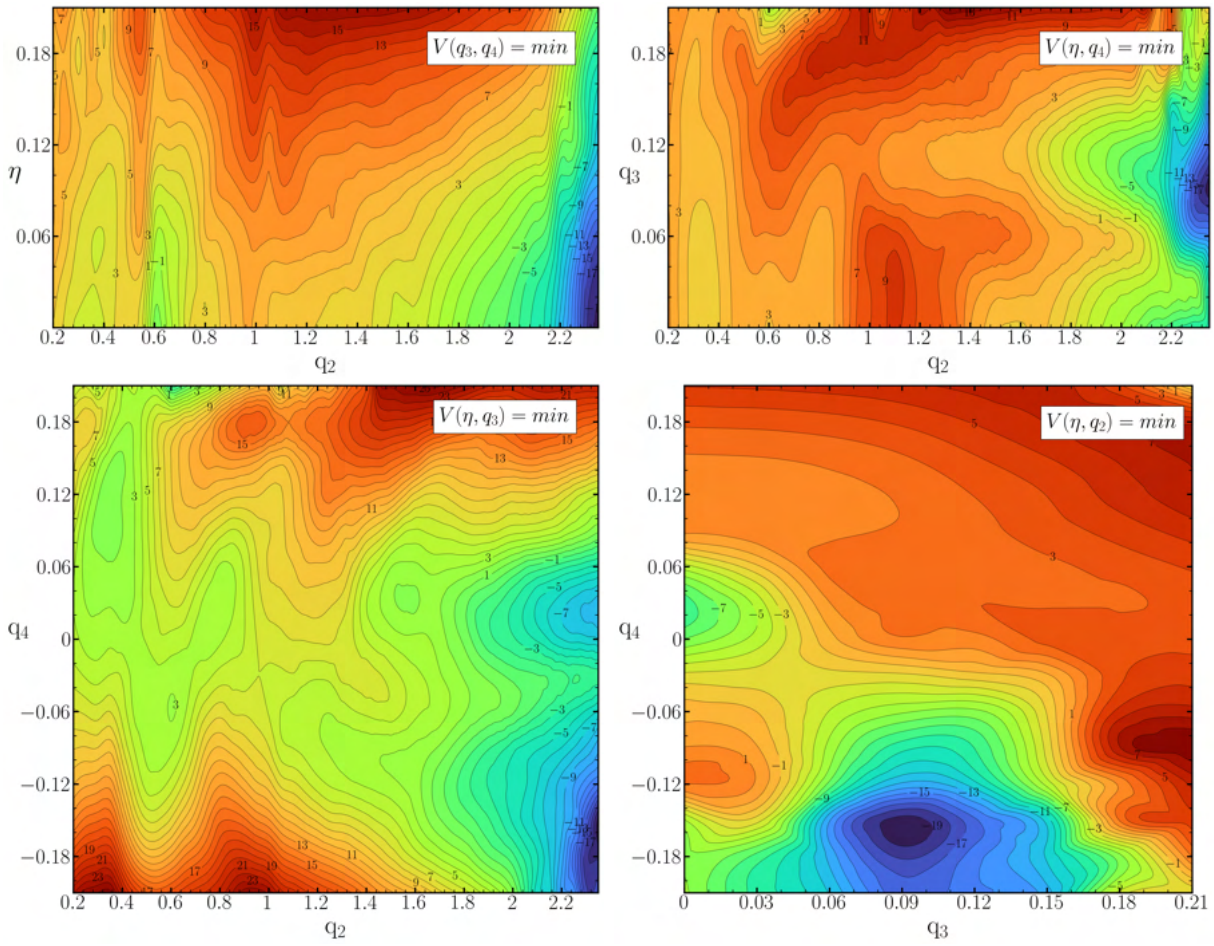

Figure 5.2: Several 4D PES cross sections ^{228}Th that are minimized in terms of energies at the coordinates that are not included in the cross-section.

framework section 3.1.5 of the Fourier parametrization $\{q_2, q_3\}$ with minimization with respect to the neck parameter, q_4, or in the coordinates $\{q_2, q_4\}$ with fixed values of q_3, which are taken mainly for the symmetric, $q_3 = 0$, fission channel. The examples of PES cross-sections are shown in Fig. 5.2, where we present all possible two-dimensional maps. If the non-axiality parameter η is not included in the description of the potential energy map, it is assumed that the nuclei are axially symmetric, i.e. $\eta = 0$.

Let us return to fig. 5.1, where a two-dimensional plane $\{q_2, q_3\}$ is shown. For almost any map in the $\{q_2, q_3\}$ plane, the following distinct regions exist:

1. First minimum, corresponding to the ground state of the system. For some actinide and especially superheavy nuclei, the ground state may have a non-axial shape [40, 115], so the fission dynamics calculations must be performed in full, four-dimensional Fourier space.

2. The first maximum or the first saddle point. This barrier separates isomeric states from the ground state.

3. The second minimum or isomeric state of the atomic nucleus, where it can remain for a relatively long time. This region is also a kind of "maneuvering space," since the nucleus can either emit a gamma quanta or a neutron, thereby thermalizing back to the ground state of the daughter nucleus, or it can undergo spontaneous fission by tunneling through the remaining barrier.

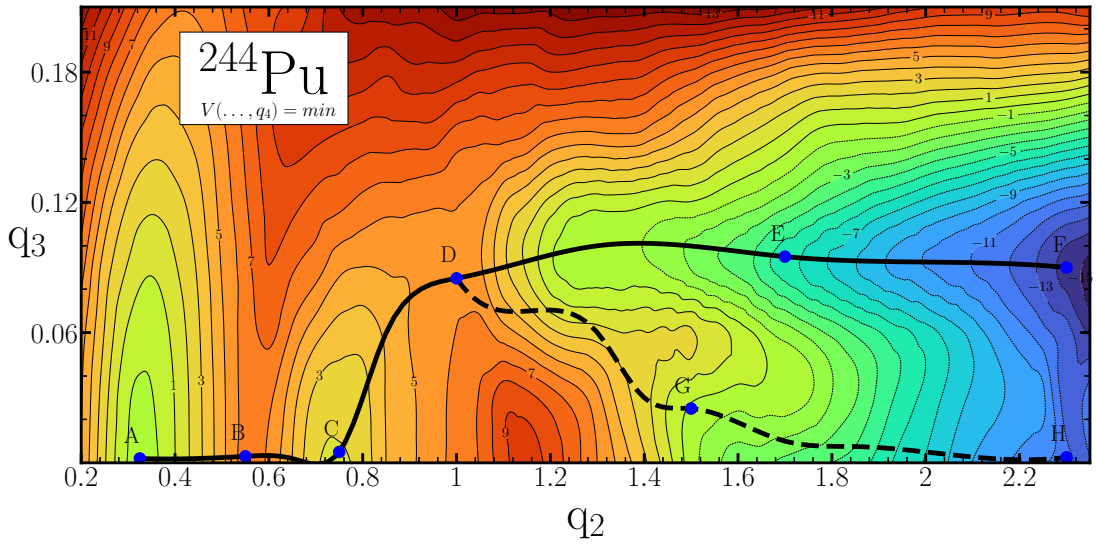

Figure 5.3: Demonstration of asymmetric (solid line) and symmetric fission path on example of ^{244}Pu PES.

4. The second maximum or second saddle point. This is the point of no return after which the system should breakup. This is the most interesting region.

One can now perform a qualitative analysis of a PES. For example, consider a compound system ^{244}Pu that is in an excited state, with the excitation energy above the fission barrier. The PES map in the coordinate plane $\{q_2, q_3\}$ when minimizing the energy with respect to the parameter q_4 is shown in Fig. 5.3. When studying the fission path, it is assumed that point A is the ground state. With sufficient energy reserve, the system easily crosses the barrier B, the isomeric region with the center at C and the second barrier at D. Then, at low over-barrier energies, the system will pass the point E and enter the asymmetric region, where a breakup will occur in the region at point F. For higher energies, there is a possibility that the system at point E will change direction to the symmetric fission region to point G, where it will travel a longer path than for the asymmetric case. At very high energies, the symmetric fission channel is more than likely. Therefore, we can immediately state that if the excitation energy of the system exceeds the value of the fission barrier by more than a few tens of MeV, the temperature of the system will exceed the value of 2 MeV. As a consequence, in the absence of orbital angular momentum, the microscopic energy effects simply become irrelevant. As we will show in the following section, the influence of the starting point and the initial excitation energy is also important for the exit point of the Langevin trajectory, which unambiguously determines the fragmentation of the nucleus in the fission process.

5.1.2 Construction of the toy model

The basis of the model is the stochastic approach discussed in subsection 4.1, using the system of Langevin equations (4.16) describing the dynamics of the surface of the nucleus (A, Z). By imposing the time step Δt and a certain set of boundary conditions on the vectors of the canonically conjugated dynamical variables $\mathbf{q}(\mathbf{t_0})$, $\mathbf{p}(\mathbf{t_0})$, one gets the solution of these equations as new vectors $\mathbf{q}(\mathbf{t_0} + \mathbf{\Delta t})$, $\mathbf{p}(\mathbf{t_0} + \mathbf{\Delta t})$ defined in the following time while $t_0 + \Delta t$. After a large number of time iterations, when the "termination conditions" for a single trajectory are fulfilled, one finally obtains the set of coordinates $\mathbf{q}^{final}$, which give complete information about the fragmentation of the nuclear surfaces A_1

and A_2 ($A_1 + A_2 = A$) by fission. The mass distributions (yields) of the fragments (FMD / FMY) are one of the main characteristics of nuclear fission. It is directly or indirectly related to other observed characteristics (distributions) of the fission process, such as the total kinetic energy distribution (TKE) or the fragment charge distributions (FCD/FCY). In addition, the knowledge of the final momenta, $\mathbf{p}^{final}$, gives us useful information about the final kinetic energy of the fragments, which contributes to the TKE.

Again let us write out the numerical solution (4.18) by replacing $\mathbf{q}(t_{n-1}) \equiv \mathbf{q}(t+\tau) = \mathbf{q}^n$, $\mathbf{q}(t_n) = \mathbf{q}^{n+1}$ and $\mathbf{p}(t_{n-1}) = \mathbf{p}^n$, $\mathbf{p}(t_n) = \mathbf{p}^{n+1}$

$$\begin{cases} q_i^{n+1} = q_i^n + \tau \sum\limits_j \left[\mathcal{M}^{-1}(\mathbf{q}^n)\right]_{ij} \left(p_j^n + \dfrac{p_j^{n+1} - p_j^n}{2}\right) \\ p_i^{n+1} = p_i^n - \tau \left(\dfrac{1}{2} \sum\limits_{jk} \dfrac{d\left[\mathcal{M}^{-1}(\mathbf{q}^n)\right]_{jk}}{dq_i} p_j^n p_k^n + \dfrac{\partial F(\mathbf{q}^n, T)}{\partial q_i} \right. \\ \qquad \left. + \sum\limits_{jk} \gamma_{ij}(\mathbf{q}^n) \left[\mathcal{M}^{-1}(\mathbf{q}^n)\right]_{jk} p_k^n \right) + \sum\limits_j g_{ij}(\mathbf{q}^n) \sqrt{\tau} \xi_j. \end{cases} \tag{5.4}$$

The function ξ_j is given by the formula (4.18), where w_k and w_{k+1} are numbers taken from a normalized Gaussian random distribution with parameters for mean $\mu = 0$ and mean square deviation $\sigma = 2$. Given this, the Helmholtz free energy F has the following expression

$$F(\mathbf{q}, T) = V(\mathbf{q}) - aT^2. \tag{5.5}$$

where the level-density parameter a depends on A, Z and also on the actual deformation $\mathbf{q}$. Its value can be determined using the phenomenological formula derived from the study of shell effects [119], which has the form:

$$a(\mathbf{q}) = 0.092A + 0.036A^{2/3} B_{\text{surf}}(\mathbf{q}) + 0.275A^{1/3} B_{\text{curv}}(\mathbf{q}) + 0.00146Z^2 A^{-1/3} B_{\text{Coul}}(\mathbf{q}), \tag{5.6}$$

In the Eq. (5.6), the coefficients $B_{\text{surf}}, B_{\text{curv}}, B_{\text{Coul}}$ are calculated using the equations (2.36) as in the LSD model. Thus, the partial differentiation of F (5.5) over the coordinates q_i gives

$$\frac{\partial F(\mathbf{q}, T)}{\partial q_i} = \frac{\partial V(\mathbf{q})}{\partial q_i} - T^2 \frac{\partial a(\mathbf{q})}{\partial q_i} \tag{5.7}$$

In the first approximation above, it is assumed that there is no significant change in temperature, i.e. T = *const*, and that it does not exceed the value of 1 MeV.

The inertia (mass) tensor $\mathcal{M}_{ij}$ is calculated within the hydrodynamic model presented in the section 3.2.2, while the friction tensor γ_{ij} is evaluated using the "wall" formula approach (3.89), i.e. $\gamma_{ij} = c_\gamma \gamma_{ij}^{\text{wall}}$, where the factor c_γ is a specific dimensionless constant to be discussed later. Now we can say that, as noted in 3.2.2, the resulting values of the friction tensor within the "wall" formula are considered too large. Therefore, very often they resort to artificial reduction of its value by the coefficient, which is in the range of 0.05 – 0.5. However, some authors use the γ_{ij} tensor without any scaling factor. A detailed discussion of this modification is given in the next section (see 5.2.2).

Formally, the deformation-dependent quantities described above should be known at each subsequent time. However, one can easily see that such a methodology would increase the computational complexity. Within the framework of a statistical model, where the number of trajectories must be of the order of 10^5, one has to perform the calculations in an approximate way by defining the potential and transport parameter functions of several variables on finite grids.

Grid calculations

As mentioned above, an effective way to perform multidimensional Langevin calculations of fission dynamics is to use a discrete grid in multidimensional deformation space, whose nodes correspond, for example, to equidistant values of the coordinate $\mathbf{q}_k$. The step between the nodes of this grid depends of course on the specific problem and the available computing power. Thus, for the purposes of this study, the constant node step of almost all coordinates is assumed to be $\Delta q_i = 0.03$. The exception is the coordinate responsible for the elongation of the system, q_2, for which $\Delta q_2 = 0.05$. These are the values that appear in the works [40, 41, 78, 115, 116, 139], which show that such a distance is optimal for the analysis of spontaneous and induced nuclear fission processes. It is also worth noting that more complex dynamic grid calculations, where the step has a non-constant value, such as in the work [20], can be used to study the fission characteristics.

Of course, the question arises: How to determine the values between the grid nodes? Obviously, one has to use some effective approximation or interpolation techniques in multidimensional spaces. There are countless approaches used in such calculations. The model developed in this thesis uses a relatively simple and convenient Gauss-Hermite approximation proposed in Ref. [77], which allows to describe the between-node values with sufficiently good accuracy. A detailed description of this method is given in the Appendix. Here we can only note that the minimum space required for a reliable reproduction of the grid values should be 3 nodes per edge. Increasing this number to 5 nodes, in the three-dimensional case, the characteristic time to determine the value of a function in a single deformation point with a relative error reaching 0.1% is $\approx 1\,\mu s$.

The size of the space required to study the fission process also varies depending on the nucleus under study. In the most general form, if one is interested in the complete path taken by the system from the ground state to the decay into fragments, it is necessary to consider the coordinate q_2 starting from the region close to the spherical configuration (i.e. $q_2 \approx 0$) and ending with the most probable breakup shape with elongation of about 2.3 – 3. For illustration, Fig. 5.4 shows various surface shapes constructed in the Fourier parametrization (3.43) in the three-dimensional coordinate representation of $\{q_2, q_3, q_4\}$. This figure shows that the limits of the asymmetry parameter q_3 must be in the region above 0.2 and can range from 0.2 (the region of actinide nuclei) to 0.3 (the region of superheavy nuclei), depending on the region of the particular nuclei. The neck thickness parameter q_4 fits perfectly in the range $[-0.21, 0.21]$, which allows to describe both diamond-like and neck shapes. The only exception is the artifact that appears in a specific extreme configuration with $\mathbf{q} = \{3, 0.3, 0.21\}$ (last in the bottom row of Fig. 5.4). Actinides generally use a three-dimensional deformation mesh with the following characteristics

$$\begin{aligned} q_2 &= [\quad 0 \quad (0.05)\ 2.35] \\ q_3 &= [-0.21\ (0.03)\ 0.21] \\ q_4 &= [-0.21\ (0.03)\ 0.21] \end{aligned} \tag{5.8}$$

or its "elongated" version:

$$\begin{aligned} q_2 &= [\quad 0 \quad (0.05)\ 2.90] \\ q_3 &= [-0.21\ (0.03)\ 0.21] \\ q_4 &= [-0.21\ (0.03)\ 0.21] \end{aligned} \tag{5.9}$$

For the SHE, the asymmetry parameter must be extended to account for super-asymmetric

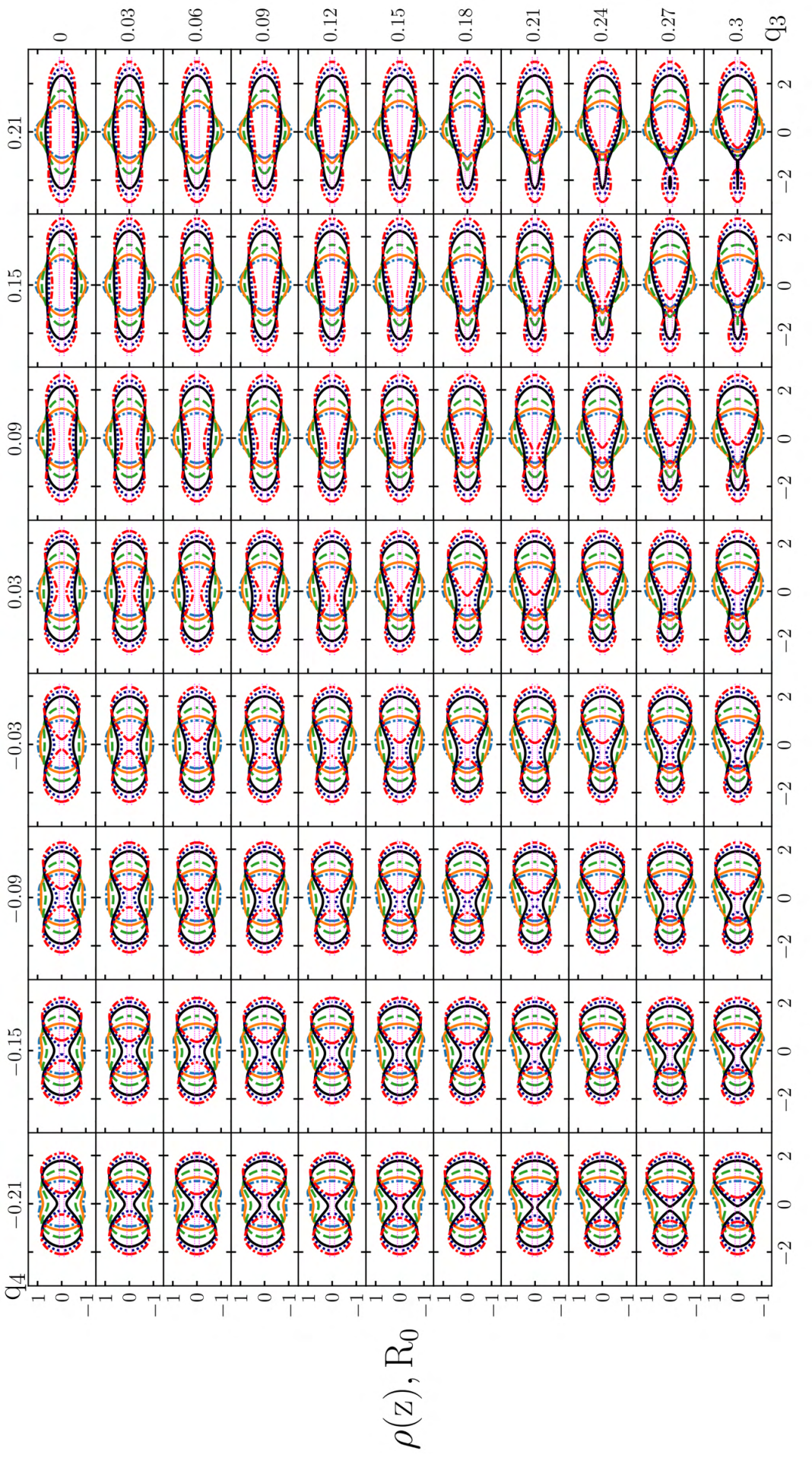

Figure 5.4: Fourier-like surface shapes for $q_2 = 0$ (blue dot-dashed line), $q_2 = 0.35$ (blue dot-dashed line), $q_2 = 1$ (green dashed line), $q_2 = 1.9$ (black solid line), $q_2 = 2.4$ (navy dotted line) and $q_2 = 3$ (red dot-dashed line). The magenta dotted line corresponds to the approximate size of the nucleon d_n.

fission

$$\begin{aligned} q_2 &= [\quad 0 \quad (0.05)\ 2.35] \\ q_3 &= [-0.27\ (0.03)\ 0.27] \\ q_4 &= [-0.21\ (0.03)\ 0.21] \end{aligned} \tag{5.10}$$

Therefore, with a given grid of potential energy, transport coefficients and all geometric characteristics of the nuclear surface, we come to the problem of boundary conditions to solve the set of Langevin equations in a unique way.

Basic boundary conditions

Before proceeding directly to the calculation of the system (5.4), it is necessary to specify the most basic boundary conditions. For this study, we consider the compound system ^{236}U formed by the thermal neutron capture by the nucleus ^{235}U. Since we are considering an induced fission reaction, the amount of excitation energy is sufficient to overcome all the barriers placed on the PES. Therefore, any one of the set of turning points (A, B, C, D) described earlier in Fig. 5.3 can be taken as the starting point $\mathbf{q}^{start}$. If the system passing through the barriers is not heated, it is most favorable to choose the point D. So from the region (5.8) only the part bounded by coordinate q_2 in the range $[q_2^{2^{nd}sad}, 2.35]$ is interesting. Next, near the point $\mathbf{q}^{start}$, using the normal distribution $\xi_{norm}(\mu, \sigma)$ with mean $\mu = 0$ and standard deviation $\sigma = 0.5\Delta q_i$, the deformation configuration $\mathbf{q}^{(1)}$ and their conjugated momentum $\mathbf{p}^{(1)}$ is determined by the following condition:

$$E_{kin}(\mathbf{q}^{(1)}) = \frac{1}{2}\sum_{ij}\left[\mathcal{M}^{-1}((\mathbf{q}^1)\right]_{ij} p_i^1 p_j^1 \equiv \Delta V = V(\mathbf{q}^{start}) - V(\mathbf{q}^1) \geq 0, \tag{5.11}$$

assuming, of course, that the conjugated momentum $\mathbf{p}_{start}$ at the start is zero.

If $E_{kin}(\mathbf{q}^{(1)}) < 0$, the procedure for selecting the point $\mathbf{q}^{start}$ is repeated. The values of the moments $p_k^{(1)}$, like the coordinates $\mathbf{q}^{(1)}$, must be randomly distributed. The mean (standard) deviation for the i^{th} momentum component within its normal distribution ξ_{norm} is $\sigma = E_{kin}^{(1)}\mathcal{M}_{ii}(\mathbf{q}^{(1)})$. To finally identify the randomly chosen momenta p_i' with the actual components of $p_i^{(1)}$ entering the Langevin equations as initial values, they must be renormalized as

$$p_k^{(1)} = p_k' \sqrt{\frac{E_{kin}^{(1)}}{\frac{1}{2}\sum_{ij}\left[\mathcal{M}^{-1}(\mathbf{q}^1)\right]_{ij} p_i' p_j'}}$$

to satisfy the condition (5.11). Alternatively, a simpler procedure is possible by using the Heisenberg Uncertainty Principle relation, which relates the uncertainty Δq_i and Δp_i to a similar renormalization procedure for the vector $\mathbf{p}^1$.

For all of them, the conjugate momentum p_2 is chosen with a positive sign, so that the trajectory runs in the direction of increasing strain. Moreover, if the trajectory turns backward and reaches the value $q_2^{2^{nd}sad}$, such a trajectory is excluded from consideration as unphysical. It is also possible that on the way to fission one of the coordinates q_i, $i = 3, 4$, reaches its limit given in (5.8) before the trajectory termination condition is satisfied. Technically, such a trajectory does not lead to a partition of the system and should be excluded. In order not to increase the computation time, i.e. to reduce the number of unphysical (failed) trajectories, it has been suggested to place "walls" at the corresponding edges of the deformation grid. At these walls the trajectory seems to bounce, changing the sign of the corresponding coupled angular momentum, which allows it to turn around and continue its evolution. At coordinate q_2 the situation is somewhat different. Once the maximum value of $q_2^{max} = 2.35$ is reached, the system stretches to more than twice the

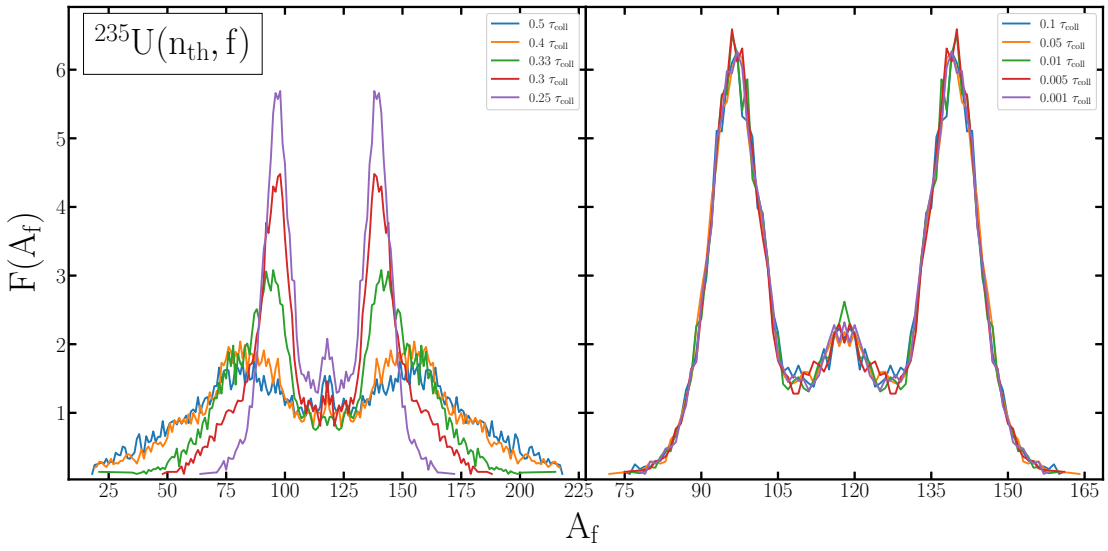

Figure 5.5: The behaviour of solution stability from iteration step on example of thermal neutron induced fission rection of ^{236}U

length of the ground state (see fig. 5.4). Therefore, we can safely assume that the system will decay beyond this value anyway, i.e. it means that here is where the fission line starts, which is actually a very rough approximation.

Time step solution stability

Now that all input parameters have been specified, the question remains of choosing the time step τ over which the integration of the system (5.4) is performed.

Note that τ is related to the characteristic relaxation time $\tau_{coll} = 2/\beta = \frac{2\mathcal{M}}{\gamma}$ and is of the order of $\sim 10^{-21}$ seconds (see scales line of the Fig. 1.1). Nevertheless, the value of this parameter is very important for the stability of our solutions. For this purpose we solve the system with different values of τ for the following values of β: 0.5, 0.4, 0.33, 0.25, 0.1, 0.05, 0.01, 0.005, 0.001. As a statistical sample for such tests, 10^4 trajectories meeting the criteria described above are sufficient. The temperature has a constant value of 0.15 MeV, which corresponds to an excitation of $V_B + 0.5 \approx .6$ MeV from the ground state. The stability of the solution is evaluated in terms of the change in the shape of the fragment mass distribution (FMD). Figure 5.5 shows the results for all the values mentioned above. It is not difficult to see that starting from a value of $0.1\tau_{coll}$, the solutions become stable, with deviations in the values not exceeding the statistical error. In fact, at large time steps, the trajectory weakly accounts for the influence of PES, passing through it almost freely. As the step is reduced, sensitivity to the numerically determined potential energy gradient appears.This gives the sawtooth curves with $\tau > 0.25\tau_{coll}$, which by the way does not disappear in the symmetric fission region even if very small steps are used, since the noise function ξ plays the main role there.

It should be noted, however, that the smaller the step, the greater the chance that the trajectory will have to be discarded from consideration because it does not satisfy a boundary condition. At this stage, this effect is negligible. For example, statistically, for every 1000 "physical" trajectories at a step of 0.05 τ, there are 867 "unphysical" trajectories, while at 0.01 τ, 0.005 τ, and 0.001 τ there are 849, 873, and 891, respectively. This insensitivity is confirmed by the second panel of Fig. 5.5.

This completes the main arrangements of the toy model. As can be seen, no estimates

or comparisons with the experimental mass distribution have been made here. However, it is safe to say that the positions of asymmetric fission peaks are well described within this simplest model as well. It is another matter that the considered nuclear reaction does not have such a serious contribution to symmetric fission, which indicates the necessity of additional conditions on the terminal configurations. Finally, the temperature is constant, which means that heating of the system, leading to increasing of the friction and diffusion tensors, weakening of quantum effects, and even thermalization processes are not taken into account. All this will be considered in further sections and subsections. Finally, it is decided that the optimal range for the time step seems to be around $0.01\tau - 0.05\tau$, of which the highest value 0.01τ is considered in this work.

This completes the main arrangements of the presented model, where, as we mentioned at the beginning of this chapter, the temperature is kept constant all along the trajectory. As can be seen, no estimates or comparisons with the experimental mass distribution have been made here. However, it is safe to say that the positions of the asymmetric peaks are well described even within this simple model. It is another matter that the considered nuclear reaction does not have such a serious contribution to symmetric fission, which indicates the necessity of assuming an additional condition for the final pre-fission configurations. Since $T = const$, the heating of the system, which leads to an increase of friction and diffusion effects and consequently to a weakening of quantum effects, is not taken into account. All these factors will be taken into account in further discussions.

5.2 Temperature effects

In 4.1 the Langevin equation system (4.16) consists of three equations, where the latter is equivalent to the energy conservation law [46] in numerical form (4.26). Then, in the framework of the model, at time $n\tau$ it can be represented by a simple relation:

$$a(\mathbf{q}(\mathbf{n}\tau))T^2 = E_{\text{total}} - E_{\text{kin}}(\mathbf{q}(\mathbf{n}\tau)) - V(\mathbf{q}(\mathbf{n}\tau)) - E_0, \tag{5.12}$$

where the total energy of the system is defined as the sum of the initial excitation energy E^*_{start} and the ground state energy V_{GS}.

$$E_{\text{total}} = E^*_{start} + V_{GS}$$

The energy E_0 in the equation 5.12 is the zero vibrational energy of the system $\frac{\hbar\omega_0^2}{2}$, which of course has a different value for each nucleus and is in the range 0.5 – 2 MeV. Let's assume for the moment that $E_0 = 1$ MeV. In addition, it is obvious that, according to the law of conservation, the energy released in the form of heat must have a positive value. As for the temperature, formally it should grow along the whole trajectory due to the presense of the dissipation of energy.

Thus, it is very interesting to look at the behavior of the excitation energy E^* at each iteration. We will consider three situations: First, with near-barrier excitations (~ 1 MeV), second, excitation close to the mean energy value (~ 10 MeV), and third, when the excitation energy is much higher than the top of the barrier. The corresponding energies are $[V_B, V_B + 2, V_B + 10, V_B + 40]$ MeV.

In addition to the previously discussed starting point near the second saddle, it is also instructive to consider starting points near the ground state (GS). In this case, the condition to be fulfilled by the initial configuration is defined by the following relation:

$$E_{kin} = E_0 - V(\mathbf{q}^{GS}) - V(\mathbf{q}^{start}) \tag{5.13}$$

The results are shown in Figs. 5.6 and 5.7, which illustrate the behavior of both the energy and the trajectories themselves on the PES in the $\{q_2, q_3\}$ plane. The behavior is quite adequate for situations with excitation energies above 10 MeV for each of the starting options. In contrast, as the excitation decreases, there are very dangerous energy changes, often going towards negative values. Analyzing the trajectories, we can see that these falls are associated with moments when the system tries to move into a region of higher values of the potential, or just to pass directly through the barriers, or it is associated with the "bounce" from the walls of the space. It is therefore not surprising that for low energy fission the numerical solutions of the Langevin equation can go beyond the energy conservation law, especially when the starting point corresponds to the ground state. This leads to the assumption that for such reactions it is best to consider the fission process starting from the second saddle region, since there is no problem with the numerical description of the energy conservation law.

Figure 5.10 shows the trajectories and dynamics of the excitation energy at a non-constant time step for both cases of starting from the ground state and from the second barrier. Comparing similar results with Figs. 5.8 and 5.9, it can be seen that the difference between these methods is not noticeable before the moment when the system starts to heat up.

It is also necessary to mention the most radical solution. If during the calculation of the trajectory a violation of the law of energy conservation is detected, this trajectory is declared unphysical and discarded from consideration. Using this approach, it was possible to obtain a fairly good FMD despite the small statistics of "physical" trajectories ($\sim 10^3$). However, the time required to compute even a few thousand trajectories from the second saddle point is tens of hours, while from the ground state, strictly speaking, is unknown to the author of this paper. Nevertheless, this problem has been studied. For this purpose, an investigation of the limiting threshold, the so-called "error", i.e. the violation of the equality (5.12), was carried out. It was found that it would take at least 30 minutes to calculate a "physical" trajectory from the ground state, where the mentioned equality is maintained up to 1 MeV. Thus, it is easy to estimate that with the statistics of 5000 "physical" trajectories, the computation time could take more than 100 days, which is contrary to the goal of this study.

It is clear from almost all of the above figures that the heating of the fission system takes place mainly in the last stage of fission, when the system passes the second fission barrier. This certainly argues in favor of considering the temperature effects of the low-energy nuclear fission process only beyond the second saddle point.

5.2.1 Shell effects at various excitations

It is known that the microscopic component of the potential associated with the shell effects gradually vanishes with increasing excitation energy and disappears completely for excitations up to 2–3 MeV per nucleon. Pairing interactions also have an excitation dependence, but they disappear even for more [140] low excitations $\approx$ 10 MeV. Since the calculation of the shell corrections is done within a standard procedure for the case of $E^* = 0$, and becomes quite time-consuming for non-zero excitations, the following effective approximation was proposed in [141]:

$$E_{\text{shell}}(E^*) = E_{\text{shell}}(E^* = 0)e^{-E^*/E_d}. \tag{5.14}$$

It should be noted that to present day the expression (5.14) is widely used in many theoretical models, providing a simple way to account for the temperature dependence of the

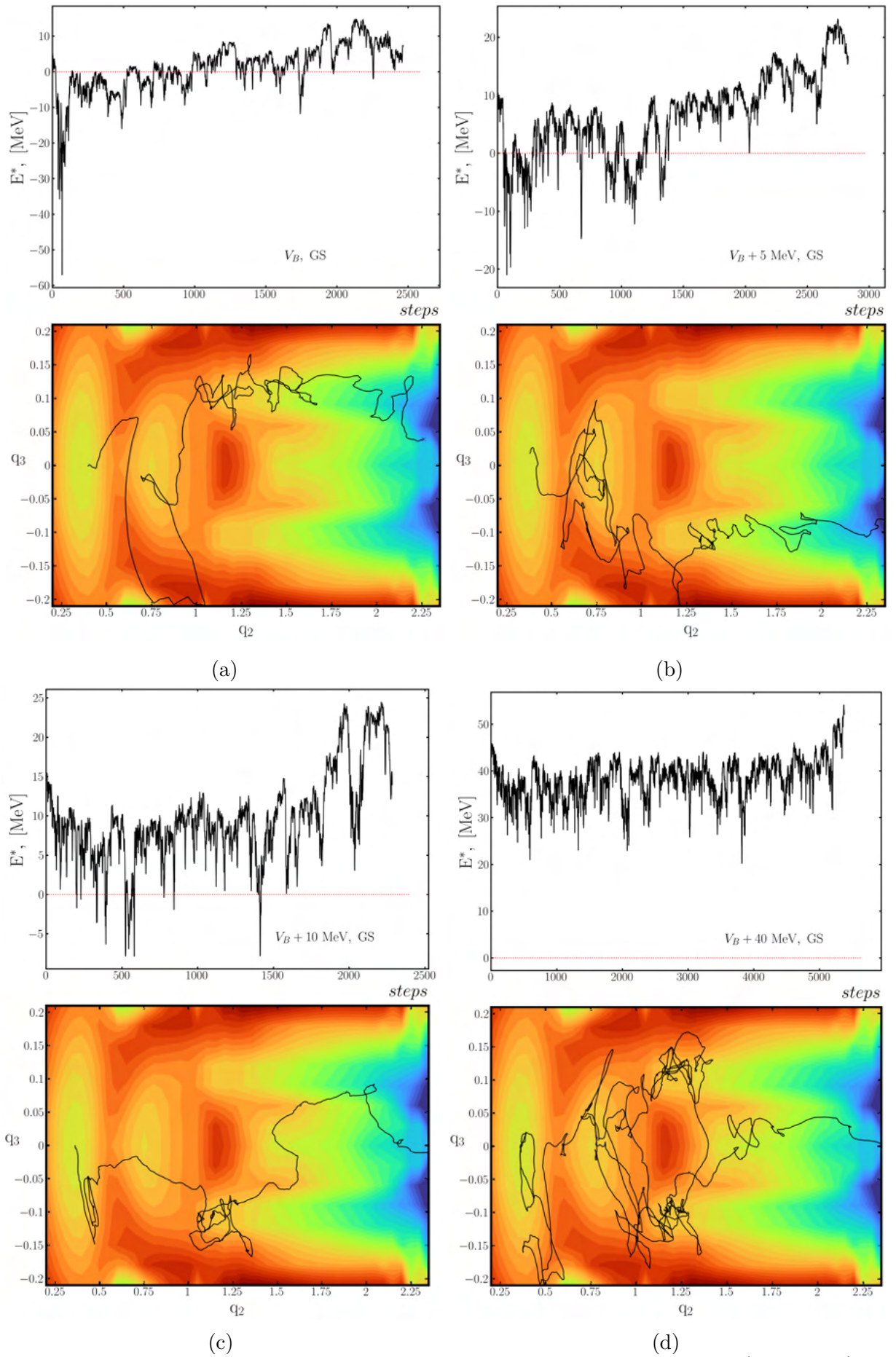

Figure 5.6: Excitation energy behavior measured in each iteration step (top panel) for the corresponding trajectory (bottom panel) starting from the ground state with different initial energies for the compound nucleus of ^{236}U.

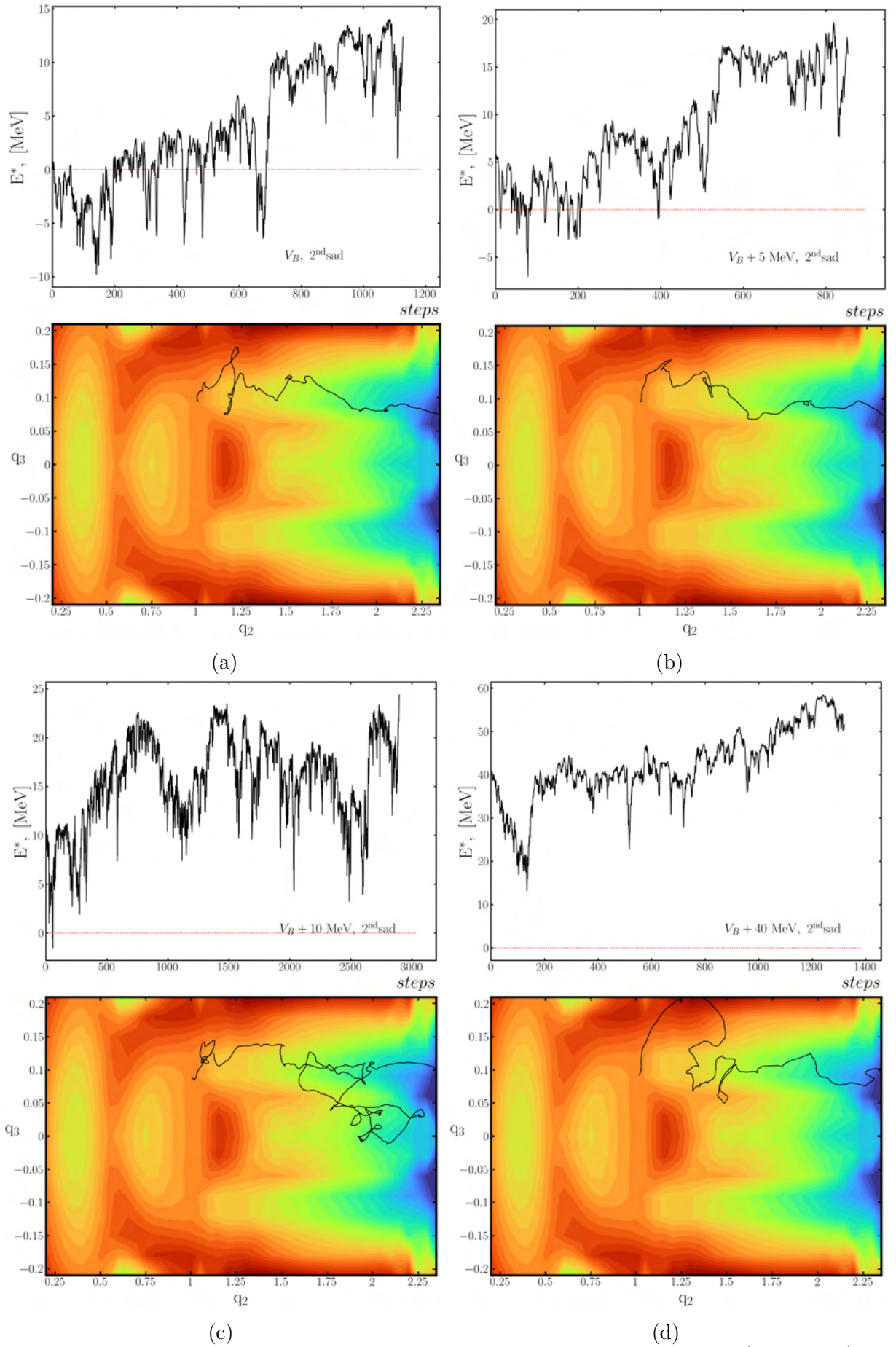

Figure 5.7: Excitation energy behavior measured in each iteration step (top panel) for the corresponding trajectory (bottom panel) starting from the second saddle with different initial excitation energies for the compound nucleus of ^{236}U.

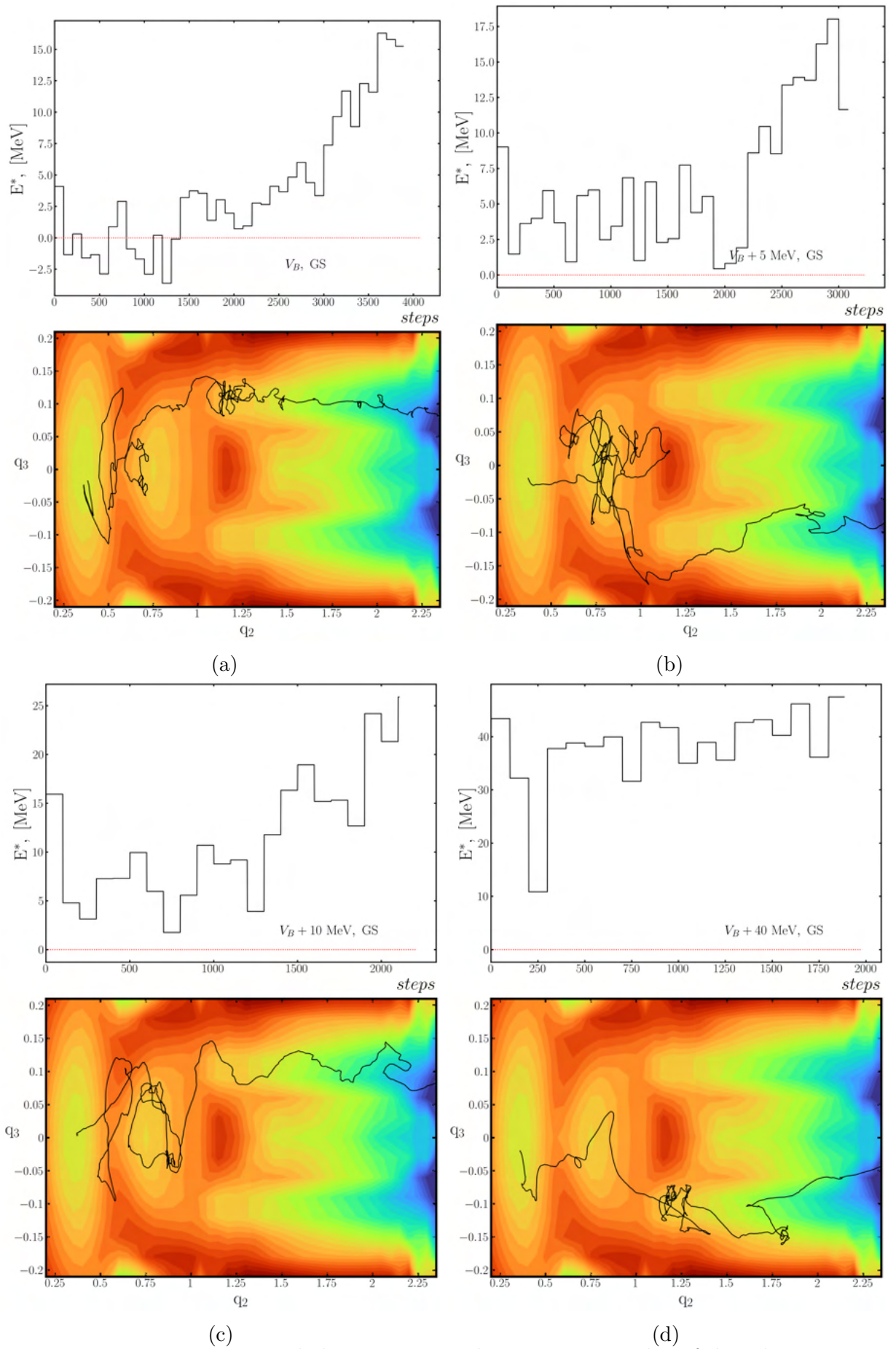

Figure 5.8: Excitation energy behavior measured at a constant value of the relaxation time (top panel) for the corresponding trajectory (bottom panel) starting from the ground state with different initial excitation energies for the compound nucleus of ^{236}U.

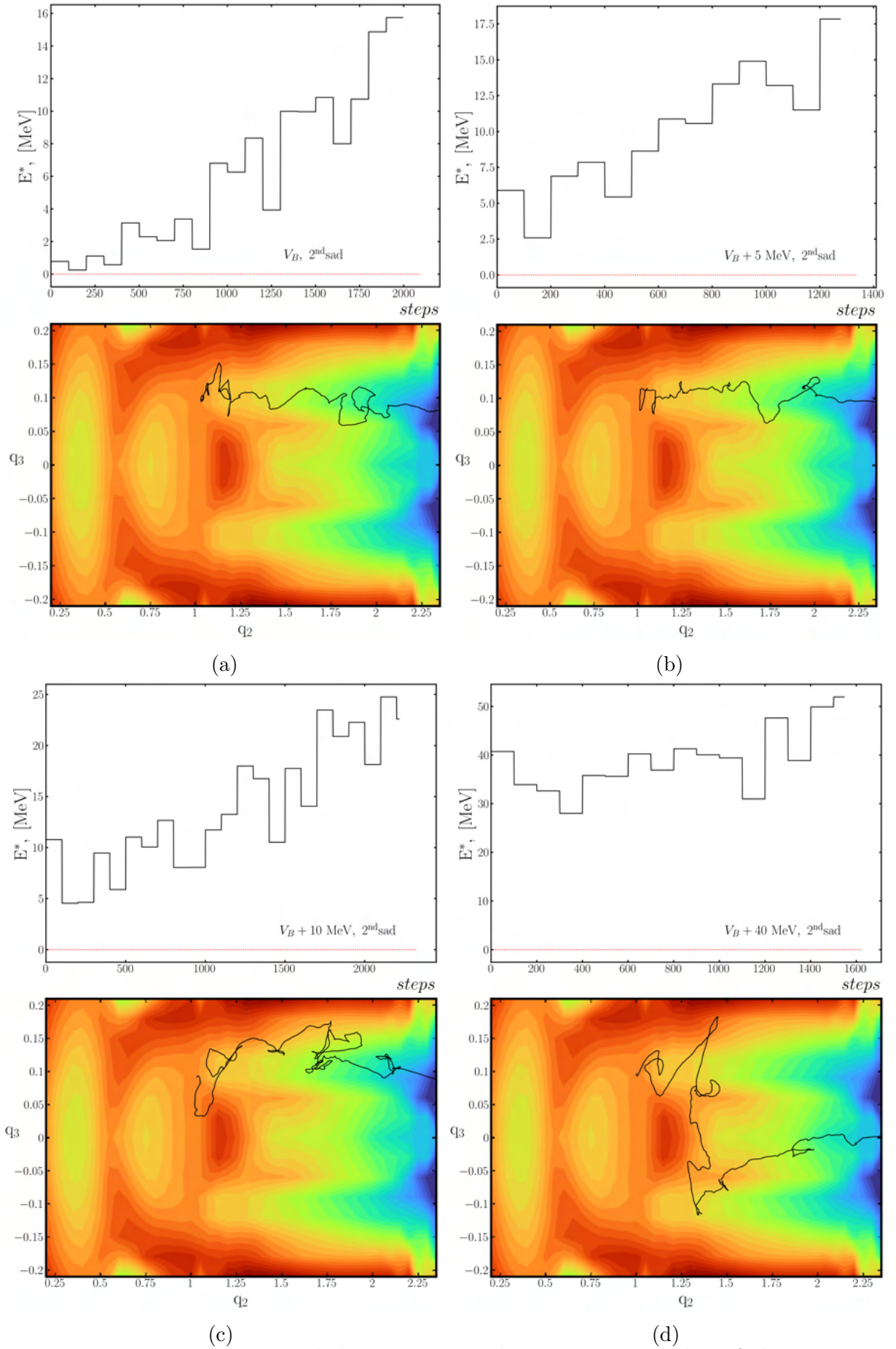

Figure 5.9: Excitation energy behavior measured at a constant value of the relaxation time (top panel) for the corresponding trajectory (bottom panel) starting from the second saddle with different initial excitation energies for the compound nucleus of ^{236}U.

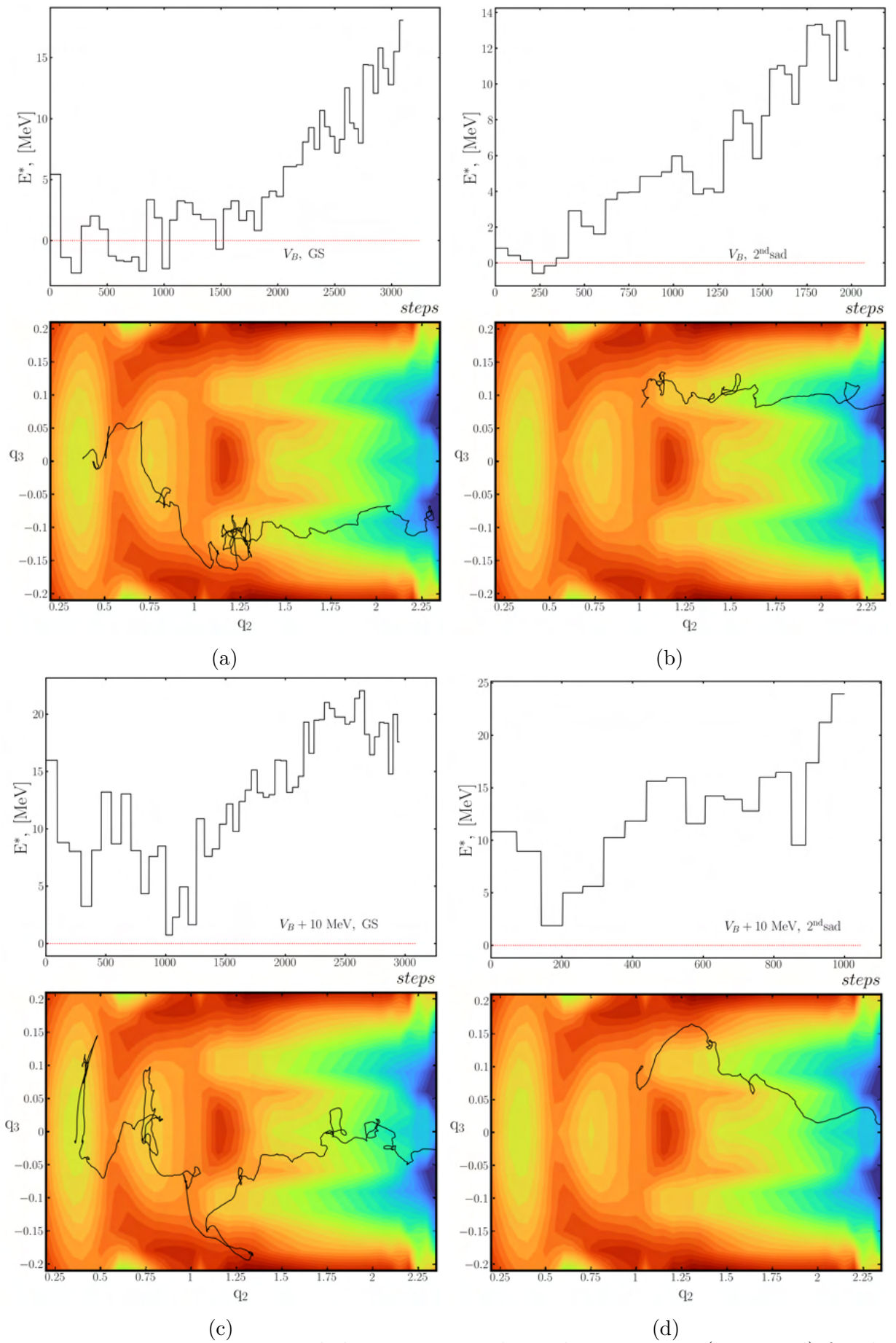

Figure 5.10: Excitation energy behavior measured at relaxation time (top panel) for the corresponding trajectory (bottom panel) starting from the ground state (a, c) and second saddle (b, d) with near-barrier and 10 MeV higher initial excitation energies for the compound nucleus of ^{236}U.

shell corrections. The decay factor E_d was defined in [141] close to the value of ≈ 20 MeV, but it is now usually a fitting parameter varying from 15 to 60 MeV.

Of course, the above approach is not the only one. For example, in the previously mentioned work [119], in addition to obtaining a phenomenological form of the density level parameter, an approximation of the temperature dependence of the free energy corrections δF (5.5) was proposed to have the following dependence on the excitation energy:

$$\delta F_{BM}(E^*) = \delta F(E^* = 0)\frac{\epsilon}{\sinh(\epsilon)} \tag{5.15}$$

where the value $\epsilon \equiv 2\pi^2 T/\hbar\omega_0$.

Attempts to improve the description of the shell and pair corrections have not ceased. In particular, recent trends have focused on considering not the excitation energy as a variable, but rather the temperature, which is related to the main factor on which the level density parameter depends. A "critical" value of the temperature makes it possible to introduce a certain threshold above which the shell corrections can be discarded. This issue has been well studied in [140], where a detailed review of the currently existing models has been performed, as well as a new approach to describe these corrections by introducing a new temperature dependence has been proposed. However, despite the very precise description, the shape of this distribution is relatively complex. Therefore, combining the idea contained in formula (5.15) and the temperature dependence from work [41], a very simple parametric representation of the temperature dependence of the generalized microscopic energy component E_{micro} has been proposed as:

$$E_{\mathrm{micro}}(T) = \frac{E_{\mathrm{micro}}(T=0)}{1+\exp\left(\frac{T-T_0}{a_0}\right)}, \tag{5.16}$$

where the parameters $T_0 = 1.5$MeV, $a_0 = 0.3$MeV have been fitted for a significant amount of even-even actinide nuclei.

Now we use the formula (5.16) to check the behavior of the FMDs by discussing various initial excitation energies of the system. The energies will range from about the barrier value to up to 200 MeV from the barrier. As described in the previous subsection, the region around the second saddle point is taken as the region from which the starting point is chosen. The number of Langevin trajectories is 10^4. Following the discussions of the previous subsections, the change of the temperature and the corresponding level density parameter along the trajectory is performed every 100 time steps.

The results of the calculations are shown in Fig. 5.11. From the first row we can see how quickly the blurring of the quantum shells begins, leading to the appearance of more fission events in the valley of symmetric fragmentation. In the second row, there is already a gradual decrease and blurring of the asymmetric peaks, while the symmetric fission valley remains almost unchanged. Finally, in the last series one can see a complete blurring of the quantum effects and the attainment of the Gaussian form of the mass distribution. One can see a clearly emerging peak in the region of symmetric fission. Unfortunately, this is an artifact due to the incompleteness of the trajectory termination conditions, as mentioned earlier.

5.2.2 Behaviour of the friction tensor

As can be seen from (5.4), the magnitude of the friction tensor γ affects, through the value of the conjugate momenta p_i, the two different quantities: the friction force and the amplitude of the Langevin force (last term of second Eqs. (5.4)) In the present model,

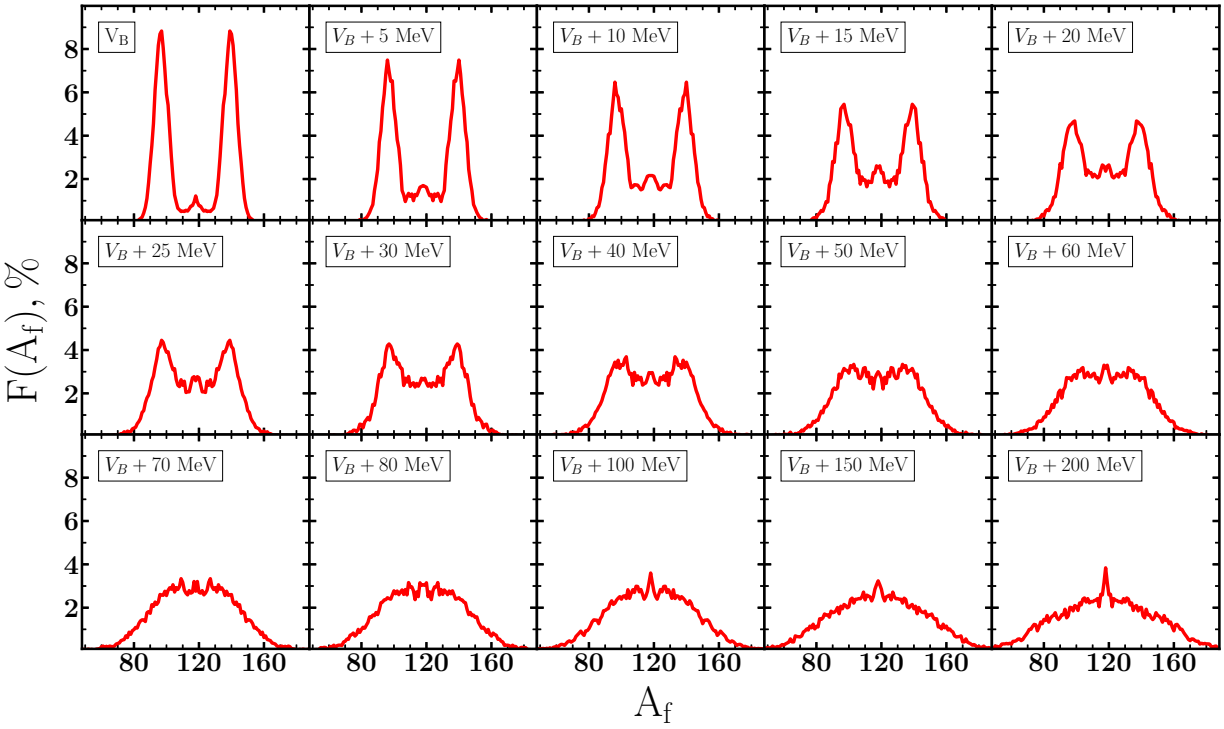

Figure 5.11: FMDs for ^{236}U fission at various excitation energies within usage of temperature corrections on E_{micro}.

as mentioned earlier, the simplest form of the tensor is used, calculated according to the "wall" formula (3.87), described in detail in 3.2.2. Often, the quantities calculated by this approach are not fully adequate to describe the required observables, and therefore may be adjusted by a certain multiplicative factor common to all tensor components, the fit of which varies depending on the actual problem. It is clear that when the system is heated (quite rapidly), part of the energy is transferred to the kinetic energy of the nucleons, which of course must affect the viscosity of the system.

Constant multiplier approach

Let is now consider the behavior of FMDs under different multipliers in front of the value of the friction tensor. The variation of the coefficient c_γ in addition to the limiting cases 0.2, 0.5 of the previously mentioned region will be extended by the following series of coefficients: 0.1, 2 and 4. Note that all results obtained earlier for the case $c_\gamma = 1$ are also included in this analysis.

For better clarity, the obtained FMDs are compared with experimental data, or to be more precise, with estimates based on experimental values. The reason for this, of course, is that the pre-fragments formed at the moment of rupture have several different configurations compared to what the detectors register, undergoing different types of decay and thermalization. Therefore, in the following we will use the term "primary FMD", i.e. the distribution formed directly at the moment of nuclear rupture, which is the main object of our study. The secondary FMDs will be understood as distributions after the process of primary fission fragments thermallization, which contribute significantly to the modification of the fission products.

Therefore, using the extensions obtained from the previous subsection, including the temperature dependence of the microscopic component of the potential (5.16), we describe the fission of the compound nucleus ^{236}U with an excitation energy close to the barrier

height value. The results of such calculations are shown in Fig. 5.12 together with the available empirical data from [142]. From this comparison, the following points can be highlighted:

1. Increasing the friction tensor leads to larger widths of the resulting primary FMD. For small values of γ, the gradient of the potential suppresses all other terms of the second equation of the system (5.4).

2. Exceeding the γ values, we do not observe practically any serious changes in the resulting FMD. Except for the distribution peaks, which gradually widen with increasing multiplier c_γ. In fact, in the case of 4γ, the behavior of the main peak is even consistent with the available experimental FMD. This is a direct consequence of the increasing interplay of the Langevin equation terms involving the friction tensor.

3. Nonlinear increase in the number of symmetric fission events as a consequence of the direct influence of the increasing amplitude of the Langevin force.

From the above we can conclude that the optimal value of c_γ is in the range [0.5,1]. For $c_\gamma > 1$, events close to symmetric fragmentation are enhanced, which is contrary to the empirically derived trend.

This results are, however, for the case of near-barrier excitation energy. Now we will consider the behaviour of FMD's at higher excitation energies: 5, 15, and 30 MeV above the barrier, respectively. Figure 5.13 presents the results of the calculations. Increasing the friction tensor leads to an almost insignificant increase in the overall width of the resulting primary FMD. At the same time, the heights of the peaks are reduced, especially in the region of $c_\gamma \in [0.1, 0.5]$. At all excitation energies discussed, weak changes in near-symmetric fission yields are observed. This may be an effect of the lack of trajectory termination conditions. Recall that the trajectory is stopped when it reaches the elongation limit $q_2 = 2.35$.

As can be seen from the comparisons with available experimental data shown in Figs. 5.13, the choice of coefficient $c_\gamma \approx 1$ remains valid. However, if the value of c_γ "floats" between 0.5 and 1 for the case close to the barrier, then it shifts strictly to 1 at 15 MeV.This suggests that some additional consideration of the temperature dependence of the friction tensor is needed.

The other important characteristic that should be checked when scaling the friction tensor is the kinetic energy of the collective motion. This is the component of the total kinetic energy that will be discussed in more detail later. The study of the influence of the friction tensor, using the "wall-window" formula [114], has shown that the contribution of the kinetic energy of the collective motion E_{kin}^{coll} at the moment of fracture decreases with

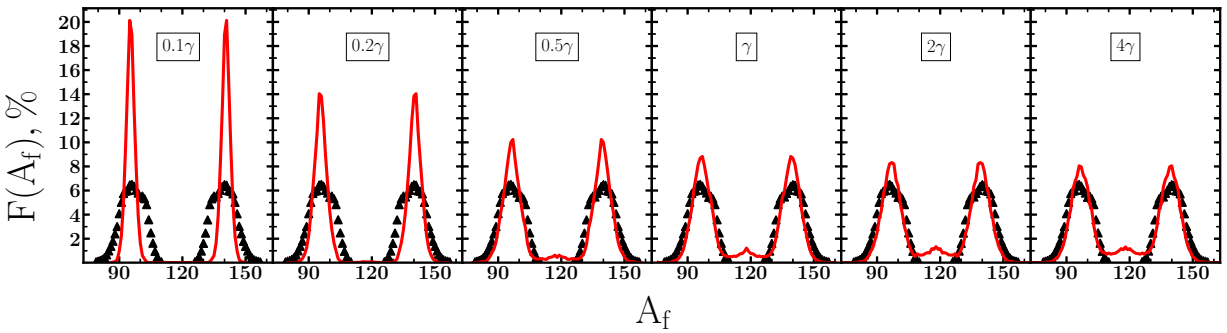

Figure 5.12: Comparison of calculated FMDs with various constant multipliers c_γ of the friction tensor for the fission reaction of ^{235}U by thermal neutrons. Experimental data taken from [142].

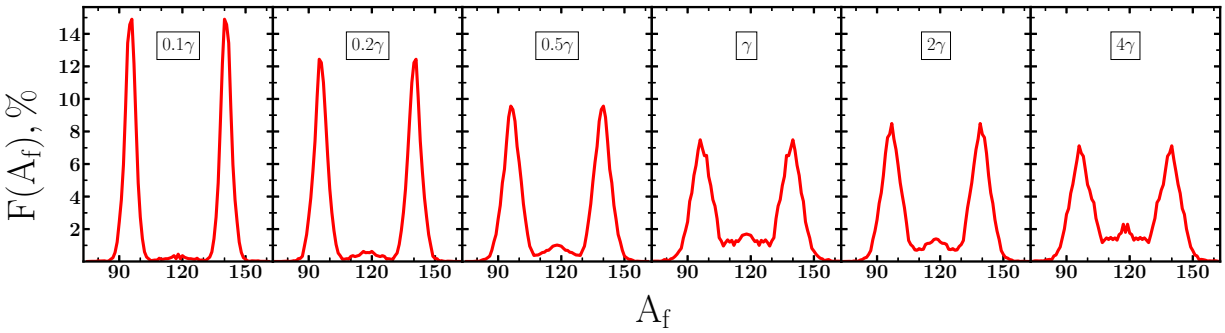

(a) At 5 MeV above barrier

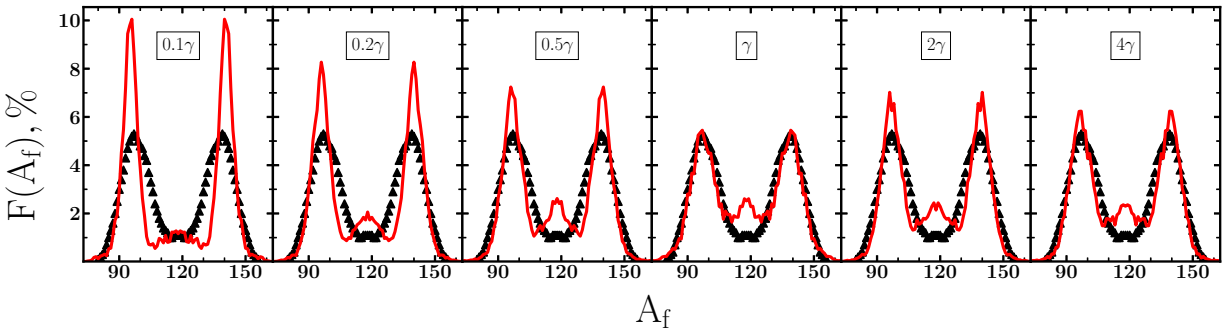

(b) At 15 MeV above barrier comparison data taken from [143]

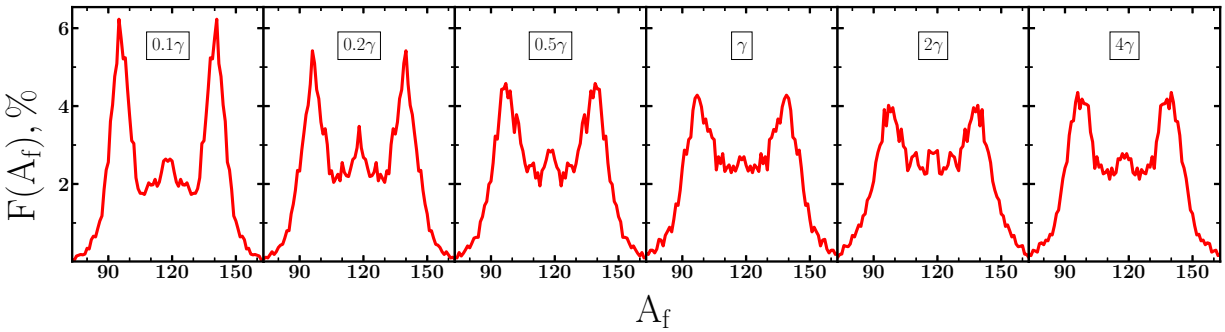

(c) At 30 MeV above barrier

Figure 5.13: Behaviour of FMDs with various constant multipliers of friction tensor for fission compound nuclei ^{236}U at different initial excitation energies.

increasing coefficient c_γ. Moreover, the decrease is monotonous. Let us check if this is indeed the case.

Figure 5.14 shows the values of E^{coll}_{kin} averaged with respect to the masses of the heavy fission fragments A_H, similar to what was done in the cited article. In addition, an extra scattering region is introduced, colored in a semi-transparent shade of the corresponding line color. This is done for a better understanding of the statistics and the number of fission events with a certain value of A_H.

Indeed, as the value of c_γ increases, there is a decrease in the energy of collective motion, since the friction tensor by definition dissipates internal energy of the compound fissile system. However, in contrast to the work [114] here we do not observe a uniform decrease, starting from $c_\gamma = 0.5$ the noticeable decrease stops, which is also not in agreement with the results obtained in the mentioned work. This seems to be directly related with using the Nix-Sierck [99] "wall-window" formula, where the "window" contribution becomes significant at the moment of nucleus rupture.

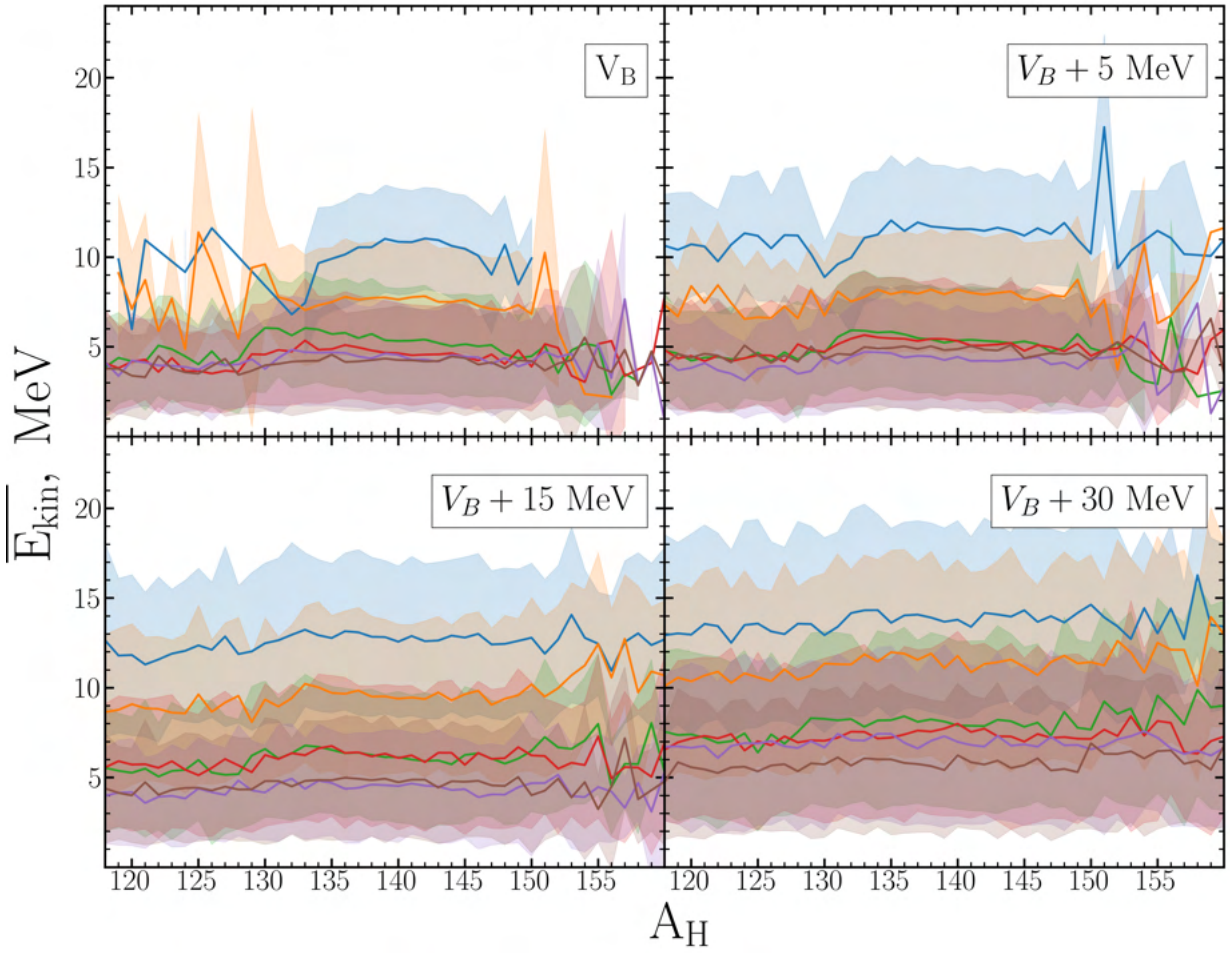

Figure 5.14: Effect of different friction tensors on the kinetic energy of the collective motion at the moment of fission, averaged over the heavy fission fragment A_H of the compound nucleus ^{236}U at different initial excitation energies. The colors correspond to multipliers in the following way: blue – 0.1, orange – 0.2, green – 0.5, red – 1, violet – 2 and brown – 4.

Temperature dependent coefficient

According to the Thomas-Fermi model, the phenomenon of friction in an atomic nucleus can strongly influence its collective motion, which ends with fission. Thus, the higher the kinetic energy of the nucleons, the more this system has viscous properties. It is known that the superfluid properties disappear as the temperature of the system increases, smoothly transitioning to a Fermi gas state. This means that at low temperatures, when almost all of the initial excitation energy is spent on overcoming energy barriers and there is practically no excess kinetic energy, the value of the tensor must be grown at higher temperatures. To determine the behavior of the friction tensor, which mainly determines the strength of the friction forces, we return to the works [107, 144].

In the article [144], in the time-dependent Hartree-Fock equation, the density matrix depends on the temperature coefficients η in the following way:

$$\eta(T) = \frac{1}{1 + \exp\left(\frac{\varepsilon_\alpha - \mu}{T}\right)}, \tag{5.17}$$

where μ is the chemical potential, ε_α is the deformation-dependent single-particle state.

Somewhat later, this idea was adopted [107] to analyze the behavior of the friction tensor when the system is heated to temperatures up to 5 MeV. It was shown that at temperatures close to zero, the friction tensor takes on relatively small values that increase

exponentially with temperature. When the temperature reaches about 2 MeV, the value of the friction tensor shows a plateau and practically does not change with T. Despite the fact that this analysis has been carried out within the quantum mechanical framework, the main features of the friction tensor given by the classical wall (or wall-window) model must be common to both types of approaches. Therefore, the temperature dependent multiplier for the friction tensor $c_\gamma(T)$ can be expressed as

$$c_\gamma(T) = \frac{0.7}{1 + \exp\left(-\frac{T - T_{crit}}{T_0}\right)} \tag{5.18}$$

where the fitted values of T_{crit} and T_0 are 0.7 MeV and 0.25 MeV, respectively.

Here in Fig. 5.15 we show the behavior of the FMDs using the above idea. Varying the excitation energy similarly as in the previous subchapter, we compare with the available experimental data the results obtained with $c_\gamma(T)$ and with the constant multiplier $c_\gamma = 1$. Unfortunately, despite the fact that both of the above approaches give almost

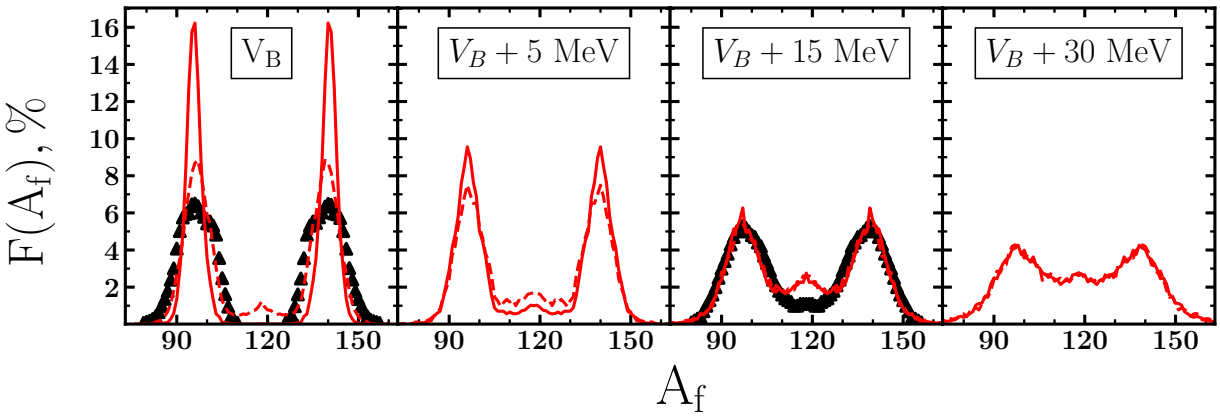

Figure 5.15: Comparison of FMDs for the ^{236}U nucleus at different initial excitation energies using $c_\gamma(T)$ (solid red) and $c_\gamma = 1$ (dashed red).

identical mass distributions for the friction tensor scaling factor, which are very close to the experimental one in the excitation energy limit above 20 MeV, they do not give good estimates of the experimental yields, especially for the distribution peak height. Curiously, the multiplier $c_\gamma = 1$ is more appropriate in this case. In fact, at small excitations, where the quantum zero point vibration effects can play a significant role, the classical approximation to describe the diffusion tensor (4.11) within the fluctuation-dissipative theorem is not able to account for the residual motion of nucleons at extremely low temperatures. Therefore, it is necessary to reconsider the definition of the diffusion tensor D_{ij} itself in the limit of $T \to 0$.

5.2.3 Effective diffusion tensor

Taking into account that the composite fissile nucleus in the case of reaction with thermal neutrons remains "cold", i.e. the temperature does not exceed 1 MeV, therefore the friction tensor also has varying small values, especially for the temperature below 0.5 MeV [107], which is typical for the initial stage of a trajectory. Since the diffusion tensor is by definition proportional to the square root of the friction tensor and the temperature such an overall dependence cannot be freely modified. The only way to introduce some modifications is to slightly redefine the temperature definition by introducing a kind of

effective temperature $T^*(T)$ which, in the limit of sufficiently high T, tends to the actual T itself and does not vanish as $T > 0$.

Why is it generally possible to modify the notion of temperature in nuclear physics? Strictly speaking, in any "statistical" system with a large number of particles, the temperature in its equilibrium state is a well-defined quantity. For the nuclear system of 200-300 particles, such a thermodynamical definition can not be fully justified, and therefore the temperature can only be treated as a certain function of the excitation energy E^*. Moreover, we are dealing with the quantum world, where fluctuations persist even at zero temperature. All these arguments open the possibility to define an effective temperature parameter T^* which plays the role of the "temperature" in diffusion tensor, allowing to apply standard relations known from classical thermodynamics.

This kind of reasoning was carried out in the work [145], where the dynamics of a damped motion in the collective phase space was considered. The study focused primarily on the behavior of the diffusion tensor entering the Fokker-Plank equation, both for steady and unsteady modes, the latter being understood as its critically small values at low temperature. In this context, the authors proposed an analytical continuation of the (quantum) fluctuation dissipation theorem. It consists in using an effective temperature that takes into account the nature of quantum fluctuations, and this parameter is related to the temperature by the following relation:

$$T^* = \frac{\bar{\omega}_0}{2} \coth\left(\frac{\bar{\omega}_0}{2T}\right), \tag{5.19}$$

where the value of ω_0 is related to the stiffness of the harmonic potential C by the relation $\omega_0 = \sqrt{|C|/\mathcal{M}}$.

Let us apply this idea within the framework of the present model, considering that for the oscillator energy $\frac{\hbar\omega_0}{2}$ the previously mentioned zero point energy E_0 is taken. Earlier it was announced that this value is equal to 1 MeV. Now this value is treated as an adjustable parameter. Let us vary this parameter from 1 to 2 MeV in steps of 0.25 MeV. The resulting FMDs are shown in Figure 5.16. At first glance, a comparative analysis shows that the most optimal values of E_0 lie in the interval of 1.25-1.50 MeV.For the sake of simplicity, we will assume that within this model this energy value, common to all isotopic chains discussed here, is $E_0 = 1.5$MeV.

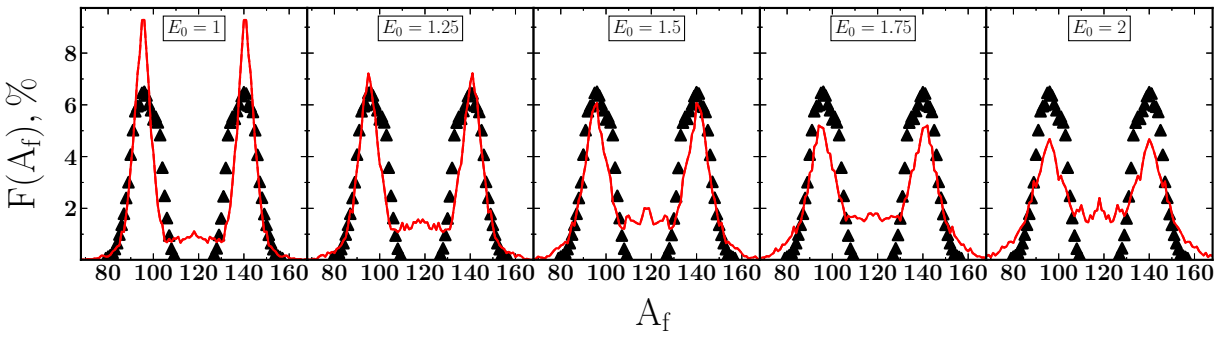

Figure 5.16: FMDs of thermal neutron induced reaction ^{235}U of calculated with various zero-point energies E_0

This completes the second phase in which we gradually introduced the important dependencies that allowed us to make the FMDs calculations more realistic. The test sample was the well-known isotope ^{236}U. Using it as an example, the behavior of the compound fissile system was studied in terms of the energy values included in the equation (5.12), which complements the system of Langevin equations (5.4). In particular, the excitation

energy E^* and its dependent temperature T. Variants of observing the law of conservation of energy in the dynamical system have been proposed. And also the behavior of the system taking into account its stepwise heating during the fission process was considered. It was found that the main process of heating of the system occurs in the last stages of fission, i.e. after overcoming the external fission barrier. Therefore, temperature dependences were introduced for the potential energy and transport coefficients (friction tensor), which affect the fission dynamics. All these dependences are taken into account in the calculations presented in the following chapters.

5.3 Boundary condition effects

In the study of temperature effects, it has been noted several times that there are an excessive number of trajectories with final configurations corresponding to near-symmetric fission, which are almost not observed in the thermal neutron-induced fission reaction of ^{235}U. Therefore, it has been assumed that this effect is caused by a special form of conditions imposed on a single trajectory to stop its time evolution. As a reminder, it consists of two simple conditions:

$$\begin{cases} q_2 \geq q_2^{max} \\ r_{neck} = 0 \end{cases} \tag{5.20}$$

where $q_2^{max} = 2.35$ is the upper limit of the deformation grid in q_2 direction (5.8), the same as in works [40, 41, 78, 115, 139].

On the other hand, there is also a disadvantage in defining initial conditions of type eqs. (5.11) and (5.13) and choosing the starting point, which certainly has less effect on FMDs, but seriously affects the computation time of the trajectory.The simplest conditions and properties obtained above, applied to the initial deformation distributions $\mathbf{q}^1$, are rather unevenly distributed over the PES. This in turn affects the "passed vs trapped" (or "physical vs unphysical") statistics. For example, in the studied system of ^{236}U, only about 30% of the trajectories are physical. Thus, by qualitatively improving the ratio of physical vs. unphysical trajectories, the computational time is reduced.

It was also mentioned that the choice of a point on the PES depends directly on the goal of the study and the type of reaction. For example, in the case of the induced fission reaction discussed, if the system has enough energy to overcome all the fission barriers, the procedure for choosing the starting points described in the previous section seems clear and straightforward. But what happens in the case of spontaneous fission out of equilibrium? The answer is not obvious...

Therefore, it is necessary to perform additional detailed studies on the influence of boundary conditions on the solution of the 5.4 system in order to obtain results closer to the available experimental data for both induced and spontaneous nuclear fission.

5.3.1 Fission criterion. Neck radius condition primate

First of all, it is necessary to turn to the problem of describing the compound fissile system whose configuration reaches the upper elongation limit. In other words, it is necessary to answer the crucial question - has the fission of the system already occurred or not? Many authors often refer to the scission line on the two-dimensional PES as the set of deformation states after which the system unambiguously undergoes rupture (i.e. the neck radius $r_{neck} = 0$ at the point where the neck is thinnest). In reality, the separation of the nucleus into fragments may depend not only on the thickness of the neck, but also

on several other quantities [78] characterizing the volume and surface properties of both fragments, their shell structures, deformation, excitation energy, relative collective speed of the fragments in the fission direction, neck curvature, etc., which will be revealed below. However, the emphasis in this subsection is on the importance of considering the neck thickness criterion and its effect on FMDs.

In practice, calculations on a finite deformation mesh often do not cover all configurations up to the scission line, but are limited to regions close to these configurations, called pre-scission states. This is due to the fact that the accuracy of the numerical determination of the PES and the transport coefficients for separated, highly elongated fragments is greatly reduced by the limitations of the numerical methods used to compute the eigenvalues of the Yukawa-folded Hamiltonian and the deformation functions of the liquid-drop model in highly elongated, neck-shaped nuclei. Thus, one can find cases on the PES that are far from rupture even though they have highly elongated shapes.

To determine the contribution of such highly elongated cases to the FMD, we will impose another condition on the neck radius that determines the trajectory termination:

$$r_{neck} \leq r_{neck}^{stop} \tag{5.21}$$

where r_{neck}^{stop} is a fixed value varying between $1-2.5$fm (see, works [20, 21, 94, 109, 139, 146]). These values are very close to the effective radius of a nucleon, denoted as r_n, which has a value of ≈ 1fm.

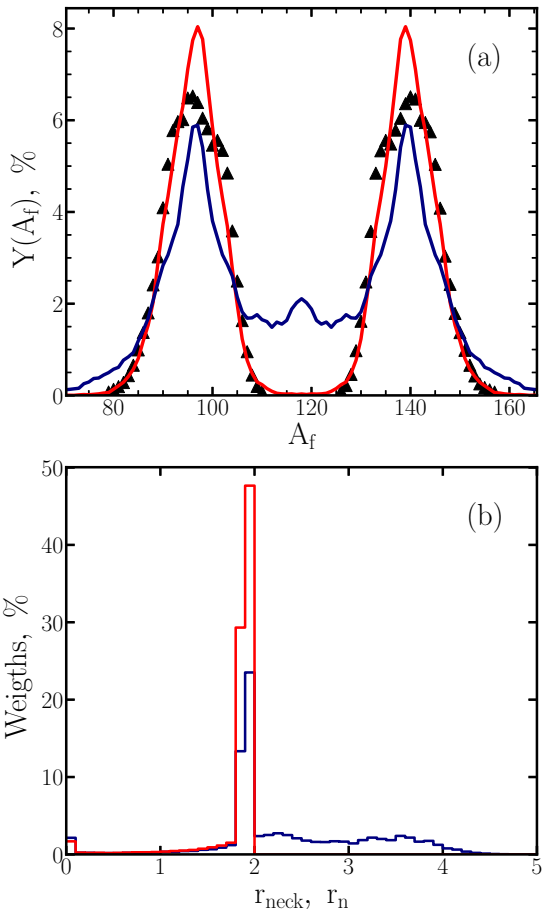

Figure 5.17: Primary FMDs (a) for thermal neutron-induced fission of ^{235}U with obligatory use of the neck radius condition (red) and without it (navy). Histogram (b) shows the r_{neck} distribution for both cases.

Thus, if the neck radius is still larger than a fixed value r_{neck}^{stop}, e.g. $2r_n$, then such a trajectory will be rejected even if the limit q_2^{max} is reached. Let us run a calculation under these conditions, and in order to get rid of the small noise, we increase the statistics by one order of magnitude, bringing the number of trajectories up to 10^5. The results are shown in Fig. 5.17(a), where the FMD obtained under the condition (5.21) is marked in red, and the condition (5.20) is marked in navy. As shown in Fig. 5.17(a), neglecting the "neck radius condition" leads to significant contributions from both nearly symmetric and highly asymmetric channels, which are not observed in the experimental distribution. This is also confirmed by the fact that for the conditions used in the previous sections, the values of the neck radii of the fissile configurations are distributed over all possible values in the region from r_n up to $4.5r_n$ with a clear peak around $2r_n$, as shown in Fig. 5.17(b).

For an explanation, one must return to Fig. 5.4, where it is seen that at elongation $q_2^{max} = 2.35$, due to the condition (5.20), some configurations can not be considered as very close to rapture. If one considers the attainment of this elongation limit as the only decisive condition for fission, one runs the risk of obtaining an unrealistic FMD. As can

also be seen in Fig. 5.4, extending this value even to $q_2^{max} \approx 2.9$, where the accuracy of determining the necessary input quantities becomes increasingly doubtful, there are still surface shapes with neck widths around $0.5R_0$. Figure 5.18 shows the increasing yields of nearly symmetric fission with a gradual shift in the value of q_2^{max} from 2.35 to 2.9. The above is a consequence of the problematic property of the Fourier shape parametrization used in this study, which is not fully capable of producing well-separated, mass-symmetric fragments for large nuclear stretches.

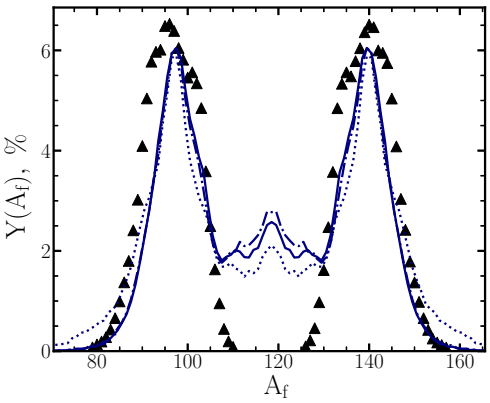

Figure 5.18: Primary FMDs for thermal neutron-induced fission of ^{235}U with optional neck radius condition at $q_2^{max} = 2.35$ (dashed line), $q_2^{max} = 2.5$ (dotted line), and $q_2^{max} = 2.9$ (solid line).

It can be concluded that in the Langevin description the decay of the nucleus strictly obeys the geometrical condition of type (5.21) imposed on the neck size of the formed surface. Therefore, the final condition must be somehow related to this geometric factor. At the same time, the definition of the scission line (i.e. where $r_{neck} = 0$) within the used surface representation does not seem to be optimal within the given configuration space. This is because in order to obtain a continuous multidimensional boundary it is necessary to include more elongated configurations, which was done for example in [139]. There is also the question of the definition of this line in the mesh used, whose step value may be too large to define both $r_{neck} = 0$ and other macroscopic quantities such as transport coefficients, while reducing the step leads to more time-consuming calculations.

However, there is a solution. Instead of looking for the boundary $r_{neck} = 0$, one can find the boundary at values of $r_{neck} = r_n$, where, from a physical point of view, the sense of breakup of the compound fissile system does not change. In fact, if the neck radius is smaller than the nucleon size, there is nothing there, so the system has collapsed. Sure, in this case the exchange of nucleons between the formed fragments is not stopped. But due to the adiabatic nature of the final stage of the fission process and instantaneous repulsion caused by the Coulomb interaction, the number of exchange events would be very small.

Unfortunately, even if the location of the scission line for one nucleus is successful, this does not make it universal for all other nuclei. The issue is of course in the PES of the fissile system. Depending on its structure, the r_{neck}^{stop} boundary will change, and this may affect the choice of configuration space. Of course, one can construct an extra large deformation space $\mathbf{q}$ and do calculations there to account for the scission line. But as mentioned above, there can be problems with the description of the properties of the system, including the PES. Therefore, it is not possible to use the unified value of the scission line $r_{neck}^{stop} = r_n$ in every case. Possibilities to avoid or solve this problem will be discussed later.

5.3.2 Improvement of initial conditions for fission reactions description

Before specifying the initial conditions for the Langevin calculations of the fission dynamics, we want to address the question of the specific selection of a set of starting points in our space of (q_i, p_i) coordinates. First of all, this concerns the reactions with available initial excitation energy comparable to or higher than the height of the fission barrier.

Throughout this chapter, there have been several discussions about the behavior of the system when its evolution is started from two different states: first, from the states close to the ground state (GS) or second, from the region close to the second (last) saddle point (LS). Our study has shown that most of the dynamical effects occur beyond the second barrier, where heating of a nucleus by dumped motion is possible down to the region with lower values of the potential energy and finally to the scission (strictly speaking, pre-scission) state. We will show that calculations from the second saddle point for $E^* \approx 6$MeV are quite effective. For this purpose we will calculate the FMD according to the initial conditions from the GS as well as from the LS states defined in subsection 5.1.1. For the trajectory termination conditions, we will use the obtained condition for the neck radius (5.21) with the sample of trajectories counting 10^5. As can be seen in Figure 5.19, the distributions of the fragment masses are almost identical for both cases. Therefore, we can safely limit the deformation grid for actinide nuclei to the following volume:

$$\begin{aligned} q_2 &= \left[q_2^{2^{nd}sad},\ 2.35\right] \\ q_3 &= [-0.21,\ 0.21] \\ q_4 &= [-0.21,\ 0.21] \end{aligned} \tag{5.22}$$

Note that only 1 per 100 trajectories initiated in the ground state overcome the barrier and evolve efficiently to fission. The rest get stuck in the potential energy well for a long time. If the calculation starts close to the saddle point, the number of "trapped" trajectories is reduced by almost an order of magnitude.

In general, this limited volume (5.22) can also be applied to spontaneous fission, where after the barrier penetration the system is at a turning point (exit point) outside the outer fission barrier.

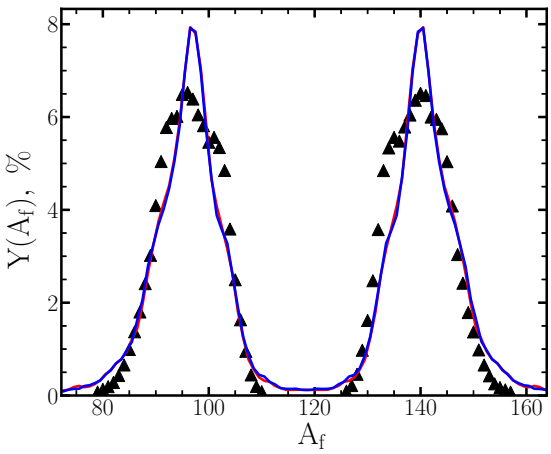

Figure 5.19: Primary FMDs for thermal neutron induced fission of ^{235}U from the GS (red) and the LS (blue) with experimental data [142]. Note that the two curves are difficult to distinguish.

As shown at the beginning of the section 5.2 at excitation energies 25 MeV, fission can be considered from the ground state. Of course, there will also be "trapped" trajectories, but their fraction will be much smaller compared to near-barrier energies. In this case it is also necessary to consider the evaporation processes of neutrons and other light particles from the compound fissile system. These processes will be discussed later, and for now it is assumed that the system reaches the initial point in the region of the last saddle and wastes energy only for overcoming the fission barriers.

Modifications of initial conditions for induced fission case

However, by introducing additional constraints, one can still improve the ratio of "passed" to "trapped" trajectories. Therefore, we use the method according to the ideas proposed in the Refs. [46, 115], where the way of generating $\mathbf{q}^1$ initial coordinates to be used in the first time step was proposed. This method consists of the following procedure: using the normal distribution ξ_{norm} with $\mu = 0$ and the standard deviation $\sigma = \frac{1}{2}\sqrt{E_0 / \frac{\partial^2 V}{\partial q_i^2}}$,

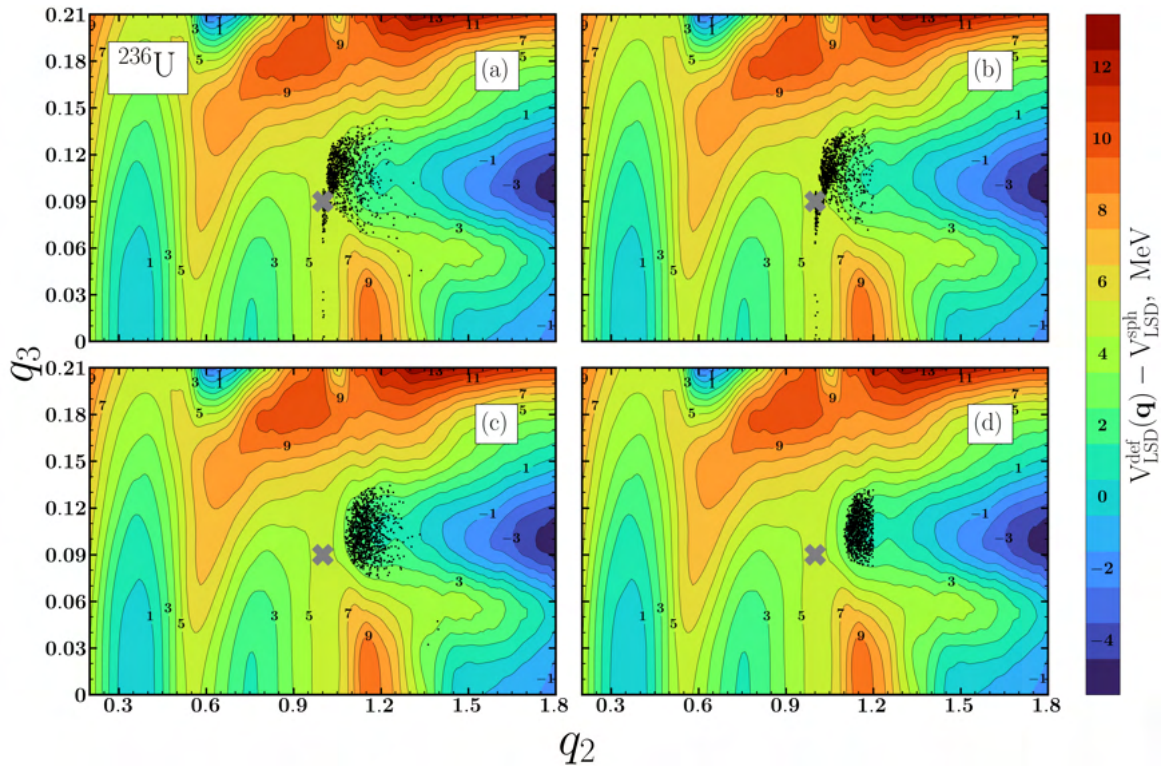

Figure 5.20: Examples of starting point distributions on the PES of ^{236}U. Panel (a) - without boundary control and subtracting E_0, (b) - without boundary control and including E_0, (c) - without control and including E_0, and (d) - with boundary control and including E_0, the gray cross indicates the location of the second saddle.

we fix the set of coordinates $\mathbf{q}^1$, which must then satisfy the following condition

$$\begin{cases} q_2^0 \geq q_2^{start} \\ \dfrac{1}{2}\sum\limits_{ij}\left[\mathcal{M}^{-1}\right]_{ij} p_i^0 p_j^0 \equiv V(\mathbf{q}^{start}) - V(\mathbf{q}^0) - E_0 \geq 0. \end{cases} \tag{5.23}$$

where $\mathbf{q}^{start}$ is an actual starting point of a trajectory, and E_0 describes a contribution of the zero-point vibration energy at that point.

The question arises whether the space of $\mathbf{q}^0$ points should be restricted to a certain volume around the point $\{\mathbf{q}^{start}\}$. Regarding the condition (5.23), such a problem can occur if the PES is sufficiently flat around this point, allowing the initial configuration to exceed the borders of the fixed grid, see Fig. 5.20(a,c). To avoid this, we can arbitrarily restrict the deformation space $\mathbf{q}^0$ to the following limits:

$$\begin{aligned} q_2 &= \left[q_2^0;\ q_2^0 + 0.2\right] \\ q_3 &= \left[q_3^0 - 0.09;\ q_3^0 + 0.09\right] \\ q_4 &= \left[q_4^0 - 0.09;\ q_4^0 + 0.09\right] \end{aligned} \tag{5.24}$$

In Fig. 5.20 we see four PES for ^{236}U, where the coordinates ($\mathbf{q}^0$ are distributed

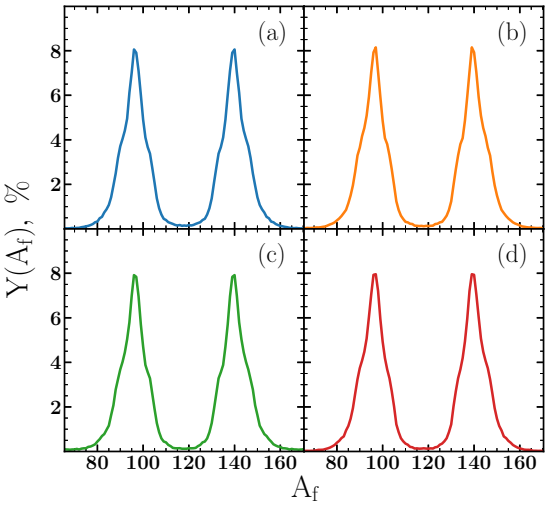

Figure 5.21: Primary FMDs for starting point distributions, where the symbol (i) corresponds to analogous cases from Fig. 5.20.

without (a,b) and with (c,d) including the
zero-point vibration energy in (5.23) and with and without constraints on the initial coordinate range (b,d). The figure in the last two panels shows the lack of sensitivity to these constraints. In this case, the ratio of traversed to not traversed trajectories in case (d) is in the interval $1 - 1.5$, which significantly reduces the computation time.

Modification of initial condition for spontaneous fission case

In the case of spontaneous fission, the main issue is again the choice of the starting point, which is in fact the exit point from under the fission barrier. Recall that spontaneous or induced fission processes are probabilistic phenomena associated with overcoming the fission barrier between the ground state or some excited state and an exit point of the same energy located outside the barrier. In a quantum approach, the probability of crossing the barrier depends roughly on the barrier shape and the number of barrier hits per time unit. In contrast, in the Langevin semiclassical approach, the barrier is not "tunneled", but must be jumped by a system with kinetic energy greater than the barrier height in the initial evolution stage. To determine this point, an in-depth analysis using the methods of action and energy path integrals starting from the ground state would be required. Unfortunately, such an analysis is beyond the scope of this work.

Instead, a very naive analysis of the PES is possible. Let us find all points of the deformation mesh where the values of the potential V are close to the ground state V_{GS}. Certainly they are all outside $\mathbf{q}^{2^{nd}sad}$. The results of such a search for points of energy relative to the equilibrium point within ≈ 0.05 MeV can be observed in Fig. 5.22, where points with $|V - V_{GS}| < 0.05$ MeV are marked in white, $|V - V_{GS}| < 0.025$ MeV in magenta, while the points corresponding to the difference smaller than 0.025 MeV are marked in gray. At first glance, the gray points should be taken as the initial configurations.

However the proximity of the energies is not sufficient to select the initial point. In addition, the distance between the ground state and the candidate points must be determined. In this way, the minimum path under the barrier is taken into account. The distance is defined as the straight path between nodes in 3D space. In this case, the an-

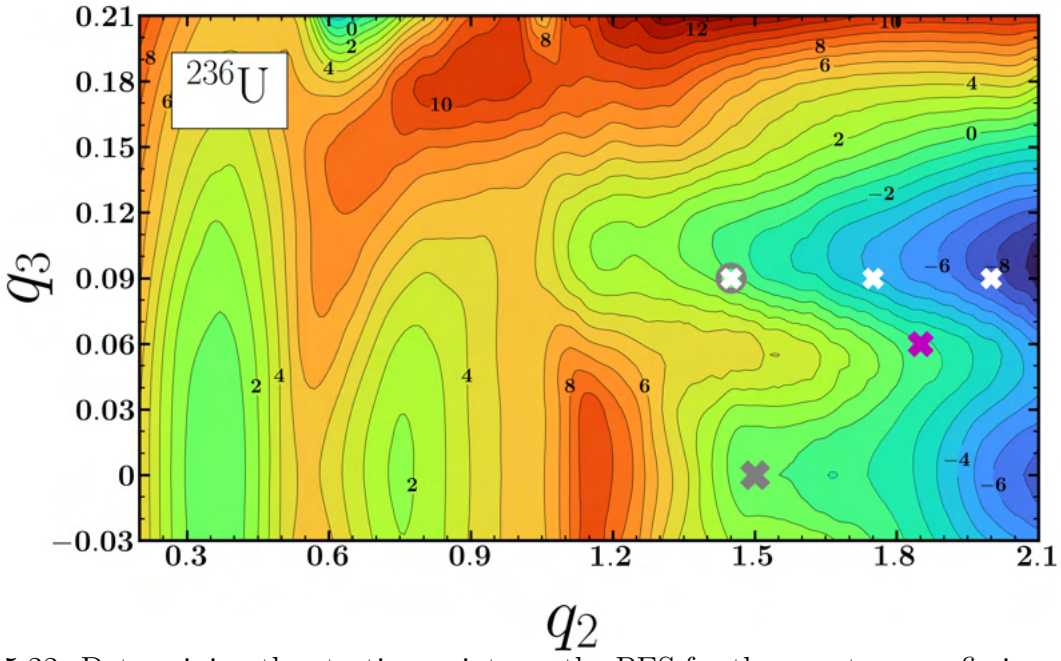

Figure 5.22: Determining the starting points on the PES for the spontaneous fission of the ^{236}U.

swer changes and now the main candidate is the earliest white coordinate marked by the gray circle. According to the distance in the three-dimensional lattice, it is closer than the gray point (significant difference in coordinate q_4, exceeding the difference in coordinate q_3). Afterwards, the procedure (5.23) defined above is run, which completes the $\mathbf{q}^1$ point formation procedure.

Strictly speaking, one point is often not enough to determine the starting positions for spontaneous fission. There should be at least two points: one in the region of asymmetric channels and one in the region of symmetric channels. This is similar to the situation observed in Fig. 5.22. To determine the statistical weight, one can, for example, use the ratio of exponentials whose exponents contain the energy differences between the ground state and the output points, or perhaps the magnitudes of the action between the selected points and the ground state. In this thesis, however, these approaches remain only as concepts that could be developed in the future. In the meantime, the "naive" version described above is used, with the search for an exit point under the barrier.

5.3.3 Neck criterion influence on fission characteristics

After proving that the trajectory termination condition is crucial for the neck size, we now consider its effect on the distributions of the fission mass fragments. For this purpose, we assume that the value of the limit radius r_{neck}^{stop} at which a trajectory is stopped can vary from $3r_n$ to 0 with a step of r_n. We set the starting points according to Fig. 5.20(d) and the constraint of Eq. (5.24), while the upper limit of elongation is $q_2^{max} = 2.35$. As can be seen in Fig. 5.23, the resulting mass distributions change their shape for different r_{neck}^{stop} radii. With decreasing neck radius, the fragment mass distribution becomes slightly narrower, and the asymmetric peak shifts towards more and more symmetric yields. At the same time, its symmetric part gradually disappears and approaches the experimental value.

To understand the dominance of the asymmetric fission channel in this nucleus, let us notice at the PES shown in Fig. 5.20 that the most similar path from the initial configuration, set around the second saddle point at $(q_2, q_3) \approx (1.0, 0.09)$, leads directly to the asymmetric valley, which is separated from the symmetric one by an edge of almost 3 MeV high, visible at $q_3 \approx 0.06$. Since the excitation energy in the initial configuration is relatively low, the random force defined by Eqs. (4.9) and (4.11) has very little chance to push the system over this edge.

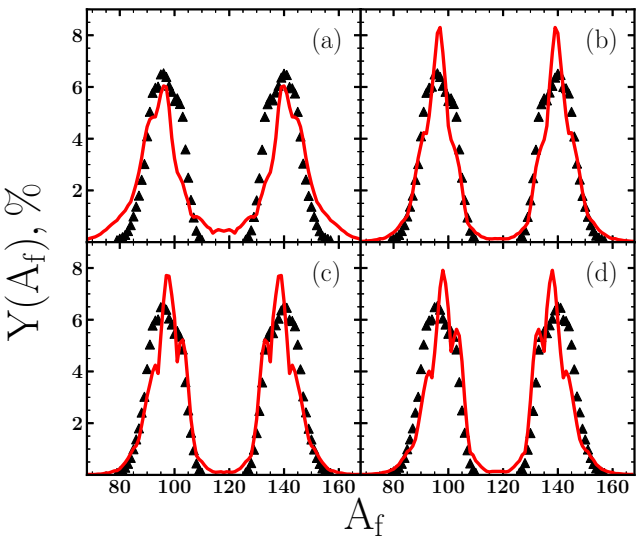

Figure 5.23: Primary FMD's for neutron-induced fission ^{235}U with variation of the neck radius r_{neck}^{stop} from $3r_n$ (a), $2r_n$ (b), r_n (c), 0 (d).

It can also be seen that, except for the extreme cases (a) and (d) with $r_{neck}^{stop} = 3\,r_n$ and $r_{neck}^{stop} = 0$, the overall behavior of the other distributions presented is generally weakly affected, which may indicate that the main contributions to the final FMD come from $r_{neck}^{stop} \in \{2r_n,\ r_n,\ 0\}$.

Stochastic character of neck-breaking

Analyzing Fig. 5.23, the question arises whether the use of a strictly fixed value of r_{neck}^{stop}, which controls the momentum of splitting into fragments of different masses (charges), is a substantial simplification of the stochastic nature of the fission phenomenon. In fact, from the same Fig. 5.23 it can be seen that, for example, the combination of variants (a)-(c) under certain statistical weights gives values closer to the available experimental data. In other words, the neck condition can be modified by using some random distribution law on the value of r_{neck}^{stop}, which will be analogous to the random rapture of the system. The attempt to find such a distribution and its effect on the fission characteristics will be discussed below.

Uniform distribution The simplest implementation of the above idea is to randomly take the value r_{neck}^{stop} from a given interval, say $[0, \alpha_r\, r_n]$, at the beginning of each trajectory with a uniform discrete distribution, where $\alpha_r \in \{1, 2, 3\}$.

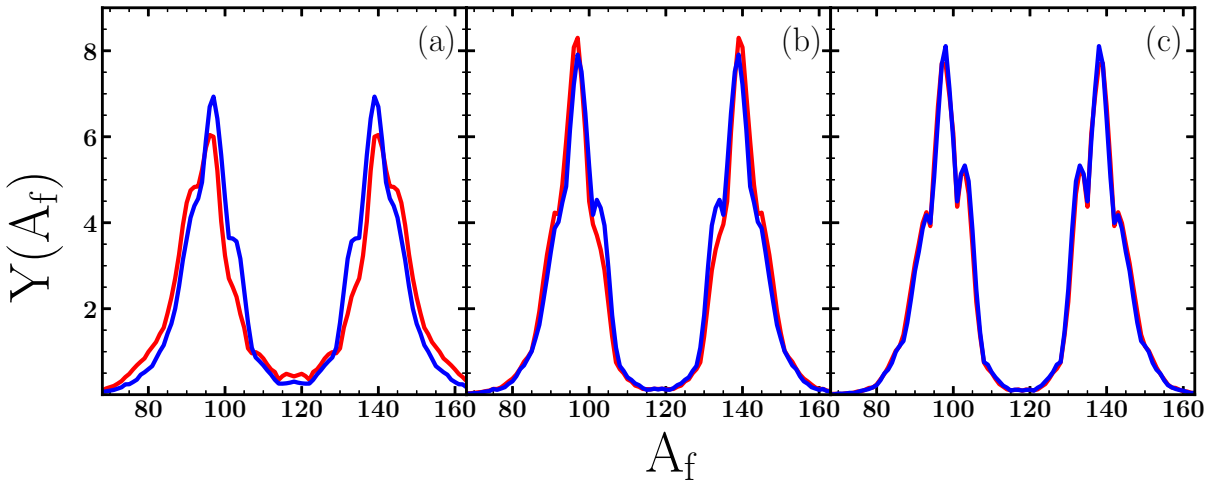

Figure 5.24: Primary FMD's for thermal neutron induced fission of ^{235}U calculated within random pick (blue) of r_{neck}^{stop} defined on the following intervals [0,3r_n] (a), [0, 2r_n] (b) and [0,r_n] (c), compared with analogous FMD's of Fig. 5.23(a)-(c).

Actually, this is an attempt to combine the panels 5.23 into a single FMD, depending on the coefficient α_r, with the same statistical weight $1/\alpha_r$. The distributions shown in Fig. 5.24 are computed for the following three intervals starting at 0 and ending at the respective values $\alpha_r \in \{1, 2, 3\}$. The results are compared with the FMDs obtained for a single value of $r_{neck}^{stop} = \alpha_r\, r_n$, shown in Fig. 5.23(a)-(c). It is clear that, going from panel (a) to (c), there is a gradual decrease in the difference between the distributions calculated with random selection or with a fixed value of r_{neck}^{stop}.

Indeed, there is no doubt that the worse the mixture of different α_r values in the resulting distribution, the closer the distribution is to the "original" one. Note, however, that a significant difference is only observed for panel (a). In the latter, a noticeable effect of the distribution of figure 5.23(a) with a much wider foot part is superimposed on the other three distributions with smaller neck radii, which are essentially very similar to each other and quite close to the experimental one.

In general, such a combination of FMD's for ^{235}U generated for different values of r_{neck}^{stop} affects its overall behavior in a rather limited way.

Gaussian distribution The concept of mixing the distributions obtained with different r_{neck}^{stop} radii is now implemented in a slightly different way, i.e. instead of using a uniform discrete distribution to generate r_{neck}^{stop} at the start of each trajectory, we will use a continuous normal distribution $\xi_{norm}(\mu, \sigma)$. Of course, the question arises about the parameters μ and σ of such a distribution. For this purpose, we have made a least-square fit of the FMD to the available experimental distributions in selected actinide nuclei with regard to these two variables. The position of the maximum μ was varied in the interval $[0, 2r_n]$ in steps of $0.5r_n$, while the variance value was varied in the interval $[0.1r_n, r_n]$ in steps of $0.1r_n$. As mentioned above, we performed such a fit not only for the ^{236}U nucleus, but also for other nuclei where the experimental values of the FMD are known [142, 147–153]. Due to the large scale of these calculations, the statistics have been reduced to 10^4 trajectories. In addition to the induced fission reactions, the spontaneous fission of actinide nuclei was also analyzed. The results of the obtained FMD are shown in Fig. 5.25.

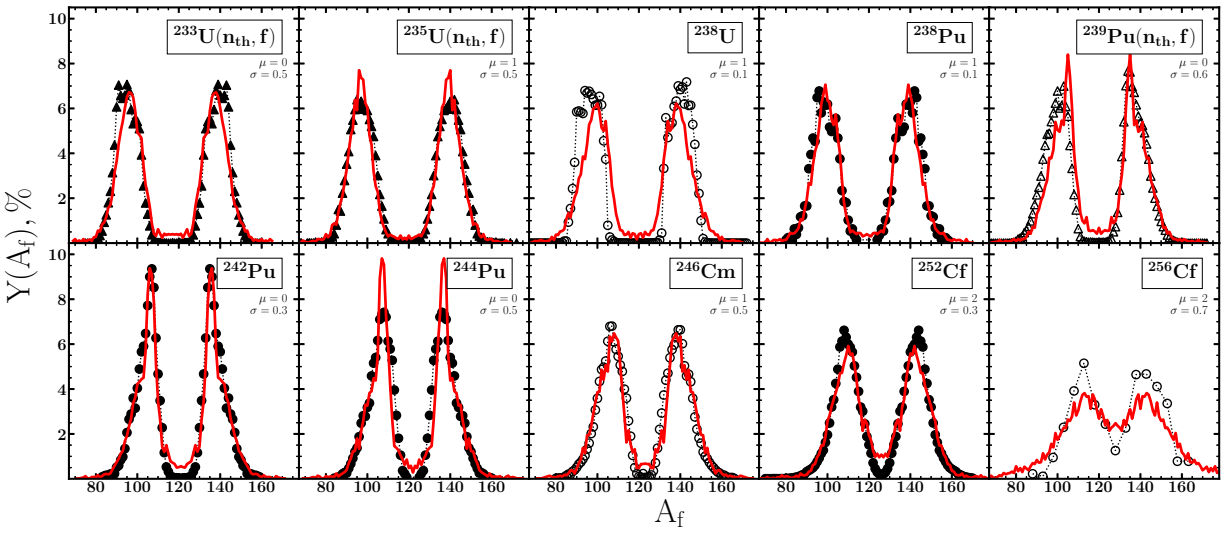

Figure 5.25: FMDs (red line) of actinide nuclei with r_{neck}^{stop} randomly chosen at the beginning of each trajectory with normal distribution $\xi_{norm}(\mu, \sigma)$. The values of μ and σ are fitted as mentioned above. Hollow triangles are secondary FMDs, circles denote spontaneous fission.

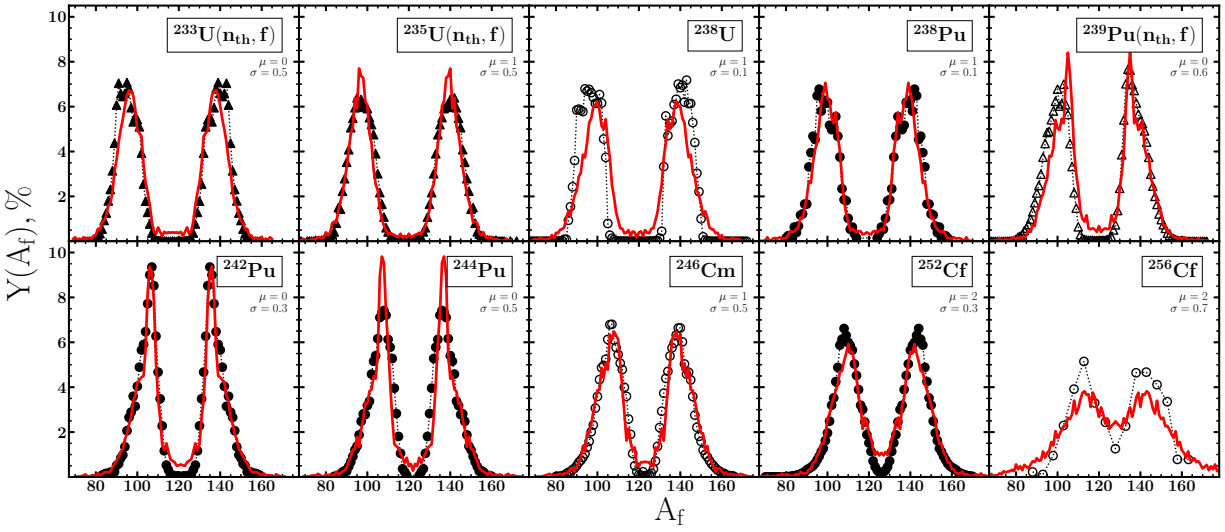

Figure 5.26: FMD of nucleus-actinides estimated within generalized distribution $\xi_{norm}(r_n, 0.5r_n)$ to their experimental analogues.

This figure is a remarkable example of the problem expressed in the previous sections about the lack of a universal and firm approach to predicting the moment of neck rupture. As we can see, the values of μ and σ are generally different for each isotope.

Nevertheless, we found that the average normal distribution function of the neck radius r_{neck}^{stop} of the form $\xi_{norm}(r_n, 0.5r_n)$ is able to reproduce the empirical FMDsin actinides in a quite reasonable way, as shown in Figure 5.26 in comparison with Figure 5.25. The study presented above confirms the stochastic character of the neck-breaking process.

Fermi-like distribution The previously suggested variants of random neck breakup require a pre-defined value of r_{neck}^{stop} at which the system breaks up into fragments. This makes the trajectory somewhat predictable, since we have a certain parameter that the trajectory should reach during its evolution in order to break into fragments with a probability of 100%. If at the beginning of the trajectory it is determined that the neck radius r_{neck}^{stop} has a significant value, the time to determine it will be relatively short, since such shapes can already appear at moderate stretching. On the other hand, if the value of r_{neck}^{stop} is too small and difficult to achieve within a given shape parameterization model, such a trajectory will take much longer to compute.

In order to more fully account for the stochastic nature of the fission process, we seek an approximation in which the system has a chance of splitting at each instant with probability P, which may functionally depend on various physical quantities such as the neck thickness parameter, surface strain, temperature, and other geometric factors. This may be possible by using a kind of the Monte-Carlo method, where the neck rupture probability at a given time step will be compared with the randomly generated number in the uniform probability distribution. If, at a given time, the number drawn is less than or equal to P, the rupture occurs and the trajectory is immediately terminated, otherwise the trajectory continues.

Now we need to specify a form of probability P that will be a marker for neck break. We assume that as soon as r_{neck} is less than or equal to r_n, the probability of fission is equal to or only slightly less than one. It is more complicated to estimate the probability for larger neck radii. As noted above, contributions to the FMD from configurations with $r_{neck} = 2r_n$ or even $3r_n$ are also possible for some isotopes, especially at low excitation energies. One can then assume that the form of such a probability distribution, depending on the neck radius or, more precisely, on the set of coordinates $\mathbf{q}$, has the following form:

$$P(\mathbf{q}) = \frac{1}{1 + e^{\frac{r_{neck}(q) - r_c}{a_r}}} \tag{5.25}$$

This probability is compared in each iteration with the probability obtained from the uniform random number generator. In Fig. 5.27 there is an example where at a certain time t the trajectory of a compound fissile system reaches the neck radius $r_{neck} \approx 2.2\, r_n$. Assuming that the distribution (5.25) is optimally characterized by $r_c = 2r_n$ and $a_r = 0.4r_n$, the probability of fission is $P_t = 0.4$. The random number drawn during this time is marked with a red arrow ($X_{rand} \approx 0.5$) and has a higher value than P_t. Therefore, the neck break does not occur at t and the trajectory continues.

Let us study the effect of varying the distribution of~(5.25) within $a_r \in [0.2, 0.8]$ and $r_c \in [2, 4]$ in units of r_n on the FMD of selected U and Fm isotopes. The statistics, however, include 10^4 stochastic trajectories. This has not been discussed before, but the $^{254-258}$Fm chain is very interesting because of the rapid transition from asymmetric to symmetric shape of their FMD due to the abrupt change in shell effects in these neighbouring nuclei.

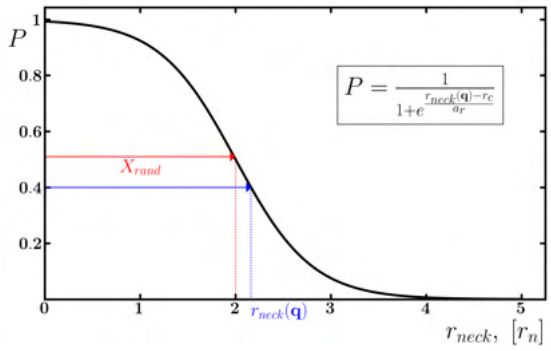

Figure 5.27: Example of checking nucleus neck rupture by the Monte Carlo method in an arbitrary trajectory step.

The first thing that strikes the eye in Figs. figs. 5.28 and 5.29 is obviously a similar pattern as in the case of the Gaussian distribution - there is no uniform variation of the distribution, which is not surprising.However, unlike the Gaussian model, there are no optimal parameters that adequately fit even three isotopes of the same element.

Second, there is a gradual broadening of the FMDs with increasing width of the distribution a_r, as in ^{238}U. Such a tendency is quite clear, since the probability of fission of more and more compact states with a substantially thick neck becomes improbably high.Other nuclei also show a similar pattern, but the tendency in question usually cuts off at $a_r = 0.5r_n$. Finally, the best reproduction of the overall shapes of the experimental FMDs is obtained for $r_c \approx 2r_n$ and $a_r \approx 0.3r_n$

The saddest situation is observed for $^{256-258}$Fm nuclei, where the transition from asymmetric to symmetric mass distribution is visible for ^{256}Fm rather than for ^{258}Fm nuclei.It can therefore be said that the problem of reproducing this property of mass distributions in Fm nuclei does not lie in one or the other implementation of the stochastic nature of fission, but rather is a consequence of the fact that we are dealing here with bimodal fission, which must be simulated using different initial conditions for the Langevin equations than those presented in the previous sections.

Excitation energy influence on final conditions

At higher temperatures, the surface of the nucleus, especially in the neck region, becomes less stable due to some local fluctuations of the nuclear surface caused by the thermal motion of the nucleons. This can cause the neck to rupture even if its radius is much larger than the radius of a single nucleon, r_n. Supplementing this statement is Fig. 5.30, which shows the FMD for the neck radius r_{neck}^{stop} changing from $2r_n$ to $4r_n$ for a compound system ^{236}U with an excitation energy of about 15 MeV above the barrier (left panel). The yields corresponding to symmetric fragmentation in the FMDs become closer to the measured values as the neck radius becomes larger, of the order of $3r_n$. As shown earlier in Fig. 5.23, the shape of the FMD for r_n is almost the same as for r_n $2r_n$. On the other hand, at high values, e.g. $r_{neck}^{stop} > 4r_n$, it is already difficult to speak of a well-defined neck, unless, of course, one observes a division into compact deformed fragments. The right panel shows the behavior of the FMD already with an excitation energy of $\approx$ 60 MeV. A similar trend can be observed there, only in contrast to the situation on the left, the optimal value for r_{neck}^{stop} shifts even towards higher values to lie in the interval between $3r_n$ and $4r_n$.

Using the generalized form of the Gaussian distribution of the r_{neck}^{stop} radius, we can see a change in FMDs with increasing excitation energy. However, as shown in Fig. 5.31 using as an example the ^{235}U fission reaction induced by neutrons with energies of 15 MeV, the number of events in the symmetric channel is much lower than expected. This feature is also indicated in Ref. [139], where the Fourier parametrization with the upper limit on elongation $q_2^{max} = 2.9$ was used as an important part of the characteristics of the reaction in question. The behaviour of the FMDs as function of the boundary q_2^{max} can be found below.

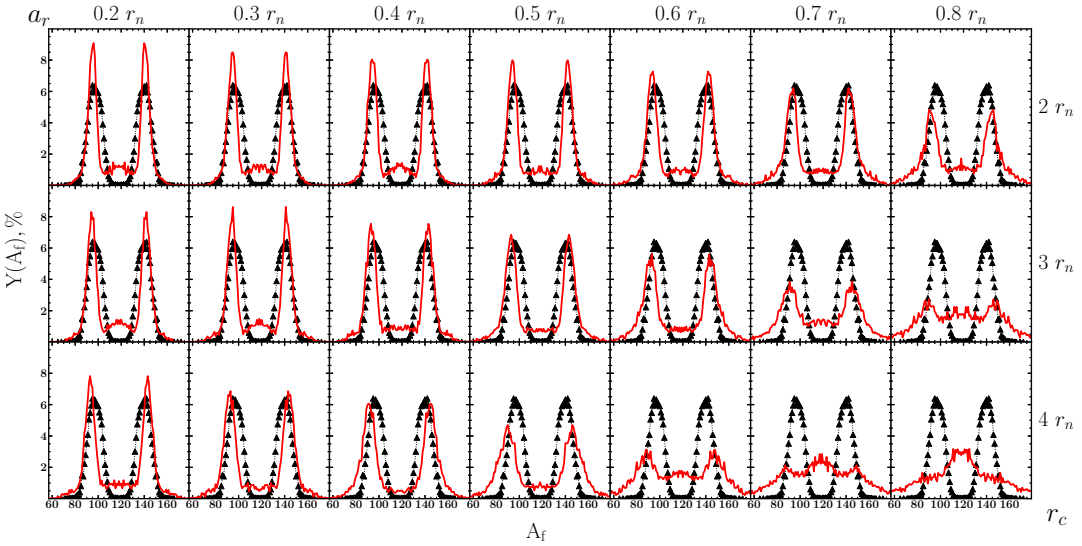

(a) For nucleus of ^{234}U with data from [147]

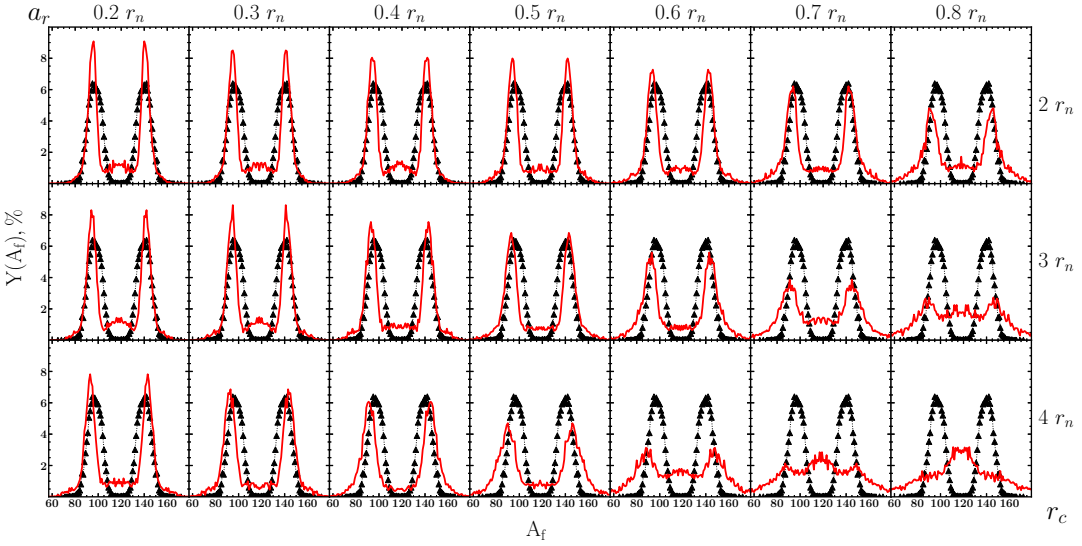

(b) For nucleus of ^{236}U with data from [142]

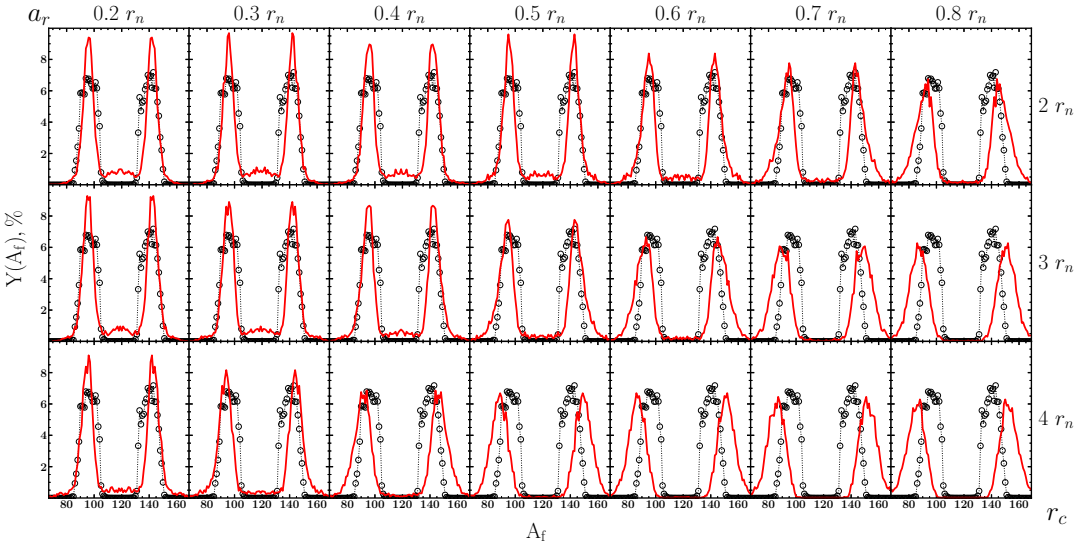

(c) For nucleus of ^{238}U with data from [148]

Figure 5.28: Comparison of FMDs calculated with Fermi-like neck breaking distribution for even-even isotopic chain of U with analogous experimental data.

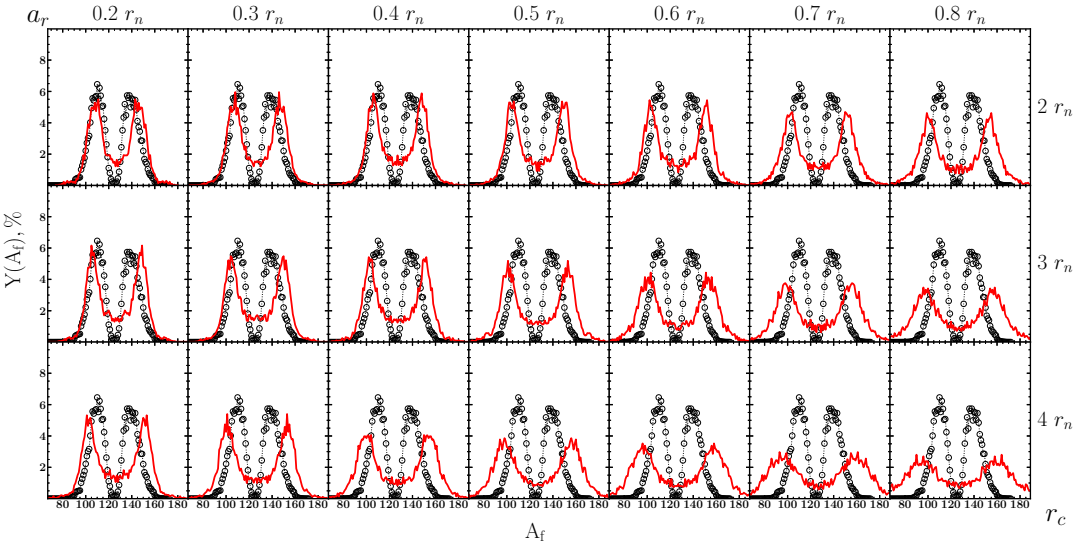

(a) For nucleus of ^{254}Fm with data from [149]

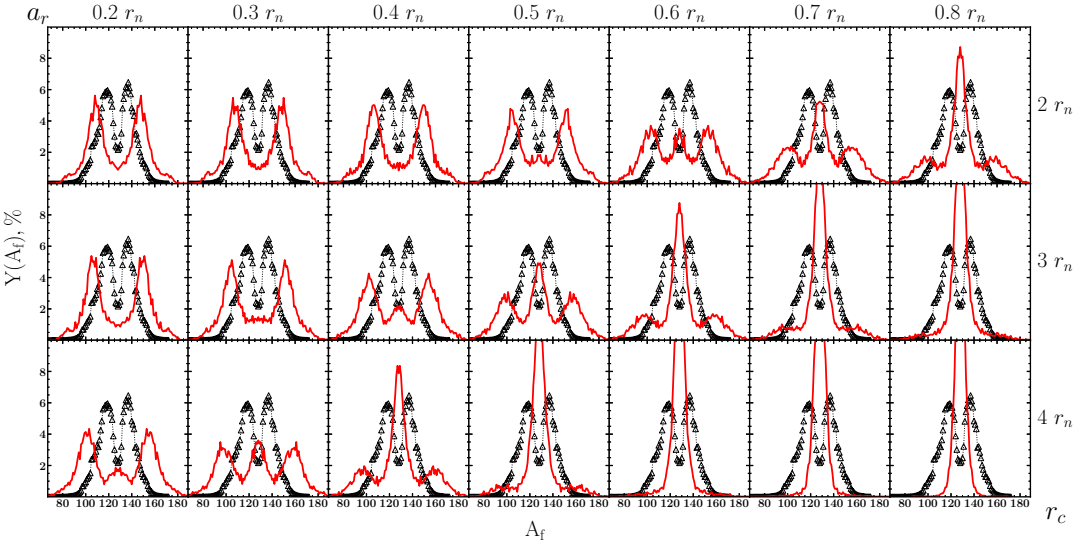

(b) For nucleus of ^{256}Fm with data from [149]

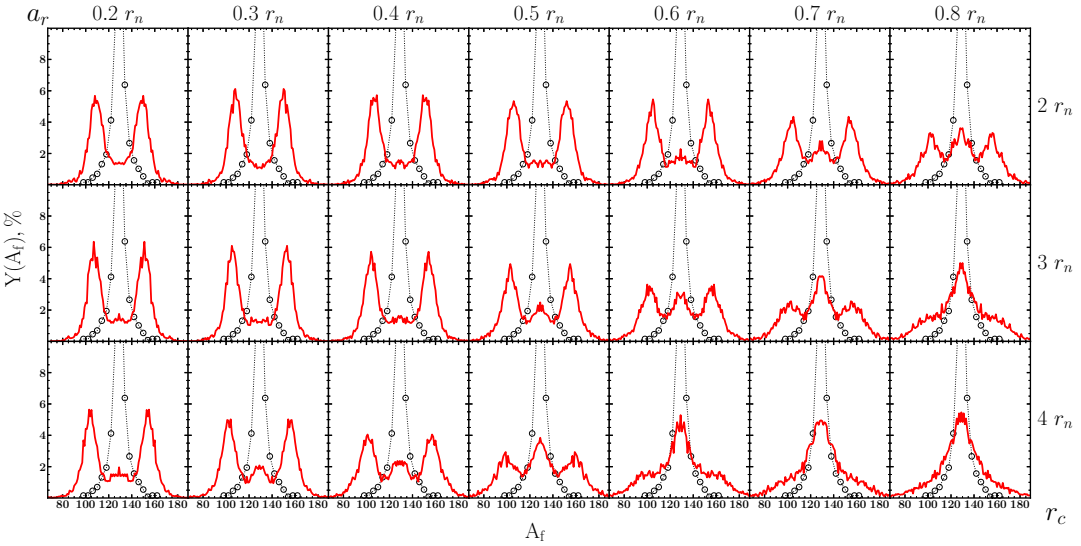

(c) For nucleus of ^{258}Fm with data from [154]

Figure 5.29: Comparison of FMDs calculated with Fermi-like neck breaking distribution for even-even isotopic chain of Fm with analogous experimental data.

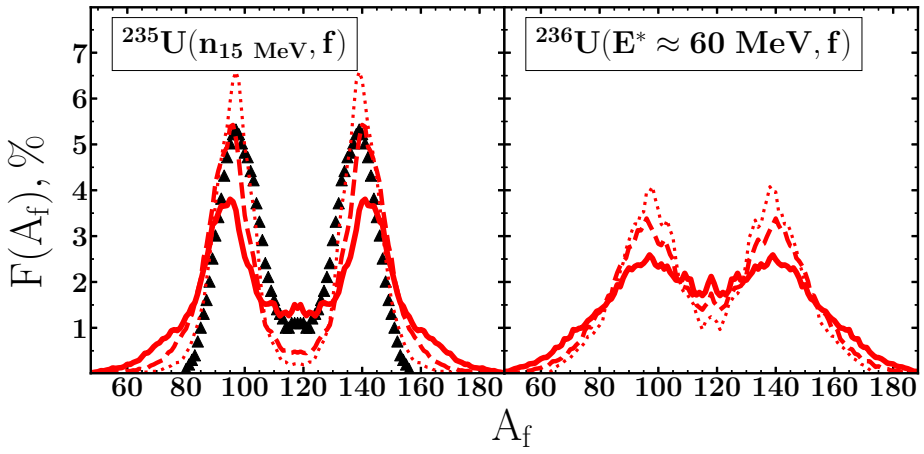

Figure 5.30: Comparison of the primary FMDs for 15 MeV neutron-induced fission of ^{235}U (left) and ^{236}U with 55 MeV excitation above the top of the barrier (right), calculated for the value of r_{neck}^{stop} equal to: $2r_n$ (dotted line), $3r_n$ (dashed line), $4r_n$ (solid line). Experimental data [143] are also shown to make the comparison clearer.

It is possible to use a different approach to describe the dependence of r_{neck}^{stop} on the excitation energy. Let us assume that r_{neck}^{stop} changes randomly as a function of temperature along the trajectory during the relaxation time interval τ introduced and discussed in the previous sections. The random value of r_{neck}^{stop} at low excitation energies should be in the region of narrow necks, say $\approx r_n$, gradually shifting to thicker necks as the excitation energy increases.

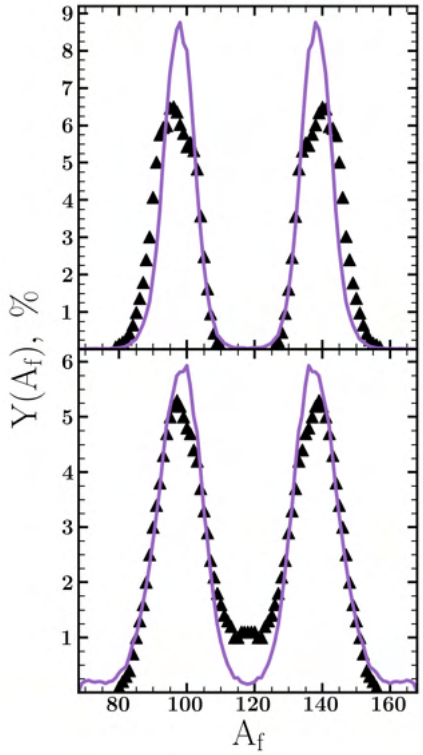

Figure 5.31: FMDs for induced fission of ^{235}U nuclei by thermal (top) and 15 MeV (bottom) neutrons using the Poisson distributed neck radius r_{neck}^{stop}.

An example of such behavior is the discrete Poisson distribution $P_{Pois}(\lambda, f)$, where the expectation λ is proportional to the temperature of the system T, and the value f, instead of the number of events, is equal to the ratio r_{neck}^{stop}/r_n at each iteration of the temperature recalculation. If $r_{neck} \leq f \cdot r_n$ means the system is collapsing. Of course, the value of λ must be much smaller than T. Otherwise, even for forced fission reactions where the excitation energy is close to the value of the barrier, the probability of dropping out values of r_{neck}^{stop} in the range of r_n and $2r_n$ will be rather large from almost the beginning of the trajectory calculation. Therefore, it was decided to relate the expectation to the temperature via a linear dependence of the type $\lambda = T/5$. Thus, at $T \approx 1$ MeV, the system will decay when r_n and $2r_n$ are reached, which is similar to the methods discussed above using random distributions: discrete uniform or continuous Gaussian. The results of calculations with the described procedure for the reaction of the forced fission of the ^{235}U nucleus by thermal and very fast neutrons are shown in Fig. 5.31.

It can be seen that in the upper panel there is quite good agreement between the obtained model and the experimental values of the primary FMDs. The predicted FMD is slightly narrower - the effect of the large number $r_{neck}^{stop} = 0$, but this together with the rest of the boundary

conditions leads to the absence of events in the valley of symmetric fission. Unfortunately, the situation is worse in the bottom panel. On the positive side: most of the distribution computed by the model agrees with the empirical data. On the negative side, the number of symmetric fission events is very small, catastrophically small. There are also tails in the asymmetric fission region, indicating the aforementioned problem of r_{neck}^{stop} values falling out over a wider range than $[r_n,\ 2r_n]$.

Regrettably, a more complex nonlinear dependence could not be found during the current research. However, it can be seen that the form of the dependence $\lambda(T)$ must have a more complex and non-trivial relationship. It is probably somehow related to the "viscosity" of the system due to the increased nucleon interaction, which grows with increasing temperature. The "viscosity effect" should contribute to the breakup probability, thereby either slowing down or speeding up the fission process. According to the lower panel of Fig. 5.32 - slowing down. But how, the author doesn't know at the moment. Anyway, let me assume that temperature is the missing component to describe the random fission of compound fissile systems. There is definitely a connection between this quantity and a Monte Carlo type procedure. But these assumptions are only hypothetical and require a detailed study in the future, outside the scope of this thesis.

Symmetric channels effect of very elongated systems

As announced in the previous subsection, it is worth considering the influence of the upper limit q_2^{max} on the shape of the FMDs, especially when near-symmetric fragmentations are taken into account. As before, our study is based on the fission reaction of the ^{235}U system stimulated by 15 MeV neutrons. In addition to the previously mentioned limits of $q_2^{max} = 2.35$ and 2.9, a set of trajectories is determined for the intermediate cases of q_2^{max} for 2.5 and 2.7. It should be noted that going beyond the safe limit of $q_2^{max} = 2.35$ increases the numerical uncertainties in the determination of the PES and transport coefficients, leading to more and more artifacts in the resulting mass distributions. This is primarily related to the limitations of the single-particle energy determination of the Yukawa-folded single-particle potential, where such large expansions become more and more difficult to handle reasonably within a single-centered harmonic oscillator basis.

Fig. 5.32 shows the results of the calculations at the aforementioned upper coordinate limits of q_2. The growth of fission events in the near-symmetric channel at each strain limit q_2^{max} starting from the limit value of 2.35 is quite noticeable. The distribution obtained at $q_2^{max} = 2.7$ is very close to its empirical counterpart; the asymmetric peak and the symmetric cleavage valley practically coincide. At $q_2^{max} = 2.9$, the overestimation of the FMD occurs in both regions. The behavior of the peak, which shifts toward symmetric fission, though not significantly, is quite interesting. Remarkably, all the above cases except $q_2^{max} = 2.7$ do not agree with the experimental fragmentation distribution, preferring yields smaller by several percent.

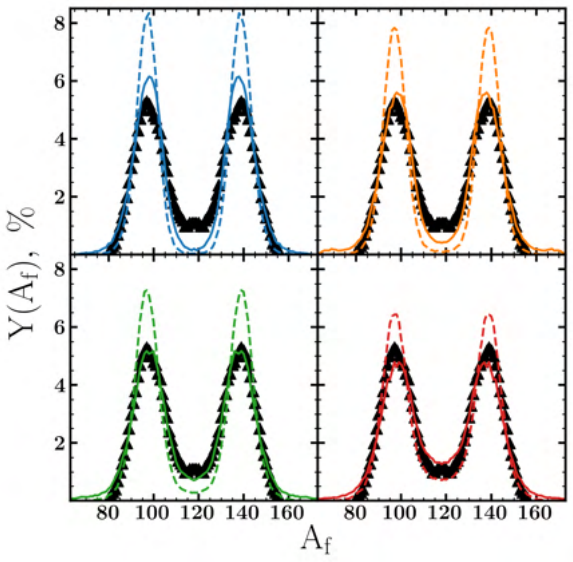

Figure 5.32: FMDs for fission of ^{235}U nuclei by thermal (dashed) and 15 MeV neutrons within different upper limit of q_2: 2.35 (blue), 2.5 (orange), 2.7 (green), 2.9 (red).

Note that this kind of growth of the contribution to the near-symmetric fission region

is typical for both thermal and 15 MeV neutron-induced reactions. It suggests that the best choice is to use the $q_2^{max} = 2.35$ limit, as done in previous works [40, 41, 81, 115], where a similar Fourier shape parameterization was used. For this value, all macroscopic and microscopic quantities entering the system of Langevin equations are determined with satisfactory accuracy.

Excitation energy and boundary limits influence on energetic characteristics of fission

The fragment mass distributions are not the only quantity that can be described by the Langevin formalism. Moreover, measuring mass distributions is a very difficult task from an experimental point of view. It is much easier to measure energy values. As known from [1], the vast majority of the energy released in fission is associated with the Coulomb interaction of the fragments. The repulsion of the two positively charged fragments significantly increases their kinetic energy compared to their collective motion toward fission just before fragmentation. Assuming that the N/Z ratio for the fission fragments remains the same as in the compound nucleus, and assuming that they interact mainly through the monopole-monopole (point charge) Coulomb force supplemented by the kinetic energy component describing their collective motion just before fission, the total kinetic energy (TKE) of the fragments can be written by the following equation:

$$\mathrm{TKE} = E_{Coul} + E_{kin}^{coll} = e^2 \frac{Z_H\, Z_L}{R_{12}} + \frac{1}{2} \sum_{ij} \left[\mathcal{M}^{-1}\right]_{ij} p_i p_j \tag{5.26}$$

where H and L denote the heavy and light fission fragments, respectively, and R_{12} is the distance between the centers of mass of the fission fragments, defined by the formula (3.46). The inertia tensor $\mathcal{M}$ is calculated for the composite nucleus of mass number A, and the value of the conjugate momentum vector $\mathbf{p}$ is taken as the corresponding momentum of the fission system.

Usually, the averaged values of the total kinetic energies are considered and compared with the corresponding empirical data. Such averaging can be done in various ways, but it is generally convenient to consider the behavior of TKE averaged over the mass of the fission fragments, e.g. the $\overline{\mathrm{TKE}}(\mathrm{A_H})$. Fig. 5.33 shows in two panels the corresponding averaged kinetic energies for ^{235}U nuclear fission reactions by thermal and 15 MeV neutrons. In both cases one observes inflated values of $\overline{\mathrm{TKE}}$ compared to the available experimental data, especially for cases with low limits q_2^{max}. It should be noted, however, that the values and

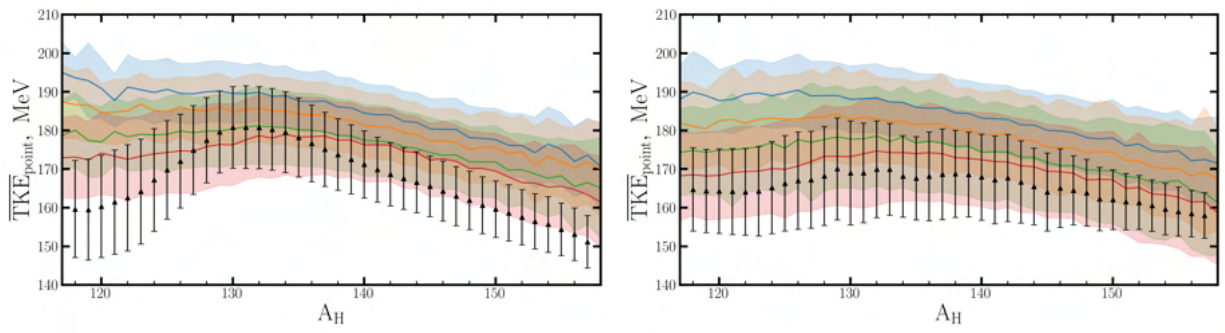

(a) by thermal neutrons (b) by 15 MeV neutros

Figure 5.33: Average total kinetic energies from heavy mass fragment for fission of ^{235}U nuclei at different upper border limit of q_2: 2.35 (blue), 2.5 (orange), 2.7 (green), 2.9 (red).

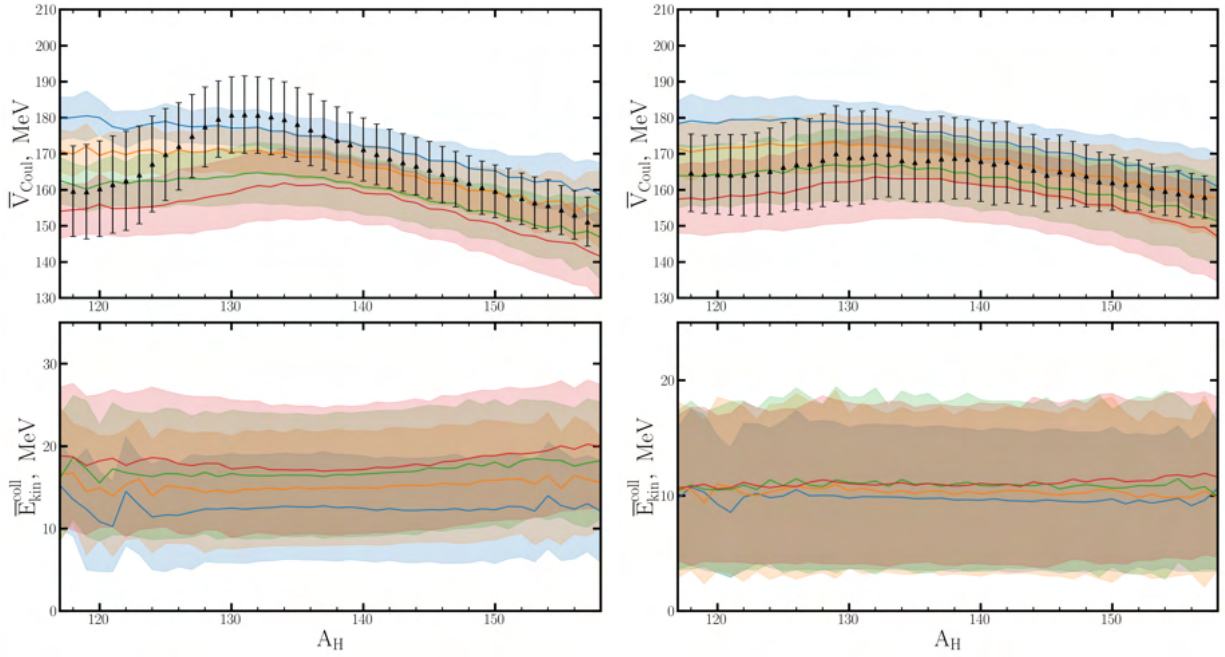

(a) by thermal neutrons (b) by 15 MeV neutrons

Figure 5.34: Decomposition of $\overline{\text{TKE}}$ calculated by Eq. (5.26) for fission of ^{235}U nuclei at various q_2^{max}.

the trend of the TKE line itself are closer for more excited systems than for reactions with thermal neutrons. It is also interesting that the last two q_2^{max} values give very close averaged TKE values, especially for the asymmetric fission regime.

To clearly understand the causes, let us consider both components separately (5.26). The decomposition is shown in Fig 5.34, where the left panel shows thermal neutron induced fission and the right panel shows the case of very fast neutrons. The first thing to note is that the averaged values of the collective motion kinetic energy are almost independent of the fragment masses. Furthermore, almost identical values are observed for all cases considered in the right panel, where the results for 15 MeV neutron fission are shown. This may indicate that in the final stages of fission the systems are in thermodynamic equilibrium and have close excitation energies. Approximately the same is observed in the left panel for the last two cases shown (for $q_2^{max} = 2.7$ and $q_2^{max} = 2.9$). It seems that the systems also reach thermal equilibrium and close excitation energies, thus reaching scission configurations.

The overestimation of $\overline{\text{TKE}}$ suggests using, to some extent, an equivalent approximation for the Coulomb interaction of fission fragments, as proposed in [23]. The repulsion of charged fragments is defined as the difference between the total Coulomb energy of the compound nucleus at the scission point $\mathbf{q}_{sc}$ and the two deformed fragments separated by an infinite distance:

$$V_{\text{Coul}}(\mathbf{q}_{sc}) = \frac{3e^2}{5r_0}\left[\frac{Z^2}{A^{1/3}}B_{\text{Coul}}(\mathbf{q}_{sc}) - \frac{Z_H^2}{A_H^{1/3}}B_{\text{Coul}}(\mathbf{q}_H) - \frac{Z_L^2}{A_L^{1/3}}B_{\text{Coul}}(\mathbf{q}_L)\right], \tag{5.27}$$

where $r_0 = 1.2$ fm, while the parameter B_C is the ratio of the Coulomb energies of the deformed and spherical nuclei, as discussed in the deformation-dependent liquid drop model, e.g. the LSD model. As proposed in [155], the surface interaction of the fragments when

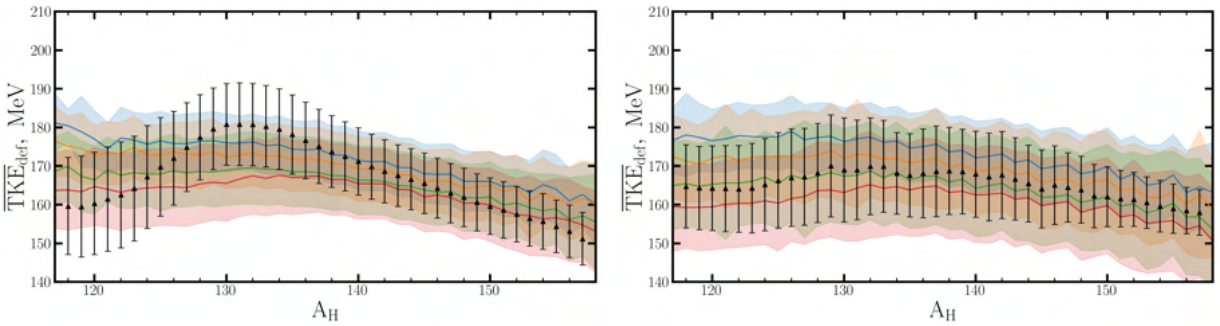

(a) by thermal neutrons (b) by 15 MeV neutrons

Figure 5.35: Average total kinetic energies calculated with accounting eqs. (5.27) and (5.28) or fission of ^{235}U nuclei at various q_2^{max}.

the nucleus neck ruptures is additionally taken into account by the following relation

$$V_{nuc}(\mathbf{q}_{sc}) = -2E_{surf}(0)\frac{\pi r_{neck}^2(\mathbf{q}_{sc})}{4\pi R_0^2} = -\frac{1}{2}E_{surf}(0)\left(\frac{r_{neck}}{R_0}\right)^2. \tag{5.28}$$

Here $E_{\mathrm{surf}} = B_{\mathrm{surf}}A^{2/3}$, and B_{surf} is the surface deformation coefficient of the LSD model [39]. In contrast to the cited work, where this energy is estimated to be of the order of 9 MeV, in the present case, due to the stochastic neck break process, it is necessary to consider this interaction for each Langevin trajectory. Figure 5.35 shows the resulting $\overline{\mathrm{TKE}}$ taking into account the corrections introduced above. The left panel for the fission reaction with thermal neutrons shows a slight change in the trend of the curve, mainly affecting the case with the $q_2^{max} = 2.35$ limit, while the energy values are shifted down by about 10 MeV, giving visibly better estimates of the TKE compared to the results from the point-charge Coulomb repulsion energy shown in Fig. 5.33. The same can be said for the results shown in the right panel of Fig. 5.35, but the TKE estimates made within a simple monopole-monopole Coulomb interaction do not deviate much from the experimental data.

This quite reasonable agreement at higher excitation energies may suggest that the corresponding fission fragments are generally more elongated over the whole range of fragment masses A_H than at low excitations. A similar idea was suggested by Shimada et al. [113], where the characteristics of the ^{235}U and ^{239}Pu nuclear fission reactions by neutrons with energies of 14 MeV were studied. To calculate these characteristics, the authors used the model associated with the solution of a four-dimensional system of Langevin equations using a two-center shell model with transport coefficients calculated within the framework of known microscopic approaches. The trajectories ended at the moment of system rupture, i.e. where $r_{neck}^{stop} = 0$. From the analysis of the obtained TKEs, extremely elongated systems were identified whose quadrupole moments correspond to fission fragments with very elongated configurations. Curiously, this does not contradict the idea that thicker necks can be randomly ruptured when the system is in excited states.

However, the authors suggest that this is due to the blurring of shell effects in the heated fragments, which are larger in the case of near-barrier fission, making the shapes closer to spherical. This statement is quite controversial, because the temperature of the fragments in this type of fission is not much higher than 1 MeV, so the shell effects still persist at a quite significant level. As shown earlier in subsection **??**, it may be possible to neglect the shell effects at excitation energies above 40 MeV, but not at 20-22 MeV.

To summarize for this subsection, we can say that

- The trajectory termination conditions imposed on the system play a dominant role

in the Langevin approach. Certainly, the set of initial configurations is also crucial, especially for systems with multiple fission valleys, such as in some Cm or Fm nuclei, where the transition from the asymmetric to the symmetric dominant fission mode is observed. In addition, as shown in [78, 115], in spontaneous fission the role of the ensemble of initial positions and conjugated momenta increases, while for induced fission it is enough to start from the region of the outer saddle point and get a satisfactory fragment mass distribution.

- There is no general rule for determining when the system decays into two fragments. However, when the values of the neck radius are close to the size of a single nucleon, the system is likely to decay. In addition, attempts were made to describe the random nature of the neck break. It turns out that the most appropriate approach tested in this thesis is a random predetermination of the terminating r_{neck} radius, done before a trajectory is started, using a Gaussian random number distribution. Fitting to the experimental distributions of some actinides showed that reasonable agreement could be obtained for a distribution of the form $xi_{norm}(r_n, 0.5r_n)$.

- It was quite interesting to find additional contributions near symmetric configurations upon extending the deformation space toward larger shape elongations, which provided an excellent description of the fission characteristics at $\approx$ 20 MeV excitations. However, when considering lower initial excitations of the system, the available limits of the form (5.8) are quite sufficient to describe the characteristics of induced (by thermal or fast neutrons) and spontaneous fission of actinide nuclei.

- A realistic quantitative relationship between neck radius, elongation, excitation energy (temperature) and/or possible other observables essential for the fission process requires further, more detailed investigations.

These conclusions and developments will be very welcome in the next subsection, where the results for even-even nuclei with charge number in the range $[90-116]$ will be studied.

5.4 Characteristics of nuclear fission at scission point

Finally, having established a reliable approach based on a realistic, though classical, Langevin approach, it is possible to obtain some realistic characteristics of the fission reaction for even-even nuclei with charge numbers in the range of $90-116$. In this section, we essentially search for the mass distributions of fission fragments, charges, and total kinetic energies obtained upon rupture of the fissile compound systems. The principles of the procedure are the same as those described in the previous subsections, in which we mostly discussed the FMDs for the test case of ^{236}U. To calculate the FMDs, an estimate of the volumes of the fragments at the scission point (more precisely, the pre-scission point) of the trajectory is required. Note that the fragment charge distributions (FCD) are derived directly from the FMDs, since the N/Z ratio is assumed to be preserved in both fragments. The total kinetic energy of the trajectory is calculated based on the resulting FCDs and using a refined form of the Coulomb potential for the deformed fragments, as well as a correction for the surface energy at the neck break (if applicable), i.e. according to eqs. (5.27) and (5.28).

Detailed study shows that some fine details of the model need to be changed in the transition from actinides to superheavy nuclei. The first relates to the configuration space used for these two categories of nuclei. For actinides, the calculations were performed

in the "standard" lattice given by (5.8), while for superheavy, with heavier masses, the limits of the mass asymmetry coordinate must be extended, as it appears on (**??**). The second point is that, unlike actinides, the fission of superheavy nuclei is considered only by the spontaneous fission mechanism. This imposes a certain peculiarity on the way the resulting distributions are analyzed. As mentioned earlier, if the model ignores multiple exit points belonging to different well-separated fission valleys, the resulting distributions may be far from realistic. On the other hand, even such a simple model can describe the fission characteristics of super-heavy nuclei, the knowledge of which can shed light on the reaction mechanisms of the fissile system formed after the collision of two nuclei.

5.4.1 Actinides case

Therefore, let us now study the fission characteristics of even-even actinide nuclei, i.e., nuclei with a charge number in the range of 90 (thorium) to 102 (nobelium), formed in either reactions:

- induced fission by thermal neutrons with ^{227,229}Th, ^{233,235}U, ^{239}Pu, ^{249}Cf, ^{255}Fm;
- photofission of $^{222-228}$Th and ^{226,230}Th by 11 and 14 MeV γ quanta, respectively;

or experienced fission from the reaction of spontaneous fission of the nuclei ^{238,240}U, $^{238,242-244}$Pu, $^{242-250}$Cm, $^{248,252-256}$Cf, ^{246,248,252,254,258}Fm, $^{254-262}$No.

The primary FMDs obtained within the developed model for most of the above reactions are shown in Fig. 5.36. It is easy to see that even though some of the experimental data used for comparison correspond to the secondary FMDs (after light particle evaporation), one observes either good agreement, or at least the theoretical curves show a similar trend to the experimental ones. This is especially true for the nuclei U, Pu and Cm. The description of the heavier actinides like Cf, Fm and No is problematic. Looking through the FMDs for the chain of Cf isotopes, it is clear that they are characterized by the presence of symmetric fission channels, which are practically not observed experimentally. In the heavy ^{256}Cf isotope, a substantial yield of symmetric fragmentation is experimentally observed, while our theoretical predictions suggest a much higher contribution of near-symmetric fission. Similar pattern is observed for the chain of Fm isotopes, where the experimentally expected rapid growth of symmetric (and compact) fission for ^{258}Fm is not observed. On the contrary, it is practically the same as in the ^{256}Fm nucleus.

Another issue is the Th isotopes. At first glance, looking at figure 5.36, the overall agreement looks quite good when compared with FMDs obtained after neutron emission. However, let us consider the FCD charge distribution and compare it with the available empirical data of the photo-fission reactions discussed in [156, 157] and shown in Fig. 5.37. Here one can see the absolutely divergent distributions for the $^{222-226}$Th nuclei. The situation is slightly better for ^{228,230}Th, where at least the position of the asymmetric peaks has been reproduced.

There are several possible reasons for the discrepancies in light thorium nuclei mentioned above:

1. The use of the generalized function ξ_{norm} to describe Gaussian-type random neck breaking,
2. Uncertainty in the choice of the exit point under the fission barrier for the case of spontaneous fission,
3. Quality of the PES determination for nuclei far from the stability line using the LSD liquid drop model parameterization for large shape expansions.

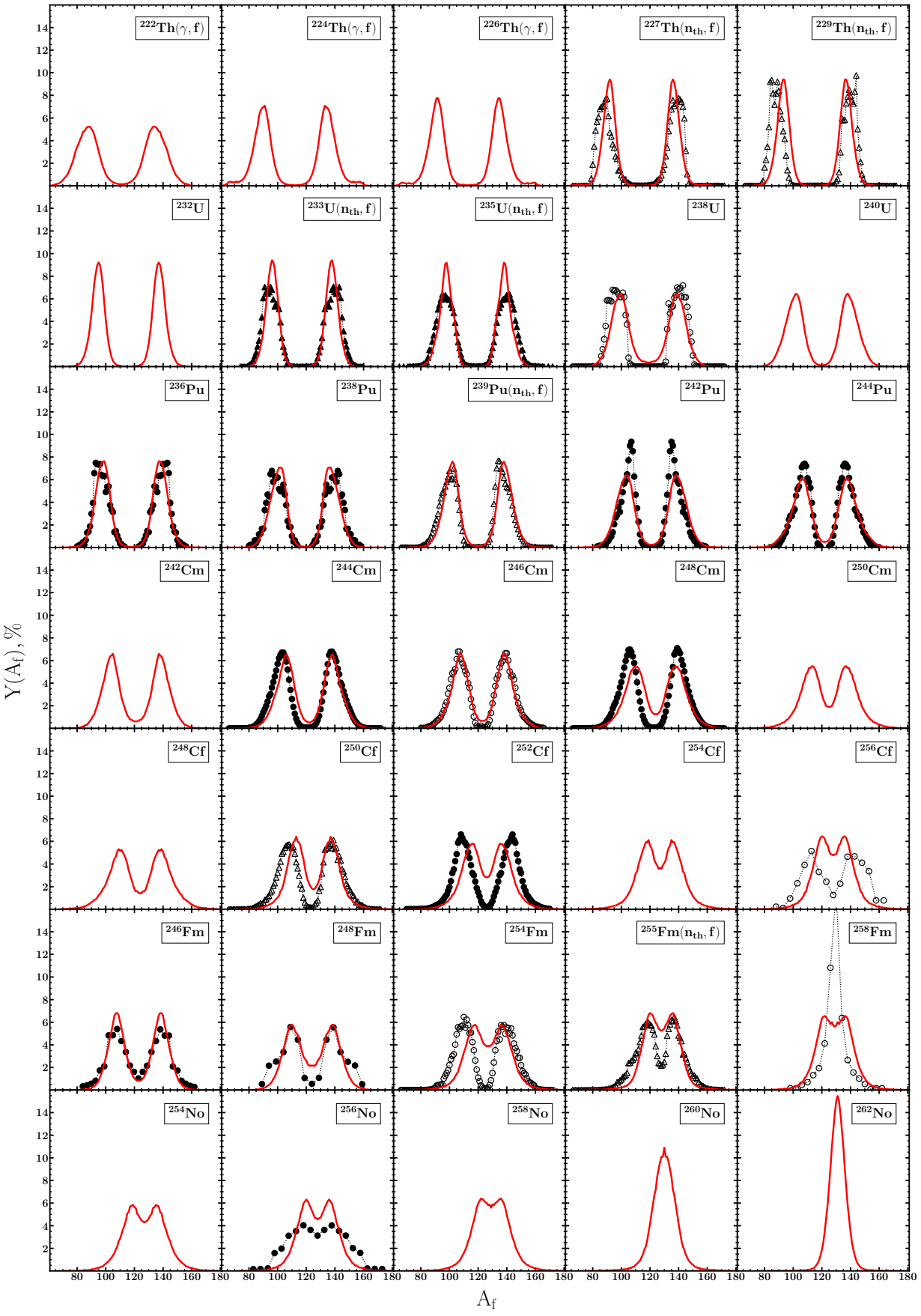

Figure 5.36: Comparison of the primary FMDs calculated within the developed model for series of even-even actinides that undergo induced or spontaneous fission with the available primary and secondary FMDs derived from experimental data [142, 147–153].

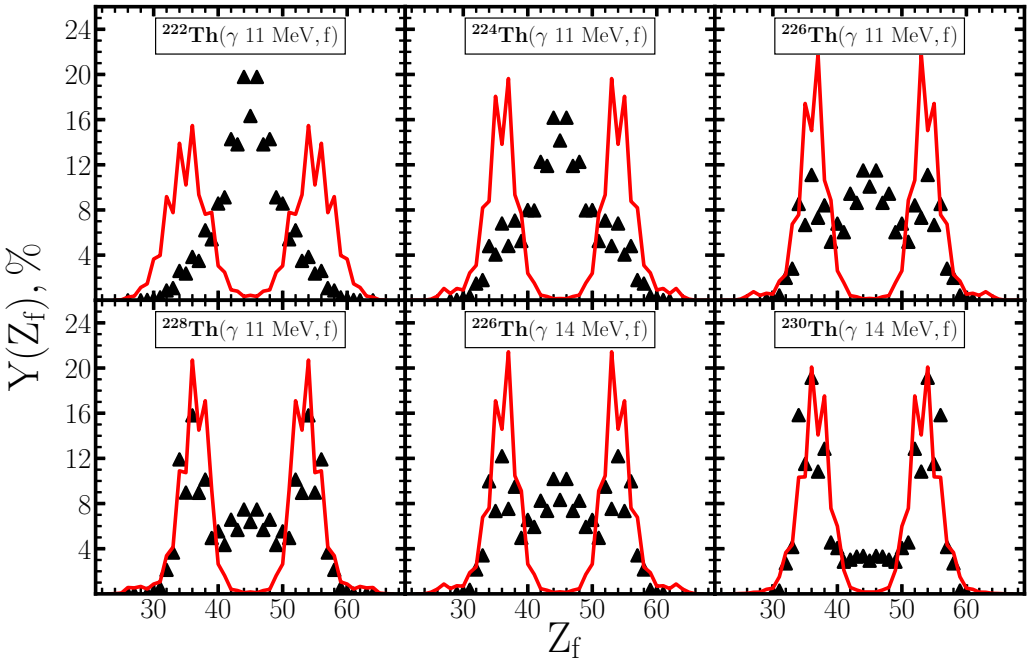

Figure 5.37: Comparison of modeled primary FCDs (red) with experimental data (black triangles) for photofission $^{222-230}$Th by 11[156] and 14[157] MeV photons.

It is not difficult to agree with the first point. As shown earlier, the introduction of unified parameters for the Gaussian distribution of the neck radius at which the nucleus is expected to fission, in contrast to the parameters obtained from the individual fit, limits the accuracy of the FMD reproduction.

The second point is also understandable. It is related to the simplicity of the method used to find the turning points. We simply look for the exit of the barrier points located in the nodes of the mesh, comparing their energy with the energy of the initial state within a small deviation $|\epsilon|$. It follows that the uncertainty of one step along the lattice may provoke a significant impact on the resulting charge distribution in some nuclei where the PES after the barrier shows a highly variable structure with multiple fission valleys as shown in Fig. 5.38.

But perhaps the most important point is the last one. Consider the PES for the nucleus ^{222}Th in the (q_2, q_3) plane, and the two cross sections (q_3, q_4) at $q_2 = 2$ and $q_2 = 2.35$, respectively. These are shown in the three panels of Fig. 5.38. It can already be seen in 5.38a that the exit of the asymmetric valley at $q_2 \approx 2.3$ is much steeper than that for the symmetric channel, attracting most of the fission trajectories. Therefore, the "easiest" way for the system starting from the mass-asymmetric saddle point at $q_2 \approx 1$ leads to the well-defined asymmetric valley.

Such behavior of the resulting distributions in light thorium isotopes is also observed in other approaches discussed in our group, e.g. in [41], where the same PES calculated in the Fourier parametrization framework was used. In this study, a simple static method was used to estimate the FMDs, based on the so-called Born-Oppenheimer [41, 158] approximation. Additionally, a random Gaussian-type neck breaking function was introduced, where the dispersion value was a fitting parameter. In addition, the value E_0 included in the definition of T^* was varied, with the overall fit resulting in FMDs being estimated for elements with $Z \in [90, 104]$.

Figure 5.39 shows the comparison of the results obtained in this work and with the above mentioned method described in [41]. It can be seen that despite the different methods

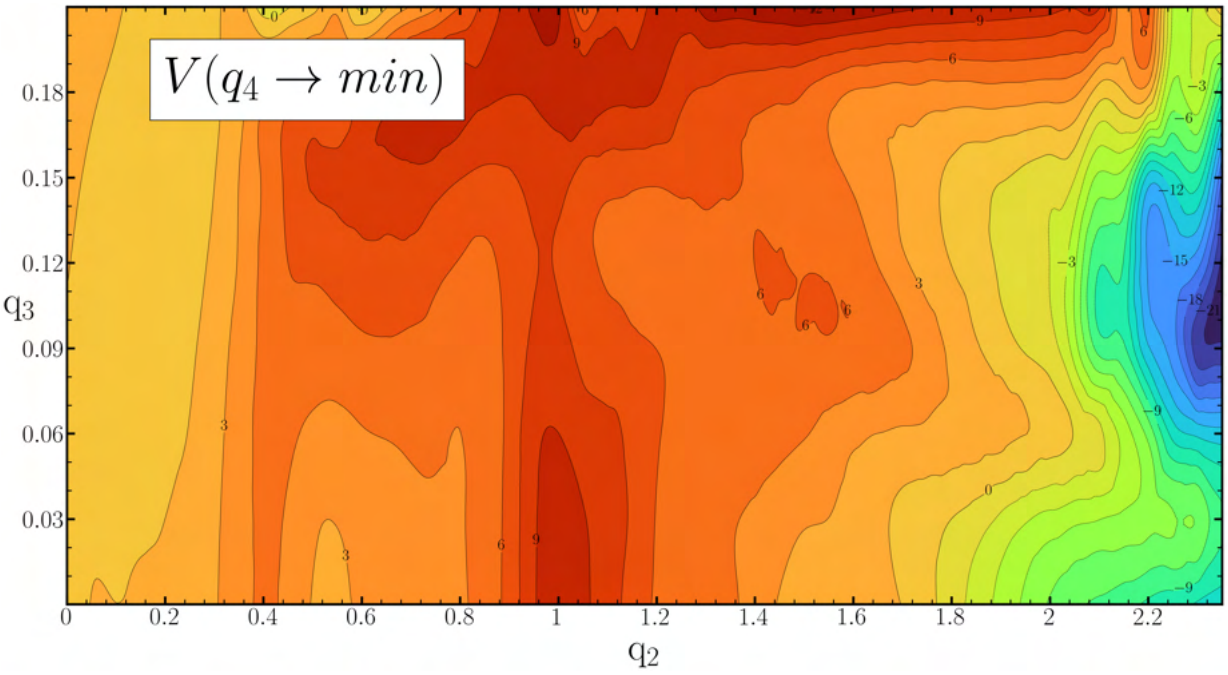

(a) PES in (q_2, q_3)-plane with minimization of q_4 coordinate

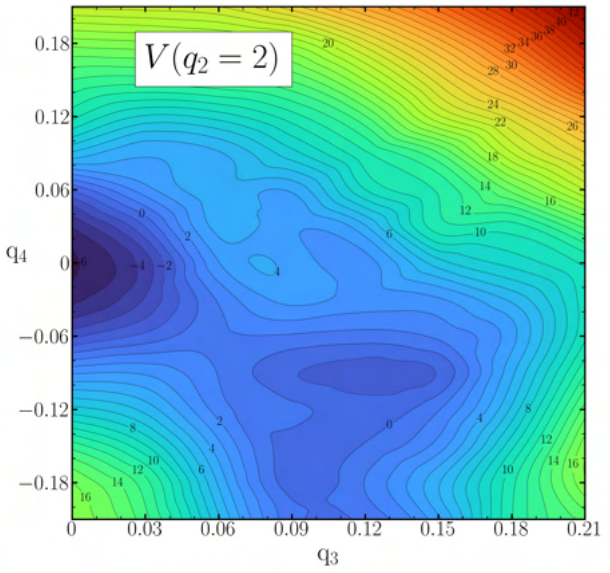

(b) Cross section of PES in (q_3, q_4)-plane for elongated form $q_2 = 2$

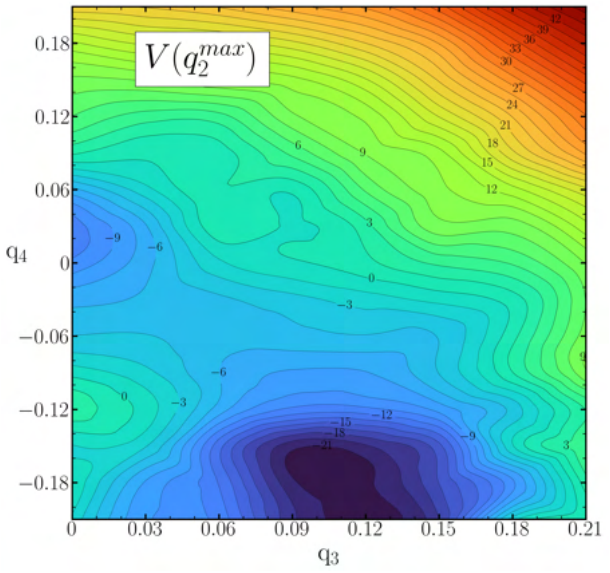

(c) Cross section of PES in (q_3, q_4)-plane at upper border limit of q_2 coordinate

Figure 5.38: Various PES maps for ^{222}Th nuclei

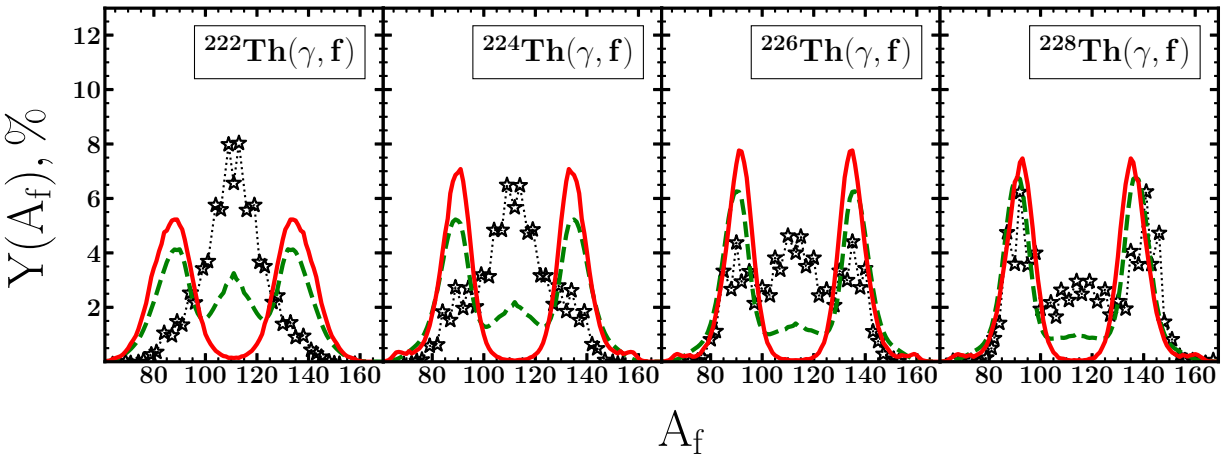

Figure 5.39: Comparison between calculated primary FMDs produced by our Langevin method (red) and the results of the Born-Oppenheimer model of Ref. [41] (dashed green). Experimental data (hollow stars) obtained from FCDs data for the photofission of $^{222-228}$Th by 11 MeV photons [157].

used, the results are quite similar. This clearly supports the third point. Furthermore, a new fitting of the optimal parameters for the neck distribution for thorium nuclei was performed in the framework of the mentioned paper, which showed a better agreement of the curves in comparison with the empirical data.

Finally, the total kinetic energy distributions are presented below. Figure 5.40 shows the two-dimensional plots of the TKE obtained from the fission fragment mass distributions for the same set of isotopes presented in Fig. 5.32. The colors represent the intensities of the average TKE as the compound nucleus splits into fragments. Two separate centers, marked with a bright color and located symmetrically on either side of the $A_H = A/2$ vertical symmetry axis of the plot, indicate that the dominant mode of fission is asymmetric; otherwise, if there is only a single bright center, the dominant fission channel is symmetric. The width of the FMD can be judged by the proximity of the two centers.

It is evident from 5.40 that for the lighter actinides the predominance of asymmetric fission is distinguishable, while for the heavier elements the two centers merge into one, showing the predominance of symmetric fission. Of course, as the mass number of fissioning nuclei increases, the average total kinetic energy of the fragments also increases, e.g. for thorium or uranium the centers are concentrated at about $160-170$ MeV, while for fermium this value already reaches $230-240$ MeV. It should be noted that the overall TKE values for the nuclei studied here are slightly higher than those measured in the experiment.

For example, for ^{258}Fm, comparing our results with the plot from [154] (see, Fig. 5.41), we can see that the peak corresponding to the symmetric contribution is very clearly visible, and there are practically no asymmetric yields. Since the fission of this isotope is spontaneous, the dominance of only one fission mode is not surprising, since the chosen starting point for Langevin calculations is in the region of the symmetric valley (see, earlier discussion on the choice of starting points in the case of Fm isotopes).

However, as mentioned in 5.3.2, if searching for an asymmetric exit point is not very difficult, determining the ratio of the probabilities of passing through one or the other point is already a non-trivial question. Especially if their number is greater than two.

It is also necessary to pay attention to some "artifacts". Of course we are talking about the isotopes $^{224-228}$Th, which have strange continuous bands at the ends of the distributions. These outliers are associated with protrusions in the corresponding mass distributions, the

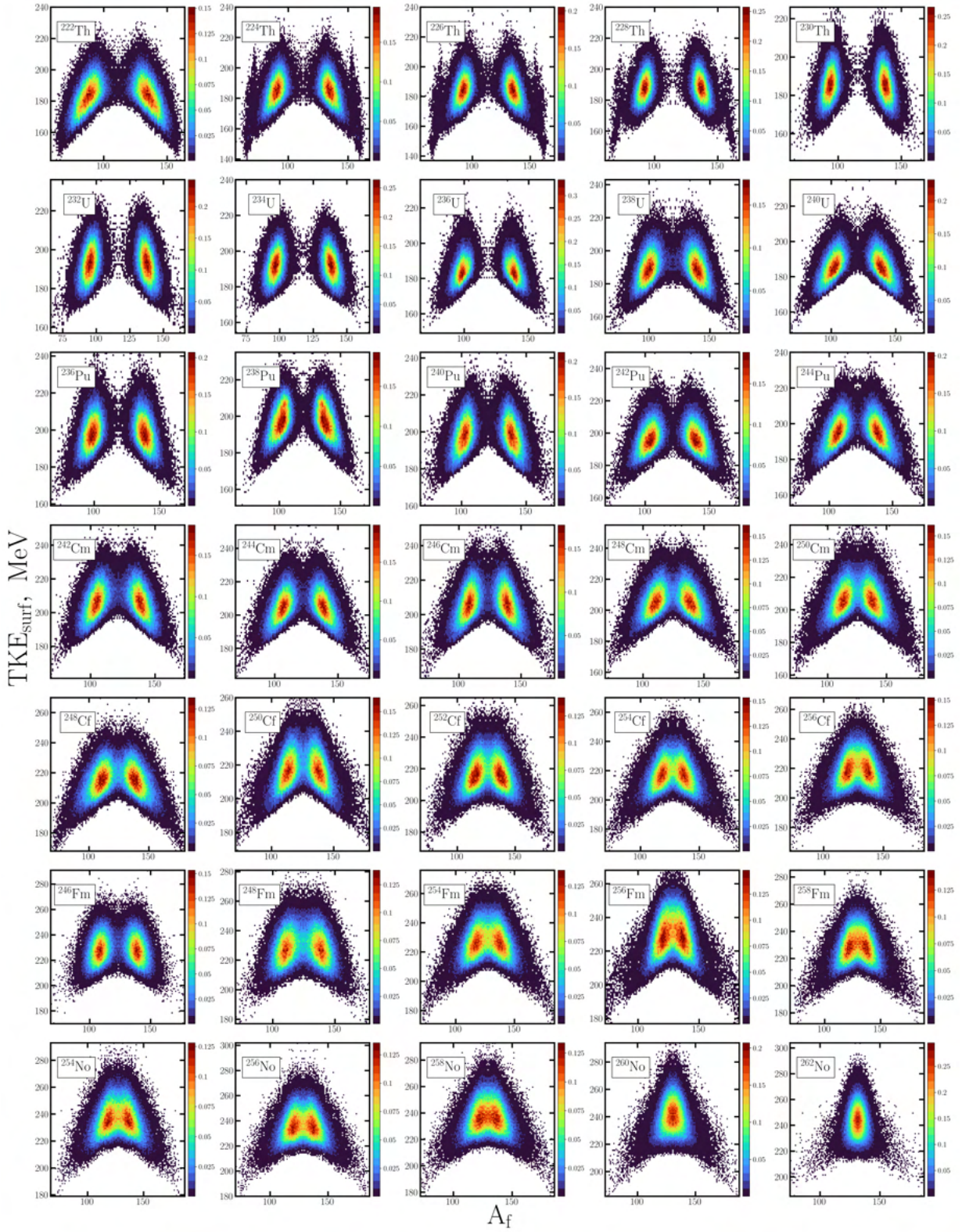

Figure 5.40: Two-dimensional distribution of TKE yields from fragment mass, for a series of even-even actinide nuclei undergoing induced and spontaneous fission, calculated within the formula eqs. (5.26) to (5.28).

reason for which seems to be related to the very PES artifacts successfully combined with the use of Gaussian random neck breaking in the presented Langevin model (see Sbs. 5.3.3).

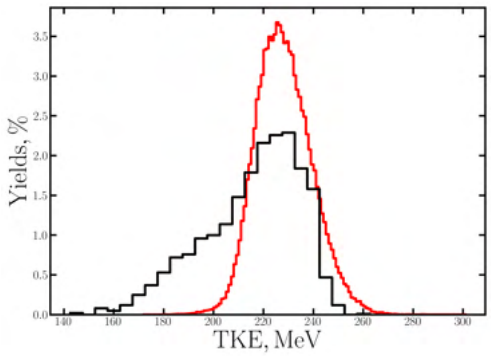

Figure 5.41: Comparison of TKE histograms for the ^{258}Fm nucleus, obtained from the Langevin model (red line) and experimental data (black line) [154].

If we look at Fig. 5.2, where different 2D slices of the potential energy hypersurface for ^{228}Th are shown, we can see that the energy fission valleys (or epicenters) are "stretched" compared to those seen for other actinides. Therefore, the random force in the Langevin equations is potentially able to push the trajectory toward more asymmetric configurations than in nuclei with stiff wells. This effect is reflected in the 2D TKE plots for light thorium isotopes, where the bright centers are washed out more than for other actinide isotopes.

Nevertheless, in general such a simple model describes the fission characteristics at the moment of fission quite well. It then seems tempting to investigate similar characteristics, particularly in terms of FMDs and TKEs, for superheavy nuclei, which will be done in the next subsection.

5.4.2 Super-heavy case

Before performing calculations for superheavy nuclei (SHN), it is necessary to mention the choice of the boundaries of the deformation space for this type of nuclei. For this purpose it is convenient to consider the following example, shown in Fig. 5.42, which shows the PES in the cross-section of (q_3, q_4) coordinates for the elongated configuration corresponding to the elongation value $q_2 = 2.1$ for the superheavy nucleus ^{284}Cn. This is a rather heavy nucleus even within the classification of super heavy nuclei, but it perfectly illustrates the idea of expanding space along the coordinate q_3. As can be seen from the Fig. 5.42a, even at zero deformation values of the higher order Fourier deformations (q_5 and q_6 variables) there is a separate small fission valley located at $q_2 = 2.2$ near the $q_3 \approx 0.21$ region where the trajectory can possibly fall. Looking at Fig. 5.4, this trajectory would describe an asymmetric fission with the mass of the heavy fragment close to the double-magic ^{208}Pb. That is, in addition to the symmetric fission typical of superheavy nuclei, there are visible super-asymmetric configurations where the heavier fission fragment tends to eventually transform into the aforementioned lead nucleus. It is therefore necessary to include configurations with greater mass asymmetry, i.e. to extend the region associated with coordinate q_3 by a few grid nodes to the value of about 0.27, as shown in 5.42b. Thus, the entire configuration space is bounded according to Eq. (5.10).

Another important difference in the calculation procedure is the assumption that superheavy systems undergo only spontaneous fission. This is related to the "survival" of the system after fusion, i.e. the compound nucleus does not have enough energy to overcome the barrier. Therefore, in this study it is assumed that the nucleus has an excitation energy close to the ground state value. However, the author is aware that the system is usually in an excited state.

Then, taking into account the above, calculations of fission characteristics for SHN are performed within the framework of the developed model. As it is known, superheavy nuclei begin with rutherfordium with charge number $Z = 104$. The presentation of the results for the even-even superheavy isotopes starts from Rf with the figures of mass distributions

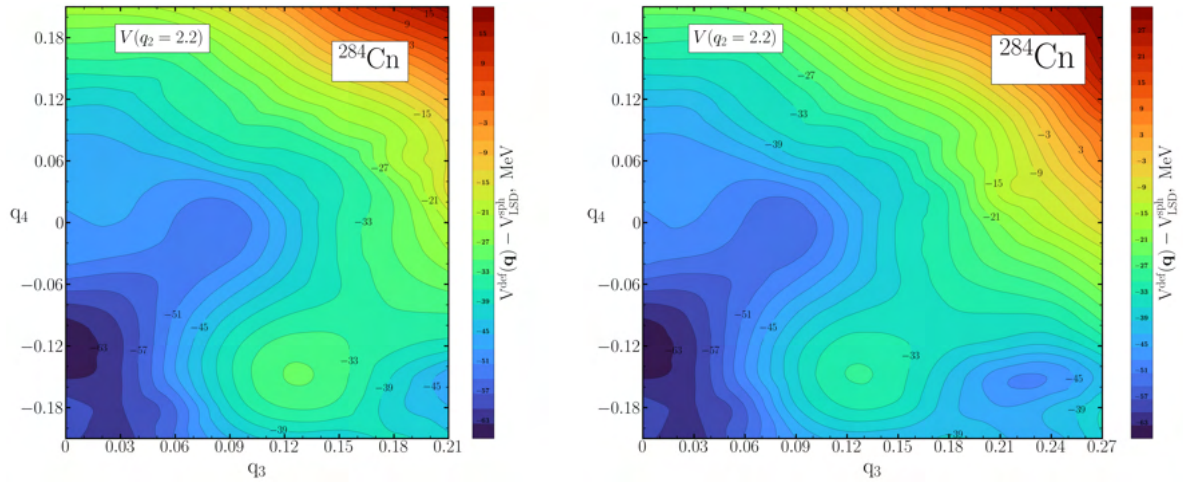

(a) q_3 Boundaries for actinide case

(b) q_3 borders for SHN case

Figure 5.42: PES cross-sections in the (q_3, q_4) plane for highly elongated configuration of the ^{284}Cn nucleus

and on the basis of them obtained 2D plots of TKE (see, Figures 5.43 and 5.44).

The available data [154, 159] on rutherfordium nuclei show good agreement with the obtained theoretical estimates, which is encouraging for the evaluation of such distributions for other superheavy elements. However, for ^{260,262}Rf a small discrepancy with the available experimental data is observed. In addition to the pronounced symmetric mode of fission, there are small asymmetric modes. While for ^{260}Rf they are isolated, for ^{262}Rf they already merge, passing through the symmetric channel. For the latter, however, the asymmetric contribution to the distribution is also observed, which is absent in the simulated FMD. Moreover, the theoretical curve for ^{260}Rf shows a super-asymmetric mode, which predicts a decay of the system into a light close to twice the magic nucleus ^{48}Ca and a heavier fragment located in the lead region. However, according to the available FMD's, where the asymmetric mode, where fragments in the following region $A_L \approx 90$ and $A_H \approx 170$. The same behavior is also observed for the chain of ^{262,264}Sg, ^{264,266}Hs and ^{270}Ds. It is quite interesting that the ternary mode effect occurs only in transition nuclei where compact symmetric fission has not yet been the dominant mode, since the number of nucleons is insufficient to form two nuclei close to double magic ^{132}Sn. Even without particle emission, nuclei with $A = 264$ do not have the strictly symmetric mode, only heavier cases do.

This is better observed by analyzing the 2D TKE histograms (see Fig. 5.44), where the intensity more clearly reflects the contributions of the FMDs. The focus here is, of course, on the behavior of the epicenters, expressed as local maxima, as well as the ends of the distributions, from which one can judge the role of each fission mode. Thus, for the previously mentioned nuclei with trimodal fission, we observe the play of two asymmetric epicenters and a single symmetric one, and at the ends of their TKEs we notice isolated "islands" near ^{65}X and ^{195}X, respectively, although the intensity in these regions is small. For the following isotopes in chains of these elements, it can be seen how the epicenters merge into a single whole and the islands at the ends first blur, then merge with the main island and almost disappear with increasing mass of the composite fissile system (see chain Hs or Ds).

On the other hand, this may be an artifact related to the peculiarities of the PES for a given isotope. Analyzing the cross section (q_2, q_3) of the considered nucleus (see, Fig. 5.45a), it clearly corresponds to the experimental data. In fact, there is even a small yield to the

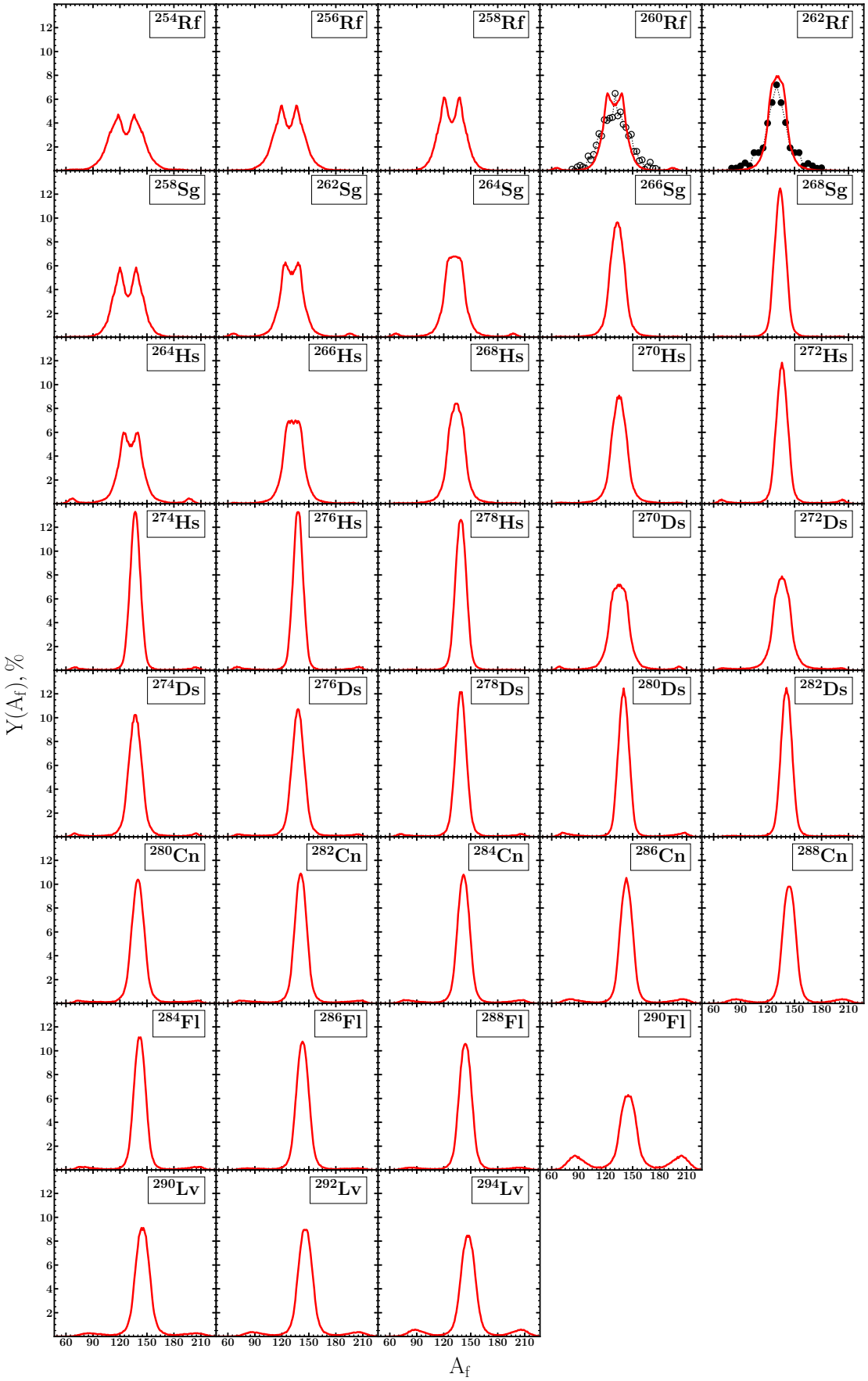

Figure 5.43: Comparison of the primary FMDs for series of even-even superheavy nuclei undergoing spontaneous fission calculated within the Langevin model developed in this thesis with the available primary and secondary FMDs derived from experimental data [154, 159].

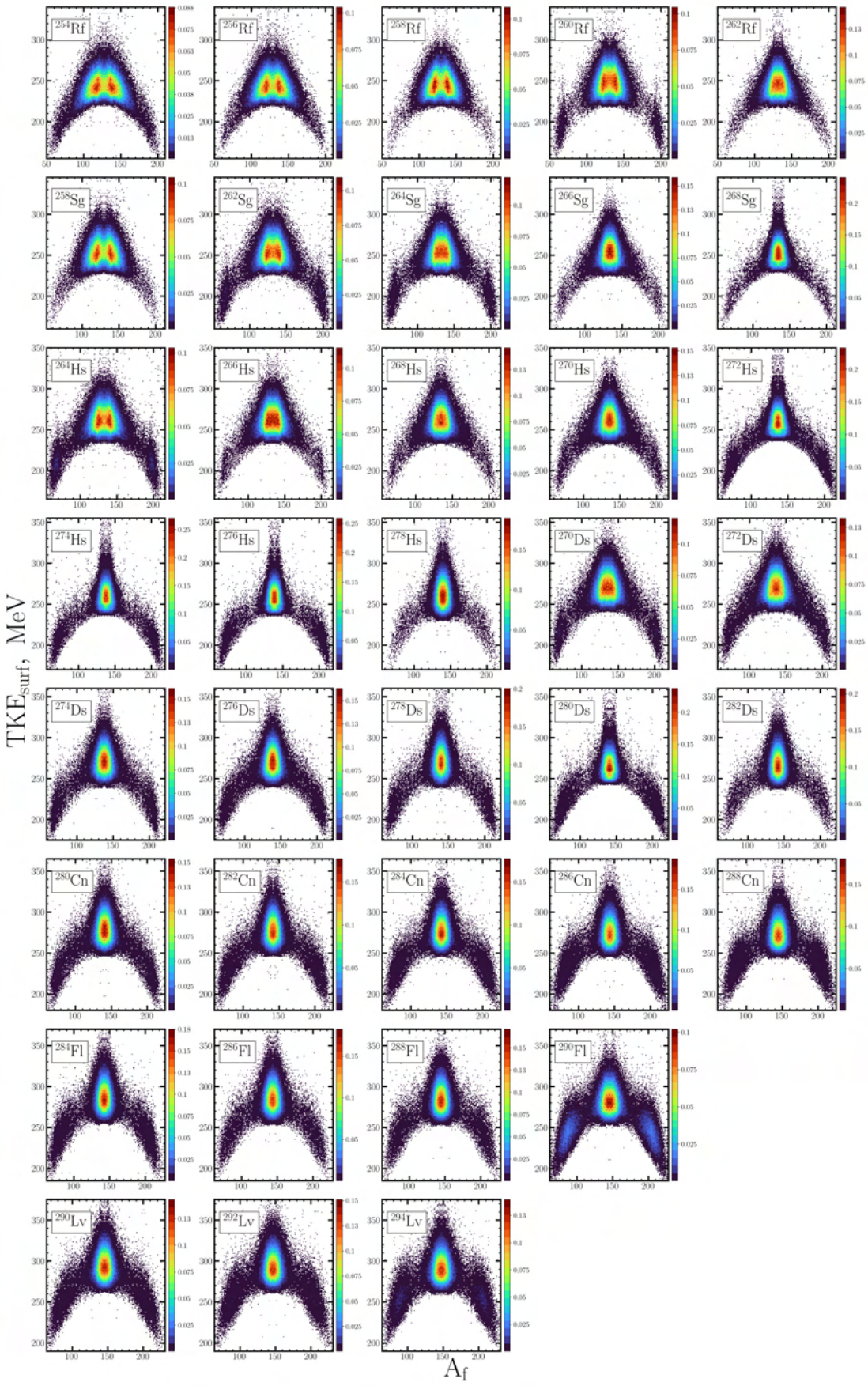

Figure 5.44: Two-dimensional distribution of TKE yields from fragment mass for a series of even-even superheavy nuclei undergoing spontaneous fission, calculated within the point-charge Coulomb repulsion formula eqs. (5.26) to (5.28).

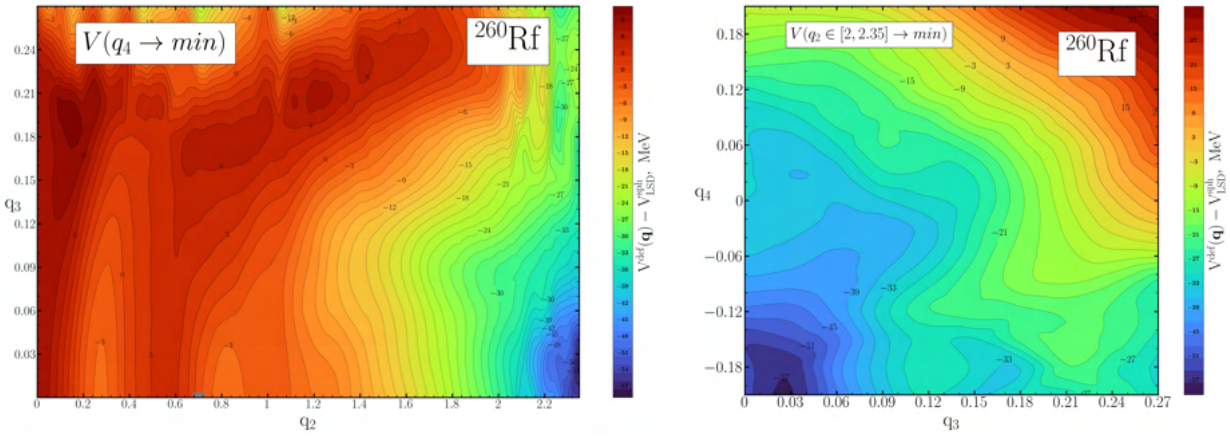

(a) In (q_2, q_3) plane with minimization in all region of q_4 coordinate

(b) In (q_3, q_4) plane with minimization by q_2 coordinate in region corresponding to the most probable scission stage

Figure 5.45: Various PES ^{260}Rf nuclei

asymmetric mode. However, if we look at the slice (q_3, q_4) with the minimization over q_2 variable in the region $q_2 \in [2, 2.35]$ (see, Fig. 5.45b), there are minima located in the region of large q_3. Therefore, under certain conditions, e.g. a sudden jump of the Langevin force components, it is possible to reach such extreme values. It should be noted, however, that due to the nature of the spontaneous phenomenon, the temperature of the compound fissile nucleus will be ≈ 0.5 MeV, so these cases are rare.

Nevertheless, the previously mentioned Hs and Ds already show a clear bimodal interplay (symmetric and super-asymmetric fission modes), which only increases in further elements. For the chains Cn, Fl, and Lv, the contribution of super-asymmetric fission is substantial, but now only the heavier fission fragment tends toward the double magic nucleus ^{208}Pb. Since this nucleus is the most stable of the heavy nuclei, the tendency of the system to such configurations increases, which can be observed in the distributions of the aforementioned chains of nuclei. This is especially noticeable for the nucleus ^{290}Fl.

Let us return to the TKE. As can be seen, as the mode of symmetric fission increases, the intensity of the epicenter increases and the whole island zone narrows, stretching towards high energies. This is quite obvious, the peak is closer to the delta function, so the scattering in the masses decreases and the main source of scattering becomes the configuration of the surface of the compound nuclei. On the other hand, starting from the copernicium, the reverse process of tail growth occurs, gradually creating half-island epicenters on the sides, noticeably decreasing the intensity of the main epicenter, as in the cases of ^{290}Fl and ^{294}Lv.

The occurrence of such high yields for the mentioned isotopes is related to the procedure for obtaining the starting point described in 5.3.2. Using this procedure, the yield point is located in the region of strongly asymmetric configurations $q_3^{start} = 0.15$. If we study the PES of other superheavy nuclei, we see that the value of q_3^{start} is lower and does not exceed the value of 0.09. Most of them are located in the region $[0, 0.06]$, i.e. close to the valley of symmetric fission, the type of which is thought to be very characteristic for SHN. For confirmation of this, one can refer to the paper [115], where PESs of these nuclei are presented, it can be seen that if the q_3^{start} coordinate of the exit point is in the specified region, due to the large value of the gradient, the major part of the trajectory will tend to the valley of symmetric fission. One can also see FMDs there that are different from those presented in this study, with a larger contribution to the distribution of the

super-asymmetric mode. There are several reasons for this. The first is the different initial conditions. The point was set manually by analyzing a small slice of the PES and usually not far from the last saddle point. Also, the fission was assumed to be forced and some excitation energy was reported. Another reason is the Langevin force, whose amplitude was slightly higher than in the present model. Therefore, the high energy obtained during the descent from the barrier gave very large yields of the super-asymmetric mode. Of course, the closer the starting point was to the last saddle point, the higher peaks were observed in the ^{210}X zones. In the present work, these shortcomings were eliminated and the effect was significantly reduced. However, there remains the question of the effect on the distribution when multiple starting points are used, which requires serious investigation in the future.

On the basis of the data obtained for SHN, I assume that such a tendency of FMD and TKE will continue for the chain of oganesson nuclei not considered in this study. For the nuclei following the oganesson with A $>$ 300 and $Z \gtrsim 120$, the FMD will either resemble a three-peak fission, as for thorium, the interaction of two super-asymmetric and symmetric modes. Or not trimodal at all, as in ruterfordium. In any case, there will be a closer interaction between ^{132}Sn, ^{160}X, and ^{208}Pb, perhaps with super-asymmetric fission playing a dominant role. However, this is *is terra incognita* for the model used in this paper and may be the subject of further research.

To summarize the entire subsection, this model, despite its naive simplicity, is an excellent tool for obtaining primary characteristics such as FMDs, FCDs, and TKEs, which provide essential information about the fission behavior of heavy nuclei. Comparison with the corresponding data obtained from experimental studies of nuclear fission shows good agreement with most of the calculated nuclei. The complete exception is the thorium chain, where the bimodality of asymmetric-symmetric fission was not achieved within this framework. Moreover, as has been repeatedly noted, not all of the compared FMDs are primary; a substantial part corresponds to secondary distributions. The next section of this chapter is devoted to remove this disadvantage.

5.5 Particle emission

The question raised about the validity of the use of secondary FMDs compared to the mass distributions obtained with the developed model is a valid one. In fact, secondary FMD usually refers to the asymptotic distribution of fission fragments when they are detected by detectors at a large distance. During their trajectory, they may undergo further decays, such as loss of mass, charge, excitation energy, angular momentum through the effect of emission of light particles such as neutrons, protons, alpha particles, and gamma quanta, or simply undergo one of the decays. The latter can be much slower, usually lasting about 10^{-16} s (see Fig. 1.2). Therefore, radioactive decays are not considered in this work. This allows us to concentrate on the study of the evaporation of light particles, which is considered to be the main source for the formation of secondary distributions.

5.5.1 Neutron evaporation process from fission fragments

First, let us consider the simplest case of de-excitation of the formed fragments from the fissioning nucleus. This is the most likely mechanism for the appearance of light particles in the case of low-energy fission. This process usually involves the emission of neutrons and γ-quanta. Since most of the energy spectrum of γ-quanta is far below the neutron separation energy, it can be assumed that the emission of γ-quanta has a negligible effect on the probability of neutron evaporation from the fission fragment. Therefore, a

relatively simple approach is used to describe the neutron emission effect [132] based on the Weisskopf approach (4.53) mentioned in section 4.3.1. The level densities are defined there, among others, in Ref. [119]. Therefore, one has to find the form of the effective transition coefficient w_n^{eff} and the excitation energy values of the right and left fragments E_L^* and E_R^*.

Excitation energy of the fission fragments

Starting with the latter, the total excitation energy of a nucleus $E^*_{\text{total}_\text{i}}$ of the nucleus (A_i, Z_i) can be determined by summing the following two terms:

$$E^*_{\text{total}_\text{i}} = E_{\text{def}_\text{i}} + E^*_i, \quad i = L, R \tag{5.29}$$

where E_{def_i} denotes the energy released by a relaxation from the actual state of deformation def_i to its ground state (g.s.), whereas E^*_i is the excitation energy transferred from the compound nucleus to the i^{th} fragment. This deformation energy for each fragment can be estimated in a first approximation within the LSD [23, 39] liquid drop model as

$$E_{def_i} \approx E_{LD}(Z_i, A_i, \mathbf{q}_i) - E_{\text{exp}}(Z_i, A_i, \text{g.s.}). \tag{5.30}$$

The deformations of fragments $\mathbf{q}_i$ in terms of the Fourier decomposition (3.43) of the surface are determined by inverse Fourier transform (5.31). At the narrowest point of the neck, the surface of the compound nucleus is split into two parts, left ρ_L and right, ρ_R (see, Fig. 5.46). Then, for the left fragment, its deformation parameters are obtained by integration in the following way:

$$\begin{aligned} a_{2n_i} &= \frac{1}{R^2_{0_i}} \int_{z_{sh}-z_0}^{z_{\text{neck}}} \rho_i^2 \left(\frac{z - z_{sh}}{z_0}\right) \cos\left(\frac{2n-1}{2}\pi \frac{z - z_{sh}}{z_0}\right) dz \\ a_{2n+1_i} &= \frac{1}{R^2_{0_i}} \int_{z_{\text{neck}}}^{z_{sh}+z_0} \rho_i^2 \left(\frac{z - z_{sh}}{z_0}\right) \sin\left(n\pi \frac{z - z_{sh}}{z_0}\right) dz \end{aligned} \tag{5.31}$$

where $R_{0_i} = (\frac{3V_i}{4\pi})_i^{1/3}$.

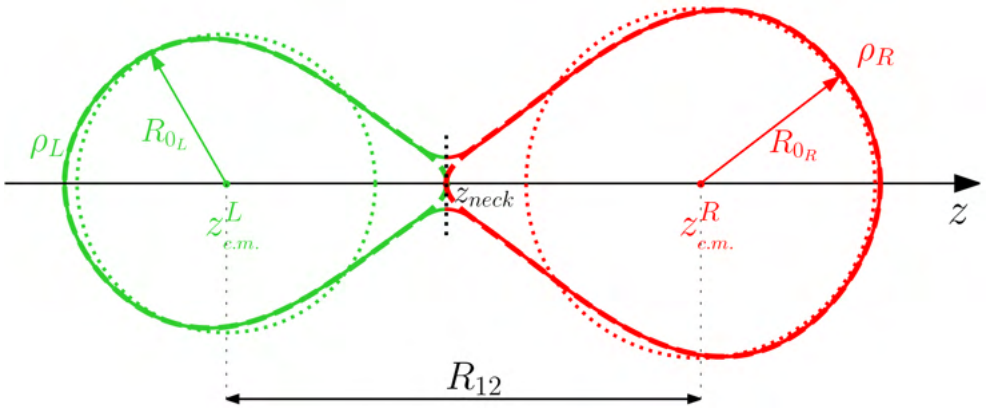

Figure 5.46: Decomposition of compound nucleus surface in vicinity of scission point into two deformed nascent fragments. Lime color denotes everything related to the surface characteristics of the left fragment while red corresponds to righ fragment. Solid line describes the profile of compound nucleus whereas dashed line - surfaces of the deformed fragments. With dotted line the spherical nuclei corresponding to both fragments are represented.

The second term in Eq. (5.29) is determined by the expression for the energy of the compound nucleus as a function of temperature $E_i^* = a(Z_i, A_i; \mathbf{q}_i)T^2$. From now on, instead of referring to the left and right fragments, we will refer to them as heavy (H) and light (L). Assuming that the temperatures of both fragments are identical at the fission point, the ratio $\frac{E_L^*}{E_H^*}$ is given by

$$\frac{E_L^*}{E_H^*} = \frac{a(Z_L, A_L; \mathbf{q}_L)}{a(Z_H, A_H); \mathbf{q}_H)}. \tag{5.32}$$

Then, using the conservation of energy law

$$E^* = E_H^* + E_L^*$$

it is easy to obtain the individual energies of the fragments, E_i^*.

The final step in this procedure is to find the maximum energy of the neutron emitted by the parent nucleus, denoted by the index (m). The conservation of energy can now be written as

$$\epsilon^{\max} = M_m + E^*_{\text{total}_\text{m}} - M_d - M_n. \tag{5.33}$$

Above, M_m, M_d, M_n are the excess masses of the parent, daughter, and neutron nuclei, respectively. These can be taken from the mass table, e.g. [160]. Considering that at the first emission the deformation of the nucleus becomes nearly spherical, the thermal excitation energy of the daughter nucleus $E^*_{d_i}$ can be determined by a simple expression:

$$E^*_{d_i} = \epsilon^{\max}_{n_i} - \epsilon_n, \tag{5.34}$$

where ϵ_n is the kinetic energy of the emitted neutron.

Charge equilibration between fission fragments

In order to solve the problem of determining the fragment charge distributions, a non-trivial question arises concerning the taking into account of the nucleon isospin structure of each fission fragment. Undoubtedly, the intrinsic energy of a fragment depends directly on the number of protons and neutrons, as shown for example in eqs. (5.32) and (5.33). To determine the number of protons, one can of course use the assumption in section 5.4.1 introduced earlier, that the proton-to-neutron ratio of the compound nucleus is preserved for fragments as well. Such a hypothesis is widely used for similar macroscopic approaches to FCDs [139, 161–163].

It is not difficult to simulate this problem in the microscopic-dynamical approach as done in Ref. [164]. In the macroscopic-microscopic model there are attempts to circumvent this problem, for example in the paper [165] it was proposed to calculate the probability of nucleon transfer at the moment of rupture. This was done by determining the most energetically favorable light fission pre-fragment in terms of nucleon composition, as well as the closest configurations to it. In another work [23], contributed by members of the research group in which the applicant participates, the mechanism of proton exchange between both fragments is based on the natural tendency of each dynamical system to minimize its interaction energy on the way to fission. This process is mainly macroscopic in nature. At the moment of fission of the compound nucleus, the most probable charge distribution among each fragment is obtained by minimizing the sum of the deformation-dependent liquid-drop energies of both fragments, subtracting the liquid-drop energy of the compound nucleus just before its fission, where the Coulomb interaction is simulated

by the point-charge term for two touching fragments

$$E_{c.e.}(Z,A,A_H,Z_H;\mathbf{q}_H,\mathbf{q}_L) = E_{LSD}(Z_H,A_H;\mathbf{q}_H) + E_{LSD}(Z-Z_H,A-A_H;\mathbf{q}_L) + \frac{e^2 Z_H(Z-Z_H)}{R_{12}} - E_{LSD}(Z,A;0) \tag{5.35}$$

where $\mathbf{q}$ corresponds to the set of Fourier deformations describing a given nucleus, the indices L, H, *comp* denote the light, heavy, and compound nuclei, respectively. As before, R_{12} is the distance between the mass centers of the fragments. This energy is computed for values of Z_H four steps to the left and right of the integer, $\mathrm{int}\left(Z\frac{A_H}{A}\right)$, and its minimum is found as a function of Z_H. The top panel of Fig. 5.47 shows the $E_{c.e.}(Z_H)$ dependence obtained from the nine-point calculation for the heavy fragment with mass number $A_H = 142$.

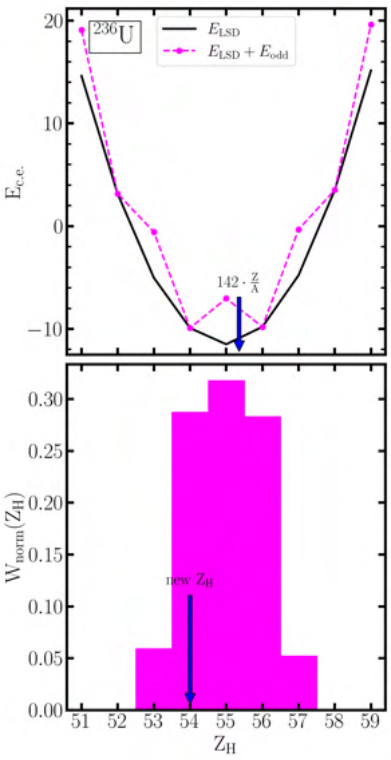

Energy of ^{236}U at scission as a function of the heavy fragment charge number using the LSD mass formula (top panel) and the Wigner distribution probability of Z_H (bottom panel)

Figure 5.47: Charge equlibration scheme

To estimate the charge distribution from the obtained $E_{c.e.}$ interaction energy values, we use the Wigner function of the form

$$W(Z_H) = \exp\left(-\frac{[E_{c.e.}(Z_H) - E_{c.e._{\min}}]^2}{E_W^2}\right), \tag{5.36}$$

which is a function of the statistical weight for the Z_H charge of the heavy fragment. The quantity $E_{c.e._{\min}}$ is the minimum value among the discrete energy series $E_{c.e.}(Z_H)$, while the value E_W is assumed to be comparable to the energy distance $\hbar\omega_0$ between harmonic oscillator shells, thus corresponding to the proton transfer between touching fragments. Here the energy E_W is refined to 5 MeV, which is slightly lower than in [23].

The final action is to use a Monte Carlo-type procedure to determine the new value of Z_H. The random variable κ is given by a random number generator obeying a uniform distribution on the interval $[0,1]$. It is superimposed on a similar normalized unit interval consisting of sections denoting the statistical weight of the previously obtained distribution $W(Z_H)$. Entering one of these sections predetermines a new value of the heavy fragment charge, whose quantity is related to that segment.

The lower panel of the Fig. 5.47 shows normalized values of the Wigner probability distribution (5.36), where the black arrow indicates the new value of the heavy fragment charge, one unit away from the original value, given by a simple assumption that

$$\frac{Z_H}{A_H} = \frac{Z}{A} = \frac{Z_L}{A_L}. \tag{5.37}$$

Finally, since we know the most probable charge number, Z_H, we calculate $Z_L = Z - Z_H$.

Using this method, it is possible to go beyond the simplistic assumption (5.37) and get a slightly more realistic charge distribution. Figure 5.48 is a clear confirmation of this statement, where a comparison of the FCDs obtained under the existing models based on interaction energy minimization or proportionality (5.37) with the evaluation of the more

advanced and complex model [166] is given. It can be seen that after using the above procedure one can see a serious redistribution of the FCD peaks, where two of the three peaks are very close to the [166] estimation.

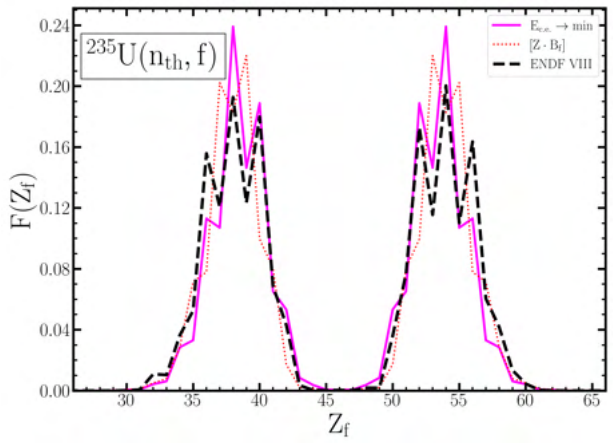

Figure 5.48: Comparison of the FCDs calculated with $[A_H B_H]_{int}$ and $E_{c.e.}$ minimization with the analog obtained in the ENDF-VIII model [166] for the thermal neutron induced fission of ^{235}U

Regrettably, the third (external) peak coincides with the charge position of the similar peak in the ENDF model, but it remains very small in magnitude and weakly corresponds to the local maximum.

However, it is difficult to disagree with the authors of Ref. [23] about the very successful way of describing the determination of equilibrium charges of fission fragments based on such a simple procedure. An even clearer demonstration can be seen in Fig. 5.49, which shows the fragment yields on (N, Z) diagrams. In the left panel of 5.49a is the diagram generated using the simplistic approach (5.37), while in the right panel 5.49b are the results within the method proposed above. As can be seen, a large number of additional nuclei appeared as fission fragments as a result of this new approach to charge equilibration, marked mainly by blue pixels corresponding to low yields.

Neutron emission from fission fragment

As mentioned before, the probability of neutron emission for a fragment with excitation energy $E^*_{\text{total}_i}$ is given by the Weisskopf formula (4.55). After dealing with the energetic quantities, the question remains about the effective transmission coefficient $w_n^{eff}(\epsilon)$, where ϵ is the energy of the emitted particle. The fact that the transmission coefficient is an effective quantity means that it is averaged over the surface of the deformed nucleus and possible angular momenta of the emitted particle. In other words, we do not know from which point on the surface the particle is evaporated, nor which direction its momentum

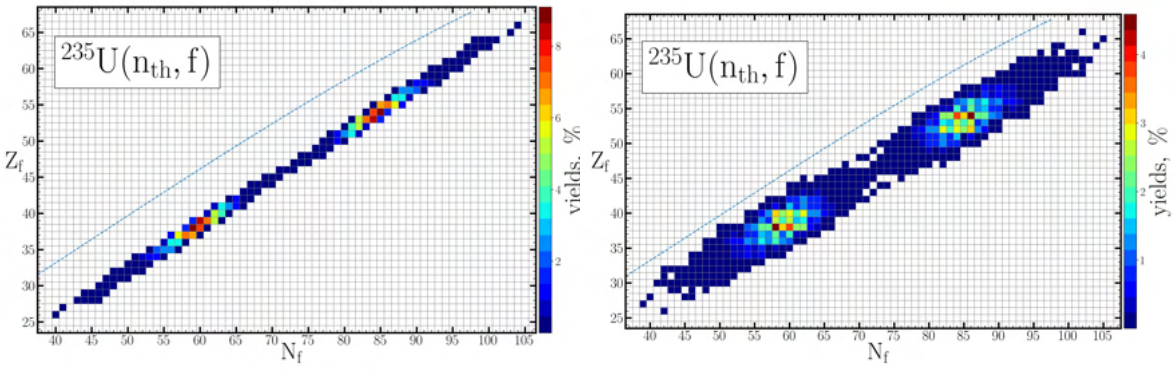

(a) Obtained via (5.37) proportionality. (b) Obtained via $E_{c.e.}$ minimization method

Figure 5.49: (N, Z) diagrams for primary fission yields for thermal neutron induced fission of ^{235}U. Dashed blue line corresponds to the beta-stability line.

is. To evaluate this quantity we adopt the idea developed in [167], which can be expressed with the following relation

$$w_n^{eff}(\epsilon) = \sigma_{\text{inv}} \cdot \epsilon,$$

where the value σ_{inv} is the so-called inverse neutron cross section, defined as

$$\sigma_{\text{inv}}(\epsilon, A_f) = \pi \left(1.7\ A_f^{1/3}\right)^2 \left[0.76 + 1.93\ A_f^{-1/3} + \frac{1.66\ A_f^{-2/3} - 0.05}{\epsilon}\right]. \tag{5.38}$$

So, th mentioned formula (4.55) can be used to define the emission width for a neutron

$$\Gamma_n(\epsilon_n^{max}) = \frac{2\mu}{(\pi\hbar)^2 \varrho_M(E_M^*)} \int_0^{\epsilon_n^{max}} \sigma_{inv}(\epsilon) \cdot \epsilon \cdot \varrho_D(E_D^*) d\epsilon \tag{5.39}$$

where μ is the reduced neutron mass.

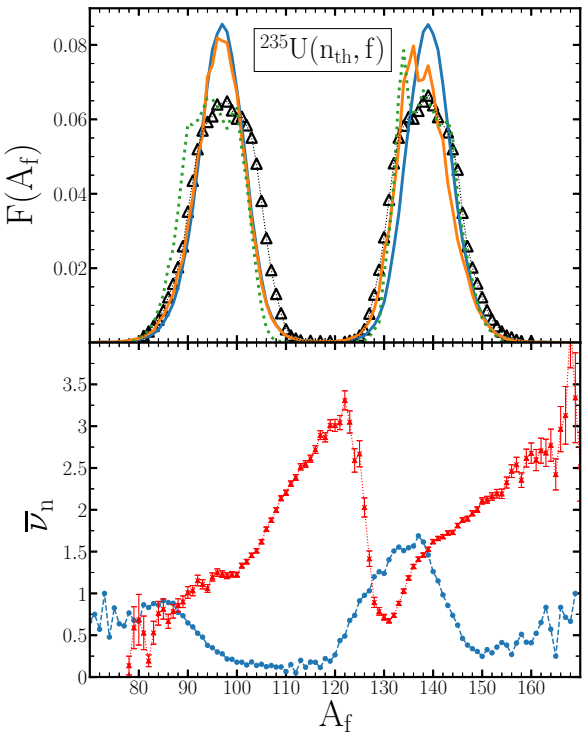

Figure 5.50: Top panel – Comparison of primary (blue line) and secondary (orange line) FMDs calculated by the developed model with secondary FMDs estimated by the ENDF-VIII model [166](green dotted line) and experiment [168] (hollow triangles). Bottom panel – Comparison of neutron multiplicities as a function of primary fission fragment mass simulated within the presented model (blue dots) with empirical data [169](red dots).

Figure 5.50 shows the effects of the above procedures, taking into account the neutron evaporation from the fission fragments produced during the decay of the compound nucleus ^{236}U. The upper panel shows the comparison of the primary and secondary FMDs calculated in the present model with similar data estimated in the model [166] and empirical points [168]. As can be seen, our curve is seriously shifted around the right peak corresponding to the heavy fragments and remains in reliably good agreement in the inner region. Unfortunately, there is a serious discrepancy of the backside of the right peak compared to the experimental points, which is not surprising since it is a direct consequence of the shape of the primary FMD.

For the other peak, the picture is the exact opposite of the perfectly described outer side. There is even a correspondence of the main peaks, but the symmetrical area is a few units beyond. The valley itself is largely in good agreement.

In the lower panel of Fig. 5.50 there is a comparison of the neutron multiplicities as a function of the primary fission fragment mass with the experimental one taken from Ref. [169]. It is easy to see that the case is even worse than for FMD. The good news is that there is a sawtooth-like appearance. The bad news is that the position and value of the "teeth" do not match the available data. The first peak should be near the symmetric fission valley. Instead, the minimum is observed. The picture is similar for the second "tooth". Instead of a significant increase of the multiplicity value in the region of very heavy fragments, it decreases. At the same time, the points of increase of the distribution for both "teeth" are quite close to each other. At first

sight, the answer to the discrepancy lies in the statistics, i.e. in the very small number of events describing the neutron multiplicity. This is partly true. The number of trajectories in the $110 \leq A_f \leq 126$ region is only 0.4 % (402 of 10^5 trajectories), and in the $A_f \geq 150$ region it is 1.1 %. Two dozen trajectories cannot give very accurate information. But what about where there are one or two orders of magnitude more?

To answer this question, it is necessary to look at the (N, Z) diagram shown in Fig. 5.51, where the color palette corresponds to the averaged values of the excitation energies of the primary fragments $E^*_{\mathrm{total_i}}$. Their distribution is quite interesting, so let's take a closer look. Unlike the work [23], it is not uniform. Two high energy regions are noticeable (the regions with $N_F \in [45, 55]$, marked in red, and the purple plus dark region $N_F \in [77, 87]$), the "teeth" from the lower panel of Fig. 5.50. There are also two low energy regions whose size does not exceed the gamma-ray threshold, i.e. 5 MeV. Consequently, the low values of neutron multiplicities in these regions are associated with configurations that have low excitation energies, i.e. there is no energy required for neutron evaporation. The authors suggest that part of the energy probably goes into the kinetic energy of the collective motion. At least such a tendency is observed in the TKE decomposition presented earlier (see Fig. 5.34), where there are small jumps at $A_H \approx 120$. However, it can also be observed that the size of such a jump is small, and the experiment indicates the departure of 2-3 neutrons.

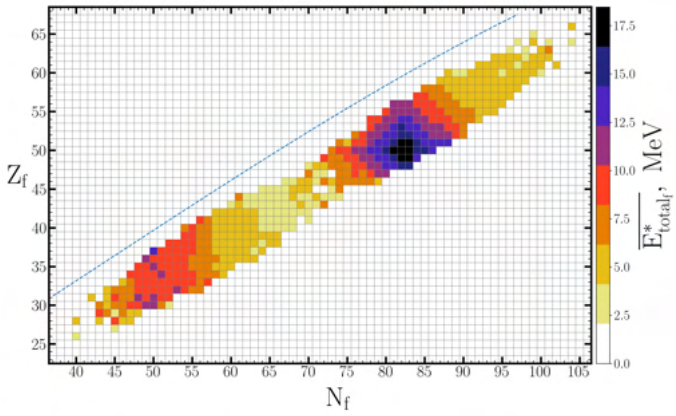

Figure 5.51: (N,Z)-diagram of the average excitation energies of the primary fission fragments after scission of the compound system ^{236}U.

Moreover, in the experimental data the minimum before the second "tooth" is in the neighborhood of $128 - 134$, close to double magic ^{132}Sn. However, in the simulation this region is slightly overestimated, or to be more precise, there is a local maximum there, not a minimum. Meanwhile, from the analysis of the (N, Z) plot, we can see that this region has an increased excitation. Why this? Probably because of the structure of the PES for the isotope in question. Moving towards the region of minimal PES states - fission valleys - the excitation energy of the system increases. Moving to other configurations of the nuclear surface, the "free" energy is lower, so that at the breakpoint the excitation energy is not as high as in the fission valleys. On the other hand, the problem of determining the configuration space limit corresponding to the elongated shapes of heavy fragments may also be indicated by the low neutron yields for fragments $A_f \geq 150$.

Another source of low excitation of light fragments could be the small number of collective coordinates, which of course affects their total excitation energy. This could be the reason for the discrepancy in the region $A_f \in [95, 110]$. In this case, taking into account the deformation of higher orders will allow us to better control the deformation of the fragments, which will significantly improve the description of the multiplicity of "delayed" neutrons. Similar conclusions were reached by the authors of [23], where, despite a modified version of the Fourier parametrization, the neutron multiplicity could not be fully described either.

The weakness of the charge redefinition procedure described in 5.5.1 is that the mini-

mization proceeds by the nucleon composition of the heavy fragment, which is close to its energy minimum. This also plays a role in neutron emission. One can see this by looking at Fig. 5.52 the behavior of the ratio of the average neutron number of the fragment to its charge number $\bar{N_{initf}}/Z_f$ and $\bar{N_{residf}}/Z_f$, where the indices $init_f$ and $resid_f$ represent before and after the evaporation process. The N/Z ratio of the compound fissile system is shown by the black dashed line. The red dashed line shows the actual distribution obtained without the charge equilibration procedure, i.e. $N_f = A_f/A \cdot N$ and $Z_f = A_f/A \cdot Z$. As you can see, the last line oscillates near the black dashed line of the N/Z relation, where the jumps are related to the rounding procedure to an integer value.

The behavior of $\bar{N_{init}}/Z$ before neutron emission is quite interesting. Instead of the expected decrease in the ratio of N_f and Z_f, especially for light nuclei, a neutron surplus is observed for fragments with masses in the range $A_f \in [70, 100] \cup [120, 140]$. In the same region there is also a decrease of the considered ratio due to neutron evaporation, which is not surprising. However, as mentioned before, this ratio remains above the dashed line N/Z due to the low excitation energy. At the boundaries and in the valley of symmetric fission the ratio remains practically unchanged. For the latter, the ratio $\bar{N}/Z_f$ is minimal, which is very close for nuclei of such nucleon composition. The reason for this large difference is, in the opinion of the author, due to the spontaneous breaking of the system described in the section 5.3.1, which makes it difficult to estimate the exact number of nucleons in the fragments formed.

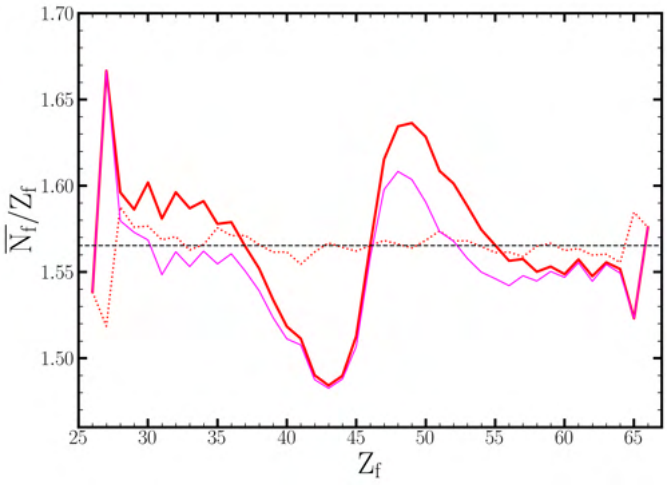

Figure 5.52: The ratio of the average neutron number of the fission fragment to its charge number, where the black dotted line is the ratio N/Z, the red dotted line is the ratio N_f/Z_f without using the charge equilibrium procedure, the red solid together with the procedure, and the magenta solid after neutron evaporation.

Thus, taking neutron evaporation into account changes the primary distribution. We will then perform the above procedure for other isotopes for which secondary distributions are available. The secondary FMDs calculated using the above procedures for proton exchange at the moment of scission and de-excitation of the hot nuclear fragments formed after scission are shown in Fig. 5.53. Very good agreement can be observed for the fission reaction: thermal neutrons ^{239}Pu. To reproduce more accurate peak behavior for both light and heavy fragments in such an approach without taking into account shell effects after redistribution of nucleons from newly formed nuclei seems impossible and is beyond the scope of this dissertation.

The situation is worse for all other nuclei. The reason for this discrepancy is, of course, the primary FMD for the corresponding fission reactions. The exception is the nucleus ^{246}Cm, where the peak of heavy fragments is shifted towards the valley of symmetric fission, which only makes the distributions worse. On the other hand, evaporation of neutrons in the case of ^{258}Fm brings the distribution width slightly closer to the available empirical FMD, but only on the heavy fragment side. The shift of the heavy peak itself is the typical trend for all calculated nucleons, suggesting either an incorrect treatment of the excitation energies associated with the introduced procedure, which in turn may be

due to the finite conditions imposed on the solution of the Langevin equations.

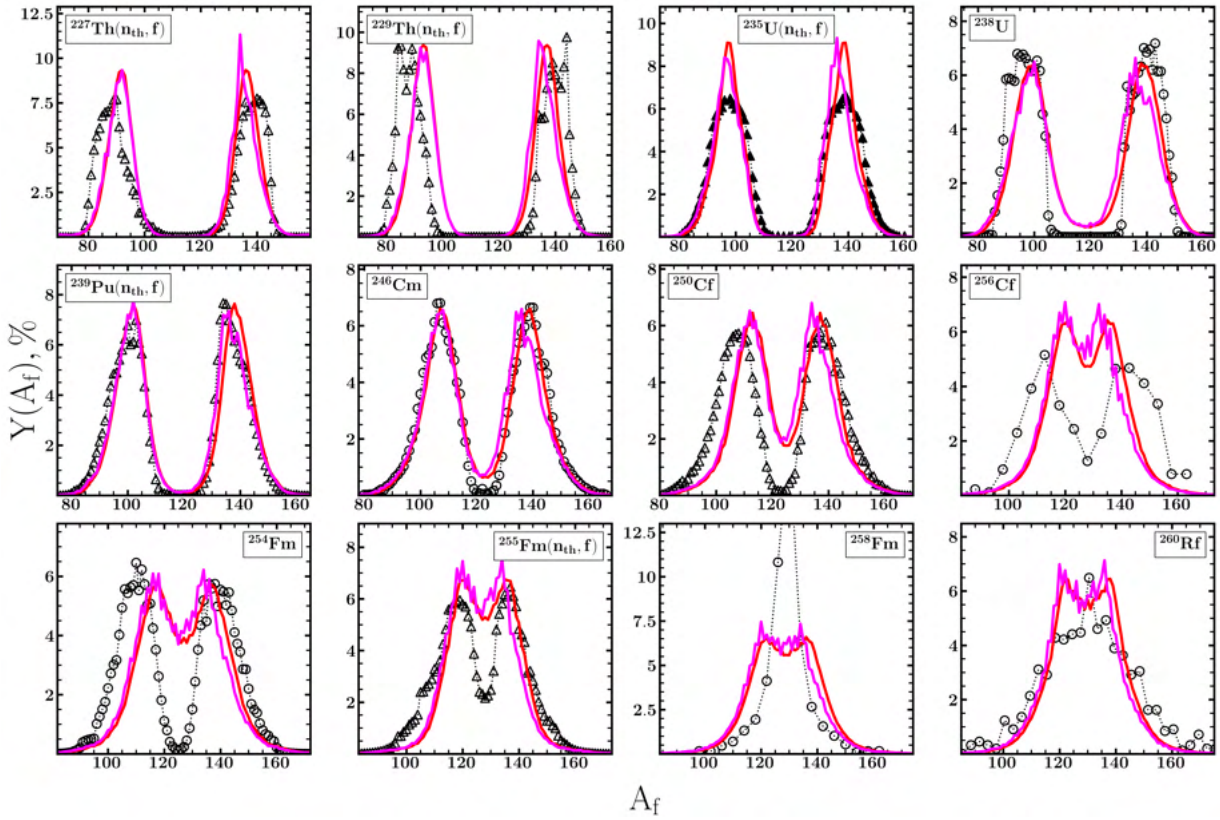

Figure 5.53: Comparison of model-calculated secondary FMDs (magenta solid) with analogous experimental data for various actinides and superheavy nuclei. The estimates of the primary FMDs (red solid) are also shown for clarity.

Nevertheless, the introduction of corrections for neutron emission affects the resulting distributions for reactions with low excitation energies. It is worth noting that the effect on the TKE has not been specifically mentioned here, as it is quite small. The reason is obvious. The distribution is determined at the moment of scission, and even though the charge number equilibration procedure is performed, the mean values are practically unchanged. Despite the importance of the described neutron evaporation mechanism and its addition to the model developed in this study, it is only a good test run before introducing an extended mechanism for the emission of light particles from the compound fissile system, where in addition to neutrons, protons and α particles are also taken into account.

5.5.2 Particle evaporation process from compound nucleus

The final subsection of this chapter is the inclusion of the process of light particle evaporation from the compound nucleus in the description of the fission process. This is the logical ending of this study, which connects the multidimensional system of Langevin equations with the Master equation responsible for the light particle emission. In other words, at last the idea underlying the classical works [108, 132], where such a coupling to describe the processes occurring after the formation of the compound nucleus was applied to the one-dimensional case. However, it should be noted that the applied formalism is used in different range of excitation energies, whose lower than in the mentioned works. The reason is that there the excited compound fissile nucleus is formed by the fusion reaction of two nuclei (fusion of superheavies) and not by neutron or γ-quanta capture.

Nevertheless, the use of this approach, where the compound fissile system moves strictly towards its decay, can shed light on understanding the process of formation of pre-scission neutrons or other light particles, such as protons or α-particles, which influence the fission characteristics.

Neutron evaporation from compound nucleus

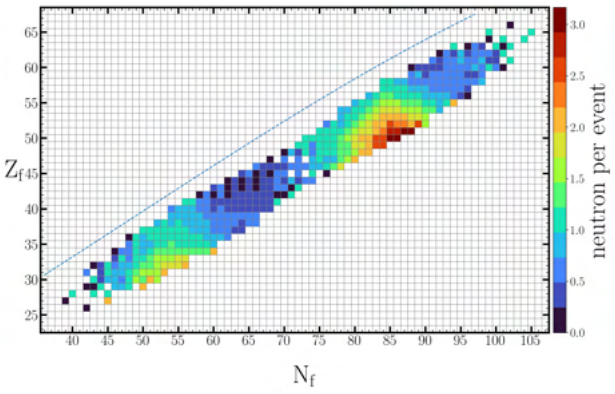

Figure 5.54: (N, Z)-diagram of the number of neutron emission from fission fragments of the compound system ^{236}U.

Obviously, as shown in the previous subsection, a certain threshold of excitation energy is required for the emission of at least one particle. For example, for a neutron to escape from an already formed fragment, its average excitation energy must be $E^*_{\text{total}H} \approx 8.5$ MeV. This is easily seen if we combine the (N, Z) diagram (see Fig. 5.51) and a similar diagramm shown in Fig. 5.54, where instead of the averaged energies the average number of neutrons emitted from the nucleus (N_{prime}, Z) during the fission of ^{235}U by thermal neutrons is given. On the one hand, it is not difficult to obtain such excitations for the compound fissile system (see Fig. 5.9). On the other hand, there is a serious difference between neutron evaporation from heated fragments and neutron emission from a heated compound nucleus. It is hidden, of course, in the times of these processes. As already mentioned, the time of evaporation process from fission fragments is very long (can reach up to 10^{-15} s), so applying Kramers's formula [170]:

$$P = 1 - \exp\left(-\Gamma_n \tau_{evap}\right), \tag{5.40}$$

Notice that the probability of this process is very close to 1 even for small widths. Obviously, when using this approach to describe the process of division of a composite, the probability P takes a different value, since $\Gamma_n \tau_{coll} \ll 1$. Therefore, the number of neutrons escaping from the "cold" composite system should be small. Consider verifying this statement by adding a departure procedure similar to the one introduced in the previous subsection. The algorithm of action is practically the same as the algorithm of departure from fission fragments. The difference is the introduction of new initial and final phases: a Monte Carlo-type procedure that determines the departure of the particle in interval $(t, t + \tau_{coll})$ and a procedure for redefining the characteristics of the new isotope. In this case, the order of operations becomes more complicated and looks as follows

1. At each moment of relaxation tau_{coll} energies are calculated similar to the formulas eqs. (5.29), (5.30) and (5.33) with the difference that a fragment nucleus is replaced by a compound nucleus;
2. Check the value of ϵ_n^{max};
3. Calculate the value of Γ_n using the formula (5.39);
4. Get a random number ζ and compare it to the probability P (5.40);
5. In the case of $P \geq \zeta$:

- emits a neutron with energy $\epsilon_n \in (0, \epsilon_n^{max}]$;
- renormalizes all inputs to the eqs. (5.4) and (5.12) quantities (mass number, PES, intrinsic energy values, tensors, etc...) and their derivatives, assuming that the core deformation does not change.

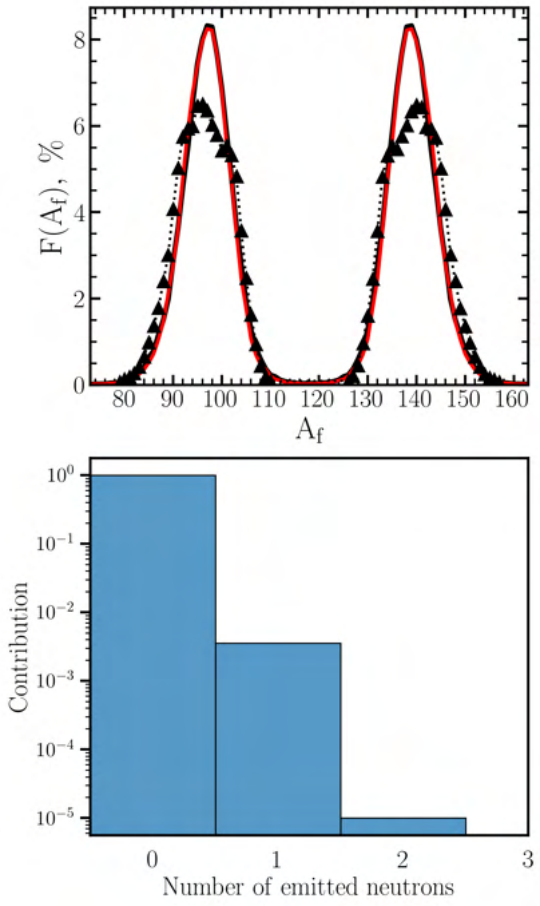

Figure 5.55: Top panel: the comparison of the primary FMDs without the procedure of neutron evaporation from the compound nucleus (black solid) and with the procedure (red solid). Also shown are analogous experimental data (black triangles). Bottom panel: histogram of the contributions of the number of neutron emission events from a compound system of pre-scission neutrons.

Such an algorithm can be used to obtain the primary FMD, which takes into account the emission of pre-scission neutrons. Fig. 5.55 shows a comparison of the estimates of the primary mass distributions for the nuclear fission reaction ^{235}U with thermal neutrons obtained in the present model with and without the algorithm described above. It is not difficult to see that these FMDs are identical, since the fraction of evaporated (see bottom panel of the histogram 5.55) neutrons from the compound nucleus is only ≈ 0.36 of the obtained trajectories (to be more precise, 358 of 10^5). This is not surprising. Despite the fact that the temperature of the system exceeds the value of 0.7 MeV (corresponding to $E^* \approx 11$ MeV), a situation satisfying the fourth point of the algorithm is rare, even though there is enough energy to separate the nucleon from the nucleus. At the same time, no large heating is observed for such a system. This is especially seen in the PES in the (q_2, q_3) section, whose behavior is quite hollow and the energy drop from the last saddle point to the gap configurations does not exceed 15 MeV. On the other hand, there is one configuration where there is a departure of two neutrons. It is true that in this sample the individual cases can be attributed to statistical error.

This is the case for reactions whose excitation energies are close to the barrier. But what happens if the system is initially in a more heated state?

To answer this question it is necessary to return to the problem discussed earlier. Recall that in subsection 5.3.1, we discussed the finite conditions for a fissile system whose initial excitation energies clearly exceed the barrier values. The subject was the fission reaction ^{235}U with very fast neutrons ($\approx 15 MeV$), and one of the main conclusions is that conditions of the type (5.8) peculiar to near-barrier reactions are not satisfied. Only when the configuration space was extended along the q_2 coordinate (from 2.35 to $2.7 - 2.9$), the fission characteristics could be better described. This mainly concerns the valley of symmetric fission, whose contribution increases with higher initial excitation energy.

Some hints/directions to overcome this problem by changing the final conditions were identified there. The first direction is to abandon the strict adherence (5.8) and "primate" the neck radius condition, i.e., when the limit of the configuration space is reached, the

system can be considered to decay despite the critical value of the neck radius of the system r_{neck}^{stop}. The introduction of such conditions allowed to significantly improve the description of asymmetric fission, rejecting a considerable number of "unphysical" configurations not typical for thermal neutron fission of the nucleus ^{235}U. And it seems that removing this constraint for reactions with higher excitation energies will improve the calculated FMDs without requiring the use of extended nuclear surface configurations. To be more certain, let us assume that once q_2^{max} is reached, a check is also made on the coordinate q_4; if it is positive, the trajectory is not considered. This check is a hedge against configurations with very thick necks. Figure 5.56 shows FMDs obtained under such an assumption. In this case, one of the most important computational conditions related to finding the system in a strictly defined configuration space remains untouched.

The second direction is also related to the value associated with the dependence of the critical radius on the initial excitation energy, which is assumed to be linear in this situation. Since we will not consider the fission of a system whose initial excitation energy does not exceed 40 MeV, we can assume that for about every 20 MeV there is a shift by a value of about r_n, as described earlier 5.3.3. Of course, when using a Gaussian distribution on r_{neck}^{stop}, the neck variation will be adjusted to fit the new range. For example, if $E_{init}^{*} \leq 20$ MeV it will remain the same, i.e. $\xi(r_n, 0.5r_n)$, while at higher energies the generator will be $\xi(r_n, r_n)$.

It should be noted in advance that the proposed solution method is probably not

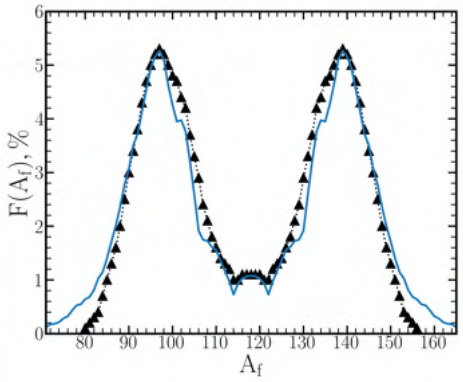

(a) for induced fission of ^{235}U by 15 MeV neutrons

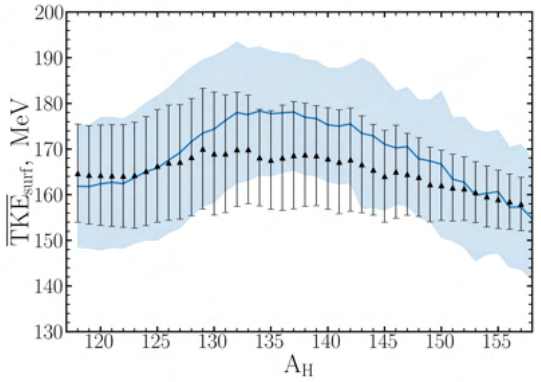

(b) for induced fission of ^{235}U by 15 MeV neutrons

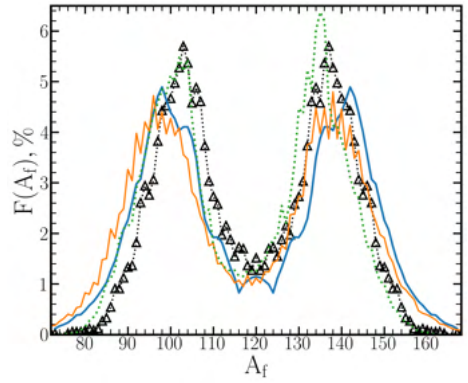

(c) for induced fission of ^{239}Pu by 13.5 MeV neutrons

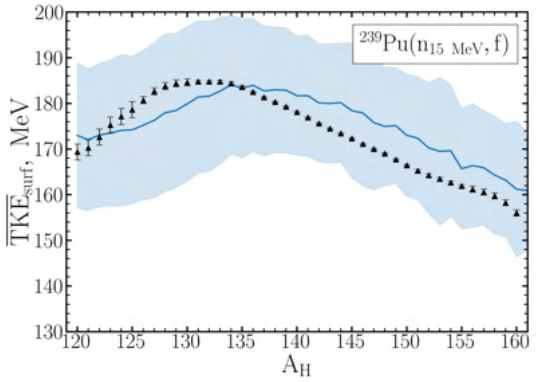

(d) for induced fission of ^{239}Pu by 15 MeV neutrons

Figure 5.56: Comparison of calculated primary (blue solid) and secondary (orange solid) FMDs and TKEs with available data from ENDF-model (green dotted) and experimental data for various fission reactions by very fast neutrons.

universal, since it will only be successfully tested on two reactions of forced nuclear fission of ^{235}U and ^{239}Pu by fast neutrons, which is not enough to fully confirm the validity of the approach.

Thus, using the above introductions from Fig. 5.56a, it is noticeable that the calculated primary FMD for the fission reaction of nuclei ^{235}U by 15 MeV neutrons agrees well with the available analogous data obtained from experiments. There is a significant difference at the edges of the distribution, where an excess of fission product yields is observed. This is the price of using the described approach, since there is no boundary condition of the type (5.23) at q_2. This, in turn, relates to the reasoning about the accuracy of the determination of the masses of the fragments to be formed for cases where the system ruptures when $r_{neck}^{stop} > 0.25R_0$. Conversely, it is noteworthy that the values $\overline{\mathrm{TKE}}(\mathrm{A_H})$ shown in Fig. 5.56b are also quite well described. The overestimation of the region $A_H \in [128, 150]$ compared to 5.35b, where an almost perfect agreement between simulated and experimentally estimated distributions is observed, is of course due to the close masses and hence charges of the fission fragments.

Let us continue to analyze the following panels of Fig. 5.56. Now they are already related to the fission reaction of the isotope ^{239}Pu. In 5.56c the comparison of primary and secondary FMDs for the fission reaction of plutonium with neutrons at a slightly lower energy of 13.5 MeV than for uranium is presented. Unfortunately, there are no mass distribution data for the 15 MeV fission reaction (or its number of points ≤ 4) in the EXFOR database, in contrast to the mean TKE [171] values. Nevertheless, the comparison of the obtained results is quite interesting. In general, the behavior of the curves predicted by the model agrees with the available data. This is especially true for the description of the averaged TKE (see Fig. 5.56d), where the main differences are the underestimation of the magnitude as well as the shift of the maximum position towards heavier fragments, which is of course due to the mass distribution. Note that the previously described procedure of charge redistribution at the breakup of the compound nucleus is taken into account here. Unfortunately, the picture is worse for FMD. Of course, the presented data [172] refer to secondary FMD, so the comparison of primary and secondary FMD is not quite correct. But even after applying the available procedure, the neutron evaporation from the fragments formed after fission differs from the compared data - the fragments are very asymmetric, which is not observed in the experiment. This leads to the same idea mentioned in the previous subsection - the temperature change is small. It seems that the simple consideration of the conservation law is not sufficient to satisfy the solution of the Langevin equations even in the case of higher excitation energies (compared to thermal or even spontaneous fission reactions). On the other hand, the estimated ENDF-VIII data (green dotted line in Fig. 5.56c) also overestimate the secondary FMD bias for the reaction in question. It appears that the temperature effect is only one of the contributors to the available discrepancy.

A legitimate question arises: "Can this be applied to photon-induced reactions of thorium nuclei?" After all, thorium photo-fission reactions have relatively close excitations (about 5 MeV lower) than for uranium and plutonium fission by very fast neutrons. It is quite interesting how much the distributions can change under new conditions. Let us apply the approach introduced above to the isotopic chain of nuclei $^{222-228}$Th, FCDs and FMDs reconstructed from them, shown in Fig. 5.57. The comparative analysis shows a positive trend for the whole chain, improving the description of ^{226,228}Th. On the other hand, for the first half of the isotopes this introduction seems to be insufficient, since their qualitative and quantitative description is missing. Also, the transition from symmetric to asymmetric fission modes could not be reproduced, echoing a similar problem in the field of

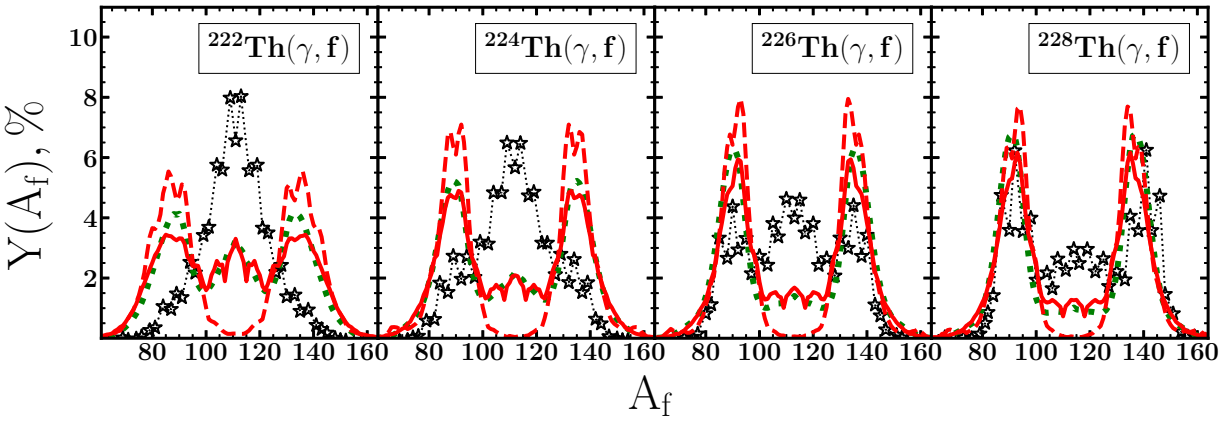

Figure 5.57: Comparison of FMDs for photo-fission reactions for even-even thorium nuclei. Red dashed line - simulated by previous final conditions, red solid line by new ones, green dashed line - data modeled in Ref. [41] , empty stars - obtained from available experimental FCDs.

heavy fermium-type actinides (see sections 5.3.3 and 5.4.1). Apparently, as already shown in [41], the problem of describing these FMDs (especially the first three) is directly related to the definition of their PES. This is confirmed by the closeness of FMDs to similar values calculated in static BOA. However, further discussion of the problems of PES construction is beyond the scope of this work.

Back to the fission reactions of the nuclei ^{235}U and ^{239}Pu by fast neutrons. More precisely, to the effect of neutron evaporation from the compound nucleus on the mass distributions, which is crucial for the other characteristics. The results comparing the primary and secondary FMDs without and with the evaporation procedure are shown in Fig. 5.58. It can be seen that the primary distributions for uranium and the secondary distribution for plutonium are essentially unchanged. At the same time, the number of events of neutrons escaping from compound nuclei has increased by more than an order of magnitude! At least according to the ratio of the number of emitted neutrons for the fission reaction ^{235}U by thermal and 15 MeV neutrons, shown in the lower panels of Fig. 5.55 and 5.58a, their ratio is 1 : 49. However, their number is not sufficient to change the primary or secondary distribution. Only the neutrons emitted after fission contribute to the distribution, because their amount is an order of magnitude greater. Therefore, to see a greater influence on the fission characteristics, the effect of particle evaporation is necessary:

- increase the number of particle species that can fly out of the compound nucleus,
- move into the region of large excitations,

which is what will be done next.

Proton and alpha-particle evaporation from compound nucleus

Having obtained reasonably good primary and secondary FMDs for the fission reactions of ^{235}U and ^{239}Pu nuclei by fast neutrons, let us investigate the influence of the effect of the escape of other particles from the compound fissile system ^{236}U in excited states $E^\star \geq 20$ MeV. However, this requires a revision of the form of the transport coefficient $w^{eff}(\epsilon)$, since the previously proposed estimate (5.38) applies only to neutrons.

For this purpose we will use the generalized coefficient $w_\nu^{eff}(\epsilon)$ proposed in [173]. In this work, while studying the transport coefficients of light particle emission from deformed

nuclei in the range of $70 \leq Z \leq 94$ and $160 \leq A \leq 240$, an approximate analytical form was proposed, which allows us to estimate the above coefficients quite accurately. In order to take into account the deformation of the core, the mentioned work assumes that the coefficient $w_\nu^{eff}(\epsilon)$ can be expressed in the following form:

$$w_v^{\text{eff}}(\varepsilon, \chi) = \frac{\int_S \tilde{w}_\nu(\varepsilon, i, \chi) d\sigma}{4\pi R_0^2} \equiv \tilde{w}_\nu(\varepsilon, \chi) B_{\text{surf}}, \tag{5.41}$$

where B_{surf} is the known ratio of the surface areas of the deformed and spherical nuclei, and $\tilde{w}^\nu$ is the average transmission coefficient per unit area. Its form, in addition to energy and particle type, also depends on other internal variables χ defined as the nucleon composition of the emitting nucleus, and its form can be expressed in generalized analytical form as

$$\begin{aligned} \tilde{w}_v(Z, A, \varepsilon) = &\left[\alpha_0 + \alpha_1 \xi + \alpha_2 \xi^2\right] \left[\beta_0 + \beta_1 \sigma + \beta_2 \sigma^2\right] \\ &\times \left[\tau_1 \omega + \tau_2 \omega^2 + \tau_3 \omega^3 + \tau_4 \omega^4\right]. \end{aligned} \tag{5.42}$$

Here the values ξ, σ, ω are dimensionless and represent the relations $\frac{Z}{Z_0}$, $\frac{A}{A_0}$, $\frac{\varepsilon}{\varepsilon_0}$, where the constant values Z_0, A_0, ε_0 are the same for all particle types and are assumed to be 80, 200, 20 MeV after the fitting process. The values before the dimensionless coefficients are given in Table 5.1.

Of course, strictly speaking, the coefficient $w_\nu^{eff}(\epsilon)$ should depend on the orbital momentum of the system L, but as shown in [173], the effect of the orbital momentum does not

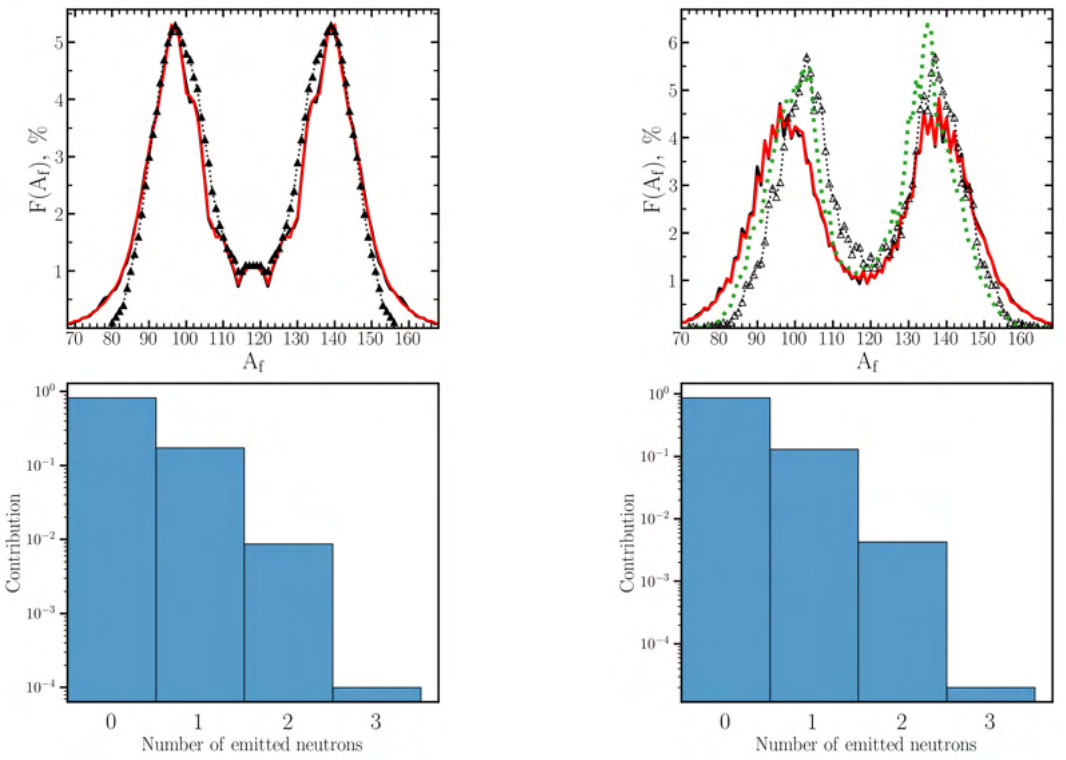

(a) Primary FMDs for fission of ^{235}U by 15 MeV neutrons

(b) Secondary FMDs for induced fission of ^{239}Pu by 13.5 MeV neutrons

Figure 5.58: Comparison primary and secondary FMDs calculated with usage (red) and without (black) neutron emission from compound nucleus with available data from ENDF-model (green dotted) and experimental data for fission reactions of ^{235}U and ^{239}Pu by very fast neutrons – top panels. On the bottom histogram of the contributions of the number of neutron emission events from compound nuclei.

Table 5.1: The fitting values from the formula (5.42) for each particle type.Taken from Ref. [173]

	Neutron	Proton	α-particle
α_0	–0.1884	–1.7084	–0.1250
α_1	0.1029	–2.1915	–0.0210
α_2	–0.0214	0.7253	0.0391
β_0	0.0582	0.1488	0.1848
β_1	0.5524	–0.1382	–0.0757
β_2	–0.1458	0.0533	0.0421
τ_1	–5.2039	1.034	2.2397
τ_2	2.2191	–3.340	–3.6214
τ_3	–0.8711	1.998	0.2884
τ_4	0.1621	–0.386	0.0894

exceed 5%. This further justifies not considering the spin-orbit interaction in the present work.

The algorithm for calculating the probability of departure of one of the particles from the compound nucleus is very similar to that described above, and also in the paper [136], where a similar problem was considered in the one-dimensional case. Very briefly, in the case of sufficient energy, first the partial widths for each of the particles are calculated, as in the previous subsection, then a Monte Carlo procedure is considered, where the total emission probability P, given by the formula (5.40), whose exponent includes the sum of the total widths Γ_ν, is compared with a random number ζ_1. If $P \geq \zeta_1$, the type and energy of the emitted particle is determined by another Monte Carlo procedure. For this, a new random number ζ_2 is generated and the resulting value is placed on a unit interval (normalized to $\sum_\nu \Gamma_\nu$). The lengths of the segments are proportional to the contributions to the total width, with the segment having the length of the neutron contribution first, followed by the proton contribution, and ending with the α particle contribution. The energy of the emitted particle is determined by the position of the number ζ_2 falling on one of the obtained segments.

Consider the resulting distributions for the system ^{236}U in the case of fission by very fast neutrons and at an excitation of the system around 40 MeV, which is sufficient to emit α-particles. The results of the calculations in terms of mass and charge distributions are shown in Figs 5.59, respectively. These are compared with FMDs obtained only for the cases of neutron emission from compound nuclei proposed in the previous subsection. Also, for clarity, the familiar histograms for the number of compound nucleus ejection events are shown in the bottom panel of the figures. It is easy to see that for the case of the 15 MeV neutron fission reaction, neither the FMD nor the FCD change practically. In fact, the main contributor to the change in the distributions remains the neutrons, whose total number remains practically unchanged: 19000 in the case of neutron emission alone versus 18300 when the emission of other particles is included. The total number of ejected protons is a value of 4300, of which about 4220 cases of ejection of a single proton from the compound system. It is therefore not surprising that the distributions obtained in Fig. 5.59a are very close to the result obtained earlier (see Fig. 5.58a). The situation is somewhat different when the system starts with higher energies. Thus, at the 40 MeV excitations shown in Fig. 5.59b, the distributions begin to show differences. Moreover, the differences in the mass distribution are smaller than in the charge distribution. Of course,

this is due to the increasing number of charged particles, primarily protons, which are not much less numerous than neutrons (46300 protons vs. 61000 neutrons). Thus, at higher energies, the probabilities of proton or neutron emission become close, which is expected since this result is consistent with the behavior of the transport coefficient (5.42) taken from [173]. However, the emission of α particles as seen in the last panel 5.59b is quite small, amounting to 1.1% of all trajectories, so its influence on the distribution is small. Probably in a more thermalized state, such as when the initial excitation energy of the system is 60 MeV from the ground state, the departure factor of the α particles will play as important a role in shaping the distributions as the protons. However, the spin-orbit interaction cannot be ignored in such states, which should be taken into account in future work.

Also, after a visual comparison of the mass and charge distributions shown in Fig. 5.59a and 5.59b, it can be seen that the latter are underestimated in the symmetric fission region, since a small increase is observed compared to the distributions of Fig. 5.59a. This can also be confirmed by looking at the second row of Fig. 5.11, where the temperature effect of the shell correction of the potential has been investigated. Other temperature effects are described in sections 5.2.2 and 5.2.3 do not play a significant role here. Therefore, the source of the discrepancy lies in the conditions imposed on the system. Consequently, the final conditions adopted in the previous subsection, which have worked well for fission in the 20 MeV energy region, are restricted here, but should be revised for medium energy fission. This will be done in the future.

This should summarize the subsection and the chapter as a whole. This subsection has shown some of the capabilities of the model developed in the course of studying nuclear fission. Using the Weisskopf formalism, the cases of evaporation of light particles from the compound fissile system in different excited states have been modeled. The results of the application of the procedure analogous to fission fragments are quite good, which can be characterized as follows: the higher the energy, the more particles evaporate from the compound system. Moreover, for excitation energies comparable to the fission barrier, the number of escape events does not exceed one percent, but at 4 times the probability of an event increases by a factor of 49. For other particles, the picture is similar, but their occurrence is in different ranges. Visible influence on the characteristics of nuclear fission, begin with excitation energies of the system ≈ 30 MeV, when the total number of departure events of light particles is close to the number of trajectories. However, the lack of empirical data has prevented more detailed and extensive studies on this subject.

Nevertheless, this chapter reflects the completeness of the work done to study low- and medium-energy fission of atomic nuclei using the semiclassical approach, whose basic ideas and methods were described in chapters 2 to 4. These were applied to the development of the model, which is based on the numerical solution of multidimensional stochastic differential Langevin equations. The first third of the Chapter was devoted to a brief introduction to the PES analysis, constructing the stable core of the model with further improvements including the dynamical variation of the excitation energy and the consequent effects on the microscopic and macroscopic properties of the nucleus. The second was related to the analysis and search for optimal boundary conditions imposed on the solutions of the Langevin equations. There, fission characteristics such as the distributions of masses, charges, and total kinetic energies were obtained for even-even nuclei with charge number in the region $[90, 116]$. Finally, the last third was devoted to the study of particle evaporation from fission fragments and compound nuclei. As mentioned above, the developed model reproduces well a wide range of primary/secondary mass and charge

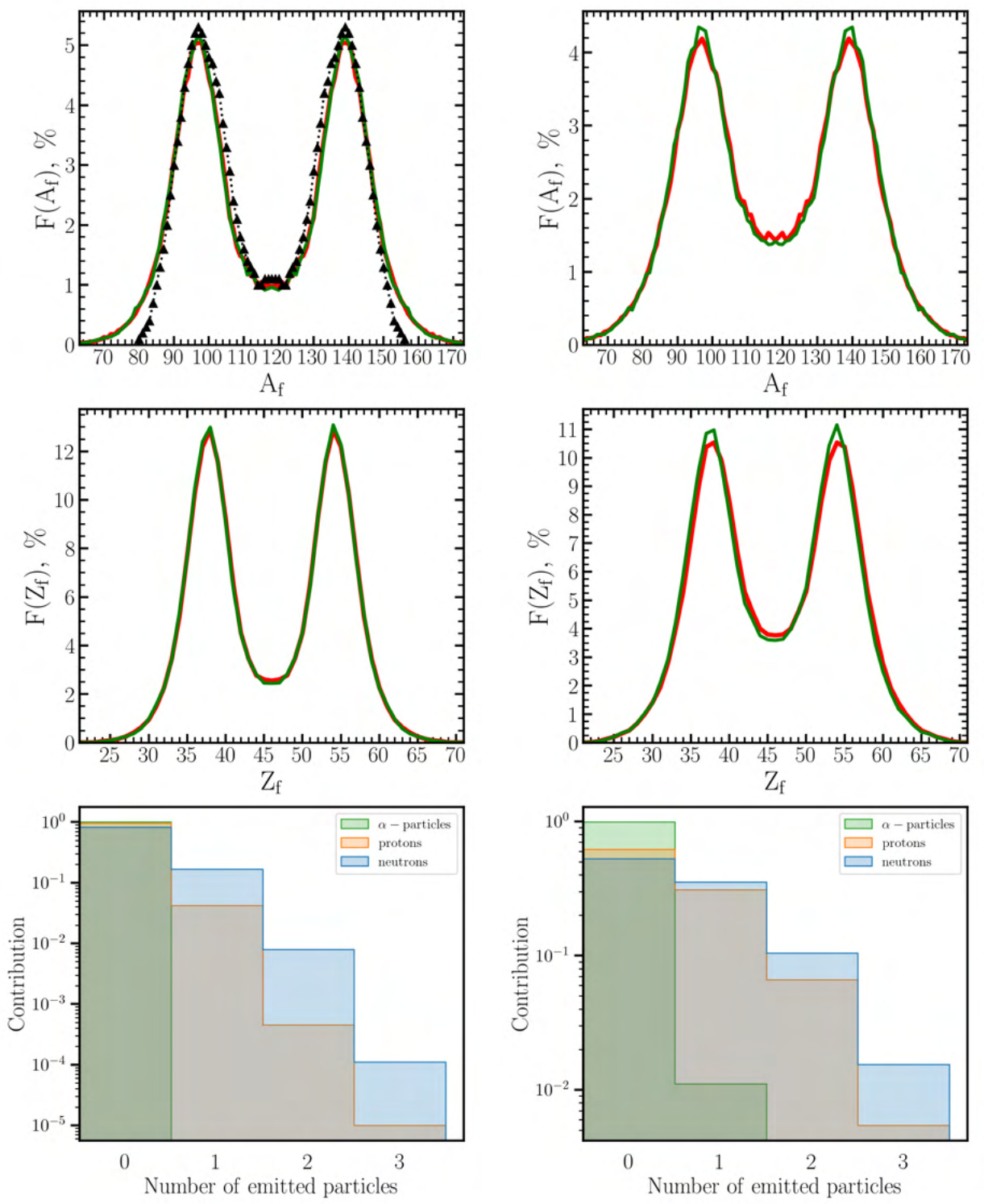

(a) Fission of ^{235}U by 15 MeV neutrons

(b) Fission of ^{236}U with initial excitation energy 40 MeV

Figure 5.59: Top panels: comparison of primary FMDs simulated within the particle emission procedure including only neutrons (red) and all particles (green) and available experimental data (for 15 MeV neutrons). Middle panels: same comparison for FCDs. Bottom panels: histogram of the contributions of the number of particle emission events from compound nuclei.

distributions of fission fragments, as well as their total kinetic energies. It is particularly good at reproducing the fission characteristics of the well-studied fission reactions ^{235}U and ^{239}Pu. Everything except the neutron emission from the fission fragments. There are only speculations as to the reasons for this discrepancy, but they are only hypothetical in nature. However, a more detailed review of the work done will be given in the next and final chapter of this work.

Summary

At the end ...

Before summarizing the results, I think it is not superfluous to make a brief summary of the work. Thus, in the present work an attempt has been made to describe the processes occurring during the fission of atomic nuclei using the macroscopic-microscopic model of the nucleus and the dissipative approach corresponding to the formalism of stochastic multidimensional Langevin equations.

In the Chapter 1, the author describes his motivation in choosing his field of interest for the problem he is considering. A brief excursion into the modern representation of atomic fission and theoretical nuclear physics is made. The basic concepts of the fission process are postulated. A brief review is given of the main theoretical approaches and methods used to study the nuclear fission process, which unfortunately have their advantages and disadvantages. It is emphasized that the main problem faced by any researcher in this field is the incredibly high complexity of the description of the nuclear fission process itself. This is expressed in the fact that there is still no generalized or unified theory of nuclear fission [1], which could describe the vast majority of the characteristics of fission. And at present, for the most part, it remains a phenomenological discipline. Moreover, even in the approaches taken, one has to balance computational speed and accuracy in predicting fission characteristics. And the following chapters are briefly explained.

Chapter 2 discusses the approach used to describe the properties of the atomic nucleus. For this purpose, the author uses a macroscopic-microscopic model of the nucleus based on two apparently contradictory representations: a liquid drop and a manybody Fermi system from the solid state. The binding energy of the system is described by the semi-phenomenological formula of the Lublin-Strasbourg Drop model. This formula has excellent performance in describing the reported energies in the range of nuclei of interest to the author. The account of shell corrections and pairing is carried out by the Strutinsky method, where the single-particle states of the nucleons are calculated in the Yukawa-folded mean-field potential, and the use of the Hartree-Fock-Bogoliubov approximation made it possible to take into account pair correlations. Of course, these components are described for different deformations of the nuclei, from which multidimensional PESs are constructed.

Therefore, the next issue raised, which was the focus of the Chapter 3 of the thesis, is the shape parameterization of atomic nuclei. The following commonly used types of parameterization were briefly described: the Nilsson oscillator method, Cassini ovaloids, Trentalange-Koonin-Sierk, and Funny Hills. Another more modern and promising parameterization, which forms the nuclear surface profile by Fourier series expansions, was also briefly reviewed. In the same chapter, attention was also given to the description of the macroscopic properties of atomic nuclei, such as the inertia tensor and the friction tensor,

[1] alas, the monograph by Wildermuth and Tan is only a stepping stone to "this" theory

which vary with the deformation of the nucleus. For this purpose, a hydrodynamic model is used to describe the inertia tensor, and approaches to determine the friction by means of the "wall" formula, the "window" formula, and their "wall-window" combination are presented. The "wall" formula is preferred because of its simplicity of calculation, although the coarseness of this one-body approach is emphasized when the system is near its fracture point.

In Chapter 4, the formalism of the dissipative approach, represented by the Langevin equations (LE) and the Fokker-Planck equations (FPE), which consider the evolution of the kernel surface given by the collective coordinates, was briefly described. The first system of equations is very close to the classical system of Hamiltonian equations with the only difference that a nonlinear stochastic term with white noise properties is added to the conjugate momentum equation. The derivation of this equation is shown and its peculiarities are discussed. A similar procedure is carried out for the FPE. The relationship between the above equations is shown. The main difference between FPE and LE is the use of process probabilities, which is very useful in describing evaporation processes. However, it is impractical to use its multidimensional version, unlike LE. Therefore, the last part of the chapter was devoted to a brief explanation of the Weisskopf formalism for describing the departure probabilities of light particles from the nucleus.

Finally, in Chapter 5, the described methods and representations were brought together to create the model capable of predicting features such as mass distributions, charges, kinetic energies, and characteristics of the emitted light particles. Understanding the validity of the model was based on comparison with available analogous experimental data. Much attention was paid to a number of problems arising in the numerical solution of the multidimensional Langevin equations, including the choice of the dimensionality of the collective space, energy minimization, stability of the solutions, temperature effects and dependence of the transport coefficients, as well as the setting of clear boundary conditions. The analysis of PESs obtained within a macro-micro model facilitates the understanding of the problems involved, but is limited to the analysis of two-dimensional cross sections and three-dimensional surfaces. A serious influence of the boundary conditions on the fission characteristics, especially the boundary conditions associated with the breaking of the system into fission fragments, is demonstrated. Tested on the description of the primary and secondary fission characteristics of the compound nucleus ^{236}U at different initial excitations, it allowed us to describe a wide range of even-even nuclei. This is the range of actinide and superheavy nuclei that undergo both forced and spontaneous fission. A comparative analysis showed a good fit to the available data. Subsequently, procedures for the evaporation of light particles, both from the compound nucleus and from the fission fragments formed, were added to the model. Despite the initial success, the secondary properties could not be described as well as the primary fragments.

Therefore, it is possible to summarize the results at once with the problems that the author was not able to overcome in the present work:

- Probably the most serious of them is the **unstable boundary conditions** imposed on the system of Langevin equations. In fact, the present model is based on solving a set of differential multidimensional equations, so both initial and final conditions must be strictly defined.

  The choice of the initial point, even excluding from consideration the first stages of nuclear fission in the form of transitions from the ground state region to the isomeric and isomeric to the last barrier (see figs. 1.1, 1.2 and 5.1), strongly affects the fission characteristics. This is especially noticeable in the case of spontaneous fission, where only one and apparently few exit points are defined. For induced

fission, this approach is still advantageous, since it is assumed that the system has enough energy to overcome the barriers and a small energy reserve remains. Note that the shape of the distribution of the next point in the neighborhood of the starting point does not affect the properties. Of course, this is within "reasonable" limits: the system should tend to descend from the barrier, and the fluctuation from the starting point in multidimensional space should not be large. In other words, if, for example, the starting point is in the region of an asymmetric fission path, then the next configuration in the iteration should not be very different from the previous one, thus preserving the adiabaticity of the process.

The final conditions are even more difficult to understand, since they are related to the vague notion of a breakpoint. In fact, it has been confirmed that the use of a representation of the neck thickness in the nucleon size is quite satisfactory for characterization, and it is not necessary to search for fission lines where configurations have a zero neck value. Nevertheless, a constant value of the neck size is not consistent with the quantum nature of fission and is a serious assumption in the stochastic approach used. Why can't it decay at a larger thickness? The search for a suitable procedure that could be consistent with the random nature of fission led to a rather strange description. The optimal procedure turned out to be one that replaced the finite neck thickness by a continuous Gaussian distribution. The fit on a series of even-even actinide nuclei showed a very good result. But not for all, e.g. for chains of thorium and fermium nuclei the results leave much to be desired... Coupled with the initial conditions, the bimodal behavior of the mass distributions cannot be described. Due to the nature of the distribution, the system cannot fully account for the nature of compact or conversely elongated types of configurations. There are also problems with the description of more initially heated cores, where it is necessary to remove the strict limitation of the gap of the system by the thickness of the neck.

- **Changes in system excitation and temperature effects**. The relatively simple method proposed in the book by Krappe and Pomorsky is unfortunately not fully realizable when solving the above system of equations. Simplified ways to take into account the law of conservation of energy assume that the system must heat up as it descends from the barrier. It has been shown that this is also difficult to realize within the framework of the stochastic method for low-energy fission. Constant control of the change of the excitation energy of the system leads to a large number of "unphysical" trajectories. A compromise is the use of energy redefinition at times close to the relaxation times of the system. However, even here there is a problem related to the times of descent from the barrier. They are relatively short. Their value in the framework of the applied approach does not exceed two orders of magnitude of the characteristic relaxation time. At the same time, the last moments before the break of the system are very important, giving information about the energy transferred to the excitation energy of the formed fission fragments.

- **Emission of light particles from fission fragments and compound nucleus**. This work attempts to account for neutron emission from fission fragments. The secondary mass distributions of spontaneous fission and thermal neutron-induced fission were analyzed using Weisskopf-type width calculations, which showed a discrepancy with the available data. The main reason was found to be an unclear determination of the excitation energy. Moving to large initial excitations of the system, the situation becomes somewhat better. For fission by neutrons with energies higher than 10 MeV. The only problem observed there is the restriction of the phenomenological

formula to the region of the nuclei (the ceiling for ^{240}Pu).

- **Surface parameterization and grid calculations**. Using a representation of the constant neck thickness, it is possible to construct a line or, more precisely, a fission surface, the analysis of which gives insight into possible pre-fission configurations of the nuclear surfaces. As can be seen, due to computational limitations, a certain amount of configuration space has been used in this paper, which is not always suitable for the solution. This is the case both for the increasing contribution of the symmetric fission valley for actinides in the region of large stretching, and for the superasymmetric configurations for superheavy actinides. Unfortunately, despite the very successful parameterization in other aspects, the implicit correlation between the elongation coordinates and the neck parameter of the nucleus does not give an accurate determination of the aforementioned fission surface. This is probably why the use of a Gaussian thickness distribution at which the system decays diminishes this problem, but does not eliminate it.

  Another point is the approximation used to calculate the values on the grid. Yes, the Gauss-Hermite procedure used is very fast for calculating tabulated quantities. However, it is based on the use of equidistant nodes and can have serious discrepancies at the boundaries of the configuration space. Also, for a more accurate determination of the pre-fission configuration of the fissile system, the mesh should be progressively densified as it approaches the fission line.

Nevertheless, the problems encountered did not prevent the author from developing a model capable of describing well the fission characteristics of heavy and superheavy nuclei, including the mass distributions (primary and secondary), the charges of the fission fragments, and their total kinetic energies. A key advantage over other similar models is that it requires only three deformation parameters, whereas others give similar results using more coordinates. This is due to the Fourier parametrization, which allows the description of the nuclear surface and whose parameters are responsible for the strain, the mass asymmetry and the neck parameter. Formally, it is not difficult to add a non-axial nucleus shape to the calculations – all the necessary ingredients for such calculations are available. Taking advantage of the assumption that the system overcomes the barrier also speeds up the calculation considerably. Finally, using the Gauss-Hermite approximation greatly accelerates the calculations. With the tabulated values of the transport coefficients and the PES for a given compound nucleus, one can obtain statistics on hundreds of thousands of trajectories in a few hours using an ordinary PC!

As has been shown, knowledge of the coordinate outputs, their conjugated momentum values, and the temperature of the system provides the key to visualizing a large number of observable and unobservable fission characteristics. While this model may fail in describing the thermalization of the compound nucleus and the fission fragments in the case of low-energy fission, a brief statistical analysis of the pre-breakup light particles emitted from the compound nucleus confirms the current understanding of the fission process. It is not difficult to modify the model so that the conditions of the conservation laws are satisfied, but this is more costly, but also feasible.

All this gives hope that, with further improvement of the model, it can become a fast and useful tool for studying the dynamics of various fission reactions, describing a larger number of fission characteristics.

The next small step?

As stated in the Introduction, the present work was not aimed at obtaining a comprehensive tool capable of describing the largest possible number of nuclear fission characteristics. The existing problems are not only related to the model itself, but also to the methods used, which are far from being complete. Moreover, it was assumed that this work would be only a small step in the direction of eliminating the present drawbacks in the description of nuclear fission.

Therefore, the present model needs to be further developed. Here are some ways to improve the developed model, which, in the author's opinion, will improve the understanding of the nuclear fission process:

- Use a better kind of parameterization based on Fourier parameterization.
- Using nonlinear lattice approaches and extending the Gauss-Hermite method to similar lattices.
- Continue research to find the relationship between system heating and random neck cracking.
- Introduce orbital interaction into the model.
- Expand the range of nuclei studied toward the intermediate nuclei $Z < 90$.
- Attempt to include fusion reactions of superheavy nuclei.

Ironic that this study, like all the others, does not set a point for any part of the understanding of nuclear fission, but only questions and thoughtful ellipses...

Appendix

The presented mathematical model is based on several software packages. Some of them were made by members of the research group in which the author belongs. For example, the program calculating the single particle energies for macroscopic-microscopic potential can be found in Ref. [62]. Other macroscopic parameters like inertia tensor and friction tensor can be found in Ref. [81] calculating in the framework of Fourier parametrization. The language of the programs is Fortran.

The author of this paper has independently developed programs using the Python 3 language to compute and visualize solutions to a multivariate system of equations. A repository for the available package will be found at the following link:

https://github.com/pvkostryukov/FEL3D

there is also an instruction on how to use this package.

Below are some of the representations used in the calculations.

Deformation functions of the LSD model

The relative surface area $B_{sur} = S(def)/S(0)$ of the deformed core is defined as follows

$$B_{sur} = \frac{1}{4\pi R_0^2} \int_{-z_0}^{z_0} dz \int_0^{2\pi} \sqrt{\rho^2 + \left(\frac{\partial \rho}{\partial \varphi}\right)^2 + \left(\rho \frac{\partial \rho}{\partial z}\right)^2}\, d\varphi \ . \tag{A.43}$$

The parameter B_{cur}, which is also included in the LSD formula, describes the relative change in the 1st order curvature of the deformed drop, in the following form

$$B_{cur} = \frac{1}{8\pi R_0} \iint_{\Sigma} \left(\frac{1}{R_1} + \frac{1}{R_2}\right) dS, \tag{A.44}$$

with $R_1(z,\varphi)$ and $R_2(z,\varphi)$ being the local principal radii of the surface. This parameter is equal in cylindrical coordinates to

$$\begin{aligned} B_{cur} = \frac{1}{8\pi R_0} \int_{z_{min}}^{z_{max}} dz \int_0^{2\pi} & \left\{ \rho^2 + \rho^2 \left(\frac{\partial \rho}{\partial z}\right)^2 + \left(\frac{\partial \rho}{\partial \varphi}\right)^2 \right\}^{-1} \times \\ & \times \left\{ \rho^2 \left(\frac{\partial \rho}{\partial z}\right)^2 - \rho \left(\frac{\partial \rho}{\partial z}\right)^2 \frac{\partial^2 \rho}{\partial \varphi^2} + \rho^2 - \rho \frac{\partial^2 \rho}{\partial \varphi^2} + 2 \left(\frac{\partial \rho}{\partial \varphi}\right)^2 \right. \\ & \left. + 2 \frac{\partial \rho}{\partial z} \frac{\partial \rho}{\partial \varphi} \rho \frac{\partial^2 \rho}{\partial z \partial \varphi} - \rho^3 \frac{\partial^2 \rho}{\partial z^2} - \rho \frac{\partial^2 \rho}{\partial z^2} \left(\frac{\partial \rho}{\partial \varphi}\right)^2 \right\} d\varphi \ . \end{aligned} \tag{A.45}$$

Gauss–Hermite approximation formula

When discussing the problem of multidimensional potential energy surfaces, we face the problem of approximation of energy values between multidimensional points in the deformation space. For the two-dimensional case it is simple, for the three-dimensional case – somewhat more complicated, and for the four-dimensional deformation mesh it requires a lot of effort.

Pomorski proposed [77] a very efficient method for approximating the multidimensional function, using Strutinsky's well-known idea of the corrected Gaussian addition procedure applied to shell correction. We will restrict ourselves here to the main points of this idea.

We consider an ensemble of N points x_i which must cover the entire interval $[a, b]$ and be ordered, i.e., $x_{i+1} > x_i$). Let x_i be the one-dimensional discrete argument of the function, and let $y_i = y(x_i)$ be its value at a given point.

Let $j_n(x, x')$ be a symmetric function of its arguments (i.e., $j_n(x, x') = j_n(x', x)$) having the following properties:

$$\int_{-\infty}^{+\infty} j_n(x, x')\, dx = 1. \tag{A.46}$$

Now, following Strutinsky, suppose that

$$P_k(x) = \int_{-\infty}^{+\infty} P_k(x')\, j_n(x, x')\, dx' \ , \tag{A.47}$$

where $k \leq n$ are even natural numbers and P_k is an arbitrary polynomial of order k. In the following, we will call the function $j_n(x, x')$ an addition function of order n^{th}. Let each discrete point (x_i, y_i) be represented by the function $\widetilde{y}_i(x)$ defined as

$$\widetilde{y}_i(x) = \int_{-\infty}^{+\infty} y_i\, \delta(x' - x_i)\, j_n(x, x')\, dx' \ , \tag{A.48}$$

where $\delta(x)$ is the δ-function of Dirac, so that

$$\widetilde{y}_i(x) = y_i\, j_n(x, x_i) \ . \tag{A.49}$$

We note immediately that the above operation turns a well-defined point in the coordinate system into an object like a "diffuse wave packet".

Using (A.46), which says that every addition function must be normalized to one, we have that

$$\int_{-\infty}^{+\infty} \widetilde{y}_i(x)\, dx = y_i \ . \tag{A.50}$$

Now construct the function $\widetilde{y}(x)$ by summing all functions $\widetilde{y}_i(x)$ corresponding to each point x_i.

$$\widetilde{y}(x) = \sum_{i=1}^{N} \omega_i\, \widetilde{y}_i(x) \ . \tag{A.51}$$

Now the function $\widetilde{y}(x)$ is an approximation of $y(x)$ if the weights ω_i are determined under the assumption that the integrals of the original and summed functions are (approximately) equal:

$$\int_a^b y(x)\, dx \approx \int_{-\infty}^{+\infty} \widetilde{y}(x)\, dx = \sum_{i=1}^{N} \omega_i\, y_i \ . \tag{A.52}$$

The Riemann summation formula for the integral of the function $y(x)$ between limits a and b gives

$$\int_a^b y(x)\,dx = \lim_{N\to\infty} \sum_{i=1}^{N} y(x_i)\,\Delta x_i \ , \tag{A.53}$$

where Δx_i is chosen at the midpoint of the distance between neighboring points of the argument

$$\Delta x_i = \frac{1}{2}\,(x_{i+1} - x_{i-1}) \tag{A.54}$$

where $x_0 = a$ and $x_{N+1} = b$. Comparing the Eqs. (A.52) and (A.53), it can be seen that a reasonable choice of weight would be

$$\omega_i = \Delta x_i \ . \tag{A.55}$$

If the number of N pairs of samples (x_i, y_i) is sufficiently large, then the condition (A.52)) is satisfied quite strictly.

Finally, the convolution function $\widetilde{y}(x)$, which approximates the true function $y(x)$, is of the form

$$\widetilde{y}(x) = \sum_{i=1}^{N} y_i\,\Delta x_i\,j_n(x, x_i) \ . \tag{A.56}$$

Let the folding function $j_n(x, x')$ be a modified Gauss function

$$j_n(x, x') = \frac{1}{\gamma\sqrt{\pi}} \exp\left\{-\left(\frac{x - x'}{\gamma}\right)^2\right\} f_n\left(\frac{x - x'}{\gamma}\right) \ , \tag{A.57}$$

where γ is the parameter and $f_n(\frac{x-x'}{\gamma})$ is the so-called correcting polynomial of order n defined by the Strutinsky condition (**??**). By performing calculations similar to those in Strutinsky's description of the shell correction, we obtain explicit expressions for the correction polynomials f_n, (where $u = \frac{x-x'}{\gamma}$):

$$\begin{aligned} f_0(u) &= 1 \ , \\ f_2(u) &= \tfrac{3}{2} - u^2 \ , \\ f_4(u) &= \tfrac{15}{8} - \tfrac{5}{2}u^2 + \tfrac{1}{2}u^4 \ , \\ f_6(u) &= \tfrac{35}{16} - \tfrac{35}{8}u^2 + \tfrac{7}{4}u^4 - \tfrac{1}{6}u^6 \ , \end{aligned} \tag{A.58}$$

Finally, the function $\widetilde{y}(x)$ approximated by the Gauss-Hermite addition function is of the form:

$$\widetilde{y}(x) = \frac{1}{\gamma\sqrt{\pi}} \sum_{i=1}^{N} y_i\,\Delta x_i \exp\left\{-\left(\frac{x - x_i}{\gamma}\right)^2\right\} f_n\left(\frac{x - x_i}{\gamma}\right) \ . \tag{A.59}$$

Since our goal is to approximate the function stored in the grid $\{x_i, y_i\}$, the smearing parameter γ must be related to the distance Δx_i between successive points. The equation (A.59) can be directly generalized to the multidimensional case (see Ref. [77]).

Bibliography

[1] L. Meitner and O. R. Frisch, Nature **143**, 239 (1939), URL https://doi.org/10.1038/143239a0.

[2] N. Bohr and J. A. Wheeler, Phys. Rev. **56**, 426 (1939), URL https://link.aps.org/doi/10.1103/PhysRev.56.426.

[3] J. Frenkel, Phys. Rev. **55**, 987 (1939), URL https://link.aps.org/doi/10.1103/PhysRev.55.987.

[4] M. Bender, R. Bernard, G. Bertsch, S. Chiba, J. Dobaczewski, N. Dubray, S. A. Giuliani, K. Hagino, D. Lacroix, Z. Li, et al., J. Phys. G: Nucl. Part. Phys. **47**, 113002 (2020), URL https://iopscience.iop.org/article/10.1088/1361-6471/abab4f.

[5] D. J. Hinde, Nuclear Physics A **553**, 255 (1993), URL https://www.sciencedirect.com/science/article/pii/037594749390627A.

[6] D. Jacquet and M. Morjean, Progress in Particle and Nuclear Physics **63**, 155 (2009), URL https://www.sciencedirect.com/science/article/pii/S0146641008000756.

[7] M. O. Frégeau, D. Jacquet, M. Morjean, E. Bonnet, A. Chbihi, J. D. Frankland, M. F. Rivet, L. Tassan-Got, F. Dechery, A. Drouart, et al., Phys. Rev. Lett. **108**, 122701 (2012), publisher: American Physical Society, URL https://link.aps.org/doi/10.1103/PhysRevLett.108.122701.

[8] A. K. Sikdar, A. Ray, D. Pandit, B. Dey, S. Bhattacharyya, S. Bhattacharya, A. Bisoi, A. De, S. Paul, S. Bhattacharya, et al., Phys. Rev. C **98**, 024615 (2018), publisher: American Physical Society, URL https://link.aps.org/doi/10.1103/PhysRevC.98.024615.

[9] C. Simenel and A. S. Umar, Progress in Particle and Nuclear Physics **103**, 19 (2018), URL https://www.sciencedirect.com/science/article/pii/S0146641018300693.

[10] K. Sekizawa, Frontiers in Physics **7** (2019), URL https://www.frontiersin.org/articles/10.3389/fphy.2019.00020.

[11] A. Bulgac, P. Magierski, K. J. Roche, and I. Stetcu, Phys. Rev. Lett. **116**, 122504 (2016), URL https://link.aps.org/doi/10.1103/PhysRevLett.116.122504.

[12] Y. Hashimoto and G. Scamps, Phys. Rev. C **94**, 014610 (2016), URL https://link.aps.org/doi/10.1103/PhysRevC.94.014610.

[13] G. Scamps and Y. Hashimoto, Phys. Rev. C **96**, 031602 (2017), publisher: American Physical Society, URL https://link.aps.org/doi/10.1103/PhysRevC.96.031602.

[14] P. Magierski, K. Sekizawa, and G. Wlazłowski, Phys. Rev. Lett. **119**, 042501 (2017), publisher: American Physical Society, URL https://link.aps.org/doi/10.1103/PhysRevLett.119.042501.

[15] A. Bulgac, Phys. Rev. C **100**, 034612 (2019), publisher: American Physical Society, URL https://link.aps.org/doi/10.1103/PhysRevC.100.034612.

[16] A. K. Kerman and S. E. Koonin, Annals of Physics **100**, 332 (1976), URL https://www.sciencedirect.com/science/article/pii/0003491676900658.

[17] R. Kubo, Rep. Prog. Phys. **29**, 255 (1966), URL https://iopscience.iop.org/article/10.1088/0034-4885/29/1/306.

[18] H. S. Yamada and K. S. Ikeda, Eur. Phys. J. B **85**, 41 (2012), ISSN 1434-6036, URL https://doi.org/10.1140/epjb/e2011-20811-8.

[19] J. Randrup and P. Möller, Phys. Rev. Lett. **106**, 132503 (2011), URL https://link.aps.org/doi/10.1103/PhysRevLett.106.132503.

[20] A. J. Sierk, Phys. Rev. C **96**, 034603 (2017), URL https://link.aps.org/doi/10.1103/PhysRevC.96.034603.

[21] L.-L. Liu, X.-Z. Wu, Y.-J. Chen, C.-W. Shen, Z.-X. Li, and Z.-G. Ge, Phys. Rev. C **99**, 044614 (2019), URL https://link.aps.org/doi/10.1103/PhysRevC.99.044614.

[22] M. D. Usang, F. A. Ivanyuk, C. Ishizuka, and S. Chiba, Scientific reports **9**, 1525 (2019).

[23] K. Pomorski and B. Nerlo-Pomorska, Acta Phys. Pol. B Proc. Suppl. **16**, 1 (2023), URL http://www.actaphys.uj.edu.pl/findarticle?series=Sup&vol=16&aid=4-A21.

[24] G. Schütte and L. Wilets, Phys. Rev. C **12**, 2100 (1975), URL https://link.aps.org/doi/10.1103/PhysRevC.12.2100.

[25] V. M. Strutinsky, Z Physik A **280**, 99 (1977), URL https://doi.org/10.1007/BF01438114.

[26] W. Nazarewicz, Nuclear Physics A **557**, 489 (1993), URL https://www.sciencedirect.com/science/article/pii/037594749390565F.

[27] T. Marumori, T. Maskawa, F. Sakata, and A. Kuriyama, Progress of Theoretical Physics **64**, 1294 (1980), URL https://doi.org/10.1143/PTP.64.1294.

[28] M. Matsuo, T. Nakatsukasa, and K. Matsuyanagi, Progress of Theoretical Physics **103**, 959 (2000), URL https://doi.org/10.1143/PTP.103.959.

[29] G. Scamps and K. Hagino, Phys. Rev. C **91**, 044606 (2015), publisher: American Physical Society, URL https://link.aps.org/doi/10.1103/PhysRevC.91.044606.

[30] C. F. v. Weizsecker, Z. Physik **96**, 431 (1935), URL http://link.springer.com/10.1007/BF01337700.

[31] H. A. Bethe and R. F. Bacher, Rev. Mod. Phys. **8**, 82 (1936), URL https://link.aps.org/doi/10.1103/RevModPhys.8.82.

[32] D. L. Hill and J. A. Wheeler, Phys. Rev. **89**, 1102 (1953), URL https://link.aps.org/doi/10.1103/PhysRev.89.1102.

[33] A. N. Bohr and B. R. Mottelson, *Nuclear Structure (in 2 volumes)* (World Scientific Publishing Company, 1998).

[34] W. D. Myers and W. J. Swiatecki, Nuclear Physics **81**, 1 (1966), URL https://linkinghub.elsevier.com/retrieve/pii/0029558266906390.

[35] M. Mayer and J. Jensen, *Elementary Theory of Nuclear Shell Structure*, Structure of matter series (Wiley, 1955), ISBN 978-0-598-63414-6, URL https://books.google.ru/books?id=9g9RAAAAMAAJ.

[36] W. D. Myers and W. Swiatecki, Annals of Physics **55**, 395 (1969), URL https://linkinghub.elsevier.com/retrieve/pii/0003491669902024.

[37] H. v. Groote and E. Hilf, Nuclear Physics A **129**, 513 (1969), URL https://linkinghub.elsevier.com/retrieve/pii/0375947469906988.

[38] A. J. Sierk, Phys. Rev. C **33**, 2039 (1986), URL https://link.aps.org/doi/10.1103/PhysRevC.33.2039.

[39] K. Pomorski and J. Dudek, Phys. Rev. C **67**, 044316 (2003), URL https://link.aps.org/doi/10.1103/PhysRevC.67.044316.

[40] C. Schmitt, K. Pomorski, B. Nerlo-Pomorska, and J. Bartel, Phys. Rev. C **95**, 034612 (2017), URL https://link.aps.org/doi/10.1103/PhysRevC.95.034612.

[41] K. Pomorski, J. M. Blanco, P. V. Kostryukov, A. Dobrowolski, B. Nerlo-Pomorska, M. Warda, Z.-G. Xiao, Y.-J. Chen, L.-L. Liu, J.-L. Tian, et al., Chinese Phys. C **45**, 054109 (2021), URL https://iopscience.iop.org/article/10.1088/1674-1137/abec69.

[42] P. Möller, W. D. Myers, H. Sagawa, and S. Yoshida, Phys. Rev. Lett. **108**, 052501 (2012), URL https://link.aps.org/doi/10.1103/PhysRevLett.108.052501.

[43] L. G. Moretto, P. T. Lake, L. Phair, and J. B. Elliott, Phys. Rev. C **86**, 021303 (2012), URL https://link.aps.org/doi/10.1103/PhysRevC.86.021303.

[44] J. C. Slater, Phys. Rev. **81**, 385 (1951), publisher: American Physical Society, URL https://link.aps.org/doi/10.1103/PhysRev.81.385.

[45] P. Ring and P. Schuck, *The nuclear many body problem*, Texts and monographs in physics (Springer, Berlin Heidelberg, 2004), 1st ed., ISBN 978-3-540-21206-5.

[46] H. J. Krappe and K. Pomorski, *Theory of Nuclear Fission*, vol. 838 of *Lecture Notes in Physics* (Springer Berlin Heidelberg, Berlin, Heidelberg, 2012), ISBN 978-3-642-23514-6 978-3-642-23515-3, URL http://link.springer.com/10.1007/978-3-642-23515-3.

[47] M. Baranger, Phys. Rev. **122**, 992 (1961), URL https://link.aps.org/doi/10.1103/PhysRev.122.992.

[48] N. N. Bogolyubov, Sov. Phys. Usp. **2**, 236 (1959), URL https://iopscience.iop.org/article/10.1070/PU1959v002n02ABEH003122.

[49] D. Gogny, *Self-consistent pairing calculations* (North-Holland Publishing Company, Netherlands, 1975), ISBN 978-0-7204-0341-1, iNIS Reference Number: 7230042.

[50] S. Krieger, P. Bonche, H. Flocard, P. Quentin, and M. Weiss, Nuclear Physics A **517**, 275 (1990), URL https://www.sciencedirect.com/science/article/pii/037594749090035K.

[51] K. Sieja and A. Baran, Physical Review C **68**, 044308 (2003).

[52] G. Audi, A. Wapstra, and C. Thibault, Nuclear Physics A **729**, 337 (2003), URL https://www.sciencedirect.com/science/article/pii/S0375947403018098.

[53] H. J. Lipkin, Annals of Physics **9**, 272 (1960), URL https://linkinghub.elsevier.com/retrieve/pii/0003491660900324.

[54] Y. Nogami, Phys. Rev. **134**, B313 (1964), URL https://link.aps.org/doi/10.1103/PhysRev.134.B313.

[55] H. Pradhan, Y. Nogami, and J. Law, Nuclear Physics A **201**, 357 (1973), URL https://linkinghub.elsevier.com/retrieve/pii/0375947473900717.

[56] P. Möller and J. Nix, Nuclear Physics A **536**, 20 (1992), URL https://linkinghub.elsevier.com/retrieve/pii/037594749290244E.

[57] H. Krappe and S. Fadeev, Nuclear Physics A **645**, 559 (1999), URL https://linkinghub.elsevier.com/retrieve/pii/S0375947498006083.

[58] V. Surin, A. Sergachev, N. Rezchikov, and B. Kuz'minov, Yadern Fiz **17**, 935 (1971), place: USSR.

[59] K. T. R. Davies and J. R. Nix, Phys. Rev. C **14**, 1977 (1976), URL https://link.aps.org/doi/10.1103/PhysRevC.14.1977.

[60] A. Dobrowolski, Ph.D. thesis, Innterdiscplinary Institute Hubert Curie (2006).

[61] P. Möller, J. Nix, W. Myers, and W. Swiatecki, Atomic Data and Nuclear Data Tables **59**, 185 (1995), ISSN 0092-640X, URL https://www.sciencedirect.com/science/article/pii/S0092640X85710029.

[62] A. Dobrowolski, K. Pomorski, and J. Bartel, Computer Physics Communications **199**, 118 (2016), URL https://linkinghub.elsevier.com/retrieve/pii/S0010465515003720.

[63] H. A. Bethe and R. F. Bacher, Rev. Mod. Phys. **8**, 82 (1936), URL https://link.aps.org/doi/10.1103/RevModPhys.8.82.

[64] B. Nerlo-Pomorska and K. Pomorski, *Theory of Atomic Nuclei for Beginners* (????), unpublished.

[65] V. Strutinsky, Nuclear Physics A **95**, 420 (1967), URL https://linkinghub.elsevier.com/retrieve/pii/0375947467905106.

[66] M. Brack, J. Damgaard, A. S. Jensen, H. C. Pauli, V. M. Strutinsky, and C. Y. Wong, Rev. Mod. Phys. **44**, 320 (1972), URL https://link.aps.org/doi/10.1103/RevModPhys.44.320.

[67] A. Dobrowolski, Ph.D. thesis, Innterdiscplinary Institute Hubert Curie (2006).

[68] R. W. Hasse and W. D. Myers, *Geometrical Relationships of Macroscopic Nuclear Physics*, Springer Series in Nuclear and Particle Physics (Springer, Berlin, Heidelberg, 1988), ISBN 978-3-642-83019-8 978-3-642-83017-4, URL http://link.springer.com/10.1007/978-3-642-83017-4.

[69] S. G. Nilsson, *Binding states of individual nucleons in strongly deformed nuclei*, CERN Yellow Reports: Monographs (1955), dan. Mat. Fys. Medd.

[70] S. G. Nilsson, C. F. Tsang, A. Sobiczewski, Z. Szymański, S. Wycech, C. Gustafson, I.-L. Lamm, P. Möller, and B. Nilsson, Nuclear Physics A **131**, 1 (1969), URL https://www.sciencedirect.com/science/article/pii/0375947469908094.

[71] G. Adeev, P. Cherdantsev, and I. Gamalya, Physics Letters B **35**, 125 (1971), URL https://linkinghub.elsevier.com/retrieve/pii/0370269371902358.

[72] V. Pashkevich, Nuclear Physics A **169**, 275 (1971), URL https://linkinghub.elsevier.com/retrieve/pii/0375947471908840.

[73] J. N. Lawrence, Tech. Rep., Los Alamos National Lab.(LANL), Los Alamos, NM (United States) (1967).

[74] R. W. Hasse, Physics Letters B **27**, 605 (1968).

[75] R. W. Hasse, Nuclear Physics A **128**, 609 (1969).

[76] S. Trentalange, S. E. Koonin, and A. J. Sierk, Phys. Rev. C **22**, 1159 (1980), URL https://link.aps.org/doi/10.1103/PhysRevC.22.1159.

[77] K. Pomorski, Computer Physics Communications **174**, 181 (2006), URL https://linkinghub.elsevier.com/retrieve/pii/S0010465505005175.

[78] P. V. Kostryukov and A. Dobrowolski, Phys. Rev. C **108**, 024605 (2023), URL https://link.aps.org/doi/10.1103/PhysRevC.108.024605.

[79] K. T. R. Davies, A. J. Sierk, and J. R. Nix, Phys. Rev. C **13**, 2385 (1976), URL https://link.aps.org/doi/10.1103/PhysRevC.13.2385.

[80] J. Blocki, Y. Boneh, J. Nix, J. Randrup, M. Robel, A. Sierk, and W. Swiatecki, Annals of Physics **113**, 330 (1978), URL https://linkinghub.elsevier.com/retrieve/pii/0003491678902087.

[81] J. Bartel, B. Nerlo-Pomorska, K. Pomorski, and A. Dobrowolski, Computer Physics Communications **241**, 139 (2019), URL https://linkinghub.elsevier.com/retrieve/pii/S0010465519300888.

[82] H. Lamb, *Hydrodynamics* (New York,: Dover publications, 1945), URL http://archive.org/details/hydrodynamics00lamb.

[83] L. L. Wilets, *Theories of nuclear fission* (Oxford, Clarendon Press, 1964), URL http://archive.org/details/theoriesofnuclea0000wile.

[84] R. L. Hatch and A. J. Sierk, Nuclear Physics A **341**, 513 (1980), URL https://www.sciencedirect.com/science/article/pii/0375947480903814.

[85] U. Brosa and D. Gross, Zeitschrift für Physik A Atoms and Nuclei **298**, 91 (1980).

[86] S. Grossmann and H. J. Krappe, Phys. Rev. C **34**, 914 (1986), URL https://link.aps.org/doi/10.1103/PhysRevC.34.914.

[87] D. H. E. Gross, Nuclear Physics A **240**, 472 (1975), URL https://www.sciencedirect.com/science/article/pii/037594747590305X.

[88] H. Hofmann, F. A. Ivanyuk, and S. Yamaji, Nuclear Physics A **598**, 187 (1996).

[89] J. R. Nix and A. J. Sierk, Physical Review C **21**, 396 (1980).

[90] H. Hofmann, *The Physics of Warm Nuclei: with Analogies to Mesoscopic Systems* (OUP Oxford, 2008), ISBN 978-0-19-152306-9, google-Books-ID: pwlREAAAQBAJ.

[91] S. Pal and T. Mukhopadhyay, Phys. Rev. C **54**, 1333 (1996), URL https://link.aps.org/doi/10.1103/PhysRevC.54.1333.

[92] A. J. Sierk and J. R. Nix, Phys. Rev. C **21**, 982 (1980), publisher: American Physical Society, URL https://link.aps.org/doi/10.1103/PhysRevC.21.982.

[93] J. Randrup and W. Swiatecki, Annals of Physics **125**, 193 (1980), URL https://linkinghub.elsevier.com/retrieve/pii/0003491680901244.

[94] G. D. Adeev, A. Karpov, P. N. Nadtochy, and D. V. Vanin, p. 733 (2005).

[95] W. J. Swiatecki, J. Phys. Colloques **33**, C5 (1972), URL http://www.edpsciences.org/10.1051/jphyscol:1972505.

[96] J. Randrup, Annals of Physics **112**, 356 (1978), URL https://www.sciencedirect.com/science/article/pii/S0003491678800049.

[97] R. G. Seyler and C. H. Blanchard, Phys. Rev. **131**, 355 (1963), publisher: American Physical Society, URL https://link.aps.org/doi/10.1103/PhysRev.131.355.

[98] W. J. Swiatecki, Nuclear Physics A **428**, 199 (1984), URL https://www.sciencedirect.com/science/article/pii/0375947484902525.

[99] J. Rayford Nix and A. J. Sierk, Nuclear Physics A **428**, 161 (1984), ISSN 0375-9474, URL https://www.sciencedirect.com/science/article/pii/0375947484902495.

[100] J. Rayford Nix, Nuclear Physics A **130**, 241 (1969), URL https://www.sciencedirect.com/science/article/pii/0375947469907301.

[101] H. Feldmeier, Rep. Prog. Phys. **50**, 915 (1987), URL https://dx.doi.org/10.1088/0034-4885/50/8/001.

[102] J. Blocki, J. Phys. Colloques **45**, C6 (1984), publisher: EDP Sciences, URL http://dx.doi.org/10.1051/jphyscol:1984658.

[103] J. Blocki, F. Brut, T. Srokowski, and W. J. Swiatecki, Nuclear Physics A **545**, 511 (1992), URL https://www.sciencedirect.com/science/article/pii/0375947492904897.

[104] G. Benettin, L. Galgani, and J.-M. Strelcyn, Phys. Rev. A **14**, 2338 (1976), publisher: American Physical Society, URL https://link.aps.org/doi/10.1103/PhysRevA.14.2338.

[105] G. Chaudhuri and S. Pal, Phys. Rev. C **63**, 064603 (2001), publisher: American Physical Society, URL https://link.aps.org/doi/10.1103/PhysRevC.63.064603.

[106] G. Kosenko, F. Ivanyuk, and V. Pashkevich, Journal of Nuclear and Radiochemical Sciences **3**, 71 (2002).

[107] F. A. Ivanyuk and K. Pomorski, Phys. Rev. C **53**, 1861 (1996), URL https://link.aps.org/doi/10.1103/PhysRevC.53.1861.

[108] Y. Abe, C. Grégoire, and H. Delagrange, Journal de Physique Colloques **47**, C4 (1986), URL https://hal.archives-ouvertes.fr/jpa-00225802.

[109] Y. Abe, S. Ayik, P.-G. Reinhard, and E. Suraud, Physics Reports **275**, 49 (1996), URL https://linkinghub.elsevier.com/retrieve/pii/0370157396000038.

[110] C. Schmitt, J. Bartel, K. Pomorski, and A. Surowiec, arXiv preprint nucl-th/0206058 (2002).

[111] C. Schmitt, J. Bartel, A. Surowiec, and K. Pomorski, Acta Physica Polonica B **34**, 2135 (2003), aDS Bibcode: 2003AcPPB..34.2135S, URL https://ui.adsabs.harvard.edu/abs/2003AcPPB..34.2135S.

[112] S. Tanaka et al., Phys. Rev. C **100**, 064605 (2019), URL https://link.aps.org/doi/10.1103/PhysRevC.100.064605.

[113] K. Shimada, C. Ishizuka, F. A. Ivanyuk, and S. Chiba, Phys. Rev. C **104**, 054609 (2021), URL https://link.aps.org/doi/10.1103/PhysRevC.104.054609.

[114] L.-L. Liu, X.-Z. Wu, Y.-J. Chen, C.-W. Shen, Z.-G. Ge, and Z.-X. Li, Phys. Rev. C **105**, 034614 (2022), URL https://link.aps.org/doi/10.1103/PhysRevC.105.034614.

[115] P. V. Kostryukov, A. Dobrowolski, B. Nerlo-Pomorska, M. Warda, Z. Xiao, Y. Chen, L. Liu, J.-L. Tian, and K. Pomorski, Chinese Phys. C **45**, 124108 (2021), URL https://iopscience.iop.org/article/10.1088/1674-1137/ac29a3.

[116] P. Kostryukov and A. Dobrowolski, in *Proceedings of the 39-th International Workshop on Nuclear Theory (IWNT-39)* (Heron Press Ltd., Sofia, Bulgaria, 2022), URL http://ntl.inrne.bas.bg/workshop/2022/contributions/p164_2022.pdf.

[117] *Fokker-Planck Equation*, Springer Series in Synergetics (Berlin, Heidelberg, ????), ISBN 978-3-642-61544-3, URL https://doi.org/10.1007/978-3-642-61544-34.

[118] A. E. Gettinger and I. I. Gontchar, J. Phys. G: Nucl. Part. Phys. **26**, 347 (2000), URL https://dx.doi.org/10.1088/0954-3899/26/4/301.

[119] B. Nerlo-Pomorska, K. Pomorski, and J. Bartel, Phys. Rev. C **74**, 034327 (2006), URL https://link.aps.org/doi/10.1103/PhysRevC.74.034327.

[120] H. A. Weidenmüller and Z. Jing-Shang, J Stat Phys **34**, 191 (1984), URL https://doi.org/10.1007/BF01770354.

[121] D. J. Hinde, D. Hilscher, and H. Rossner, Nuclear Physics A **538**, 243 (1992), URL https://www.sciencedirect.com/science/article/pii/037594749290775F.

[122] E. Strumberger, K. Dietrich, and K. Pomorski, Nuclear Physics A **529**, 522 (1991), URL https://linkinghub.elsevier.com/retrieve/pii/037594749190584S.

[123] G. D. Adeev and V. V. Pashkevich, Nuclear Physics A **502**, 405 (1989), URL https://www.sciencedirect.com/science/article/pii/0375947489906799.

[124] C. Ngô and H. Hofmann, Z Physik A **282**, 83 (1977), URL https://doi.org/10.1007/BF01881009.

[125] S. Grossmann and H. J. Krappe, Z Physik A **298**, 41 (1980), URL https://doi.org/10.1007/BF01416027.

[126] P. Fröbrich, B. Strack, and M. Durand, Nuclear Physics A **406**, 557 (1983), URL https://www.sciencedirect.com/science/article/pii/0375947483903779.

[127] K. Pomorski and H. Hofmann, J. Phys. France **42**, 381 (1981), publisher: Société Française de Physique, URL http://dx.doi.org/10.1051/jphys:01981004203038100.

[128] G. D. Adeev and I. I. Gonchar, Z Physik A **320**, 451 (1985), URL https://doi.org/10.1007/BF01415722.

[129] P. Fröbrich and S. Y. Xu, Nuclear Physics A **477**, 143 (1988), URL https://www.sciencedirect.com/science/article/pii/0375947488903661.

[130] U. Brosa and W. Cassing, Z Physik A **307**, 167 (1982), URL https://doi.org/10.1007/BF01414832.

[131] F. Scheuter and H. Hofmann, Nuclear Physics A **394**, 477 (1983), URL https://www.sciencedirect.com/science/article/pii/0375947483901197.

[132] H. Delagrange, C. Gregoire, Y. Abe, and N. Carjan, in *International Conference on Heavy Ion Nuclear Collisions in the Fermi Energy Domain Hicofed 86* (Caen, France, 1986), vol. 47, pp. C4–305–C4–315, URL https://hal.archives-ouvertes.fr/jpa-00225800.

[133] A. Iwamoto and R. Herrmann, Z. Physik A - Hadrons and Nuclei **338**, 303 (1991), URL https://doi.org/10.1007/BF01288194.

[134] K. Dietrich, K. Pomorski, and J. Richert, Z. Physik A - Hadrons and Nuclei **351**, 397 (1995), URL https://doi.org/10.1007/BF01291145.

[135] P. Fröbrich, I. I. Gontchar, and N. D. Mavlitov, Nuclear Physics A **556**, 281 (1993), URL https://www.sciencedirect.com/science/article/pii/037594749390352X.

[136] K. Pomorski, J. Bartel, J. Richert, and K. Dietrich, Nuclear Physics A **605**, 87 (1996), place: Netherlands INIS Reference Number: 27071624.

[137] P. Fröbrich, Nuclear Physics A **545**, 87 (1992), URL https://www.sciencedirect.com/science/article/pii/037594749290449T.

[138] V. Weisskopf, Phys. Rev. **52**, 295 (1937), URL https://link.aps.org/doi/10.1103/PhysRev.52.295.

[139] L.-L. Liu, Y.-J. Chen, X.-Z. Wu, Z.-X. Li, Z.-G. Ge, and K. Pomorski, Phys. Rev. C **103**, 044601 (2021), URL https://link.aps.org/doi/10.1103/PhysRevC.103.044601.

[140] F. A. Ivanyuk, C. Ishizuka, M. D. Usang, and S. Chiba, Phys. Rev. C **97**, 054331 (2018), URL https://link.aps.org/doi/10.1103/PhysRevC.97.054331.

[141] A. Ignatyuk, G. Smirenkin, and A. Tishin, Yadernaya Fizika **21**, 485 (1975).

[142] G. Simon, J. Trochon, F. Brisard, and C. Signarbieux, Nuclear Instruments and Methods in Physics Research Section A: Accelerators, Spectrometers, Detectors and Associated Equipment **286**, 220 (1990), URL https://linkinghub.elsevier.com/retrieve/pii/016890029090224T.

[143] P. Dyachenko, B. Kuzminov, and M. Tarasko, Sov. J. Nucl. Phys. **8**, 165 (1969).

[144] F. A. Ivanyuk, Z. Physik A - Atomic Nuclei **334**, 69 (1989), URL http://link.springer.com/10.1007/BF01294388.

[145] H. Hofmann and D. Kiderlen, Int. J. Mod. Phys. E **07**, 243 (1998), URL https://www.worldscientific.com/doi/abs/10.1142/S0218301398000105.

[146] K. Mazurek et al., Eur. Phys. J. A **53**, 79 (2017), ISSN 1434-601X, URL https://doi.org/10.1140/epja/i2017-12262-1.

[147] P. Geltenbort, F. Gönnewein, and A. Oed (????).

[148] C. Romano, Y. Danon, R. Block, J. Thompson, E. Blain, and E. Bond, Phys. Rev. C **81**, 014607 (2010), publisher: American Physical Society, URL https://link.aps.org/doi/10.1103/PhysRevC.81.014607.

[149] K. H. Schmidt, B. Jurado, C. Amouroux, and C. Schmitt, Nuclear Data Sheets **131**, 107 (2016), URL https://www.sciencedirect.com/science/article/pii/S0090375215000745.

[150] L. Demattè, C. Wagemans, R. Barthélémy, P. D'hondt, and A. Deruytter, Nuclear Physics A **617**, 331 (1997), URL https://www.sciencedirect.com/science/article/pii/S0375947497000328.

[151] F. Pleasonton et al., Phys. Rev. C **8**, 1018 (1973), URL https://link.aps.org/doi/10.1103/PhysRevC.8.1018.

[152] D. C. Hoffman, J. B. Wilhelmy, J. Weber, W. R. Daniels, E. K. Hulet, R. W. Lougheed, J. H. Landrum, J. F. Wild, and R. J. Dupzyk, Phys. Rev. C **21**, 972 (1980), publisher: American Physical Society, URL https://link.aps.org/doi/10.1103/PhysRevC.21.972.

[153] D. C. Hoffman, D. M. Lee, K. E. Gregorich, M. J. Nurmia, R. B. Chadwick, K. B. Chen, K. R. Czerwinski, C. M. Gannett, H. L. Hall, R. A. Henderson, et al., Phys. Rev. C **41**, 631 (1990), publisher: American Physical Society, URL https://link.aps.org/doi/10.1103/PhysRevC.41.631.

[154] E. K. Hulet, J. F. Wild, R. J. Dougan, R. W. Lougheed, J. H. Landrum, A. D. Dougan, M. Schadel, R. L. Hahn, P. A. Baisden, C. M. Henderson, et al., Phys. Rev. Lett. **56**, 313 (1986), publisher: American Physical Society, URL https://link.aps.org/doi/10.1103/PhysRevLett.56.313.

[155] M. Borunov, P. Nadtochy, and G. Adeev, Nuclear Physics A **799**, 56 (2008), URL https://linkinghub.elsevier.com/retrieve/pii/S0375947407007828.

[156] K. H. Schmidt, S. Steinhäuser, C. Böckstiegel, A. Grewe, A. Heinz, A. R. Junghans, J. Benlliure, H. G. Clerc, M. de Jong, J. Müller, et al., Nuclear Physics A **665**, 221 (2000), URL https://www.sciencedirect.com/science/article/pii/S037594749900384X.

[157] A. Chatillon, J. Taïeb, H. Alvarez-Pol, L. Audouin, Y. Ayyad, G. Bélier, J. Benlliure, G. Boutoux, M. Caamaño, E. Casarejos, et al., Phys. Rev. C **99**, 054628 (2019), URL https://link.aps.org/doi/10.1103/PhysRevC.99.054628.

[158] K. Pomorski, F. A. Ivanyuk, and B. Nerlo-Pomorska, Eur. Phys. J. A **53**, 59 (2017), URL http://link.springer.com/10.1140/epja/i2017-12250-5.

[159] M. R. Lane, K. E. Gregorich, D. M. Lee, M. F. Mohar, M. Hsu, C. D. Kacher, B. Kadkhodayan, M. P. Neu, N. J. Stoyer, E. R. Sylwester, et al., Phys. Rev. C **53**, 2893 (1996), URL https://link.aps.org/doi/10.1103/PhysRevC.53.2893.

[160] M. Wang, G. Audi, F. G. Kondev, and X. Naimi, S.and Xing, Chinese Physics C **41**, 030003 (2017), URL https://dx.doi.org/10.1088/1674-1137/41/3/030003.

[161] J. Randrup and P. Möller, Phys. Rev. C **88**, 064606 (2013), publisher: American Physical Society, URL https://link.aps.org/doi/10.1103/PhysRevC.88.064606.

[162] Y. Aritomo, S. Chiba, and F. Ivanyuk, Phys. Rev. C **90**, 054609 (2014), publisher: American Physical Society, URL https://link.aps.org/doi/10.1103/PhysRevC.90.054609.

[163] M. Albertsson, B. G. Carlsson, T. Døssing, P. Möller, J. Randrup, and S. Åberg, Phys. Rev. C **103**, 014609 (2021), publisher: American Physical Society, URL https://link.aps.org/doi/10.1103/PhysRevC.103.014609.

[164] M. Verriere, N. Schunck, and D. Regnier, Phys. Rev. C **103**, 054602 (2021), publisher: American Physical Society, URL https://link.aps.org/doi/10.1103/PhysRevC.103.054602.

[165] P. Möller and T. Ichikawa, The European Physical Journal A **51**, 173 (2015), URL https://doi.org/10.1140/epja/i2015-15173-1.

[166] D. A. Brown, M. B. Chadwick, R. Capote, A. C. Kahler, A. Trkov, M. W. Herman, A. A. Sonzogni, Y. Danon, A. D. Carlson, M. Dunn, et al., Nuclear Data Sheets **148**, 1 (2018), URL https://www.sciencedirect.com/science/article/pii/S0090375218300206.

[167] I. Dostrovsky, Z. Fraenkel, and G. Friedlander, Phys. Rev. **116**, 683 (1959), URL https://link.aps.org/doi/10.1103/PhysRev.116.683.

[168] M. Asghar, C. Carles, R. Chastel, T. Doan, M. Ribrag, and C. Signarbieux, Nuclear Physics A **145**, 657 (1970).

[169] A. Al-Adili, D. Tarrío, K. Jansson, V. Rakopoulos, A. Solders, S. Pomp, A. Göök, F.-J. Hambsch, S. Oberstedt, and M. Vidali, Phys. Rev. C **102**, 064610 (2020), URL https://link.aps.org/doi/10.1103/PhysRevC.102.064610.

[170] H. Kramers, Physica **7**, 284 (1940), URL https://linkinghub.elsevier.com/retrieve/pii/S0031891440900982.

[171] V. Surin, A. Sergachev, N. Rezchikov, and B. Kuz'minov, Yadern Fiz **14**, 935 (1971), place: USSR, URL http://inis.iaea.org/search/search.aspx?orig_q=RN:03022964.

[172] A. Pica, A. T. Chemey, L. Yao, W. Loveland, H. Y. Lee, and S. A. Kuvin, Phys. Rev. C **102**, 064612 (2020), publisher: American Physical Society, URL https://link.aps.org/doi/10.1103/PhysRevC.102.064612.

[173] A. Dobrowolski, K. Pomorski, and J. Bartel, Phys. Scr. **T154**, 014030 (2013), URL https://iopscience.iop.org/article/10.1088/0031-8949/2013/T154/014030.